

AD-A250 213



AFOSR-TR- 92 0349

DTIC
S **ELECTE** **D**
MAY 19 1992
C

POLY-WRI-1589-92

**In-Situ Fault Detection by the
Hybrid Ray-Mode Method**

**Final Technical Report to
Air Force Office of Scientific Research
Grant No. AFOSR-90-0088**

Submitted by

Leopold B. Felsen
Polytechnic University
Weber Research Institute
Route 110
Farmingdale, New York 11758

April 20, 1992

DECLASSIFICATION STATEMENT A
Approved for public release;
Distribution Unlimited

92-13010



92 5 14 1315

REPORT DOCUMENTATION PAGE			Form Approved OMB No. 0704-0188	
Public reporting burden for this collection of information is estimated to average 1 hour per response, including the time for reviewing instructions, searching existing data sources, gathering and maintaining the data needed, and completing and reviewing the collection of information. Send comments regarding this burden estimate or any other aspect of this collection of information, including suggestions for reducing this burden, to Washington Headquarters Services, Directorate for Information Operations and Reports, 1215 Jefferson Davis Highway, Suite 1204, Arlington, VA 22202-4302, and to the Office of Management and Budget, Paperwork Reduction Project (0704-0188), Washington, DC 20503.				
1. AGENCY USE ONLY (Leave blank)		2. REPORT DATE 4/20/92	3. REPORT TYPE AND DATES COVERED Final Report 3/1/90-9/30/91	
4. TITLE AND SUBTITLE In-Situ Fault Detection by the Hybrid Ray-Mode Method			5. FUNDING NUMBERS Grant No. AFOSR-90-0088	
6. AUTHOR(S) Felsen, Leopold B.				
7. PERFORMING ORGANIZATION NAME(S) AND ADDRESS(ES) Polytechnic University Weber Research Institute Route 110 Farmingdale, NY 11758			8. PERFORMING ORGANIZATION REPORT NUMBER POLY-WRI-1589-92	
9. SPONSORING/MONITORING AGENCY NAME(S) AND ADDRESS(ES) Air Force Office of Scientific Research Bolling AFB, D.C. 20332-6448 NE			10. SPONSORING/MONITORING AGENCY REPORT NUMBER Proj. Task No. 2306/A3	
11. SUPPLEMENTARY NOTES The view, opinions and/or findings contained in this report are those of the author(s) and should not be construed as an official Department of the Army position, policy, or decision, unless so designated by other documentation.				
12a. DISTRIBUTION/AVAILABILITY STATEMENT Approved for public release; distribution unlimited.			12b. DISTRIBUTION CODE	
13. ABSTRACT (Maximum 200 words) See over				
14. SUBJECT TERMS Gaussian beam complex-source-point method; beam-to-mode conversion in elastic plates; transducer output modeling by Gaussian beams; hybrid beam-mode methods; weak debond ultrasonic			15. NUMBER OF PAGES	
			16. PRICE CODE	
17. SECURITY CLASSIFICATION OF REPORT UNCLASSIFIED	18. SECURITY CLASSIFICATION OF THIS PAGE UNCLASSIFIED	19. SECURITY CLASSIFICATION OF ABSTRACT UNCLASSIFIED	20. LIMITATION OF ABSTRACT UL	

The objective of this research effort has been to develop algorithms for in-situ location and identification, by ultrasound, of flaws in plates or laminated layered elastic materials. Achieving this objective requires detailed knowledge of the excitation, propagation, scattering and detection of high frequency sound waves in the unflawed and flawed environments. Based on an understanding of these fundamental wave phenomena, one may then attempt to construct analytical models with accompanying algorithms, so as to parametrize the NDE problem in terms of "good observables."

During this final period, the research program under the predecessor Grant No. AFOSR-86-0318 was phased out. Major effort was expanded on completing research items initiated under the predecessor grant, and on preparing final manuscripts for publication. For the description of these previous studies, the readers should refer to the Final Report on the predecessor grant.

A new phase was initiated during the current period, namely, a systematic study of nonspecular reflection of ultrasonic acoustic beams impinging from a fluid onto planar and cylindrical layered elastic materials. The nonspecular effect occurs when the incident beam is phase matched to a leaky mode in the structure and thereby causes the reflected field to be dominated by strong interaction between the specularly reflected beam profile and the leaky mode. The resulting interference pattern is a sensitive indicator of the leaky mode, and therefore of the state of the layers (including bonding layers) which generate that mode. Our effort has generalized previous studies -- which have dealt only with well-collimated (Fresnel zone) incident and reflected regimes, and only for plane geometries -- to arbitrary regimes allowing diverging incident beams. The new results show that the nonspecular effects are strongly affected the incident beam profile and by surface curvature.

Table of Contents

Documentation Page	
Abstract	1
I. Background and Accomplishments	2
A. Previous Effort	2
B. Present Accomplishments	2
II. Publications	4
III. Personnel	4
Appendices	5
A. In Situ Fault Detection by the Hybrid Ray-Mode Method, Final Technical Report, Grant No. AFOSR-86-0318	
B. Multiple Reflected Beam Synthesis of Fields Excited by a High-Frequency Oblique Beam Input in an Elastic Plate	
C. Ultrasonic Beam Method for Localized Weak Debonding in a Layered Aluminum Plate	
D. Source Field Modeling by Self-Consistent Gaussian Beam Superposition (Two-Dimensional)	
E. Three-Dimensional Source Field Modeling by Self-Consistent Gaussian Beam Superposition	
F. Non-Specular Reflection of Beams from Submerged Elastic Structures	



Accession For	
NTIS GR&I	<input checked="" type="checkbox"/>
ERIC IAR	<input type="checkbox"/>
Unannounced	<input type="checkbox"/>
Justification	
By _____	
Distribution/	
Availability Codes	
Dist	Avail and/or Special
A-1	

Abstract

The objective of this research effort has been to develop algorithms for in-situ location and identification, by ultrasound, of flaws in plates or laminated layered elastic materials. Achieving this objective requires detailed knowledge of the excitation, propagation, scattering and detection of high frequency sound waves in the unflawed and flawed environments. Based on an understanding of these fundamental wave phenomena, one may then attempt to construct analytical models with accompanying algorithms, so as to parametrize the NDE problem in terms of "good observables."

During this final period, the research program under the predecessor Grant No. AFOSR-86-0318 was phased out. Major effort was expended on completing research items initiated under the predecessor grant, and on preparing final manuscripts for publication. For the description of these previous studies, the reader should refer to the Final Report on the predecessor grant.

A new phase was initiated during the current period, namely, a systematic study of nonspecular reflection of ultrasonic acoustic beams impinging from a fluid onto planar and cylindrical layered elastic materials. The nonspecular effect occurs when the incident beam is phase matched to a leaky mode in the structure and thereby causes the reflected field to be dominated by strong interaction between the specularly reflected beam profile and the leaky mode. The resulting interference pattern is a sensitive indicator of the leaky mode, and therefore of the state of the layers (including bonding layers) which generate that mode. Our effort has generalized previous studies -- which have dealt only with well-collimated (Fresnel zone) incident and reflected regimes, and only for plane geometries -- to arbitrary regimes allowing diverging incident beams. The new results show that the nonspecular effects are strongly affected the incident beam profile and by surface curvature.

I. BACKGROUND AND ACCOMPLISHMENTS

A. Previous Effort

For general information and previous accomplishments pertaining to this effort on in-situ fault detection by the hybrid ray-mode method, the reader is referred to the final report on the predecessor grant, appended as Appendix A.

B. Present Accomplishments

1. Completion of pending tasks

During the present period, the phase-out period for this effort, research tasks initiated earlier were brought to completion, and major effort was expended to prepare manuscripts for publication of the results. Publications are listed in Section II and are identified by [] in the text. With reference to Appendix A, items in this category include the following:

- a. Multiple reflected beam synthesis of fields excited by a high frequency oblique beam input in an elastic plate.

This study was motivated by the results in item II.A2 of Appendix A, which showed that the initial field profile is beam-like before it eventually converts into the guided modes of the plate. The beam model was utilized in the flaw detection scheme proposed in item II.A3 and Ref. [7] of Appendix A. The present study extended the previous investigation by systematically tracking the initial beam through successive multiple reflections (with P-S coupling) in order to identify the limits of resolution due to overlapping multiples. The results are contained in [1], and a copy of the manuscript is attached as Appendix B.

- b. Ultrasonic beam method for localized weak debonding in a layered aluminum plate.

This is a completion of item II.A3 of Appendix A. A manuscript has been prepared and published [2], and is attached as Appendix C.

- c. Transducer output modeling by Gaussian beam decomposition.

This effort is described in item II.B of Appendix A. During the present period, manuscript [9] of Appendix A has been published (see [3] in Sec. II) and is attached as Appendix D. A manuscript dealing with the three-dimensional Gaussian beam modeling (see Ref. [10] in Appendix A) has been published [3]. It is attached as Appendix E.

2. New task: nonspecular reflection of bounded beams from multi-layer fluid-immersed elastic structures.

Anomalous nonspecular reflection of bounded beams from fluid-immersed layered elastic structures is a sensitive indicator of the physical properties of the layers, including those formed by adhesive bonds. The nonspecular effect occurs when the incident beam is phased matched to one of the leaky modes in the structure, thereby giving rise to strong coupling between the relevant leaky mode and the geometrically reflected beam profile. Previous studies of this phenomenon have been restricted to planar geometries and to the Fresnel zones of highly collimated input and output fields. To exploit this diagnostic tool more universally, we have generalized the previous analyses so that they apply to *arbitrarily* collimated or diverging input and output fields. Moreover, *cylindrically curved* layers have been considered. These generalizations have been accomplished through rigorous spectral analysis, complex-source-point modeling of a Gaussian input beam (see item II.A1 of Appendix A), and uniform asymptotics for reduction of the spectral integrals. The results in [4] and [5], attached as Appendix F, show the sensitivity of the nonspecular effect with respect to the degree of collimation of the input beam and the type of leaky mode (Rayleigh or Lamb) for planar configurations. Layer curvature introduces further modifications. These new effects have been explained and quantified in terms of physical wave processes, and their understanding enlarges substantially the signal processing options for parametric inversion of output data.

3. Summary

Taken together, the accomplishments under Grants AFOSR-86-0318 and AFOSR-90-0088 have identified new options for the analytical modeling of wave phenomena that are encountered when high frequency beams are used for QNDE of layered elastic materials in vacuum or in a fluid. These options have been expressed in terms of robust wave objects such as beams, guided modes and leaky modes, with self-consistent combinations constructed so as to reproduce observable features in data. We have referred to these algorithms, which have been developed by simultaneous use of the physical space and spectral wavenumber domains, as observable-based parametrizations (OBP).

In order to test the utility of the OBP options for processing of real data and for design of experiments aimed at extraction of specific NDE information, we have made contact with Prof. Dale Chimenti at John Hopkins University, Baltimore, MD, to coordinate our studies with his experimental program. However, this collaboration could not be pursued due to termination of the present program.

II. Publications

- [1] S. Zeroug and L.B. Felsen, "Multiple Reflected Beam Synthesis of Fields Excited by a High-Frequency Oblique Beam Input in an Elastic Plate," to be published in J. Acoust. Soc. Am.
- [2] L.B. Felsen and S. Zeroug, "Ultrasonic Beam Method for Localized Weak Debonding in a Layered Aluminum Plate," J. Acoust. Soc. Am., 90(3), 1991, pp.1527-1538.
- [3] J.M. Klosner, L.B. Felsen, I.T. Lu and H. Grossfeld, "Three-Dimensional Source Field Modeling by Self-Consistent Gaussian Beam Superposition, J. of Acoustical Society of America, Vol. 91, No. 4, 1992, pp. 1809-1822.
- [4] S. Zeroug and L.B. Felsen, "Non-Specular Reflection of Beams from Submerged Elastic Structures," submitted to J. of Nondestructive Evaluation, March 1992.
- [5] S. Zeroug and L.B. Felsen, "Non-Specular Reflection of Bounded Beams from Multilayer Fluid-Immersed Elastic Structures: Complex Ray Method Revisited," Review of Progress in Quantitative Non-Destructive Evaluation, D.O. Thompson and D. Chimenti, Eds., Plenum Press, New York, Vol. 11, 1992 (to be published).

III. Personnel

Dr. L.B Felsen, University Professor, Principal Investigator.

Dr. J.M. Klosner, Professor, Dept. of Mechanical Engineering.

S. Zeroug, Ph.D. Candidate, Dept. of Electrical Engineering.

APPENDICES

APPENDIX B

Multiple reflected beam synthesis of fields excited by a high-frequency oblique beam input in an elastic plate

Smaïne Zeroug and Leopold B. Felsen

Department of Electrical Engineering/Weber Research Institute, Polytechnic University, Farmingdale, New York 11735

(Received 30 May 1991; accepted for publication 18 November 1991)

Transducer-excited beams provide important diagnostic tools for ultrasonic nondestructive evaluation (NDE) of elastic materials. For bonded multilayer elastic plates, an obliquely injected high-frequency compressional (P) beam creates interior dynamic fields that are sensitive to weak debonding between the layers. In an effort to clarify the wave phenomena that are operative under these conditions of excitation, a highly idealized model has been chosen wherein a lossless plate in vacuum is insonified by an internal oblique P -beam source. This problem was analyzed in a previous investigation [Lu, Felsen, and Klosner, *J. Acoust. Soc. Am.* **87**, 42–53 (1990)] by expressing the total field in terms of a sum of P - S (vertically polarized or in-plane) coupled normal modes. While the resulting field assumed oscillatory modal patterns at interior cross sections far from the source region, the modally synthesized field near the source clearly outlined profiles interpretable as incident and singly or multiply reflected P - S coupled beams. The problem is therefore studied here directly by Gaussian beam tracing as implemented via our previously employed complex ray field algorithm. The results clarify the observed phenomena by revealing the successive buildup from initially well-resolved beams into oscillatory mode patterns synthesized by overlapping multiples. For the same idealized model, the beam algorithm has been applied elsewhere to the detection and identification of weak debonding in a layered plate [Felsen and Zeroug, *J. Acoust. Soc. Am.* **90**, 1527–1538 (1991)]. With an understanding of the physical mechanisms that arise in the beam-to-mode conversion, one may now explore how their utility is affected under realistic NDE conditions.

PACS numbers: 43.35.Pt, 43.35.Zc

INTRODUCTION

The present study is concerned with the analytic modeling of the dynamic fields generated in a lossless elastic plate in vacuum by an internally injected high-frequency oblique Gaussian compressional (P) beam. In a previous investigation [Lu, Felsen, and Klosner, *J. Acoust. Soc. Am.* **87**, 42–53 (1990)], the total field generated by such a beam was modeled through expansion into a sum of P - S coupled normal modes. While the resulting field assumed oscillatory modal patterns at interior cross sections far from the source region, the modally synthesized field near the source revealed profiles that are evidently attributable to incident and singly or multiply reflected P - S coupled beams. The synthesis in this paper is therefore performed by tracking the input beam via P - S coupled multiple reflections as implemented via our complex ray algorithm, and the results are compared with an independently derived modal reference solution.¹

In the pursuit of these objectives, we begin in Sec. I with a summary review of our previously developed analysis and synthesis options, which include (a) decomposition into continuous plane wave spectra; (b) expansion into normal modes; (c) expansion into multiply reflected beams; and (d) combination into a self-consistent beam-mode hybrid that emphasizes the best features of each. Details of the implementation of option (c) via the asymptotic (saddle point) reduction of an initial rigorous representation in terms of

spectral beam integrals with complex-source-point (CSP) excitation are presented in Sec. II. The asymptotic solutions for the scalar P and S potentials as well as the horizontal and vertical displacements include the fully developed multiple beam fields and also paraxial approximations that describe the major contributions in simplified form. For the problem parameters employed in our previous studies,¹ Sec. III contains detailed numerical comparisons between the beam tracking results and the modal reference solution along the upper and lower plate boundaries, and in transverse cross sections. Primary emphasis is placed on the ability of beam field clusters, as identified by the P - S beam trajectories, to construct local features of the total field response. Such local construction works well for the first few multiples, which can be clearly resolved, but its quality deteriorates for clusters corresponding to higher-order multiples, due to non-negligible overlap with preceding and successive multiples. When this overlap occurs, the internal fields undergo a transition from beamlike to modelike behavior, and the beam algorithm per se has reached the limits of its phenomenological utility, although adding enough overlapping beams will reconstruct even fine details in the total field response. Useful estimates are provided for an assessment of the strengths and the domains of influence of the individual beam multiples, and predictions based on the estimates are confirmed by the data.

Although the model in these studies is highly idealized, the relevant wave mechanisms remain intact even under more realistic conditions encountered, for example, in NDE applications. Of course, the quantitative effects of realistic environments will have to be explored before one may judge the ultimate utility of NDE techniques² that seem promising for the idealized case.

I. FORMULATION

We consider a lossless elastic isotropic plate of thickness a , with Lamé constants λ and μ , and density ρ , embedded in vacuum and excited by an interior time-harmonic line source at $(x, z) = (x', z')$, as shown in Fig. 1. The y -independent displacement fields $u(x, z)$ and $w(x, z)$ along x and z , respectively, and the stress $\Sigma(x, z)$ in the plate, can be derived from two potentials $\Phi(x, z)$ and $\Psi(x, z)$ representing the compressional (p) and vertically polarized (s) waves with respective speeds $v_p = [(\lambda + 2\mu)/\rho]^{1/2}$ and $v_s = [\mu/\rho]^{1/2}$. If the line source excites only compressional waves, the potential fields satisfy the wave equations (a time dependence $e^{-i\omega t}$ is assumed and suppressed),³

$$\left(\frac{\partial^2}{\partial x^2} + \frac{\partial^2}{\partial z^2} + k_p^2\right)\Phi(x, x'; z, z') = -\delta(x - x')\delta(z - z'), \quad k_p = \frac{\omega}{v_p}, \quad (1a)$$

$$\left(\frac{\partial^2}{\partial x^2} + \frac{\partial^2}{\partial z^2} + k_s^2\right)\Psi(x, x'; z, z') = 0, \quad k_s = \frac{\omega}{v_s}. \quad (1b)$$

The boundary conditions accompanying (1) are the vanishing of the normal and shear components, σ_z and τ_{xz} , respectively, of the stress field $\Sigma(x, z)$, at the plate surfaces $z = 0, a$. In terms of the potentials Φ and Ψ , σ_z and τ_{xz} , on a plane $z = \text{const.}$, are expressed as³

$$\sigma_z = \lambda \left(\frac{\partial^2}{\partial x^2} + \frac{\partial^2}{\partial z^2}\right)\Phi + 2\mu \left(\frac{\partial^2}{\partial x^2}\Phi + \frac{\partial^2}{\partial x \partial z}\Psi\right), \quad (2a)$$

$$\tau_{xz} = \mu \left[2 \frac{\partial^2}{\partial x \partial z}\Phi + \left(\frac{\partial^2}{\partial x^2} - \frac{\partial^2}{\partial z^2}\right)\Psi\right]. \quad (2b)$$

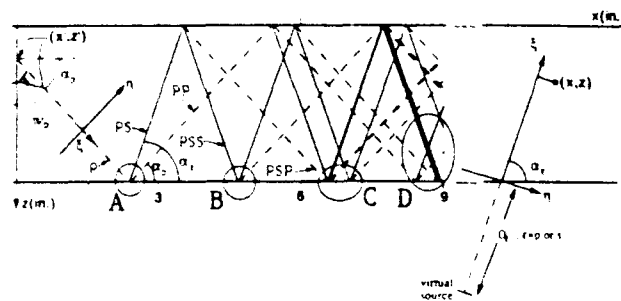


FIG. 1. Physical configuration, with global (x, z) and beam centered (ξ, η) coordinate systems. Input and output beam schematics, with multiple beam reflections and couplings between source and observer, are shown in correct proportion for the problem parameters listed below. Dashed lines: P -beam axis trajectories. Solid lines: S -beam axis trajectories. Plate parameters: $a = 0.3$ in., $v_p = 1.209 \times 10^3$ in./s, $v_s = 2.36 \times 10^3$ in./s, $\rho = 2.53 \times 10^{-4}$ lb s²/in.⁴. Incident beam parameters (complex source point modeling): $f = 20$ MHz, $u_p = 0.0335$ in., $\alpha_s = 45^\circ$, $(\hat{x}, \hat{z}) = (x' + ib_p \cos \alpha_s, z' + ib_p \sin \alpha_s)$, $(x, z) = (0.0, 0.06)$ in., $b_p = 0.3$ in. ($i = \sqrt{-1}$).

while the horizontal and vertical displacements, respectively, are

$$u = \frac{\partial \Phi}{\partial x} - \frac{\partial \Psi}{\partial z}, \quad (3a)$$

$$w = \frac{\partial \Phi}{\partial z} + \frac{\partial \Psi}{\partial x}. \quad (3b)$$

II. SOLUTION

A. Spectral decomposition

Plane-wave spectral decomposition along the x coordinate, via Fourier transform, leads to^{4,5}

$$\hat{V}(k; z, z') = \int_{-\infty}^{\infty} V(x, x'; z, z') \times \exp[-ik(x - x')] d(x - x'), \quad (4a)$$

with the inverse

$$V(x, x'; z, z') = \frac{1}{2\pi} \int_{-\infty}^{\infty} \hat{V}(k; z, z') \exp[ik(x - x')] dk. \quad (4b)$$

Here, V and \hat{V} are potential vectors in the configuration and spectral domains, respectively,

$$V = \begin{bmatrix} \Phi \\ \Psi \end{bmatrix} \quad \text{and} \quad \hat{V} = \begin{bmatrix} \hat{\Phi} \\ \hat{\Psi} \end{bmatrix}. \quad (5)$$

The spectral potential functions $\hat{\Phi}$ and $\hat{\Psi}$ satisfy the reduced wave equations

$$\left(\frac{d^2}{dz^2} + \kappa_p^2\right)\hat{\Phi}(k; z, z') = -\delta(z - z'), \quad \kappa_p^2 = k_p^2 - k^2, \quad (6a)$$

$$\left(\frac{d^2}{dz^2} + \kappa_s^2\right)\hat{\Psi}(k; z, z') = 0, \quad \kappa_s^2 = k_s^2 - k^2, \quad (6b)$$

with boundary conditions at $z = 0, a$,

$$\lambda \left(-k^2 + \frac{d^2}{dz^2}\right)\hat{\Phi} + 2\mu \left(\frac{d^2}{dz^2}\hat{\Phi} + ik \frac{d}{dz}\hat{\Psi}\right) = 0, \quad (7a)$$

$$2ik \frac{d}{dz}\hat{\Phi} + \left(-k^2 - \frac{d^2}{dz^2}\right)\hat{\Psi} = 0. \quad (7b)$$

The solutions of (6) can be synthesized in terms of upgoing and downgoing compressional and shear waves that are coupled at the plate boundaries.⁶ If ray paths are associated with these waves, one distinguishes four categories depending on the directions of departure from the line source and arrival at the observer (see Fig. 2). The total spectral field is comprised of the sum of the fields of each category,

$$\hat{V}(k; z, z') = \sum_{i=1}^4 \hat{V}^{(i)}(k; z, z'). \quad (8)$$

In category 1, for instance, the first three reflections (without distinction between P and S waves) are shown by the ray paths in Fig. 3. Summing all waves in this category we can express

$$\hat{V}^{(1)}(k; z, z') = \mathbf{E}(a - z) \cdot \mathbf{R}^d \cdot \mathbf{E}(a - z') \cdot [\mathbf{I} + \mathbf{F}^{u,d} + (\mathbf{F}^{u,d})^2 + \dots] \cdot \mathbf{S}, \quad (9)$$

or, compactly,

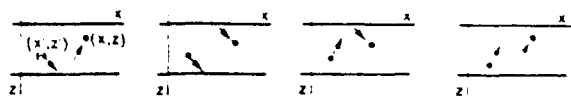


FIG. 2. The four ray categories that order the propagation process according to waves that are upgoing or downgoing, respectively, with respect to the source depth z' and arrive at z from an upward or downward direction.

$$\hat{V}^{(1)}(k; z, z') = \mathbf{E}(a - z) \cdot \mathbf{R}^d \cdot \mathbf{E}(a - z') \cdot (\mathbf{I} - \mathbf{F}^{u,d})^{-1} \cdot \mathbf{S}, \quad (10a)$$

where \mathbf{I} is the identity matrix, \mathbf{E} is the propagator matrix,

$$\mathbf{E}(d) = \begin{pmatrix} e^{i\kappa_p d} & 0 \\ 0 & e^{i\kappa_s d} \end{pmatrix}, \quad (10b)$$

\mathbf{S} is the source vector corresponding to a P line source,

$$\mathbf{S} = \begin{pmatrix} -1/[2i\kappa_p] \\ 0 \end{pmatrix}, \quad (10c)$$

and \mathbf{F} is the reverberation matrix given by

$$\mathbf{F}^{u,d} = \mathbf{Q}^u \cdot \mathbf{Q}^d \quad (10d)$$

$$\mathbf{Q}^u = \mathbf{E}(z') \cdot \mathbf{R}^u \cdot \mathbf{E}(z'); \quad (10e)$$

$$\mathbf{Q}^d = \mathbf{E}(a - z') \cdot \mathbf{R}^d \cdot \mathbf{E}(a - z'). \quad (10f)$$

The reflection matrices \mathbf{R}^u and \mathbf{R}^d are phase referenced at $z = 0$ and $z = a$, respectively (the upper sign goes with "u"),

$$\mathbf{R}^{u,d} = \begin{pmatrix} R_{pp} & \pm R_{ps} \\ \pm R_{sp} & R_{ss} \end{pmatrix}, \quad (10g)$$

with the following expressions for the plane-wave reflection and coupling coefficients:

$$R_{pp} = R_{ss} = [4k^2 \kappa_p \kappa_s - (\kappa_s^2 - k^2)^2] D^{-1}, \quad (11a)$$

$$R_{ps} = 4(\kappa_s^2 - k^2) k \kappa_s D^{-1}, \quad (11b)$$

$$R_{sp} = -4(\kappa_s^2 - k^2) k \kappa_p D^{-1}, \quad (11c)$$

$$D = 4k^2 \kappa_p \kappa_s + (\kappa_s^2 - k^2)^2. \quad (11d)$$

Including the contributions from the other categories, it is found that

$$\begin{aligned} \hat{V}(k; z, z') &= \sum_{l=1}^4 \hat{V}^{(l)}(k; z, z') \\ &= \sum_{l=1}^4 \mathbf{T}^{(l)} \cdot (\mathbf{I} - \mathbf{F}^{(l)})^{-1} \cdot \mathbf{S} + \Delta^{(l)}, \end{aligned} \quad (12)$$

with

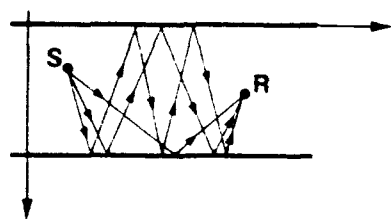


FIG. 3. The first three multiple reflected ray paths for wave fields in category 1

$$\mathbf{T}^{(l)} = \begin{cases} \mathbf{E}(a - z) \cdot \mathbf{R}^d \cdot \mathbf{E}(a - z'), & l = 1, \\ \mathbf{E}(z - z'), & l = 2, \\ \mathbf{E}(z) \cdot \mathbf{R}^u \cdot \mathbf{E}(z'), & l = 3, \\ \mathbf{E}(z' - z), & l = 4, \end{cases} \quad (12a)$$

$$\mathbf{F}^{(l)} = \begin{cases} \mathbf{F}^{u,d}, & l = 1, 2, \\ \mathbf{F}^{d,u}, & l = 3, 4. \end{cases} \quad (12b)$$

The vector $\Delta^{(1)}$ removes the direct wave when it does not exist in the respective category,

$$\Delta^{(l)} = \begin{cases} 0, & l = 1, 3, \\ -U(z' - z) \mathbf{E}(z - z') \cdot \mathbf{S}, & l = 2, \\ -U(z - z') \mathbf{E}(z' - z) \cdot \mathbf{S}, & l = 4, \end{cases} \quad (12c)$$

$$U(\bar{z}) = \begin{cases} 1, & \bar{z} > 0, \\ \frac{1}{2}, & \bar{z} = 0, \\ 0, & \bar{z} < 0. \end{cases} \quad (12d)$$

B. Alternative representations

From the closed form expression of the solution in (4b) and (12), it is possible to derive alternative representations with different physical content. These alternatives, discussed in detail in Ref. 6, are summarized here. For convenience, the superscript "l" for the lth category is omitted in what follows.

1. Modal representation

By deforming the integration contour around the pole singularities k_m satisfying the resonance equation

$$\det(\mathbf{I} - \mathbf{F}) = 0, \quad (13)$$

one may write the total field as a sum of normal modes,

$$\begin{aligned} V(x, x', z, z') &= \sum_{m=1}^{M_t} V_m(x, x', z, z'), \\ V_m &= i \lim_{k \rightarrow k_m} [(k - k_m) \hat{V} e^{ik(x - x')}], \end{aligned} \quad (14)$$

with \hat{V} given by (12). Explicitly, (13) becomes

$$(1 - e^{i(\kappa_p + \kappa_s)a})^2 - R_{pp}^2 (e^{i\kappa_p a} - e^{i\kappa_s a})^2 = 0, \quad (15a)$$

or equivalently,⁷

$$\frac{\tan(\kappa_s a/2)}{\tan(\kappa_p a/2)} = -\frac{1 \pm R_{pp}}{1 - (\pm) R_{pp}} \quad \text{for symmetric/antisymmetric modes.}$$

2. Ray representation

By power series expansion of $(\mathbf{I} - \mathbf{F})^{-1} = \sum_{n=0}^{\infty} \mathbf{F}^n$, one may write the total field as a sum of generalized ray integrals V_n :

$$\begin{aligned} V(x, x', z, z') &= \sum_{n=1}^{\infty} V_n(x, x', z, z'), \\ V_n &= \frac{1}{2\pi} \int_{-\infty}^{\infty} \mathbf{T} \cdot \mathbf{F}^n \cdot \mathbf{S} \exp[ik(x - x')] dk. \end{aligned} \quad (16)$$

The factor $\mathbf{T} \cdot \mathbf{F}^n \cdot \mathbf{S}$ can be expanded further to yield V_n as a sum of ordinary ray integrals $J_{n,\mu}$ and $J'_{n,\nu}$ with μ or ν indexing the different P or S waves, respectively, with the same n ,

$$V_n = \begin{bmatrix} \Phi_n \\ \Psi_n \end{bmatrix} \quad (17a)$$

$$\Phi_n = \sum_{\mu=1}^{\mu_M} J_{n,\mu},$$

$$J_{n,\mu} = \frac{1}{2\pi} \int_{-\infty}^{\infty} B_{n,\mu}(k) \exp[iP_{n,\mu}(k)] dk, \quad (17b)$$

$$\Psi_n = \sum_{\nu=1}^{\nu_M} J'_{n,\nu},$$

$$J'_{n,\nu} = \frac{1}{2\pi} \int_{-\infty}^{\infty} B'_{n,\nu}(k) \exp[iP'_{n,\nu}(k)] dk. \quad (17c)$$

Here, $B_{n,\mu}$ and $B'_{n,\nu}$ are amplitude functions that incorporate excitation coefficients, reflection coefficients, etc., while $P_{n,\mu}$ and $P'_{n,\nu}$ are rapidly varying phase functions having the generic form

$$\begin{Bmatrix} P_{n,\mu} \\ P'_{n,\nu} \end{Bmatrix} = k(x - x') + \kappa_p z_p + \kappa_s z_s, \quad (18)$$

with $z_{p,s}$ denoting the vertical projections of all ray segments associated with the P and S waves, respectively. A generalized ray with $n = 1$ and $l = 1$ (category 1), emanating from a P source, is schematized in Fig. 4(a). Grouped within it are eight ordinary P and S rays (four of each), shown in Fig. 4(b). These eight ordinary rays, each having four segments, can be denoted by $P^d PPP^u$, $P^d PPS^u$, $P^d PSP^u$, $P^d SPP^u$, $P^d PSS^u$, $P^d SPS^u$, $P^d SSP^u$, and $P^d SSS^u$. The superscripts on the first and last segments denote the downward departure and upward arrival of the ordinary ray.

For example, the ordinary ray integral $J'_{1,6}$ corresponding to ray $P^d SPS^u$ [$n = 1, \nu = 6$, in category 1; see Fig. 4(b)] is

$$J'_{1,6} = \frac{1}{2\pi} \int_{-\infty}^{\infty} B'_{1,6}(k) \exp[iP'_{1,6}(k)] dk, \quad (19a)$$

where

$$B'_{1,6}(k) = -1/(2i\kappa_p)(R_{sp}^d)^2 R_{ps}^u, \quad (19b)$$

$$P'_{1,6}(k) = k(x - x') + \kappa_p(2a - z') + \kappa_s(2a - z). \quad (19c)$$

3. Hybrid ray-mode expansion

A hybrid form combining modes and generalized rays results from partial series expansion of the resonance matrix,

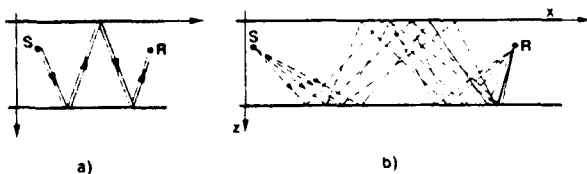


FIG. 4. Generalized and ordinary rays. (a) Generalized ray $n = 1, l = 1$ [see (16)]. (b) The eight ordinary ray paths [see (17a) and (17b)] associated with the plane wave congruences corresponding to the generalized ray path in (a), with the P source only. P -ray trajectories: dashed lines. S -ray trajectories: solid lines.

$$(\mathbf{I} - \mathbf{F})^{-1} = \sum_{n=0}^{N-1} \mathbf{F}^n + (\mathbf{I} - \mathbf{F})^{-1} \cdot \mathbf{F}^N, \quad (20)$$

which, upon substitution into (12) and (4b), yields a finite sum of generalized ray integrals and an integral remainder R'_N ,

$$V(x, x', z, z') = \sum_{n=0}^{N-1} V_n(x, x', z, z') + R'_N(x, x', z, z'), \quad (21a)$$

where

$$R'_N(x, x', z, z') = \frac{1}{2\pi} \int_{-\infty}^{\infty} \mathbf{T} \cdot (\mathbf{I} - \mathbf{F})^{-1} \cdot \mathbf{F}^N \cdot \mathbf{S} \exp[ik(x - x')] dk. \quad (21b)$$

The remainder integral can be efficiently evaluated on a "rapid convergence" path C_N that passes through the observer-dependent saddle point of the integrand corresponding to $n = N$. Modal pole singularities intercepted during the contour deformation furnish contributions, which establish the hybrid form; the number of intercepted normal modes is determined uniquely by the saddle point for $n = N$ and the associated path C_N . The resulting hybrid ray-mode representation becomes

$$V(x, x', z, z') = \sum_{n=0}^{N-1} V_n + \sum_m V_m + R_N, \quad (22a)$$

where

$$R_N = \frac{1}{2\pi} \int_{C_N} \mathbf{T} \cdot (\mathbf{I} - \mathbf{F})^{-1} \cdot \mathbf{F}^N \cdot \mathbf{S} \exp[ik(x - x')] dk. \quad (22b)$$

When parametrizing measured or synthetic numerical data in terms of the hybrid algorithm, one chooses N so as to include all well-resolved "raylike" features in the data. For the collimated beam input, the meaning of raylike is clarified in the discussion to follow. Since the ray-mode decomposition is self-consistent [see (20)], the choice of N does not affect the result of the total field in (22) but it will affect the rapidity of convergence as well as the quality of the "basic physics" responsible for generating the data at the observer.

C. Beam excitation

By analytic continuation of the real coordinates of the line source in Sec. I to complex values,⁹⁻¹¹

$$\bar{x} = x' + ib_p \cos \alpha_p, \quad \bar{z} = z' + ib_p \sin \alpha_p, \quad b_p > 0, \quad (23)$$

the wavefield generated by the P -wave isotropic line source is converted into a P -wave directional beam source (Fig. 1). This complex source point (CSP)-generated beam has its waist centered at (x', z') ; its $(1/e)$ width w_p at the waist is related to the complex displacement parameter b_p via $w_p^2 = 2b_p/k_p$, from which one recognizes that b_p itself expresses the Fresnel length corresponding to w_p . The angle α_p denotes the direction of the beam axis with respect to the horizontal axis.

The CSP-extended wave potentials $\tilde{\Phi}$ and $\tilde{\Psi}$ (the overtilde denotes beam excitation quantities) continue to satisfy

formally the respective wave equations and boundary conditions. The convergence of the different representations, however, needs to be verified in each case. This aspect has been considered in Ref. 1. Use of the global or plate-tied x -coordinate spectral decomposition leads to convergence problems for strongly oblique spectra with respect to beam axes that characterize nearly horizontal propagation. Problems also arise from nonphysical growth of evanescent spectra upon reflection at the boundaries. It has been found that, in the modal representation, these problems can be deemphasized by ignoring evanescent modes with eigenvalues $k_m > k_p$, since their excitation strength by the P -beam input is minimal. In the ray representation, these problems are avoided by tracking the CSP-extended ordinary ray integrals along local coordinates defined with respect to the axes of the individual beams.

III. FIELD SYNTHESIS BY BEAM MODELING

The CSP-extended normal mode expansion in (14) has been used in Ref. 1 as a reference solution for charting the evolution of a P -beam input inside the plate. The numerical results show that the field behaves initially as a well-collimated beam that converts eventually into oscillatory mode-like patterns; the latter are a consequence of interference between overlapping multiple P - S coupled reflections. These observations suggest that in the near zone or early phases of the field, a beam (ray) modeling would be numerically more efficient and physically more appealing than mode summation, while in the intermediate region of conversion from beamlike to modelike character, a hybrid scheme would be an attractive option. Accordingly, here we explore synthesis of the fields in terms of beams as furnished by the CSP-extended ray expansion. As in our previous investigation,¹ the CSP-extended mode expansion in (14) with (23) will serve as a reference solution. In the following, we shall refer to the CSP-extended ray field as a "complex ray" field; the "beam axis" is the trajectory along which the complex ray field magnitude is maximal.

In principle, at any given observation point, the potential field vector \tilde{V} is obtained by summing over all ordinary complex ray integrals, $n = 1, \infty$; $l = 1, 4$; $\mu = 1, \mu_M$, $\nu = 1, \nu_M$. The generic form of each component of \tilde{V} , henceforth denoted by \tilde{J}_ϵ , involves an analytically continued complex ray integral as in (17b) or (17c), evaluated along a multiple reflection trajectory; for brevity we use ϵ instead of n, μ or n, ν to denote either a P or S ordinary ray. In particular, the function \tilde{P}_ϵ in (18) accounting for the accumulated complex phase along the (P, S) propagation path becomes

$$\tilde{P}_\epsilon(k; x, z) = k(x - x' - ib_p \cos \alpha_p) + \kappa_p \tilde{d}^{(l)} + \kappa_p N_p a + \kappa_s N_s a + \kappa_e z_1, \quad (24a)$$

where

$$\tilde{d}^{(l)} = \begin{cases} a - z' - ib_p \sin \alpha_p, & l = 1, 2 \\ z' + ib_p \sin \alpha_p, & l = 3, 4, \end{cases} \quad (24b)$$

with $N_\epsilon = N_{p,s}$, denoting the number of (P, S) excursions across the plate, and z_1 denoting the vertically projected segment that connects the latest complete excursion with the

observer. The complex ray integral can be evaluated asymptotically by the saddle point method⁵ applied in the complex k plane to the analytically continued integrand. The integration path is deformed from the real axis, where the phase is highly oscillatory, to a steepest descent path (SDP) that traverses the first-order complex saddle point k_{sad} defined by

$$\frac{d\tilde{P}_\epsilon(k_{\text{sad}}; x, z)}{dk} = 0, \quad \text{with} \quad \frac{d^2\tilde{P}_\epsilon(k_{\text{sad}}; x, z)}{dk^2} \neq 0. \quad (25)$$

The first-order steepest descent evaluation yields⁵

$$\tilde{J}_\epsilon(x, x', z, z') \sim (1/2\pi) \sqrt{2\pi i [d^2\tilde{P}_\epsilon(k_{\text{sad}}; x, z)/dk^2]^{-1}} \times \tilde{B}_\epsilon(k_{\text{sad}}) \exp[i\tilde{P}_\epsilon(k_{\text{sad}}; x, z)], \quad (26)$$

where $\arg(\sqrt{\cdot}) = \arg(dk)$, with dk denoting an element at k_{sad} of the SDP.

As has been shown,² (26) corresponds to a beam field. The same expression without the CSP extension corresponds to a real ray field. While a multiple reflected real ray field generally yields a significant contribution for all launch angles from the source, a multiple reflected complex ray field is significant only over a relatively restricted angular spectrum surrounding the beam axis; this paraxial domain of influence limits the angular spectrum of significant ray fields at the observation point, even after multiple reflections. For the problem configuration in Sec. II, where the P -beam input radiates downward (see Fig. 1), complex ray fields with upward launching angles at the source (categories 3 and 4 in Fig. 2) can be predicted, and are indeed verified, to have negligible contributions at all observation points. The paraxial approximation of (26) for the direct (P) complex ray was obtained in Ref. 2 as

$$\tilde{\Phi}(\xi, \eta) \sim \frac{\exp(i\pi/4)}{2\sqrt{2\pi}} \times \frac{\exp\{ik_p[\xi + \eta^2/(2R_p(\xi))] - \eta^2/w_p^2(\xi)\}}{\sqrt{k_p(\xi - ib_p)}}; \quad (27)$$

with (ξ, η) denoting the local coordinates along, and transverse to, the P beam axis (Fig. 1). We note that for this complex ray, $\tilde{B}_\epsilon = (i/2\kappa_p)$. In (27), $R_p(\xi)$ is the on-axis radius of curvature of the beam wave front, while $w_p(\xi)$ is the $1/e$ width at a distance ξ from the waist. Along the ξ axis, i.e., $\eta = 0$, the complex ray amplitude decays like

$$1/2\sqrt{2\pi} [k_p \sqrt{\xi^2 + b_p^2}]^{-1/2}, \quad (28)$$

while for fixed ξ it decays transversely in Gaussian fashion like

$$\exp[-\eta^2/w_p^2(\xi)], \quad (29)$$

with $w_p(\xi)$ given by

$$w_p(\xi) = w_p(0) [1 + \xi^2/b_p^2]^{1/2}; \quad w_p(0) = 2b_p/k_p. \quad (30)$$

A paraxial expression for the multiple reflected complex ray field has also been derived in Ref. 2. It yields a Gaussian beam, which, when compared to (27), may be interpreted as a complex ray field emanating from an equivalent virtual CSP located at distance $D_\epsilon - i\gamma_{\epsilon p} b_p$ along the extension of

the last segment of the corresponding input beam into the infinitely extended medium (see Fig. 1, on the extended part on the right; $\epsilon = p$ or s). The distance D_ϵ is given by

$$D_\epsilon = \gamma_{ep} L_p + \gamma_{es} L_s, \quad (31)$$

with

$$\gamma_{ep} = k_\epsilon \sin^2 \alpha_\epsilon / k_p \sin^2 \alpha_p, \quad (32a)$$

$$\gamma_{es} = k_\epsilon \sin^2 \alpha_\epsilon / k_s \sin^2 \alpha_s. \quad (32b)$$

Here L_p (L_s) denotes the total distance traversed by P (S) waves along the corresponding multiple reflected beam axes, not including the last segment,

$$L_{p,s} = z_{p,s} / \sin \alpha_{p,s}, \quad z_p = a - z' + N_p a, \quad z_s = N_s a, \quad (33)$$

where $N_{p,s}$ denotes the number of complete (P, S) excursions across the plate. The angles $\alpha_{p,s}$ are related by

$$k_p \cos \alpha_p = k_s \cos \alpha_s. \quad (34)$$

The equivalent paraxial beam has a Fresnel length,

$$b_\epsilon = \gamma_{ep} b_p, \quad (35)$$

and minimum waist

$$w_\epsilon = \sqrt{2b_\epsilon / k_\epsilon}. \quad (36)$$

The total distance along this equivalent beam to the on-axis projection of the observer location is therefore given by

$$\xi + D_\epsilon = \xi + \gamma_{ep} L_p + \gamma_{es} L_s, \quad (37)$$

and the $1/e$ width there is [see (28)],

$$w_\epsilon(\xi) = w_\epsilon \left[1 + (\xi + \gamma_{ep} L_p + \gamma_{es} L_s)^2 / \gamma_{ep}^2 b_p^2 \right]^{1/2}, \quad (38)$$

with w_ϵ given in (36). The amplitude decays along the axis like²

$$k_\epsilon \sin \alpha_\epsilon / \sqrt{2\pi} |\tilde{B}_\epsilon(k_{\text{sad}}^0)| \left[k_\epsilon \sqrt{(\xi + D_\epsilon)^2 + \gamma_{ep}^2 b_p^2} \right]^{-1/2}. \quad (39)$$

As defined in Eqs. (17), \tilde{B}_ϵ is a function incorporating excitation coefficients as well as reflection and coupling coefficients. The on-axis real value k_{sad}^0 of the saddle point is given by

$$k_{\text{sad}}^0 = k_\epsilon \cos \alpha_\epsilon. \quad (40)$$

To determine whether a multiple reflected complex ray is significant at a given observation point, two parameters have to be considered: the width of its paraxial domain of influence and its on-axis strength. We shall use (38) to estimate the first parameter, the width $\hat{\eta}_\epsilon(\xi)$, and (39) to obtain the second parameter, the magnitude $A_\epsilon(\xi)$, at a location ξ on the axis. Selecting $\hat{\eta}_\epsilon(\xi)$ arbitrarily as the value of η that corresponds to an amplitude decay to 5% of the on-axis maximum, and noting that $e^{-3} \approx 0.05$, one has

$$\hat{\eta}_\epsilon(\xi) = \sqrt{3} w_\epsilon(\xi), \quad (41)$$

with $w_\epsilon(\xi)$ given in (38). It is convenient to use the horizontal projection $\Delta_\epsilon(\xi)$ given by [see (38)]

$$\begin{aligned} \Delta_\epsilon(\xi) &\approx \frac{\hat{\eta}_\epsilon(\xi)}{\sin \alpha_\epsilon} \\ &= \frac{\sqrt{3}}{\sin \alpha_\epsilon} \sqrt{\frac{2b_\epsilon}{k_\epsilon} \left(1 + \frac{(\xi + \gamma_{ep} L_p + \gamma_{es} L_s)^2}{\gamma_{ep}^2 b_p^2} \right)^{1/2}}. \end{aligned} \quad (42)$$

The on-axis magnitude of each complex ray is given by (39). However, in order to compare the strengths of various complex ray fields, it is convenient to express this quantity relative to the magnitude of the direct P complex ray, given by (28), evaluated at the lower boundary (i.e., after it traverses a distance l_p)

$$l_p = (a - z') / \sin \alpha_p. \quad (43)$$

Dividing (39) by (28) (with $\xi = l_p$) yields the on-axis *normalized* magnitude of the multiple reflected complex ray field potential as

$$\begin{aligned} A_\epsilon(\xi) &= 2\sqrt{k_\epsilon k_p} \sin \alpha_\epsilon |\tilde{B}_\epsilon(k_{\text{sad}}^0)| \\ &\quad \times \{ (l_p^2 + b_p^2) / [(\xi + D_\epsilon)^2 + \gamma_{ep}^2 b_p^2] \}^{1/4}. \end{aligned} \quad (44)$$

So far we have focused on the parameters of the complex ray fields representing the potentials Φ and Ψ , but similar formulas can also be derived for the physical observables, the horizontal (u) and vertical (w) displacements. Since the displacement fields are derived from the potential fields in the spectral domain, the derivative operations in (3a) and (3b) become multiplications by spectral wave numbers. These multiplicative factors are incorporated into the slowly varying amplitude terms of the integrand inside the spectral integrals, which are then evaluated asymptotically, as described above and in more detail in Ref. 2, to yield the complex ray displacement fields

$$u = ik_{\text{sad}} \Phi \pm i\kappa_s \Psi; \quad (45a)$$

$$w = -(\pm) i\kappa_p \Phi + ik_{\text{sad}} \Psi, \quad (45b)$$

with the upper (lower) sign denoting upgoing (downgoing) waves. Accordingly, the amplitudes of the displacement fields u and w , due to the Φ potential only, are

$$|u| = |k_{\text{sad}} \Phi|, \quad |w| = |\kappa_p \Phi|, \quad (46a)$$

while those due to the Ψ potential only, are

$$|u| = |\kappa_s \Psi|, \quad |w| = |k_{\text{sad}} \Psi|, \quad (46b)$$

where k_{sad} is the complex saddle point and $\kappa_{p,s}(k_{\text{sad}})$ as defined in (6a) and (6b) are likewise complex, but their complex-plane deviations from their on-axis ($\eta = 0$) real values, as $|\eta|$ increases, are minimal over the distance $\hat{\eta}_\epsilon(\xi)$. Therefore, it is sufficient to use the on-axis real value for k_{sad} as given in (40), which leads to real values for κ_p and κ_s ,

$$\kappa_{p,s} = k_{p,s} \sin \alpha_{p,s}. \quad (47)$$

The formula in (42) is then used to evaluate the horizontally projected widths of the paraxial domain of influence of the various complex ray displacement fields, while their on-axis magnitudes are obtained from (46a) and (46b). Again, for convenience, these magnitudes can be expressed with reference to $|u|$ and $|w|$ derived from the direct P complex ray potential Φ , evaluated at the lower surface. In particular: For a P ray,

$$\left(\frac{|\bar{u}(\xi)|}{|\bar{w}(\xi)|} \right) = A_p(\xi); \quad (48a)$$

for an S ray:

$$\left(\frac{|\bar{u}(\xi)|}{|\bar{w}(\xi)|} \right) = \left(\frac{\sin \alpha_s / \cos \alpha_p}{\cos \alpha_s / \sin \alpha_p} \right) \frac{k_s}{k_p} A_s(\xi), \quad (48b)$$

TABLE I. On-axis normalized magnitudes $|\bar{u}|$ and $|\bar{w}|$, and horizontal projections of $\hat{u}_e(\xi)$ in (41) for the first ten complex rays. These quantities are evaluated at the lower and upper plate surfaces, i.e., $\xi = a/\sin \alpha_{p,s}$, 0. Subscripts b and t denote these two locations. Formulas (42), (44) and (48a) and (48b) are used to generate this data. The normalizations of $|\bar{u}|$ and $|\bar{w}|$ are with respect to the maximum magnitudes 4.847×10^{-7} in. and 4.878×10^{-7} in., of u and w , respectively, derived from the direct P complex ray evaluated at the lower surface.

CSP ray	$2\kappa_p B_e(k)$	N_p/N_s	D_e (in.)	$ \bar{u}_b / \bar{u}_t $	$ \bar{w}_b / \bar{w}_t $	$\Delta_{p,s}/\Delta_{e,t}$ (in.)
P	1	0/0	0.0	1.00/—	1.00/—	0.124/0.082
PS	R_{ip}	0/0	1.152	1.38/1.28	0.54/0.50	0.124/0.145
PP	R_{pp}	0/0	0.340	0.51/0.38	0.51/0.38	0.124/0.225
PSS	$R_{ip}R_{is}$	0/1	1.474	0.61/0.65	0.24/0.25	0.167/0.145
$PSSS$	$R_{ip}(R_{is})^2$	0/2	1.796	0.31/0.29	0.12/0.11	0.167/0.190
$PSSP$	$R_{ip}R_{is}R_{ps}$	0/2	0.530	0.33/0.25	0.33/0.25	0.167/0.274
PSP	$R_{ip}R_{ps}$	0/1	0.434	0.52/0.67	0.52/0.67	0.249/0.145
PPS	$R_{pp}R_{ip}$	1/0	2.592	0.50/0.52	0.19/0.20	0.249/0.225
$PSSSS$	$R_{ip}(R_{is})^3$	0/3	2.117	0.14/0.15	0.05/0.06	0.213/0.190
PPP	$(R_{pp})^2$	1/0	0.764	0.16/0.19	0.16/0.19	0.336/0.225

with $A_{p,s}(\xi)$ given by (44). The overbar on u and w denotes normalized quantities.

IV. NUMERICAL RESULTS

We now employ the paraxial relations in Sec. III to calculate the magnitudes and widths of the paraxial domains of influence of the first few complex rays, for comparison with results predicted from the full asymptotic complex ray fields given by (26), (25), and (24). Furthermore, we test the beam modeling algorithm against the mode series algorithm for the total field magnitude at horizontal and vertical cuts of the plate, and show that both algorithms yield consistently the same results. We conclude by highlighting the advantages of the beam modeling in the observation range not too far from the source.

The parameters used for the numerical simulation are the same as in Ref. 2. The aluminum plate has thickness $a = 0.3$ in., wave velocities $v_p = 2.36 \times 10^5$ (in./s), $v_s = 1.209 \times 10^5$ (in./s), and density $\rho = 2.53 \times 10^{-4}$ (lb s²/in.³). The 20-MHz P source has its waist centered at $x' = 0.0$ in., $z' = 0.06$ in., with width at the waist $w_p = 0.0335$ in., and beam axis inclination angle $\alpha_p = 45^\circ$.

Figure 1 shows the plate and beam source geometry. The axes of P and S beams along the various segments are shown as dashed and solid lines, respectively. The notation P , PS , PP , etc. identifies the wave process along each segment of the beam axes. Moving away from the $x = 0$ cross section along a constant- z path close to the lower surface, one encounters the beam axes of the following complex rays:

$P, PS, PP, PSS, PSSS, PSSP, PSP, PPS, PSSSS, PPP$, etc.

Table I contains pertinent parameters for the horizontal and vertical displacement fields u and w , respectively, carried along these complex rays. The parameters are $\Delta_{p,s}(\xi)$ from (42), and $|\bar{u}(\xi)|$ and $|\bar{w}(\xi)|$ from (48a), (48b) and (44). Both are computed at the lower and upper surfaces, i.e., at $\xi = 0$, $a/\sin \alpha_e$; the subscripts b (bottom) and t (top) are used to designate these two locations. The first four columns of Table I indicate the complex ray considered; the expressions for the excitation function B_e are required for the de-

termination of $A_{p,s}(\xi)$, and those for N_p and N_s for the determination of D_e from (31), (32a), (32b), and (33). The values of $|\bar{u}|$ and $\Delta_{p,s}$ listed in the fifth and seventh columns of Table I are utilized in Fig. 5 to sketch the paraxial domains of influence (shaded) of the various complex rays. A number next to the centerline (beam axis) indicates the magnitude $|\bar{u}|$ at that location normalized with respect to the maximum magnitude 4.847×10^{-7} in. of u generated at the lower surface by the direct incident complex ray. For each complex ray the horizontal width of the shaded area corresponds to twice the value of $\Delta_{p,s}(\xi)$. These qualitative sketches are confirmed by plotting along the lower boundary the horizontal displacement field magnitude $|\bar{u}|$ (normalized to the magnitude $|u|$ of the direct P complex ray displacement field) contributed individually by these rays, and obtained from the full asymptotic result in (26), (46a), and (46b) applied separately to each complex ray integral (Fig. 6). It

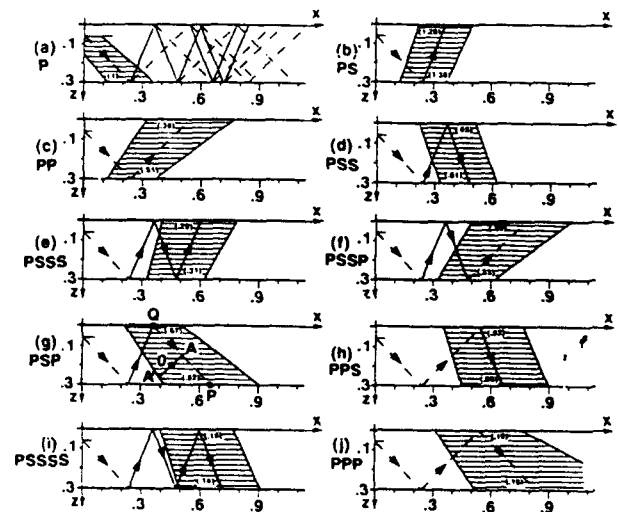


FIG. 5. Estimates of the paraxial domains of influence for the complex ray fields listed in Table I. The horizontal widths of the shaded areas correspond to twice the values of Δ_e listed in the last column of Table I. The numbers between parentheses refer to the normalized magnitudes $|\bar{u}|$ at the lower and upper surfaces (see the legend of Table I).

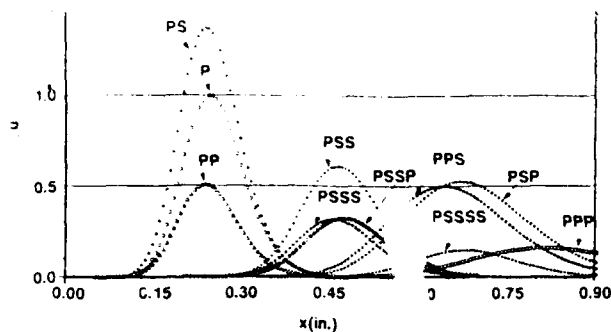


FIG. 6. Normalized magnitude $|u|$ of horizontal displacement u along lower surface $z = 0.3$ in. (for actual magnitudes, multiply by 4.847×10^{-7} in.). Contributions of the individual complex rays listed in Table I are identified. Parameters are as in Fig. 1.

may be observed that the normalized magnitudes and the widths in Table I agree well with the data plotted in Fig. 6, thereby confirming the validity of the formulas derived in Sec. II.

The sketches in Fig. 5 help to predict the number of complex rays that contribute to the total horizontal displacement field at any observer location within the region $x < 0.6$ in. (for $x > 0.6$ in., additional rays would have to be included). Roughly speaking, for a given observer location, a complex ray contributes to the total field if the observer falls within its shaded area. Knowing that at the edge of the shaded paraxial domain of influence, the magnitude decays approximately to 5% of the value at the centerline, one may assess qualitatively the importance of the contribution of each ray by estimating the normal distance from the observer to the centerline and referring to the magnitude at the centerline. While formulas (48a), (48b), and (44) yield the correct normalized ray field magnitude along the centerline, a good approximation is obtained when assuming a linear variation between the magnitude values at the upper and lower surfaces, which are given between parentheses for each ray in Fig. 5. Moreover, the off-axis magnitude can be approximated through multiplying the magnitude at the point of intersection of the normal from the observer to the

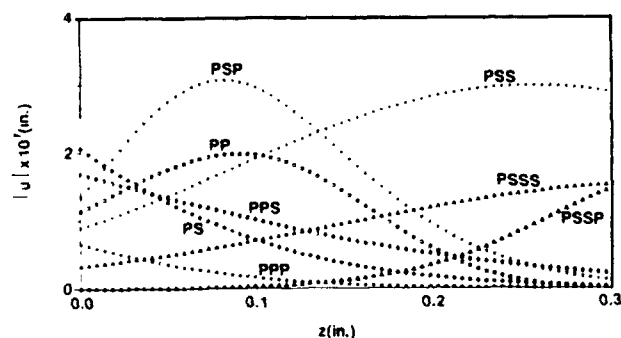


FIG. 7. Contributions of individual complex rays to displacement $|u|$ at cross section $x = 0.45$ in. Parameters are as in Fig. 1.

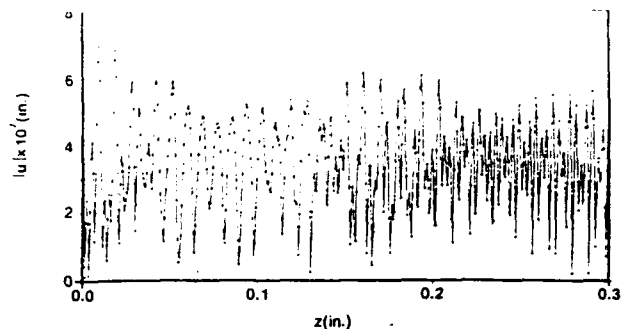


FIG. 8. Displacement $|u|$ at cross section $x = 0.45$ in. Solid curve: mode summation reference solution. Dots: sum of complex rays whose individual magnitudes are identified in Fig. 7. Parameters are as in Fig. 1.

centerline by the factor $\exp(-3r^2)$, with r being the ratio of the observer-centerline and edge-centerline distances along the same normal. For example, if one seeks to synthesize the total field along the cross section at $x = 0.45$ in., these sketches reveal that the important contributors are the rays PP , PSS , PSP , $PSSS$, PPS , PS , $PSSP$, and for fine tuning (especially for small z) also PPP . Figure 7 shows the individual magnitude profiles of these ray fields along the vertical cut $x = 0.45$ in. as computed from (26) and (46a) and (46b). All of the rays have significant strengths, including ray PPP near the upper end of the plate, i.e., $z < 0.05$ in. To illustrate use of this procedure, refer to Fig. 5(g), where the ray is PSP , the observer O is located at $x \approx 0.45$ in., $z \approx 0.20$ in., $r = OA/A'A \approx \frac{1}{2}$, $QA/QP \approx \frac{1}{2}$; one deduces that the normalized magnitude at A is approximately $0.67 - (QA/QP) \cdot (0.67 - 0.52) \approx 0.595$, whereas at point O it is $0.595 \cdot \exp[-3(1/2)^2] \approx 0.28$. The actual magnitude at O is then $0.28 \cdot 4.847 \times 10^{-7} = 1.357 \times 10^{-7}$ in., which

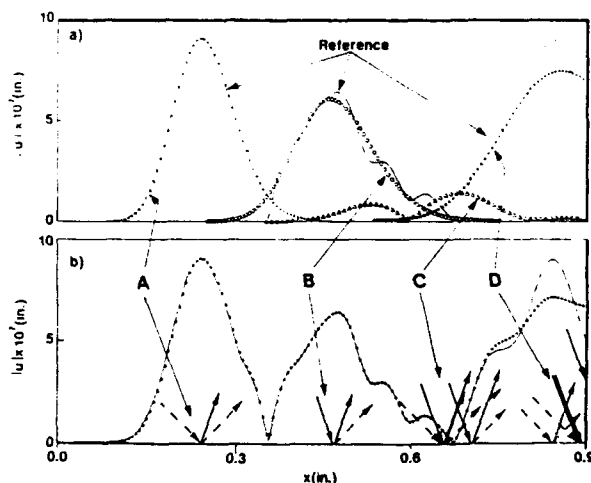


FIG. 9. Displacement $|u|$ along lower plate surface. Solid curve: reference solution. (a) Local reconstruction, using complex ray clusters identified in regions A, B, C, D of Fig. 1. (b) Reconstruction (dots) using sum of complex ray clusters in (a); good agreement for $x < 0.6$ in., but discrepancies for $x > 0.6$ in. due to the omission of complex rays beyond region D. Parameters are as in Fig. 1.

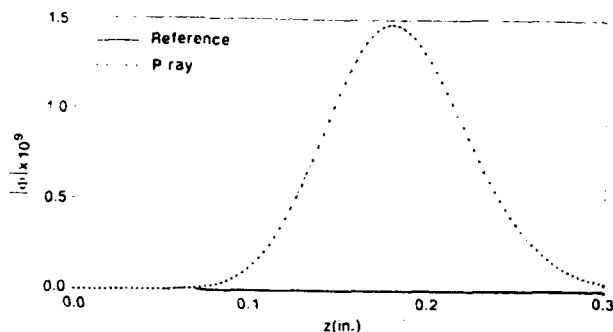


FIG. 10. Magnitude of Φ potential at cross section $x = 0.12$ in. Solid curve: reference by mode summation (64 modes). Dots: P complex ray. Parameters are as in Fig. 1.

turns out to be a reasonably good approximation of the correct magnitude plotted in Fig. 7 for the PSP ray at the location $z = 0.20$ in. Adding the contributions of the complex ray fields in Fig. 7, with inclusion of phase information from (26) and (45a) and (45b), one obtains the total field magnitude $|u|$ identified in dots in Fig. 8, which is seen to agree with the reference curve (solid line) obtained from the mode summation algorithm.

For another comparison between the beam and mode summation algorithms, the horizontal displacement magnitude $|u|$ on the lower surface of the plate is plotted in Fig. 9. The solid line in both parts (a) and (b) is the reference solution obtained by mode summation; all other curves have been generated using (26) and (45a) and (45b). Contributions from the complex ray clusters identified by their beam axes within regions A–D in Fig. 1, and repeated on the bottom of Fig. 9(b), have been calculated individually and plotted in Fig. 9(a). The cluster A is obtained by summing the contributions along the first three complex rays P , PP , and PS , with inclusion of phase information. Their individual normalized magnitudes at the lower surface are shown in the region $x < 0.40$ in. in Fig. 6. One observes that the relevant complex ray clusters synthesize the local surface displacement very well in region A, reasonably well in region B (but with some loss of fine detail), less well in region D, and very poorly in region C. The deterioration of the quality of the local reconstruction with increase in the number of reflections is due to spillover contributions from complex ray fields at earlier and later reflections. This fact is demonstrated in Fig. 9(b), where the sum of the individual contributions is identified by dots. The fine structure in region B has now been recovered, region C is synthesized very well, and only region D is deficient because of the truncation of the complex ray sum at region D. The numerical efficiency and physical clarity of the beam synthesis is evident when compared with the mode series reference sum that requires 64 modes. As seen in Fig. 9(a) and predicted from the sketches of Fig. 5, complex rays P , PP , and PS in Fig. 1 suffice to synthesize the total horizontal displacement field at the plate lower surface for $x < 0.3$ in. Away from this region, PSS , $PSSP$, and $PSSS$ also begin to play a role, and so forth as x increases. For $x > 0.45$ in., the first cluster (P , PP , and PS) can be omitted because its contribution becomes negligible.

A more striking illustration of the merits of the beam modeling is given in Fig. 10, which shows the magnitude of the Φ potential at cross section $x = 0.12$ in. near the source. The reference solution (solid line) generated by the mode summation algorithm in (14) with (23), accounting for 64 CSP-extended normal modes, is recovered by the *single* direct P complex ray field computed from (26). Moving away from the source, the number of reflections proliferates and the beam summation becomes numerically less convenient and physically more obscure. Mode summation may then be preferable.

V. SUMMARY

In this presentation, we have established the utility of a direct beam tracking algorithm for synthesis of the total dynamic fields generated near, and at moderate distances from, an oblique high-frequency Gaussian P beam injected into a lossless elastic plate. It has been shown that predictable beam clusters for early multiples can synthesize local prominent features in the total field, thereby rendering the clusters phenomenologically correct descriptors for the wave physics. This circumstance can be employed in a weak debonding detection and identification scheme, as has already been demonstrated² for the highly idealized model employed in this study. To what extent such a scheme is compromised by realistic NDE conditions remains to be explored. Nevertheless, together with the mode summation algorithm in Ref. 1, the present results permit the construction of a beam–mode hybrid for systematic and physically incisive charting of the field response anywhere in the plate.

ACKNOWLEDGMENT

This work has been supported by the U.S. Air Force Office of Scientific Research under Grant No. AFOSR-86-0318.

¹ I. T. Lu, L. B. Felsen, and J. M. Klosner, "Observables due to Beam-to-Mode Conversion of a High-Frequency Gaussian P Wave in an Aluminum Plate in Vacuum," *J. Acoust. Soc. Am.* **87**, 42–53 (1990).

² L. B. Felsen and S. Zeroug, "Ultrasonic Beam Method for Localized Weak Debonding in a Layered Aluminum Plate," *J. Acoust. Soc. Am.* **90**, 1527–1538 (1991).

³ W. M. Ewing, W. C. Jardetzky, and F. Press, *Elastic Waves in Layered Media* (McGraw-Hill, New York, 1957).

⁴ L. M. Brekhovskikh, *Waves in Layered Media* (Academic, New York, 1960), Sec. 8.

⁵ L. B. Felsen and N. Marcuvitz, *Radiation and Scattering of Waves* (Prentice-Hall, Englewood Cliffs, NJ, 1973).

⁶ I. T. Lu and L. B. Felsen, "Ray, Mode and Hybrid Options for Source-Excited Propagation in an Elastic Plate," *J. Acoust. Soc. Am.* **78**, 701–714 (1985).

⁷ B. A. Auld, *Acoustic Fields and Waves in Solids* (Wiley, New York, 1975), Vol. II.

⁸ Y. H. Pao and R. R. Gajewski, "The Generalized Ray Theory and Transient Responses of Elastic Solids," in *Physical Acoustics* (Academic, New York, 1977), Vol. XIII, Chap. 6.

⁹ L. B. Felsen, "Complex-Source-Point Solutions of the Field Equations and Their Relation to the Propagation and Scattering of Gaussian Beams," in *Symposia Matematica*, Istituto di Alta Matematica (Academic, New York, 1976), Vol. 18, pp. 40–56.

¹⁰ L. B. Felsen, "Geometrical Theory of Diffraction, Evanescent Waves, Complex Rays and Gaussian Beams," *Geophys. J. R. Astron. Soc.* **79**, 77–88 (1984).

¹¹ M. Couture and P. A. Belanger, "From Gaussian Beam to Complex-Source-Point Spherical Wave," *Phys. Rev. A* **24**, 355–359 (1981).

Ultrasonic beam method for localized weak debonding in a layered aluminum plate

Leopold B. Felsen and Smaine Zeroug

Department of Electrical Engineering/Weber Research Institute, Polytechnic University, Farmingdale, New York 11735

(Received 14 September 1990; revised 22 May 1991; accepted 23 May 1991)

Weakened bonds in layered materials cannot easily be detected by vertically probing ultrasonic beams because the flaw is insensitive to the predominantly compressional (P) wave input. By tilting the incident P beam, which is taken to be Gaussian in this model study, it is possible to generate tangential shear components parallel to the bond line and thereby induce scattering from the flawed region. This scenario is explored here for a two-layer aluminum plate with a weak localized debond. A two-dimensional obliquely incident Gaussian P beam, modeled rigorously by the complex source point technique, is tracked through multiple reflections with P - SV coupling. Its interaction with the flaw is treated in the Born approximation that renders the induced source distribution along the flaw equal to the unperturbed field multiplied by the weak debonding profile, taken here as quasi-Gaussian. The resulting scattered field is computed by spectral wave-number synthesis, and the displacements of the plate surface generated by the incident and scattered fields furnish the desired data. The accuracy of the computation is confirmed by comparison with an independent solution developed previously^{3,4} by modal summation. Examination of the data reveals a weak, but separately identifiable contribution due to the scattering if the incident beam interacts directly with the flaw without having undergone reflection. Because all relevant phenomena are dominated by quasi-Gaussian wave processes, a simple Gaussian beam tracking and scattering model is proposed and found to be capable of explaining the relevant features in the data. This beam modeling of the problem is then applied to determine from the data the location, extent, and strength of the Gaussian debonding profile. Both the forward and inverse algorithms are structured around physically transparent wave processes and can easily be implemented.

PACS numbers: 43.35.Zc

INTRODUCTION

Obliquely incident (predominantly P wave) beam inputs from an ultrasonic transducer into a layered bonded composite elastic plate are suitable for detection of weak debonds because they generate on the bond lines the tangential shear to which this kind of flaw responds. In previous studies, the beam-flaw interaction and scattering mechanisms were explored by expressing the fields in both the unflawed and flawed environments in terms of the set of P - SV coupled modes capable of propagating in the plate.¹⁻⁵ The reference data generated in this manner exhibit beamlike features of the fields in observation domains covered by only a few P - SV coupled beam reflections between the outer boundaries of the perfectly bonded plate, thereby indicating that the normal modes are not matched to the features observed in the data. Such features in the data shall be referred to as "observables." The problem is therefore restructured here by direct beam tracking. As before,^{1,2} our model is two-dimensional and comprises a two-layer aluminum plate in vacuum, with a weak debond region modeled by a quasi-Gaussian pliability profile.

In what follows, we outline the solution strategy for tracking the input beam via a rigorous complex source point (CSP) algorithm through multiple P - SV coupled reflections to an observer on the upper or lower boundaries of the

unflawed plate for the purpose of establishing the horizontal and vertical displacements that would be measured with a detector on these boundaries. The flawed environment is defined next, with a description of the analytical procedure employed for generating the scattered field and its contribution to the particle displacements on the plate surfaces. Because of the assumed quasi-Gaussian pliability profile along the flaw line, the scattered field can likewise be modeled as quasi-Gaussian. For convenient tracking of these quasi-Gaussian (incident and scattered) beams, we introduce a paraxial propagation algorithm that simplifies the forward (direct) problem substantially. Moreover, via back propagation, this algorithm can be employed for the inverse problem aimed at source as well as flaw location and identification using the measured displacements on the surfaces of the unflawed and flawed plate environments. In this manner, the forward and inverse problems have been modeled entirely in terms of beam propagation events.

Extensive numerical computations have been carried out to establish the validity of the strategy proposed above. This is done by comparing results generated from the beam algorithm with the previous reference data obtained by mode summation. Representative samples are included to illustrate (1) the buildup of the observables in the reference data by selective addition of beams, (2) the quality of Gaussian matching to the observables, and (3) the quality of the

In a final comparison, the paraxial algorithm is employed for detecting, locating, and identifying the parameters of a flaw from the surface displacement data produced by the forward reference solution.

I. FORMULATION

A. Background

The physical configuration, schematized in Figs. 1 and 2, involves a bonded plate of thickness a and the constitutive parameters (Lamé constants) λ , μ , and (density) ρ , with excitation provided by a two-dimensional ultrasonic time-harmonic (of the form $e^{-i\omega t}$) Gaussian P -beam input whose waist is centered at $(x, z) = (x', z')$ and whose inclination with respect to the x axis is α_p . A longitudinally oriented thin flaw of length $2l$ is centered at (x_f, z_f) .

The physical observables generated by the input forcing function are the horizontal and vertical displacements $u(x, z)$ and $w(x, z)$, respectively. To set the tone for the present investigation, it is useful to summarize the spectral considerations for the unflawed plate³ that enter into the generation and interpretation of the data. The interpretation may require use of different coordinate systems "matched" to particular phenomena [for example, beam-centered coordinates instead of the plate coordinates (x, z)]. Moreover, it may be convenient to use the scalar potentials $\Phi(x, z)$ and $\Psi(x, z)$ pertaining to compressional (P) and vertically polarized shear (SV) motion, respectively, to generate the displacements⁶

$$u = \frac{\partial \Phi}{\partial x} - \frac{\partial \Psi}{\partial z}, \quad w = \frac{\partial \Phi}{\partial z} + \frac{\partial \Psi}{\partial x}. \quad (1)$$

The P and SV waves have the propagation speeds $v_p = [(\lambda + \mu)/\rho]^{1/2}$ and $v_s = [\mu/\rho]^{1/2}$, respectively. For waves "tied" to the plate, the spectral decomposition is along x or z . Decomposition along x organizes the response in terms of a plane-wave spatial spectral continuum with (horizontal) wave number k :

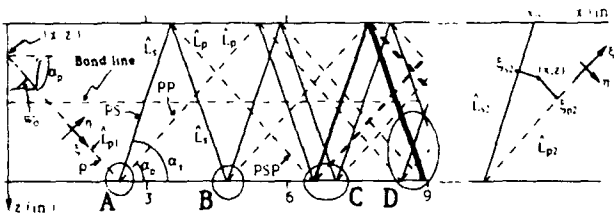


FIG. 1. Trajectories of the incident and reflected beam axes in the unflawed plate, with P - S coupled species and path lengths \hat{L}_p, \hat{L}_s for a complete excursion between the boundaries identified. The initial segment from the source location is \hat{L}_{p1} , and the final segment along the beam axis to the point ξ_{p2} or ξ_{s2} nearest the observer is \hat{L}_{p2} or \hat{L}_{s2} for a final P or SV beam, respectively (see last sketch). Here, (ξ, η) are the beam-centered coordinates, with η denoting the paraxial perpendicular displacement of an observation point (x, z) from the nearest point ξ on the axis. Dashed lines: P waves; solid lines: SV waves. Plate parameters: $a = 0.3''$, $v_p = 1.209 \times 10^3$ in./s, $v_s = 2.36 \times 10^3$ in./s, $\rho = 2.53 \times 10^{-4}$ lb s²/in.⁴. Incident beam parameters (CSP modeling): $f = 20$ MHz, $w_0 = 0.0335$ in., $\alpha_p = 45^\circ$, $(\tilde{x}, \tilde{z}) = (x' + ib_p \cos \alpha_p, z' + ib_p \sin \alpha_p)$, $(x', z') = (0.0, 0.06)$ in., $b_p = 0.3$ in., $(i = \sqrt{-1})$.

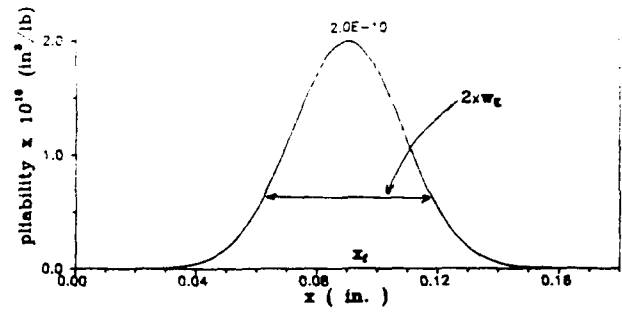


FIG. 2. Assumed pliability profile in (33): $K_0 = 5.000 \times 10^9$ lb/in.³, $(x_f, z_f) = (0.09, 0.15)$ in., $w_k = 0.025$ 99 in.

$$A(x, z) = \frac{1}{2\pi} \int_{-\infty}^{\infty} \hat{A}(z, \kappa) \exp[ikx] dk, \quad (2)$$

where $\hat{A}(z, \kappa)$ is the z -dependent spectral wave amplitude corresponding to $A(x, z)$, and $\kappa = \kappa(k)$ is the vertical wave number. The relation between k and κ is expressed by the dispersion equations

$$k^2 + \kappa_{p,s}^2 = k_{p,s}^2, \quad k_{p,s} = \omega/v_{p,s}, \quad \text{for } P, SV \text{ waves}, \quad (3)$$

with $\text{Im}(k \text{ or } \kappa) \geq 0$ to ensure convergence when the wave number is nonreal; ω is the source angular frequency. It may be recalled that P - SV coupling at the layer boundaries implies that both wave types have the same horizontal wave number k . Alternatively, decomposition along z organizes the response in terms of a discrete spectrum of guided modes with vertical wave number κ_m :

$$A(x, z) = \sum_m \hat{A}_m(z, \kappa_m) \exp[ik_m(\kappa_m)x], \quad x > 0, \quad (4)$$

where m is the mode index and $\hat{A}_m(z, \kappa_m)$ contains the vertical mode function as well as modal amplitude factors.

Although the displacements in (1) involve contributions from the differentiated compressional and shear potential simultaneously, one may encounter parameter regimes where either Φ or Ψ predominates. The observed displacements can then be anticipated from the form of the appropriate dominant potential. This observation is based on the spectral representation, for each spectral x - or z -based plane-wave element, of the displacements in (1):

$$\hat{u} = ik\hat{\Phi} \pm i\kappa_s\hat{\Psi}, \quad \hat{w} = \pm i\kappa_p\hat{\Phi} + ik\hat{\Psi}. \quad (5)$$

Thus for large $\kappa_{p,s}/k$, w is dominated by Φ , and u is dominated by Ψ . This guideline can be employed to select input beams that favor the excitation of strong compression or strong shear.³

B. Beam parametrization

The guided modes in Ref. 3 are phenomenologically unsuited to construct the observables in the early phases where the nonflawed plate fields, before encountering several reflections, appear more beamlike than modelike. Therefore, in this region the wave fields should be modeled in terms of beam functions. Beam modeling is based on the generalized ray integral superposition in Eq. (15) of Ref. 3 and modified

for P -beam input by the CSP substitution in Eq. (18) of Ref. 3

$$\tilde{x} = x' + ib_p \cos \alpha_p, \quad \tilde{z} = z' + ib_p \sin \alpha_p, \quad b_p > 0, \quad (6)$$

where i is the imaginary unit, an overtilde denotes a complex quantity associated with the CSP model, and the subscript p refers to quantities associated with the P -beam source. The CSP-generated beam has its waist centered at (x', z') ; the $(1/e)$ width w_0 of the waist is related to the complex displacement parameter b_p via $w_0^2 = 2b_p/k_p$, from which one recognizes that b_p itself expresses the Fresnel length corresponding to w_0 .

The generic form V_v of the beam integral for the $(\Phi$ or $\Psi)$ potential along a multiple-reflection trajectory (Fig. 1) is

$$V_v(x, z) = \frac{1}{2\pi} \int_{-\infty}^{\infty} dk F_v(k) \times \exp[i\tilde{\theta}_v(k; x, z)], \quad v = p, s, \quad (7)$$

where $F_v(k)$ is a function incorporating dependence on the source parameters as well as on the reflection and coupling coefficients. The function $\tilde{\theta}_v(k; x, z)$ is the accumulated complex phase along the (P, SV) propagation paths:

$$\begin{aligned} \tilde{\theta}_v(k; x, z) &= k(x - x' - ib_p \cos \alpha_p) + \kappa_p(a - z' - ib_p \sin \alpha_p) \\ &\quad + \kappa_p N_p a + \kappa_s N_s a + \kappa_s z_l, \end{aligned} \quad (8)$$

where $N_v = N_{p,s}$ denotes the number of (P, SV) excursions across the plate, and z_l denotes the vertically projected segment from the last complete excursion to the observer. The integral in (7) can be evaluated asymptotically by the saddle point method,⁷ applied in the complex k plane to the analytically continued integrand

$$V_v(x, z) \sim \frac{1}{2\pi} \sqrt{\frac{2\pi i}{\partial^2 \tilde{\theta}_v(k_{\text{sad}}; x, z)/\partial k^2}} F_v(k_{\text{sad}}) \times \exp[i\tilde{\theta}_v(k_{\text{sad}}; x, z)], \quad (9)$$

where $\arg(\sqrt{\cdot}) = \arg(dk)$, with dk denoting an element at k_{sad} along the steepest descent path. The first-order saddle point k_{sad} is defined by

$$\frac{\partial \tilde{\theta}_v(k_{\text{sad}}; x, z)}{\partial k} = 0, \quad \text{with} \quad \frac{\partial^2 \tilde{\theta}_v(k_{\text{sad}}; x, z)}{\partial k^2} \neq 0. \quad (10)$$

Equation (9) furnishes the contribution of each beam. The superposition of all possible beam contributions at the observation point (x, z) furnishes the beam-modeled total field.

1. Paraxial field

An explicit analytic solution for the saddle point is difficult, but an approximate expression in the paraxial region near the beam axis is easily obtainable through expansion of the phase function $\tilde{\theta}_v(k; x, z)$ up to the quadratic term. We consider first the incident P -beam potential $\Phi(x, z)$ before encountering a boundary. The phase of this beam is given by (8), with

$$N_p = N_s = 0, \quad \kappa_p(a - z') + \kappa_s z_l \rightarrow \kappa_p(z - z'), \quad (11)$$

and the source function is given by [Eq. (7) of Ref. 3]

$$F_p(k) = -1/(2ik_p). \quad (12)$$

After changing coordinates from the global (x, z) to the beam-centered (ξ, η) system (Fig. 1),

$$\begin{aligned} x - x' &= \xi \cos \alpha_p + \eta \sin \alpha_p, \\ z - z' &= \xi \sin \alpha_p - \eta \cos \alpha_p, \end{aligned} \quad (13)$$

the paraxial region of the beam is defined by

$$|\eta| \ll \sqrt{\xi^2 + b_p^2}. \quad (14)$$

When $\eta = 0$, i.e., for observation points on the beam axis, the saddle point is found to be real:

$$k_{\text{sad}}^0 = k_p \cos \alpha_p. \quad (15)$$

Paraxial expansion of $\tilde{\theta}_v(k; x, z)$ then leads easily to the off-axis saddle point

$$k_{\text{sad}} = k_p \cos \alpha_p + k_p \eta \sin \alpha_p / (\xi - ib_p) \quad (16)$$

and to the corresponding complex paraxial phase

$$\begin{aligned} \theta_p(k_{\text{sad}}; \xi, \eta) &= k_p [\xi - ib_p + \eta^2 / 2\xi (1 + b_p^2 / \xi^2)] \\ &\quad + i \{ \eta^2 / [(2b_p/k_p)(1 + \xi^2/b_p^2)] \}. \end{aligned} \quad (17)$$

From (9) and (17), the exponential amplitude profile on a transverse plane $\xi = \text{const}$ is given by

$$\exp[-\eta^2 / w_p^2(\xi)], \quad (18)$$

where $w_p(\xi)$ is the beam width at ξ ,

$$w_p^2(\xi) = w_p^2(0)(1 + \xi^2/b_p^2), \quad w_p^2(0) = w_0^2 = 2b_p/k_p, \quad (19)$$

and, as mentioned earlier, b_p is identified as the Fresnel length of the paraxial beam corresponding to the beam waist $(1/e)$ width $w_p(0)$. The real phase variation at ξ is given by

$$\exp\{ik_p[\xi + \eta^2/2R_p(\xi)]\}, \quad R_p(\xi) = \xi + b_p^2/\xi, \quad (20)$$

where $R_p(\xi)$ is the on-axis radius of curvature of the beam wave front. Normalizing (9) by omitting the constant term $\exp(k_p b_p)$ [see (17)], the full paraxial beam field is

$$\begin{aligned} \Phi(\xi, \eta) &\sim \exp(i\pi/4)/(2\sqrt{2\pi}) \\ &\quad \times \frac{\exp\{ik_p[\xi + \eta^2/[2R_p(\xi)]] - \eta^2/w_p^2(\xi)\}}{\sqrt{k_p(\xi - ib_p)}}, \end{aligned} \quad (21)$$

with $\arg[\sqrt{k_p(\xi - ib_p)}]$ chosen such that it tends to zero as $b_p/\xi \rightarrow 0$. Expression (21) is in accord with variously derived widely used formulas in the literature.⁸⁻¹² Deriving (21) here from the CSP expression, which is an exact solution of the wave equation, permits a better understanding of the nature of the paraxial approximation.¹³

For the multiple-reflected beam, the beam-centered (ξ, η) coordinates (see Fig. 1) along the last segment are, with $v = p$ or s ,

$$\begin{aligned} x - x' &= (z_p \cot \alpha_p + z_s \cot \alpha_s) + \xi \cos \alpha_v + \eta \sin \alpha_v, \\ z_l &= \xi \sin \alpha_v - \eta \cos \alpha_v, \end{aligned} \quad (22)$$

where

$$z_p = a - z' + N_p a, \quad z_s = N_s a, \quad (22')$$

and z_p are related by

$$k_p \cos \alpha_p = k_v \cos \alpha_v. \quad (23)$$

The phase in (8) now becomes

$$\begin{aligned} \bar{\theta}_v(k; \xi, \eta) = & k(z_p \cot \alpha_p + z_v \cot \alpha_v + \xi \cos \alpha_v \\ & - \eta \sin \alpha_v - ib_p \cos \alpha_p) \\ & + \kappa_p(z_p - ib_p \sin \alpha_p) + \kappa_v z_v \\ & + \kappa_v(\xi \sin \alpha_v - \eta \cos \alpha_v). \end{aligned} \quad (24)$$

Approximating paraxially by expanding up to second order in the off-axis distance η and in the deviation in k from the on-axis saddle point value $k_{\text{sad}}^0 = k_v \cos \alpha_v$, one obtains, for the saddle point corresponding to an off-axis observer at (ξ, η) ,

$$\begin{aligned} k_{\text{sad}} = & k_v \cos \alpha_v + \frac{\eta}{\sin \alpha_v} \left(\frac{L_p - ib_p}{k_p \sin^2 \alpha_p} \right. \\ & \left. + \frac{L_v}{k_v \sin^2 \alpha_v} + \frac{\xi}{k_v \sin^2 \alpha_v} \right)^{-1}. \end{aligned} \quad (25)$$

Here,

$$L_v = z_v / \sin \alpha_v, \quad (25')$$

represents the total distance traversed by P and (or) SV waves along their respective beam axes. The resulting com-

plex phase in (24) becomes, after rearrangement that exhibits the radius of curvature $R_v(\xi)$ of the beam wave front and the beam width $w_v(\xi)$,

$$\begin{aligned} \bar{\theta}_v(k_{\text{sad}}; \xi, \eta) \simeq & C + k_v [\xi + \gamma_{vp} L_p + \gamma_{vs} L_s - i\gamma_{vp} b_p] \\ & + k_v \eta^2 / 2R_v(\xi) + i\eta^2 / w_v^2(\xi), \end{aligned} \quad (26a)$$

with

$$\gamma_{vp} = k_v \sin^2 \alpha_v / k_p \sin^2 \alpha_p, \quad (26b)$$

$$\gamma_{vs} = k_v \sin^2 \alpha_v / k_s \sin^2 \alpha_s,$$

$$\begin{aligned} R_v(\xi) = & \xi + \gamma_{vp} L_p + \gamma_{vs} L_s \\ & + \gamma_{vp}^2 b_p^2 / (\xi + \gamma_{vp} L_p + \gamma_{vs} L_s), \end{aligned} \quad (26c)$$

$$w_v^2(\xi) = \frac{2\gamma_{vp} b_p}{k_v} \left(1 + \frac{(\xi + \gamma_{vp} L_p + \gamma_{vs} L_s)^2}{\gamma_{vp}^2 b_p^2} \right), \quad (26d)$$

$$C = (k_p - k_v \gamma_{vp})(L_p - ib_p) + (k_s - k_v \gamma_{vs})L_s. \quad (26e)$$

Furthermore, using the lowest-order approximation $k_{\text{sad}} \simeq k_{\text{sad}}^0$, which is adequate for an amplitude function,

$$\begin{aligned} \frac{\partial^2 \bar{\theta}_v(k_{\text{sad}}^0; \xi, 0)}{\partial k^2} = & - \frac{k_v}{k_v^2 \sin^2 \alpha_v} (\xi + \gamma_{vp} L_p \\ & + \gamma_{vs} L_s - i\gamma_{vp} b_p). \end{aligned} \quad (27)$$

When the results in (26) and (27) are substituted into (9), one finds

$$V_v(\xi, \eta) \sim k_v \sin \alpha_v \frac{\exp[i(C_1 - \pi/4)]}{\sqrt{2\pi}} F_1(k_{\text{sad}}^0) \frac{\exp\{ik_v [\xi + \gamma_{vp} L_p + \gamma_{vs} L_s + \eta^2 / 2R_v(\xi)] - \eta^2 / w_v^2(\xi)\}}{[k_v (\xi + \gamma_{vp} L_p + \gamma_{vs} L_s - i\gamma_{vp} b_p)]^{1/2}}, \quad (28)$$

where

$$C_1 = C - ik_v \gamma_{vp} b_p, \quad (28')$$

with the argument of the square root in the denominator of (28) chosen such that it tends to zero as $(\gamma_{vp} b_p)(\xi + \gamma_{vp} L_p + \gamma_{vs} L_s)^{-1} \rightarrow 0$. Comparing (28) with (21), one observes that the paraxial beam field V_v at (ξ, η) may be regarded as emanating from an equivalent virtual $v = p$ or s CSP located at $(\xi, \eta) = (-\gamma_{vp} L_p - \gamma_{vs} L_s - i\gamma_{vp} b_p, 0)$ outside the plate region in the *infinitely extended* medium. This equivalent paraxial beam has a Fresnel length

$$b_v = \gamma_{vp} b_p \quad (29)$$

and minimum waist

$$w_v = \sqrt{2b_v / k_v}. \quad (30)$$

On the upper plate surface $z_l = a$, this beam field gives rise to the real phase variation

$$\begin{aligned} \text{Re}[\bar{\theta}_v(k; x, z_l = a)] = & C' + k_v \cos \alpha_v x \\ & + (k_v \sin^2 \alpha_v / 2R_v)(x - x_0)^2, \end{aligned} \quad (31)$$

where x_0 is the intersection point of the beam axis with the surface (see Fig. 1) and

$$\begin{aligned} C' = & k_p L_p + k_s L_s + k_v [- (x' + L_p \cos \alpha_p \\ & + L_v \cos \alpha_v) \cos \alpha_v + a \sin \alpha_v]. \end{aligned} \quad (31')$$

C. Flaw characterization and excitation

1. Characterization

We consider longitudinally varying bond imperfections that manifest themselves only with respect to the shear resistance while retaining full strength in the normal direction. When the bond thickness t is much less than the ultrasonic wavelength and uniform shear stress through the thickness of the bond is assumed, one may express the jump discontinuity $\Delta u = u^+ - u^-$ of the horizontal displacement $u(x, z)$ across the bond layer as^{4,14}

$$\Delta u(x, z_f) = \tau_{zx}(x, z_f) / K(x), \quad K(x) = \mu_d(x) / t. \quad (32)$$

Here, $\tau_{zx}(x, z_f)$ is the shear stress, $\mu_d(x)$ is the shear modulus along the debond, and $K(x)$ is the spring stiffness variation in the bond model comprising distributed weightless springs. We shall assume for the reciprocal of $K(x)$, i.e., the pliability profile, the Gaussian function

$$1/K(x) = (1/K_0) \exp\{ - [(x - x_f) / w_K]^2 \}, \quad (33)$$

where w_K is the $1/e$ width, $(1/K_0)$ is the maximum strength, and x_f is the location of the maximum (see Fig. 2).

2. Excitation

With the flaw in place and knowledge of the incident field at the flaw from the results in Sec. I B, one may formulate the scattering problem. In general, this requires the solu-

tion of a surface integral equation for the unknown induced sources on the flaw.¹⁷ However, in view of the assumed weakness of the imperfection, the induced sources can be approximated by those sources corresponding to the incident field on the flaw (Born approximation).¹⁶ Accordingly, from (32), the displacement discontinuity across the weakened zone becomes

$$\Delta u(x, z_f) \approx \Delta u'(x, z_f) = \tau_{zx}(x, z_f)/K(x), \quad (34a)$$

$$\tau_{zx}(x, z_f) = \mu \left(2 \frac{\partial^2 \Phi'(x, z_f)}{\partial x \partial z} \right), \quad (34b)$$

where $\tau_{zx}(x, z_f)$ is the shear stress over the debond region induced by the incident P -beam potential $\Phi'(x, z_f)$ in the perfectly bonded plate, and $K(x)$ is taken from (33).

D. Flaw scattered fields

1. Formulation in the spectral domain

The displacements u^s and w^s can be evaluated by superposition in the configurational domain of the fields radiated by the induced sources $\Delta u'(x', z_f)$:⁴

$$u^s(x, z) = \int_{x_f-2l}^{x_f+2l} \Sigma_{zx}(x', z_f; x, z) \Delta u'(x', z_f) dx', \quad (35a)$$

$$w^s(x, z) = \int_{x_f-2l}^{x_f+2l} \Sigma_{xz}(x', z_f; x, z) \Delta u'(x', z_f) dx', \quad (35b)$$

where $2l$ is the length of the weak debond region, and the Green's stress functions Σ_{zx} and Σ_{xz} represent the shear stress along the perfect bond line at z_f due to horizontally and vertically polarized concentrated forces, respectively.

For modeling by beams, it is more convenient to synthesize the scattered fields in the spectral domain.¹⁷ The displacements in (35) can be derived via (1) from the scattered potentials Φ^s and Ψ^s . With the details relegated to Appendix A, the source terms for these potentials are, respectively,

$$S_p^{d,u}(k, z_f) = \pm i(k/k_z^2) \widehat{\Delta u'}(k, z_f), \quad (36a)$$

$$S_s^{d,u}(k, z_f) = i[(k^2 - k_z^2)/2\kappa_z k_z^2] \widehat{\Delta u'}(k, z_f), \quad (36b)$$

where $\widehat{\Delta u'}(k, z_f)$ is the spectrum of the induced source in (32). The debond scatters symmetrically in the upward and downward directions, as distinguished by the superscripts "d" and "u" in (36) (see Fig. 3); the plus sign in (36a) corresponds to "d." Before encountering reflection, the scattered potential fields are

$$(\Phi^s)^{d,u}(x - x_f, z) = \frac{1}{2\pi} \int_{-\infty}^{\infty} (\widehat{\Phi^s})^{d,u}(k, z) \times \exp[ik(x - x_f)] dk, \quad (37a)$$

$$(\Psi^s)^{d,u}(x - x_f, z) = \frac{1}{2\pi} \int_{-\infty}^{\infty} (\widehat{\Psi^s})^{d,u}(k, z) \times \exp[ik(x - x_f)] dk, \quad (37b)$$

where

$$\begin{aligned} (\widehat{\Phi^s})^{d,u}(k, z) &= S_p^{d,u} \exp[\pm i\kappa_p(z - z_f)], \\ (\widehat{\Psi^s})^{d,u}(k, z) &= S_s^{d,u} \exp[\pm i\kappa_s(z - z_f)]. \end{aligned} \quad (38)$$

Multiple-reflected scattered spectra are generated in the

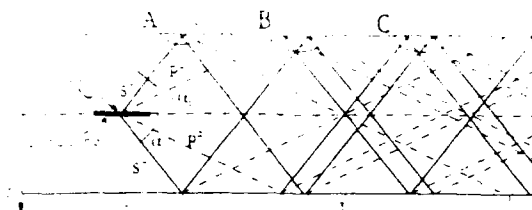


FIG. 3. Trajectories of the axes of beams scattered by debond. Dashed lines: P waves; solid lines: SV waves.

same manner as for sources incident in the unflawed plate; in particular, we shall use the ray integral expansion as in Eq. (15) of Ref. 3.

We shall show in Sec. III that because of the assumed Gaussian pliability profile in (33) for the flaw, the induced source distribution in (34) when the incident beam axis passes through x_f can be matched to a linearly phased Gaussian

$$\begin{aligned} \Delta u'(x, z_f) &= U_0 \exp\{-[(x - x_f)/w_{\Delta u}]^2\} \\ &\times \exp[i\Omega(x - x_f)], \quad \Omega = k_v \cos \alpha_v, \end{aligned} \quad (39)$$

where U_0 is the maximum amplitude, $w_{\Delta u}$ is the $1/e$ width, Ω represents the phase gradient, and x_f locates the maximum of the debond profile. The spectrum of (39) is

$$\widehat{\Delta u'}(k, z_f) = \sqrt{\pi} w_{\Delta u} U_0 \exp\{-[(k - \Omega)/2]w_{\Delta u}\}^2. \quad (40)$$

This induced source distribution gives rise to P and SV scattered fields in the shape of Gaussian beams. These beams generate similarly behaved P and SV displacements on the upper surface. Therefore, the beam parametrization in Sec. I B for the field in the unflawed plate applies equally well to the flaw scattered fields. We shall exploit this feature in the construction of the inversion algorithm.

II. INVERSE PROBLEM

In view of the remarks at the end of Sec. I D, the prominent features in the unflawed and flaw scattered displacement fields on the upper surface can be parametrized in terms of phased Gaussians. By reversing the forward processes in Sec. I B, the beam model can be employed for construction of a back propagation algorithm that locates the flaw and identifies its features. This is the inversion strategy.

A. Beam modeling of observed displacements on the upper surface

A Gaussian SV beam (either incident directly or flaw scattered) impinging obliquely on the upper surface of the plate produces displacements having a projected paraxial phase (31):

$$\begin{aligned} C'' + (k_z \cos \alpha_z) x \\ + [(k_z \sin^2 \alpha_z)/(2R_z)](x - x_0)^2 = 0, \end{aligned} \quad (41)$$

where α_z is the incidence angle of the beam axis, R_z is the on-axis radius of curvature of the incident wave front, x_0 is its intersection point on the surface, and C'' denotes a constant

phase term. Applying a least-squares-fitting technique to this data yields both the linear and quadratic coefficients in (41). From the former coefficient one may estimate α_s , and from the latter one may estimate the radius of curvature R_s . The amplitude profile of the data permits direct estimation of the maximum amplitude and the determination of the $1/e$ width of the projected Gaussian that matches the data (see Appendix B). This completes the characterization of the observed data in terms of beams. It should be noted that in the flaw scattered case, the SV beam contribution produces a clearly identifiable precursor in the total horizontal displacement (see Fig. 12), thereby legitimizing single-beam modeling.

B. Actual or induced source reconstruction

As will be seen, the flaw identification algorithm requires knowledge of the sources that establish the scattered field as well as those that establish the incident field at the flaw site in the absence of the flaw. The sources (actual or induced) are located at the site of the waist of the appropriate back propagated beam. From the procedure in Sec. II A the incidence angle α_s , radius of curvature R_s , and $1/e$ width $w_s(L_s)$ of the SV beam that established the data are known, and one may determine the waist location L_s and $1/e$ width $w_s(0)$ along a direct path from formulas (42). The relative strengths of the displacements at the source and flaw sites are derived in the spectral domain via the potentials $\hat{\Phi}$ and $\hat{\Psi}$: On the beam axes, where displacement and potential maxima occur, their values in the physical domain are readily inferred from the spectral formulas since here the spectral wave numbers k and κ_{ps} are real. Thus on the incident beam axis from the actual source, $k = k_p \cos \alpha_p$, $\kappa_p = k_p \sin \alpha_p$ and similarly for the other beam segments. This substitution is used repeatedly in what follows.

1. Direct path to waist (Fig. 4)

Here, one has

$$L_s = R_s \left[1 + 4R_s^2 / (k_s^2 w_s^4) \right]^{-1/4}, \quad (42)$$

$$w_s(0) = \left[4(R_s - L_s)L_s / k_s^2 \right]^{1/4},$$

with the Fresnel length

$$b_s = \sqrt{(R_s - L_s)L_s}. \quad (43)$$

The projected $1/e$ width of the Gaussian beam on a horizontal plane at the waist is

$$\bar{w}_s(0) = w_s(0) / \sin \alpha_s. \quad (44)$$

The quantity $L_s \sin \alpha_s$ must be smaller than the plate thickness a if the waist is to be located on a direct path. The strength of the source distribution is determined by starting from the maximum horizontal displacement field $|u_s|_{\max}$ in the data on the upper surface. These data contain the combined contributions of the incident SV , reflected SV - SV , and converted SV - P beams. In the spectral domain [from (1)],

$$\hat{u}_s = ik\Gamma_{ps}^u \hat{\Psi} - (-i\kappa_s)\hat{\Psi} - (i\kappa_s)\Gamma_{ss}^u \hat{\Psi}, \quad (45)$$

where $\hat{\Psi}$ refers to the incident SV spectral potential, and Γ_{ss}^u and Γ_{ps}^u are the plane-wave reflection and coupling coefficients at the upper surface given in Ref. 3 and evaluated at

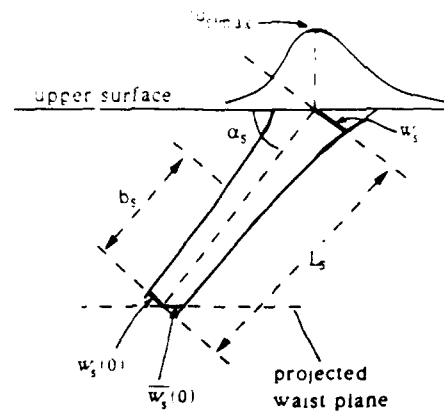


FIG. 4. Back propagation schematic for SV -beam data on the plate upper surface via a direct path to waist. $L_s \sin \alpha_s < a$. a = plate thickness.

the incidence angle α_s . The horizontal displacement attributed only to the SV wave incident along the direction α_s is $\hat{u}_{\alpha_s} = i\kappa_s \hat{\Psi}$ and can be used to remove $\hat{\Psi}$ from (45). The quantities \hat{u}_s , \hat{u}_{α_s} , and $\hat{\Psi}$ attain their maxima essentially along the beam axis, and the spectral wave numbers there are real and related by $k = k_s \cos \alpha_s$, $\kappa_s = k_s \sin \alpha_s$. Using these relations in the already modified equation (45), one may derive the following expression for the maximum displacement amplitude due to the incident SV beam in the physical domain:

$$|u_{\alpha_s}|_{\max} = |\sin \alpha_s / [\cos \alpha_s \Gamma_{ps}^u + \sin \alpha_s (1 - \Gamma_{ss}^u)]| |u_s|_{\max}. \quad (46)$$

Back propagation of $|u_{\alpha_s}|_{\max}$ along the beam axis from the upper plate surface at L_s to the waist location at $L_s = 0$ (see Fig. 4) depends solely on the factor $A(L_s) = [k_s(L_s^2 + b_s^2)^{1/2}]^{-1/2}$, where b_s is the beam Fresnel distance. The maximum amplitudes at L_s and $L_s = 0$ are therefore related by $A(L_s)/A(0)$, so that the maximum horizontal displacement strength $|u_s(0)|_{\max}$ at the waist is given by

$$|u_s(0)|_{\max} = (L_s^2/b_s^2 + 1)^{1/4} |u_{\alpha_s}|_{\max}. \quad (47)$$

2. Reflected path to waist (Fig. 5)

If the surface data is established by reflection, the impinging SV beam may be modeled equivalently by a virtual source outside the plate region, with the waist location L_s , width $w_s(0)$, and Fresnel distance b_s determined from (42) and (43). Then in terms of the parameters defined in Fig. 5, the location of the actual P source is given by

$$l_p = (L_s - a/\sin \alpha_s)/\gamma_{sp}, \quad z_p = a - l_p \sin \alpha_p, \quad (48)$$

where

$$\gamma_{sp} = (k_s/k_p)(\sin^2 \alpha_s/\sin^2 \alpha_p) \quad (48')$$

and

$$\alpha_p = \cos^{-1} [\cos \alpha_s (k_s/k_p)] \quad (49)$$

is the incident P -beam angle. The $1/e$ width $w_p(0)$ and Fresnel distance b_p of the Gaussian beam matched to the P beam at the waist are

Determination of the pliability profile parameters is now straightforward. The 1/e width w_k is given by

$$1/w_k^2 = 1/\bar{w}_p^2(0) - 1/\bar{w}_p^2(d), \quad (60)$$

where $\bar{w}_p(0)$ and $\bar{w}_p(d)$ are the projected 1/e widths of the induced displacement in (44) and incident stress in (59) on the debond line, respectively. The maximum strength of the pliability profile follows from (34a) as

$$1/K_0 = \Delta u_{\max} / \tau_{zx, \max}, \quad (61)$$

with Δu_{\max} and $\tau_{zx, \max}$ given in (57) and (58), respectively.

It should be noted that this inversion procedure has been based on the availability of the horizontal displacement field data. However, the procedure can be applied as well to data of the vertical displacement field, in which case the locations and extents of the sources are derived from formulas analogous to those above, whereas the source strengths require some modification of these formulas. Furthermore, it has been assumed from the problem structure that the relevant upper surface data is generated by a Gaussian *SV* beam. Should this information not be available *a priori*, the nature of the impinging field can be established by examining the observed $|u|_{\max}/|w|_{\max}$ ratio. As the plots in Fig. 7 show, the relative maximum strength of $|u|/|w|$ differs depending on whether a *P* or *SV* wave is incident. Since the incidence angle is known through the data processing in Sec. II A, one may refer to Fig. 7 to decide whether the displacement is caused by a *P* or *SV* wave.

III. NUMERICAL RESULTS

To test the beam model developed in Sec. II for the forward and inverse problems in the unflawed and flawed plate environments, we return to reference data computed previously by mode series summation.^{1,4} In the reference data the beamlike appearance of the fields not too far away from the beam source provided the motivation for the present study.

The problem geometry for the unflawed and flawed bonded plates is shown in Figs. 1 and 3, respectively. For the computations, we use the same physical quantities as in Ref. 4 as follows.

We use an aluminum plate of thickness $a = 0.3$ in., with the wave velocities $v_p = 2.36 \times 10^5$ (in./s), $v_s = 1.209 \times 10^5$ (in./s) and density $\rho = 2.53 \times 10^{-4}$ (lb s²/in.⁴). The source is a 20-MHz *P* beam with the waist centered at $x' = 0.0$ in., $z' = 0.06$ in., a width at the waist of $w_0 = 0.0335$ in., and a beam axis inclination angle $\alpha_p = 45^\circ$. The flaw (weak debond) is a Gaussian pliability profile [see (33) and Fig. 2] centered at $x_f = 0.09$ in., $z_f = 0.15$ in., with a maximum strength of $K_0 = 5 \times 10^9$ (lb/in.³) and a 1/e width $w_k = 0.02599$ in. (this corresponds to a debond length $2l = 0.09$ in., with a pliability strength 20 times weaker at the edges than at the center).

A. Beam parametrization in the unflawed plate

The solid curve in Fig. 8 is the reference solution obtained by mode summation for the horizontal displacement u on the lower surface of the unflawed plate. All other

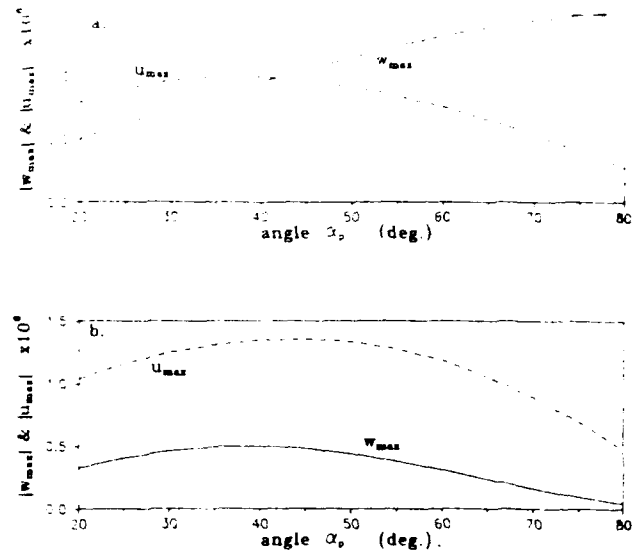


FIG. 7. Maximum displacements $|u|_{\max}$ (dashed curves) and $|w|_{\max}$ (solid curves) as a function of the *P*-wave downward incidence angle α_p . Case of the unflawed plate. Source parameters are as in Fig. 1, except that $z' = 0.12$ in. If $|u|_{\max}/|w|_{\max} > 2.5$, the wave incident on the upper surface is *SV*. If $|u|_{\max}/|w|_{\max} < 1$ or ≈ 1 , the incident wave is *P* (Ref. 4). Note that $k_p \cos \alpha_p = k_s \cos \alpha_s$. (a) First peak on the plate lower surface (ray cluster A in Fig. 1). The data identifies an incident *P* wave. (b) First peak on the plate upper surface generated by the converted beam in Fig. 1. The data identifies an incident *SV* wave.

curves have been generated by beam tracking along the trajectories in Fig. 1 using the *full beam* CSP asymptotic expressions (9) and (10). Contributions from the ray clusters identified within regions A–D in Fig. 1 have been calculated individually and plotted in Fig. 8(a); these ray clusters are repeated at the bottom of Fig. 8(b). One observes from Fig. 8(a) that the relevant ray clusters synthesize the local surface displacements very well in region A, reasonably well in region B (but with some loss of fine detail), less well in region D, and very poorly in region C. The deterioration of the

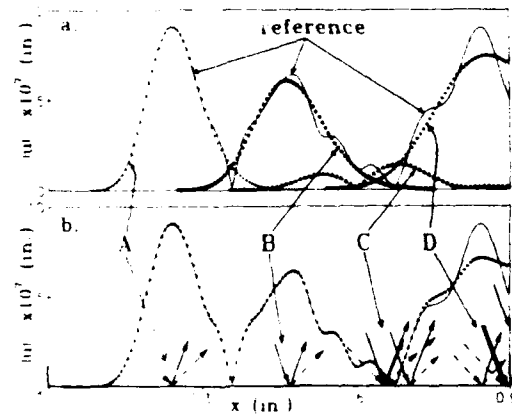


FIG. 8. Horizontal displacement u on the lower surface of the unflawed plate generated by the incident beam in Fig. 1. Solid curve: reference solution. (a) Local reconstruction using the wave species identified in regions A–D of Fig. 1. (b) Reconstruction (●) using the sum of the wave species in (a), good agreement for $x < 0.6$ in., but discrepancies for $x > 0.6$ in. due to the omission of the wave species beyond region D.

quality of the local reconstruction with the increase in the number of reflections is due to spillover contributions from beams at earlier and later reflections. This fact is demonstrated in Fig. 8(b), where the sum of the individual contributions is identified by the heavy dots. The fine structure in region B has now been recovered, region C is synthesized very well, and only region D is deficient because of the truncation there of the beam sum.

The numerical efficiency and physical clarity of the beam synthesis is evident when compared with the mode series reference sum that requires 64 modes. As seen in Fig. 8(a), beams *P*, *PP*, and *PS* in Fig. 1 suffice to synthesize the total horizontal displacement field at the plate lower surface for $x < 0.3$ in. Away from this region, the *PSS*, *PSSP*, and *PSSS* also begin to play a role, and so forth as x increases. For $x > 0.45$ in., the first cluster (*P*, *PP*, and *PS*) can be omitted because its contribution becomes negligible. Estimates of the contributing beams in any region of observation can be made by looking at the relevant beam widths. These aspects are explored in detail in a separate study.¹⁸ As the number of reflections proliferates, beam summation becomes numerically less convenient and physically more obscure. Mode summation may then be preferable.

B. Beam modeling in the flawed plate

The shearing stress generated by the input beam along the bond line of the unflawed plate, as calculated from (34b), is shown in Fig. 9; the amplitude profile centered at $x = 0.09$ in. has the shape of a projected Gaussian, and the phase is quasilinear. The linear portion of the phase on the projected plane $z = z_f$ is equal to $k_p \cos \alpha_p$, where $\alpha_p = 45^\circ$. The product of the pliability profile in Fig. 2 with the incident shear stress in Fig. 9 yields, as (34a) stipulates, the induced sources on the flaw. The result is shown by the heavy dots in Fig. 10. Gaussian fitting to the amplitude and straight line fitting to the phase agree very well and lead to the linearly phased Gaussian-shaped distribution assumed in (39). The parameters U_0 and $w_{\Delta u}$ are obtained from this Gaussian matching. Figure 11 shows the scattered horizontal displacements on the upper plate surface, with the solid curve for the mode summation reference data.

Beam modeling of the scattering problem can now be performed as in Sec. II A with reference to the beam axis trajectories in Fig. 3. Figure 11(a) depicts the separate con-

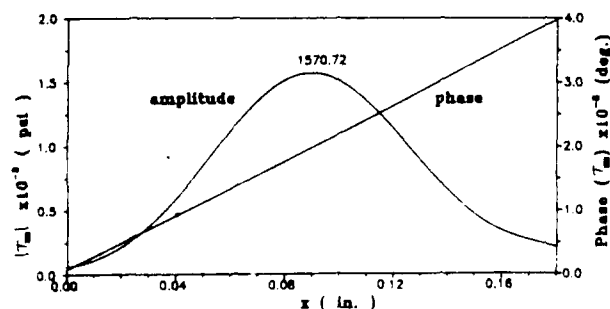


FIG. 9 Amplitude and phase of the shearing stress generated by the incident *P* beam along the bond line $z_f = 0.15$ in. in the unflawed plate. Source parameters are as in Fig. 1.

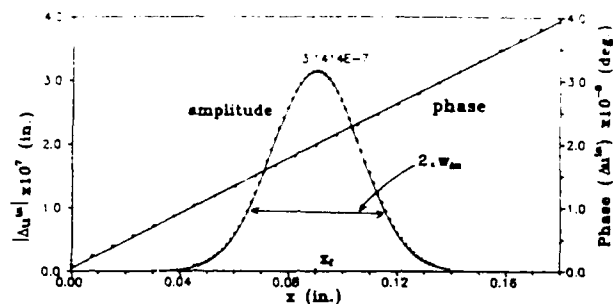


FIG. 10. Displacement source distribution induced on the flaw. ●: actual profiles of amplitude and phase obtained from the incident shearing stress (Fig. 9) and pliability profile (Fig. 2). Solid lines: amplitude (Gaussian) fit from (39), with the parameters $U_0 = 3.1414$ in., $w_{\Delta u} = 0.023$ in.; phase (linear) fit with $\Omega = k_p \cos 45^\circ$. The incident shear stress and pliability profile parameters are as in Figs. 2 and 9.

tributions from the beam clusters in regions A–C of Fig. 3; the first and second peaks of the reference curve are well reconstructed by clusters A and B, respectively. Summing over all 15 beam contributions from A–C, as in Fig. 11(b), does well for $x < 0.3$.

The amplitudes of the total horizontal displacement fields at the upper surface for the unflawed and flawed plates are shown in Fig. 12. Clearly visible as a precursor is the weak, but identifiable, scattered *S*-beam contribution.

C. Flaw reconstruction

The flaw parameters (location, extent, and strength) can be reconstructed from the upper surface displacements generated in Sec. III B by following the back propagation sequence in Sec. II C. The displacement data for the unflawed and flawed cases are shown in Fig. 13(a) and (b), respectively, which are enlargements of portions of Fig. 12. Following the data processing described in connection with (41), one may extract from the precursor data in the region $0.13 < x < 0.16$ of Fig. 13(b) the angle of incidence, radius of curvature of the incident wave front, projected $1/e$ width, and maximum amplitude of the data producing the scattered *SV* beam on the surface:

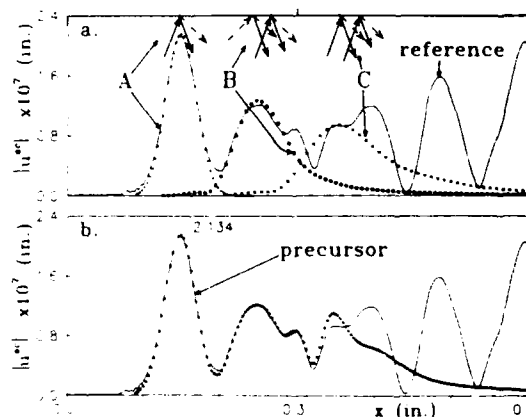


FIG. 11. Horizontal displacement $|u^*|$ on the upper plate surface due to flaw scattering. Solid curve: reference solution. (a) Local reconstruction using the wave species identified in regions A–C of Fig. 3. (b) Reconstruction (●) using the sum of the wave species in (a).

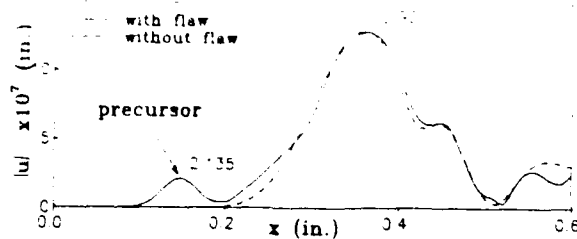


FIG. 12. Total horizontal displacement amplitudes on the upper plate surface of the unflawed and flawed plates. It is shown that the precursor (Fig. 11) in the otherwise quiescent region is due to flaw scattering (parameters are as in Figs. 1 and 3).

$$\alpha_s = 59^\circ, \quad R_s = 0.50 \text{ in.},$$

$$w_s = 0.0270 \text{ in.}, \quad |u_s|_{\max} = 2.135 \times 10^{-7} \text{ in.}$$

Then using the back propagation formulas in (42), (43), (46), and (47), we construct the flaw location, width $w_s(0)$, and strength $|u_s(0)|_{\max}$ of the horizontal displacements at the flaw. In addition, $|\Delta u|_{\max}$ is deduced from (57). By the same route applied to the unflawed data in the region $0.30 < x < 0.42$ of Fig. 13(a), one finds, for the incident SV beam at the upper surface,

$$\alpha_s = 68.7^\circ, \quad R_s = 2.174 \text{ in.},$$

$$w_s = 0.07548 \text{ in.}, \quad |u_s|_{\max} = 12.88 \times 10^{-7} \text{ in.}$$

From formulas (48)–(51) and (54), this data is back propagated to the lower surface and then to the P -source beam location, furnishing the input parameters $w_p(0)$, etc. Forward propagation establishes the induced shear stress field $\tau_{zx}(x, z_f)$ at the flaw of the strength and width given by (58) and (59), respectively. The flaw parameters w_K and K_0 then follow from (60) and (61). The results are shown in Table I, which lists the source and flaw parameter values for generating the surface displacement data; the values reconstructed by the beam algorithm; and, also, the auxiliary parameters that enter into the algorithm (those pertaining to the induced sources on the flaw and the scattered SV beam).

IV. CONCLUSION

In a previous two-dimensional model study of ultrasound scattering from a smoothly tapered weak debond of moderate extent in a two-layer elastic plate,⁴ it was found that the surface displacements generated by an obliquely injected Gaussian P beam in unflawed and flawed plates have distinct features that suggest suitability of a multiple-reflect-

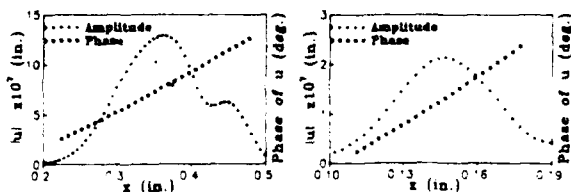


FIG. 13. Amplitude and phase of horizontal displacements u for portions of Fig. 12 (a) Without flaw; (b) with flaw (precursor).

TABLE I. Comparison of initial and reconstructed parameters

Problem parameters	Values for generating initial data	Reconstructed values
P beam source		
l_p	0.339 in.	0.321 in.
$w_p(0), w_0$	0.0335 in.	0.0338 in.
$ u_p(0) _{\max}$	5.940×10^{-7} in.	5.935×10^{-7} in.
Debond pliability		
(x_f, z_f)	(0.09, 0.15) in.	(0.082, 0.168) in.
K_0 (lb./in. ³)	5.000×10^9	5.002×10^9
w_K	0.02599 in.	0.02565 in.
Scattered SV beam		
L_s		0.182 in.
$\bar{w}_s(0)$		0.02305 in.
$ \Delta u _{\max}$		3.152×10^{-7} in.
Induced shear stress on flaw		
$ \tau_{zx} _{\max}$ (lb./in. ²)		1576.4
$\bar{w}_p(d)$		0.0525 in.

ed beam algorithm for efficient forward analysis as well as inversion of the data. The weak debond responds to tangential shear that can be induced on the bond line by an oblique (but not by a vertically incident) P beam. Subject to Born-type approximations validated by the weak-scatter assumption, we have shown that the problem can indeed be modeled effectively by simple beam tracking that is intimately tied to the actual wave processes (i.e., the observables) which are operative here. Combining paraxial approximations with CSP modeling of Gaussian P , SV , and P - SV coupled beam multiples, we have constructed a forward algorithm for reproducing the unflawed and flaw scattered data on the upper plate surface, and we have shown how the input source as well as the flaw location, extent, and strength can be reconstructed from this data by simple back propagation. Central to the beam modeling has been the assumption that the smoothly tapered debond profile can be approximated by a Gaussian; this leaves the Gaussian imprint as well on the flaw scattered SV beam, which appears as a distinct and readily identifiable precursor in the total signal.

The simple physical model employed in this study may be a poor approximation to actual debonds. Nevertheless, it serves to demonstrate that smoothly tapered weak flaw zones of moderate extent, even of a more general type, should be amenable to detection and identification by a beam-modeling scheme such as the one presented here. Refinements can be achieved by Born-type induced Gaussian-like volume source distributions for representing fault regions, improved Born approximations, etc., but it remains to be seen how the algorithm is complicated thereby. Extension to three-dimensional beam inputs is straightforward and already being considered. Extension to curved layer geometries is planned for the near future; an advantage of the Gaussian beam algorithm is the ability to adapt it to environments that deviate from the plane layer prototype. Finally, even when the input beam and/or flaw profile deviate from Gaussian shapes, the method pursued here remains relevant be-

case Gaussians are useful basis functions for representing arbitrary fields^{12, 13} and for windowed signal processing.¹⁴

ACKNOWLEDGMENT

This work has been supported by the US Air Force Office of Scientific Research under Grant No. AFOSR-86-0318.

APPENDIX A: EQUIVALENT POTENTIAL SOURCES FOR THE SCATTERING PROBLEM

Taking the Fourier transform of (35a), one obtains, for the spectrum of the scattered horizontal displacement $u^s(x, z)$,

$$\begin{aligned} \widehat{u}^s(k, z) = & \int_{x_f-l}^{x_f+l} dx' \exp(-ikx') \Delta u'(x', z_f) \\ & \times \int_{-\infty}^{\infty} dx \exp[-ik(x-x')] \Sigma_{xx}(x-x', z_f; z). \end{aligned} \quad (A1)$$

The second integral in (A1) is the spectrum of $\Sigma_{xx}(x-x', z_f; z)$. The first integral becomes the spectrum $\widehat{\Delta u}'(k, z_f)$ of the induced source distribution (subjected to the Born approximation) as the integration limits are extended to $-\infty$ and $+\infty$. This latter operation is justifiable because at the limits $x_f \pm l$ the Gaussian induced source strength is assumed to have decayed to negligible magnitudes compared to the maximum value attained at x_f . Therefore, with similar considerations for $u^s(x, z)$ in (35b),

$$\begin{aligned} \widehat{u}^s(k, z) &= \widehat{\Sigma}_{xx}(k; z_f, z) \widehat{\Delta u}'(k, z_f), \\ \widehat{u}^s(k, z) &= \widehat{\Sigma}_{zz}(k; z_f, z) \widehat{\Delta u}'(k, z_f). \end{aligned} \quad (A2)$$

Expressions for $\widehat{\Sigma}_{xx}(k; z_f, z)$ and $\widehat{\Sigma}_{zz}(k; z_f, z)$ can be derived from the stress tensor forms given in the Appendix of Ref. 4:

$$\begin{aligned} \widehat{\Sigma}_{xx}(k; z_f, z) &= [\mu/(2\rho\omega^2)] \{ -(\pm 2) k^2 \exp[\pm i\kappa_p(z-z_f)] \\ &\quad + (\pm 1) (k^2 - \kappa_s^2) \exp[\pm i\kappa_s(z-z_f)] \}, \end{aligned} \quad (A3a)$$

$$\begin{aligned} \widehat{\Sigma}_{zz}(k; z_f, z) &= [\mu/(2\rho\omega^2)] \{ -2\kappa_p \exp[\pm i\kappa_p(z-z_f)] \\ &\quad - (k^2 - \kappa_s^2) (k/\kappa_s) \exp[\pm i\kappa_s(z-z_f)] \}, \end{aligned} \quad (A3b)$$

where the plus and minus signs correspond to downgoing and upgoing waves, respectively.

Recalling that $(\mu/\rho\omega^2) = (v_s^2/\omega^2) = (1/k_s^2)$ and substituting (A3) into (A2) yields

$$\begin{aligned} \widehat{u}^s(k, z) &= (ik) \{ (\pm ik/k_s^2) \widehat{\Delta u}'(k, z_f) \exp[\pm i\kappa_p(z-z_f)] \\ &\quad - (\pm i\kappa_s) \{ i(k^2 - \kappa_s^2)/(2k_s^2\kappa_s) \widehat{\Delta u}'(k, z_f) \\ &\quad \times \exp[\pm i\kappa_s(z-z_f)] \} \}, \\ \widehat{u}^s(k, z) &= (\pm i\kappa_p) \{ (\pm ik/k_s^2) \widehat{\Delta u}'(k, z_f) \\ &\quad \times \exp[\pm i\kappa_p(z-z_f)] \} \end{aligned} \quad (A4a)$$

$$\begin{aligned} &+ (ik) \{ i(k^2 - \kappa_s^2)/(2k_s^2\kappa_s) \widehat{\Delta u}'(k, z_f) \\ &\quad \times \exp[\pm i\kappa_s(z-z_f)] \}. \end{aligned} \quad (A4b)$$

From (A4a) and (A4b) one may identify the potentials by comparing with (1) in the spectral domain

$$\begin{aligned} (\widehat{\Phi}^s)^{d,u}(k, z) &= (\pm ik/k_s^2) \widehat{\Delta u}'(k, z_f) \\ &\quad \times \exp[\pm i\kappa_p(z-z_f)], \end{aligned} \quad (A5a)$$

$$\begin{aligned} (\widehat{\Psi}^s)^{d,u}(k, z) &= i(k^2 - \kappa_s^2)/(2k_s^2\kappa_s) \widehat{\Delta u}'(k, z_f) \\ &\quad \times \exp[\pm i\kappa_s(z-z_f)], \end{aligned} \quad (A5b)$$

thereby obtaining the equivalent source potentials corresponding to the scattered P and SV waves in (38), respectively:

$$\begin{aligned} \widehat{S}_p^{d,u}(k, z_f) &= \pm i(k/k_s^2) \widehat{\Delta u}'(k, z_f), \\ \widehat{S}_s^{d,u}(k, z_f) &= i(k^2 - \kappa_s^2)/(2\kappa_s k_s^2) \widehat{\Delta u}'(k, z_f). \end{aligned} \quad (A6)$$

APPENDIX B: GAUSSIAN MATCHING TO OBSERVED DATA

To estimate the $1/e$ width w_s of the Gaussian that matches the quasi-Gaussian data referenced to the point O where the beam axis intersects the surface, the following scheme has been found effective. The projections $\Delta x_{A,B}$ of the $1/e$ widths $w_{A,B} = \Delta x_{A,B} \sin \alpha_s$ of the incident SV beam onto the plate surface at points A and B , respectively (see Fig. B1), can be deduced by locating these points through the fraction $1/e$ of the beam amplitude maximum in the on-surface data. In the present case, we have access only to the maximum $|u_s|_{\max}$ at point O . However, knowing that the amplitude maximum along the beam axis depends on the factor $A(L_s) = [k_s(L_s^2 + b_s^2)]^{-1/2}$, one finds by simple approximation that the maxima at A , B , and O are related by

$$\begin{aligned} \max(A, B) &\approx \max(O) (1 \pm \beta d_{OA,OB}), \\ d_{OA,OB} &= \Delta x_{A,B} \cos \alpha_s, \end{aligned} \quad (B1)$$

where

$$\beta = L_s [2(L_s^2 + b_s^2)]^{-1}, \quad \text{with } \beta d_{OA,OB} \ll 1. \quad (B1')$$

Here, L_s is the distance traveled by the beam from the waist location to the surface, b_s is the Fresnel distance, and $d_{OA,OB}$ are the distances from O to A and O to B , respectively (see

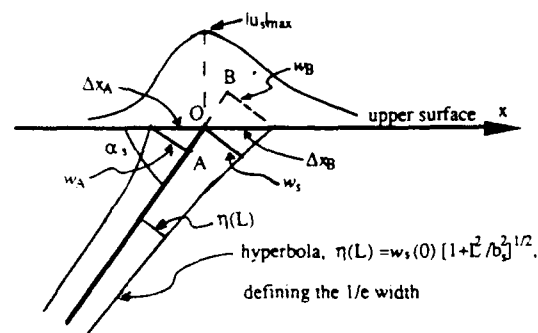


FIG. B1 Parameters pertaining to the Gaussian matching of the surface data.

Fig. B1. In (B1) the plus sign corresponds to A . From (19),
 $w(L) = w(0)(1 + L^2/b^2)^{-1/2} \approx w_{A,B}(1 \pm 2\beta d_{01,0h})$ (B2)

To obtain $w \equiv w(L)$ from (B2) and (B1), one needs to know β and, therefore, requires the values for L and b . To deduce L and b from (42) and (43), we first make a zeroth-order estimate of w , as $w \approx (\frac{1}{2})(\Delta x_A + \Delta x_B) \sin \alpha$, where $\Delta x_{A,B}$ are obtained by taking $(1/e) u_{i,max}$ (at O). From this value of w , combined with R , and α , determined from the processing of the phase data, one may obtain from (42) and (43) approximate values of the waist-to-surface distance L , and the Fresnel distance b , and thereby the first approximation to β in (B1'). The next approximation recomputes $\Delta x_{A,B}$ by taking $1/e$ of the maxima at A and B as specified by (B1). Then w is estimated to a better approximation according to (B2).

Should the upper surface data to the right of the maximum be distorted because of interference with subsequent peaks, a good w extraction is still possible from the left side only because w in (B2) can be specified either in terms of w_A or w_B .

¹ I. T. Lu, L. B. Felsen, and J. M. Klosner, "Beam-to-Mode Conversion of a High Frequency Gaussian P-Wave in an Aluminum Plate in Vacuum," in *Proceedings of ASME Symposium on New Directions in the Ultrasonic NDE of Advanced Materials* (MD-9), 27 November–2 December 1988, Chicago, IL.

² I. T. Lu, L. B. Felsen, J. M. Klosner, and C. Gabay, "Beam and Mode Analysis of Weak Bonding Flaws in a Layered Aluminum Plate," in *Elastic Wave Propagation*, edited by M. F. McCarthy and M. A. Hayes (Elsevier, New York, 1989), pp. 205–210.

³ I. T. Lu, L. B. Felsen, and J. M. Klosner, "Observables Due to Beam-to-Mode Conversion of a High-Frequency Gaussian P Wave in an Aluminum Plate in Vacuum," *J. Acoust. Soc. Am.* **87**, 42–53 (1990).

⁴ I. T. Lu, L. B. Felsen, J. M. Klosner, and C. Gabay, "Beams and Modes for Scattering from Weak Bonding Flaws in a Layered Aluminum Plate," *J. Acoust. Soc. Am.* **88**, 496–504 (1990).

⁵ I. T. Lu, L. B. Felsen, and J. M. Klosner, "Beam-to-Mode Conversion in an Aluminum Plate for Ultrasonic NDE Applications," *ASME J. Eng. Mater. Technol.* **112**, 236–240 (1990).

⁶ J. D. Achenbach, *Wave Propagation in Elastic Solids* (North-Holland, Amsterdam, 1973).

⁷ L. B. Felsen and N. Marcuvitz, *Radiation and Scattering of Waves* (Prentice-Hall, Englewood Cliffs, NJ, 1973), Chap. 4, Sec. 4.2.

⁸ A. E. Siegman, *Lasers* (University Science Books, Mill Valley, CA, 1984), Chap. 16.

⁹ H. A. Haus, *Waves and Fields in Optoelectronics* (Prentice-Hall, Englewood Cliffs, NJ, 1984), Chap. 5.1.

¹⁰ V. Cerveny, M. M. Popov, and I. Psencik, "Computation of Wave Fields in Inhomogeneous Media—Gaussian Beam Approach," *Geophys. J. R. Astron. Soc.* **70**, 109–128 (1982).

¹¹ B. P. Newberry, T. A. Gray, E. F. Lopes, and R. B. Thompson, "Evaluation of Ultrasonic Beam Models for the Case of a Piston Transducer Radiating Through a Liquid–Solid Interface," in *Review of Progress in Quantitative NDE*, edited by D. O. Thompson and D. E. Chimenti (Plenum, New York, 1986), Vol. 5A, pp. 127–128.

¹² J. J. Wen and M. A. Breazeale, "A Diffraction Beam Field Expressed as the Superposition of Gaussian Beams," *J. Acoust. Soc. Am.* **83**, 1752–1756 (1988).

¹³ M. Couture and P. A. Belanger, "From Gaussian Beam to Complex-Source-Point Spherical Wave," *Phys. Rev. A* **24**, 355–359 (1981).

¹⁴ A. Pilarski, "The Coefficient of Reflection of Ultrasonic Waves from an Adhesive Bond Interface," *Arch. Acoust.* **3**, 41–54 (1983).

¹⁵ Y.-H. Pao and V. Varatharajulu, "Huygens' Principle, Radiation Conditions, and Integral Formulas for the Scattering of Elastic Waves," *J. Acoust. Soc. Am.* **59**, 1361–1371 (1976).

¹⁶ J. E. Gubernatis, E. Domany, J. A. Krumhansl, and M. Huberman, "The Born Approximation in the Theory of the Scattering of Elastic Waves by Flaws," *J. Appl. Phys.* **48**, 2812–2819 (1977).

¹⁷ L. B. Felsen, "Real Spectra, Complex Spectra, Compact Spectra," *J. Opt. Soc. Am. A* **3** (4), 486–496 (1986).

¹⁸ S. Zeroug and L. B. Felsen, "Multiple Reflected Beam Synthesis of Fields Excited by a High-Frequency Oblique Beam Input in an Elastic Plate," submitted to *J. Acoust. Soc. Am.*

¹⁹ D. Gabor, "Theory of Communication," *J. Am. Inst. Electr. Eng.* **93**, 429–457 (1946).

²⁰ M. J. Bastiaans, "A Sampling Theorem for the Complex Spectrogram and Gabor's Expansion of a Signal in Gaussian Elementary Signals," *Opt. Eng.* **20**, 594 (1981).

²¹ P. D. Einziger, S. Raz, and M. Shapira, "Gabor Representation and Aperture Theory," *J. Opt. Soc. Am.* **3**, 508 (1986).

²² L. B. Felsen, J. M. Klosner, I. T. Lu, and Z. Grossfeld, "Source Field Modeling by Self-consistent Gaussian Beam Superposition (Two-Dimensional)," *J. Acoust. Soc. Am.* **89**, 63–72 (1991).

²³ B. Z. Steinberg, E. Heyman, and L. B. Felsen, "Phase Space Beam Summation for Time-harmonic Radiation from Large Apertures," *J. Opt. Soc. Am. A* **8**, 41–59 (1991).

Source field modeling by self-consistent Gaussian beam superposition (two-dimensional)

L. B. Felsen,^{a)} J. M. Klosner,^{b)} I. T. Lu,^{a)} and Z. Grossfeld^{b)}
 Polytechnic University, Farmingdale, New York 11735

(Received 19 February 1990; accepted for publication 5 August 1990)

Gaussians are useful models for high-frequency source field inputs into complex environments because they approximate the outputs of certain transducers, have favorable spectral and filtering properties, and can be propagated similar to ray fields. By recent analytic developments, any source field can be expressed exactly as a self-consistent superposition of Gaussians on a discretized (configuration)–(wave number) phase space lattice. This extends the use of Gaussians systematically to realistic transducer outputs. The method is already being applied to electromagnetic and acoustic propagation. It is here extended to modeling the radiation from transducers into an elastic solid. Restricting to the two-dimensional case, a distribution of forces over a finite, one-dimensional planar aperture is expanded self-consistently into Gaussian basis elements, which are then propagated into the unbounded medium. Numerical results reveal how successive addition of Gaussians for the compressional and shear potentials, as well as the displacements, homes in systematically on the assumed aperture profile, and on an independently generated numerical reference solution for the radiated near and far fields. Moreover, it is demonstrated how different self-consistent choices of beams affect the convergence. Furthermore, the validity of complex-source-point modeling of the Gaussians is explored for later applications where the input will be required to propagate across interfaces, as in a layered medium.

PACS numbers: 43.20.Ye, 43.20.Wd, 43.60.Qv

INTRODUCTION

Analytical modeling of ultrasonic NDE requires understanding of the propagation properties of source-excited high-frequency fields in an elastic environment. The sources may be actual, as generated by a transducer, or they may be induced in a fault region that disturbs the unflawed surroundings. One effective approach to dealing with wave phenomena in the source-excited configuration is to decompose the source distribution into basis elements, propagate each basis element from the source region to the receiver, and recombine them to synthesize the total field. Because Gaussian beams have favorable propagation characteristics and represent physically observable entities, they have played a prominent role in many modeling schemes.^{1,2} Gaussian beams individually may furnish approximate replica of fields generated by ultrasonic transducers with smoothly tapered aperture distribution. These beams, because they are highly focused, are conventionally propagated through the environment by paraxially approximated phases and amplitudes, thereby facilitating description of beam preserving narrow-angle encounters with planar and curved interfaces, etc.² However, scattering from localized fault zones or abrupt terminations is not beam preserving, and the output from many transducers (like flat pistons) gives rise to side lobes and other marked deviations from a well collimated Gaussian.

To cope with non-Gaussian effects without losing the attractiveness of the Gaussians, various efforts have been afoot to employ a distribution or superposition of Gaussian basis fields for modeling general source configurations. Some of these schemes, like those based on Hermite or Laguerre Gaussian expansions, are rigorous while others are more heuristic.¹⁻³ We shall introduce here a new procedure whereby an arbitrary planar source distribution is decomposed *rigorously* into a discrete superposition of linearly phased and nonphased Gaussian elements located self-consistently on a lattice in a (configuration)–(spectral wave number) phase space. Nonphased elements generate forward propagating beams, whereas phased elements generate tilted beams. This beam lattice synthesis has recently been applied to electromagnetic and acoustic fields,⁴ and it is here developed for elastic fields. The basic properties of this beam algorithm have been discussed in connection with these earlier applications,⁴ and we present here a similar treatment for the elastic case.

In what follows, the beam synthesis is illustrated for two simple models of time-harmonic finite planar aperture source distributions in an unbounded elastic solid: linearly phased smoothly tapered, and abruptly truncated, aperture profiles. The problem is two-dimensional and involves compressional (*P*) and vertically polarized shear (*SV*) waves. The formulation and formal solution by Green's function and spectral techniques is presented in Sec. I. The beam lattice expansion is summarized in Sec. II, and various options for evaluating the propagation of individual beams are developed in Sec. III. Some representative numerical results for aperture, near-field, and far-field synthesis, extract-

^{a)}Dept. of Electrical Engineering, Weber Research Institute.

^{b)}Dept. of Mechanical and Industrial Engineering.

ed from a very comprehensive set of data, are shown and discussed in Sec. IV, with concluding remarks in Sec. V.

I. THEORY

An infinite homogeneous elastic isotropic medium characterized by Lamé constants λ , μ , and by density ρ is assumed to be excited by a y -independent, z -directed pressure or body force distribution $f(x)$ [with suppressed harmonic time dependence $\exp(-i\omega t)$] acting on a plane surface $z = 0$ between $-a < x < a$ (Fig. 1). Following Ref. 5 the body force problem can be reformulated as a boundary value problem defined as

$$\sigma_{zz}(x, 0^+) = \begin{cases} -f(x)/2, & \text{for } -a < x < a \\ 0, & \text{for } |x| > a \end{cases}, \quad u(x, 0) = 0, \quad (1)$$

where σ_{zz} and u are, respectively, the vertical normal stress and horizontal displacement. The resulting elastic fields at $z > 0^+$ can be derived from two potentials $\Phi(x, z)$ and $\Psi(x, z)$, which represent pressure (P) and vertically polarized shear (SV) waves, respectively. The potentials due to the distributed source $f(x)$ can, in turn, be synthesized in terms of a scalar line force excitation at $(x', z') = (x', 0)$ as follows (see the Appendix):

$$\Phi(x, z) = \frac{-1}{4\pi\rho\omega^2} \int f(x') \frac{\partial g_p}{\partial z} dx', \quad (2)$$

$$\Psi(x, z) = \frac{-1}{4\pi\rho\omega^2} \int f(x') \frac{\partial g_s}{\partial x} dx',$$

where $g_{p,s}$ satisfy the two-dimensional (x, z) wave equations $(\nabla^2 + k_{p,s}^2)g_{p,s}(x, z; x', z') = -4\pi\delta(x - x')\delta(z - z')$,

$$k_{p,s} = \omega/v_{p,s}, \quad (3)$$

subject to a radiation condition at $|R| \rightarrow \infty$, where $R = (x, z)$. With subscripts p and s referring to the compressional and shear waves, respectively, $v_{p,s}$ in (3) are the compressional and shear wave propagation speeds

$$v_p = \sqrt{(\lambda + 2\mu)/\rho}, \quad v_s = \sqrt{\mu/\rho}. \quad (3')$$

The solution of (3) is given by

$$g_{p,s} = i\pi H_0^{(1)}(k_{p,s}r), \quad r = \sqrt{(x - x')^2 + (z - z')^2}, \quad (4)$$

where $H_0^{(1)}$ is the Hankel function. In terms of the potentials in (2), the displacements u and w in the horizontal (x) and vertical (z) directions, respectively, are given by

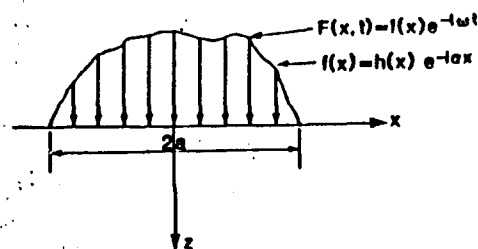


FIG. 1. Body force distribution in an infinite domain.

$$u(x, z) = \frac{\partial \Phi(x, z)}{\partial x} - \frac{\partial \Psi(x, z)}{\partial z}, \quad (5a)$$

$$w(x, z) = \frac{\partial \Phi(x, z)}{\partial z} + \frac{\partial \Psi(x, z)}{\partial x},$$

and the vertical normal stress component by

$$\sigma_{zz}(x, z) = \lambda \left(\frac{\partial^2 \Phi(x, z)}{\partial x^2} + \frac{\partial^2 \Phi(x, z)}{\partial z^2} \right) + 2\mu \left(\frac{\partial^2 \Phi(x, z)}{\partial z^2} + \frac{\partial^2 \Psi(x, z)}{\partial x \partial z} \right). \quad (5b)$$

The potentials can be decomposed into plane-wave spectra by Fourier transforming along the x coordinate,

$$\hat{\Lambda}(k, z) = \int_{-\infty}^{\infty} \Lambda(x, z) e^{-ikx} dx, \quad \Lambda = \Phi \text{ or } \Psi, \quad (6a)$$

with the inverse

$$\Lambda(x, z) = \frac{1}{2\pi} \int_{-\infty}^{\infty} \hat{\Lambda}(k, z) e^{ikx} dk. \quad (6b)$$

The resulting spectral amplitudes, expressed in terms of the source spectrum $\hat{f}(k)$, are

$$\begin{aligned} \hat{\Phi}(k, z) &= [\hat{f}(k)/2\rho\omega^2] e^{i\kappa_p z}, \\ \hat{\Psi}(k, z) &= [\hat{f}(k)k/2\rho\omega^2\kappa_s] e^{i\kappa_s z}, \\ \kappa_{p,s} &= \sqrt{k^2 - k_{p,s}^2}, \end{aligned} \quad (7)$$

with $\text{Im } \kappa_{p,s} > 0$. By inserting (7) into (6b), one obtains the plane-wave spectral representations for Φ and Ψ , and by inserting into (5) and performing the partial differentiations on the integrands, one obtains the corresponding representations for the displacements and normal stresses. This completes the problem formulation and solution strategy.

II. GAUSSIAN BEAM EXPANSION

Motivated by the considerations in the Introduction we now seek to express the solution for the potentials and displacements defined in Sec. I in terms of a self-consistent discretized Gaussian beam expansion over a configuration-wave number phase-space lattice (see Fig. 2). For the aperture function $f(x)$, this expansion becomes⁶

$$f(x) = \sum_n \sum_m A_{mn} W(x - mL_x) e^{in\pi x}, \quad (8)$$

where $W(x)$ is a normalized Gaussian window function defined by

$$W(x) = \left(\frac{\sqrt{2}}{L_x} \right)^{1/2} \exp\left(-\frac{\pi x^2}{L_x^2} \right), \quad \int |W(x)|^2 dx = 1. \quad (9)$$

The spatial displacement index m in (8) locates each Gaussian envelope along the space coordinate x , whereas the spectral displacement index n tags the superimposed linear phase shift. The spatial lattice separation parameter L_x (which also defines the width of the Gaussian) and the spectral lattice separation parameter Ω [which defines the width of its spectrum; see (14)] are constrained by the condition

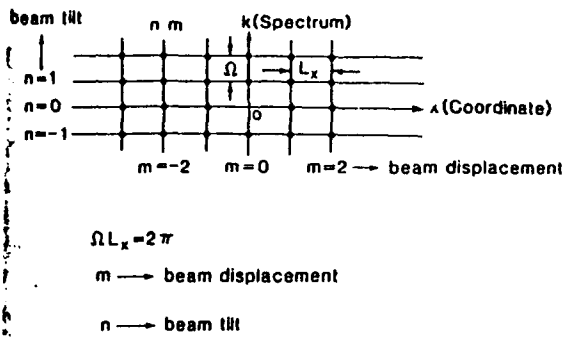


FIG. 2. Phase-space lattice.

$$\Omega L_x = 2\pi. \quad (10)$$

The amplitude coefficients are expressed in terms of a biorthogonal function $\gamma(x)$,⁶

$$A_{mn} = \int_{-\infty}^{\infty} f(x) \gamma^*(x - mL_x) \exp(-in\Omega x) dx, \quad (11)$$

where $\gamma(x)$ is determined from the biorthogonality relation

$$\int W(x) \gamma^*(x - mL_x) \exp(-in\Omega x) dx = \delta_m \delta_n, \quad (11a)$$

$$\delta_q = \begin{cases} 1, & \text{for } q = 0 \\ 0, & \text{for } q \neq 0, \end{cases}$$

and the asterisk denotes the complex conjugate. For the Gaussian window in (9), the function $\gamma(x)$ is given by

$$\gamma(x) = \left(\frac{1}{\sqrt{2}L_x} \right)^2 \left(\frac{K_0}{\pi} \right)^{-1/2} \exp\left(\pi \frac{x^2}{L_x^2} \right) S_j, \quad (12)$$

with $K_0 = 1.854\,074\,68$ representing the complete elliptic integral of the first kind of argument $1/2$.

A similar expansion can be performed in the spectral domain. Here,

$$\hat{f}(k) = \sum_m \sum_n A_{mn} \hat{W}(k - n\Omega) e^{-imkL_x}, \quad (13)$$

where

$$\hat{W}(k) = (\sqrt{2}L_x)^{1/2} \exp[-\pi(k^2/\Omega^2)] \quad (14)$$

is the spatial Fourier spectrum of $W(x)$. The evident symmetry of the spatial and spectral forms of the expansion facilitates simultaneous interpretation of wave phenomena in the spatial and spectral domains. The index n in (13) places the spectral peaks at $k_n = n\Omega = 2\pi n/L_x$, thereby identifying

$$\theta_{p,s}^{(n)} = \sin^{-1}(2\pi n/k_{p,s}L_x) \quad (14a)$$

later on as the angle of tilt of the n th P and S beam axes away from the normal to the aperture.

The Gaussian beam expansions for the potential and displacement fields in, and away from, the aperture plane

can be obtained by substituting (8) into (2) and (5) (spatial superposition form), or by substituting (13) into (7), (6b) and (5) (plane-wave spectral form). Choosing the latter, we find

$$\begin{aligned} & [\Phi(x,z), \Psi(x,z)] \\ &= \frac{(\sqrt{2}L_x)^{1/2}}{4\pi\rho\omega^2} \sum_m \sum_n A_{mn} [B_{p,mn}(x,z), B_{s,mn}(x,z)], \end{aligned} \quad (15)$$

and

$$u = \frac{(\sqrt{2}L_x)^{1/2}}{4\pi\rho\omega^2} \sum_m \sum_n A_{mn} \left(\frac{\partial B_{p,mn}(x,z)}{\partial x} - \frac{\partial B_{s,mn}(x,z)}{\partial z} \right), \quad (16a)$$

$$w = \frac{(\sqrt{2}L_x)^{1/2}}{4\pi\rho\omega^2} \sum_m \sum_n A_{mn} \left(\frac{\partial B_{p,mn}(x,z)}{\partial z} + \frac{\partial B_{s,mn}(x,z)}{\partial x} \right). \quad (16b)$$

The beam functions $B_{p,s,mn}$ are defined by the integrals

$$B_{p,mn}(x,z) = \int_{-\infty}^{\infty} \exp[i\hat{q}_p(k)] dk, \quad (17)$$

$$B_{s,mn}(x,z) = \int_{-\infty}^{\infty} \frac{k}{K_s} \exp[i\hat{q}_s(k)] dk,$$

with

$$\hat{q}_{p,s}(k) = k(x - mL_x) + \kappa_{p,s}z + (i/4\pi)(kL_x - 2\pi n)^2. \quad (18)$$

These expansions, which are valid anywhere in the half-space $z > 0$, reduce to their form in the aperture plane when $z \rightarrow 0^+$.

The beam integrals become physically more transparent when they are expressed in angular spectrum form in local rotated beam-centered coordinates (ξ, η) (Fig. 3). The coordinate transformation is given by

$$\begin{aligned} (x - mL_x) &= \eta \sin \theta_{p,s}^{(n)} + \xi \cos \theta_{p,s}^{(n)}, \\ z &= \eta \cos \theta_{p,s}^{(n)} - \xi \sin \theta_{p,s}^{(n)}, \end{aligned} \quad (19)$$

where the beam angles $\theta_{p,s}^{(n)}$ are defined in (14a). The angular spectrum variable will be denoted by β . Because of the different normalizations introduced by the compressional and shear wave propagation speeds v_p and v_s , we append to

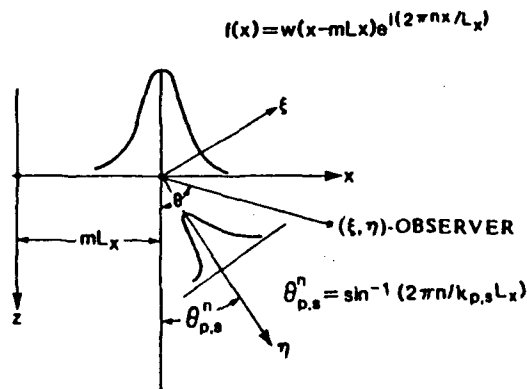


FIG. 3. Coordinate transformation for tilted beam.

β the distinguishing subscripts p and s to identify spectral integration of quantities pertaining to compression and shear. Accordingly,

$$\beta_{p,s} = \sin^{-1}(k/k_{p,s}), \quad k_{p,s} = \omega/v_{p,s}. \quad (20)$$

With this notation, it must be kept in mind that $\beta_{p,s}$ are generally complex spectral variables, whereas $k_{p,s}$ denotes the fixed compressional and shear wave numbers. The phase in (18) then becomes

$$\hat{q}_{p,s}(\beta_{p,s}) = k_{p,s} [\eta \cos(\beta_{p,s} - \theta_{p,s}^{(n)}) + \xi \sin(\beta_{p,s} - \theta_{p,s}^{(n)}) + i(k_{p,s} L_x^2/4\pi)(\sin \beta_{p,s} - \sin \theta_{p,s}^{(n)})^2]. \quad (21)$$

The integration in the complex β_p and β_s planes proceeds along the well known Sommerfeld contours C_p and C_s .⁷

III. APPROXIMATE EVALUATION OF THE BEAM INTEGRALS

A. Saddle point asymptotics

Because the phases defined in (18) or (21) vary rapidly at sufficiently large distances away from the aperture plane, the beam integrals can be evaluated asymptotically by the saddle point method, whereby the integration paths are deformed into paths of steepest descent (SDP) through saddle points at which the functions are stationary. Implementing the integration in the complex k -plane yields the following asymptotic result (cf. Ref. 7),

$$\left\{ \frac{B_{p,mn}(x,z)}{B_{s,mn}(x,z)} \right\} = \left\{ \frac{1}{k^{(0)}/\kappa_s^{(0)}} \right\} \left(\frac{-2\pi}{i\hat{q}_{p,s}''(k^{(0)})} \right)^{1/2} \times \exp[i\hat{q}_{p,s}(k^{(0)})], \quad (22)$$

with the saddle points $k^{(0)}$ defined by

$$\frac{d\hat{q}_{p,s}(k)}{dk} = 0 \quad \text{at } k^{(0)}, \quad (22a)$$

and $\hat{q}_{p,s}(k)$ given in (18). Here, the superscript "0" denotes evaluation at the stationary points $k^{(0)}$ with the subscripts p,s on $\hat{q}_{p,s}$ distinguishing the wave type to which $k^{(0)}$ refers. In the angular spectrum domain, the saddle point condition becomes explicitly, via (21),

$$-\eta \sin(\beta_{p,s}^{(0)} - \theta_{p,s}^{(n)}) + \xi \cos(\beta_{p,s}^{(0)} - \theta_{p,s}^{(n)}) + i(k_{p,s} L_x^2/2\pi)(\sin \beta_{p,s}^{(0)} - \sin \theta_{p,s}^{(n)}) \cos \beta_{p,s}^{(0)} = 0. \quad (23)$$

An alternate form is obtained by substituting the transformation [see (19) and Fig. 3]

$$\xi = r_m \sin(\theta - \theta_{p,s}^{(n)}), \quad \eta = r_m \cos(\theta - \theta_{p,s}^{(n)}) \quad (24)$$

into (23) to yield

$$\sin(\beta_{p,s}^{(0)} - \theta) - i(b_{p,s}/r_m \cos^2 \theta_{p,s}^{(n)}) \times (\sin \beta_{p,s}^{(0)} - \sin \theta_{p,s}^{(n)}) \cos \beta_{p,s}^{(0)} = 0, \quad (25)$$

where

$$b_{p,s} = k_{p,s} [(L_x \cos \theta_{p,s}^{(n)})^2/2\pi] \quad (25a)$$

and

$$r_m = [(x - mL_x)^2 + z^2]^{1/2} = (\eta^2 + \xi^2)^{1/2}. \quad (25b)$$

It may be noted that the parameter $b_{p,s}$, which plays a crucial role in the complex source point analysis, is equivalent to the

Fresnel length of the projected beam waist transverse to the beam axis along $\theta_{p,s}^{(n)}$. The asymptotic result, after performing the integration, is readily inferred from (22).

B. Far-field approximation

Because the phases $\hat{q}_{p,s}$ are complex, the numerical search for the saddle points is generally time consuming. Therefore, it is useful to explore approximate alternatives that simplify the determination of the saddle points, and, subsequently, of the beam integrals. One such simplification occurs for observation distances r_m from the beam waist center ($x = mL_x, z = 0$) so large that

$$\epsilon_{p,s} \equiv b_{p,s}/r_m \ll 1. \quad (26)$$

Upon expanding $\beta_{p,s}^{(0)}$ in (25) in terms of the small parameters $\epsilon_{p,s}$ (omitting the subscripts),

$$\beta^{(0)} = \beta_0 + \epsilon\beta_1 + \epsilon^2\beta_2 + \dots, \quad (27)$$

and equating the coefficients of the powers of ϵ to zero, one obtains an explicit expression for the saddle point

$$\beta_{p,s}^{(0)} = \theta + i(b_{p,s}/r_m \cos^2 \theta_{p,s}^{(n)}) \times \cos \theta (\sin \theta - \sin \theta_{p,s}^{(n)}) + \dots, \quad (28)$$

which, when substituted into (22), yields the final results

$$\left\{ \frac{B_{p,mn}(x,z)}{B_{s,mn}(x,z)} \right\} = k_{p,s} \left\{ \frac{\cos \theta}{\sin \theta} \right\} \left(\frac{2\pi}{ik_{p,s} r_m} \right)^{1/2} \times \exp\{ik_{p,s} r_m [1 + i(b_{p,s}/2r_m) \times (\sin \theta - \sin \theta_{p,s}^{(n)})^2 \cos^{-2} \theta_{p,s}^{(n)}]\}. \quad (29)$$

To obtain (29), the two-term expansion (28) has been retained for the phases but only the first term for the amplitudes.

C. Paraxial approximation

Explicit results can also be obtained in the paraxial region near the beam axis. A small dimensionless parameter

$$\bar{\epsilon}_{p,s} = \xi/(\eta - ib_{p,s}), \quad |\bar{\epsilon}_{p,s}| = [\xi^2/(\eta^2 + b_{p,s}^2)]^{1/2} \ll 1 \quad (30)$$

is introduced, and the angle $\beta_{p,s}^{(0)}$ is now expanded in powers of $\bar{\epsilon}$ as in (27). Substituting into (23) and proceeding as above yields

$$\beta_{p,s}^{(0)} = \theta_{p,s}^{(n)} + \bar{\epsilon}_{p,s} + \dots, \quad (31)$$

from which one finds via (18) and (22),

$$\left\{ \frac{B_{p,mn}(x,z)}{B_{s,mn}(x,z)} \right\} = k_{p,s} \left\{ \frac{\cos \beta_{p,s}^{(0)}}{\sin \beta_{p,s}^{(0)}} \right\} \sqrt{\frac{2\pi}{ik_{p,s}(\eta - ib_{p,s})}} \times \exp\{ik_{p,s} [\eta + ib_{p,s} \xi^2/2(\eta^2 + b_{p,s}^2)]\}. \quad (32)$$

D. Complex source point model

The complex source point (CSP) method furnishes a useful alternative to approximating the beam integrals in the paraxial region. It is known^{8,9} that assigning complex values to the source coordinates in the two-dimensional free-space

potential Green's functions $g_{p,s}$ in (4) generates a beam-like wave field that continues to satisfy the source-free wave equation and outgoing wave condition. Interpreting (4) in the beam-centered coordinate system (ξ, η) , the complex source coordinates will be taken as $\bar{\xi}' = 0$, $\bar{\eta}' = ib_{p,s}$, with the overbar denoting a complex quantity. Already at moderately large values of $k_{p,s}\bar{r}$, the analytically continued solution may be approximated by its asymptotic large-argument form,

$$g_{p,s} \sim i\pi(2/\pi k_{p,s}\bar{r})^{1/2} \exp(ik_{p,s}\bar{r} - i\pi/4), \quad \bar{r} = \sqrt{\xi^2 + (\eta - ib_{p,s})^2}, \quad \text{Re}(\bar{r}) > 0, \quad (33)$$

where \bar{r} is the complex distance to the observer. In the original global coordinates, the complex distance \bar{r} can be recognized as the distance between the observer at (x, z) and the complex source point at $(mL_x + ib_{p,s} \sin \theta_{p,s}^{(n)}, ib_{p,s} \cos \theta_{p,s}^{(n)})$:

$$\bar{r} \equiv \bar{r}_m = [(x - mL_x - ib_{p,s} \sin \theta_{p,s}^{(n)})^2 + (z - ib_{p,s} \cos \theta_{p,s}^{(n)})^2]^{1/2}. \quad (34)$$

When \bar{r} in (33) is expanded paraxially, one finds

$$\bar{r} = (\eta - ib_{p,s}) + (\xi^2/2)\bar{e}_{p,s} + \dots, |\bar{e}_{p,s}| \ll 1, \quad (35)$$

which leads to

$$g_{p,s} \sim i \exp(k_{p,s}b_{p,s}) [2\pi/ik_{p,s}(\eta - ib_{p,s})]^{1/2} \times \exp\{ik_{p,s}[\eta + ib_{p,s}\xi^2/2(\eta^2 + b_{p,s}^2)]\}, \quad (36)$$

thereby providing a form as in (32). Performing a detailed comparison of (32) and (36) leads to the following CSP expressions for the beam integrals:

$$\left\{ \frac{B_{p,mn}(x,z)}{B_{s,mn}(x,z)} \right\} \sim -\exp(-k_{p,s}b_{p,s}) \left\{ \frac{\partial/\partial z}{\partial/\partial x} \right\} g_{p,s}, \quad (37)$$

with $g_{p,s}$ taken from (36). In the far zone $b_{p,s}/r_m \ll 1$, the alternative approximation

$$\bar{r} = r_m - ib_{p,s}\eta/r_m, \quad r_m = \sqrt{\xi^2 + \eta^2} \quad (38)$$

$$\times \exp\{ik_{p,s}r_m[1 + i(b_{p,s}/r_m)(1 - \cos(\theta - \theta_{p,s}^{(n)}))]\}. \quad (39)$$

Expanding (33) with (38) to $O(b_{p,s}/r_m)$ in the phase and $O(1)$ in the amplitude, substituting into (37), and comparing with (29) confirms that both results agree in the far zone.

Corresponding expressions for the potential fields in (15) are given by

$$\begin{aligned} \left\{ \frac{\Phi(x,z)}{\Psi(x,z)} \right\} &= -k_{p,s} \frac{(\sqrt{2}L_x)^{1/2}}{4\pi\rho\omega^2} \\ &\times \sum_m \sum_n A_{mn} e^{-k_{p,s}b_{p,s}} \left\{ \frac{\partial g_{p,s}/\partial z}{\partial g_{p,s}/\partial x} \right\}, \end{aligned} \quad (40)$$

and for the displacements in (16) by

$$\begin{aligned} \left\{ \frac{u}{w} \right\} &= -\frac{(\sqrt{2}L_x)^{1/2}}{4\pi\rho\omega^2} \sum_m \sum_n A_{mn} \left[k_{p,s} e^{-k_{p,s}b_{p,s}} \left\{ \frac{\partial^2/\partial x \partial z}{\partial^2/\partial z^2} \right\} \right. \\ &\times g_{p,s} - k_{p,s} e^{-k_{p,s}b_{p,s}} \left. \left\{ -\frac{\partial^2/\partial x \partial z}{\partial^2/\partial x^2} \right\} g_{p,s} \right], \end{aligned} \quad (41)$$

The expressions in (37), (40), and (41), with (37), have been used in the numerical calculations that follow. The CSP format, when it applies, systematizes and simplifies the numerically more cumbersome saddle point asymptotics. For the parameters selected in the computations, $g_{p,s}$ can be approximated by its far zone expression in (33). Although validity of the resulting CSP formula has been established only in the paraxial region, that formula has been retained intact for all observation angles away from each beam axis. This greatly simplifies the overall numerics and, as will be seen, the damage caused thereby is insignificant.

IV. NUMERICAL RESULTS

A sequence of numerical calculations has been carried out in order to: (1) assess the validity of the asymptotic complex source point (CSP) formulation to represent the asymptotic beam integrals, and (2) gain insight into how the choice of parameters in the Gaussian beam lattice representation of the aperture excitation affects the behavior of the elastic wave fields. Data have been generated for a range of beam basis elements spanning the interval from very wide to very narrow in the aperture plane. Both near and far fields of the potentials and displacements have been determined from (15) and (16) by asymptotic evaluation of the beam integrals of (17).

All results are plotted for observation points along a circular contour with radius R centered in the aperture. Although a planar cut would be better suited to revealing the physical behavior of the near zone fields, the circular contour has been retained throughout for convenience. The test aperture fields have a linear phase taper with amplitude profiles $h(x)$ that are (a) smoothly tapered toward the edges, and (b) uniform (abruptly truncated). Specifically,

$$h(x) = \begin{cases} \cos^2(\pi x/2a), & |x| < a, \quad \text{case a,} \\ 1, & |x| < a, \quad \text{case b.} \end{cases} \quad (42)$$

A. Beam Integral asymptotics versus CSP

To test the quality of the various approximations described in Sec. III, results from the saddle-point expression (22) for the beam integrals (labeled BI) and from the CSP representation in (37), with (36), are compared with a reference solution that has been obtained by direct numerical integration from the exact form in (2). Figures 4 and 5 show typical comparisons (selected from a comprehensive set of data) between beam integrals evaluated asymptotically from (22) and by CSP from (36) and (37). For a narrow nontilted beam ($L_x = 0.2\lambda_p$) (Fig. 4), with observations at $R = 5\lambda_p$, CSP is seen to reproduce the BI results (which, in turn, agree completely with the reference solution) within the angular regions $|\theta_p| < 80^\circ$, $|\theta_s| < 42^\circ$; agreement for the displacements in these regions is to within 1%. Near ($R = 10\lambda_p$) and far ($R = 250\lambda_p$) field results for a wide nontilted beam ($L_x = 10\lambda_p$) are shown in Figs. 5 and 6. Observe that CSP reproduces the BI results over the entire angular region of the near field, and over the narrow angular region produced in the far field by wide Gaussians. It has also been found that the far field phases agree well within the

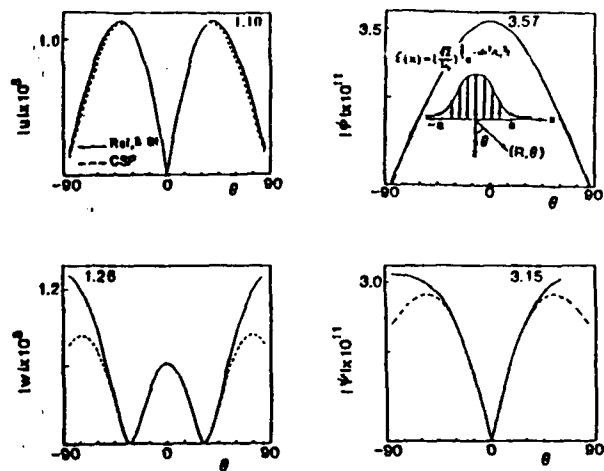


FIG. 4. Potential and displacement response at $R = 5\lambda_p$ to a body force distribution defined by a single Gaussian basis function. Narrow nontilted beam $L_x = 0.2\lambda_p$, $n = 0$. Beam parameters (Fresnel lengths): $b_p = 0.04\lambda_p$, $b_s = 0.07\lambda_p$. The numbers on the graphs express the peak amplitudes.

paraxial zone $|\theta| < 15^\circ$; since the amplitudes are negligible elsewhere, the discrepancies there are of no consequence. Narrow tilted beams ($|n| > 0$) have evanescent spectra away from the aperture plane [$\theta_{p,n}^{(n)} = \sin^{-1}(2n\pi/k_{p,n}L_x)$ is complex], and they therefore contribute negligibly in their far zones. The far zone for Fig. 4 has already been reached at $R = 5\lambda_p$. On the other hand, wide tilted beams ($|n| > 0$) are important contributors in the far zone, as illustrated in Fig. 7 for a wide basis element in the aperture plane. Here, $L_x = 10\lambda_p$, $n = 9$, $\theta_{p,n}^{(9)} = 64^\circ, 29^\circ$, and the angular regions of good agreement between BI and CSP are, respectively, $|\theta - \theta_{p,n}^{(9)}| < 5^\circ$, $|\theta - \theta_{s,n}^{(9)}| < 20^\circ$. The observation circle at $R = 50\lambda_p$ is within the Fresnel zone for the shear waves but outside that zone for the compressional waves. The linear phasing ($n = 9$) produces distinct P and SV beams along axes θ_p and θ_s , respectively, that appear separately in the

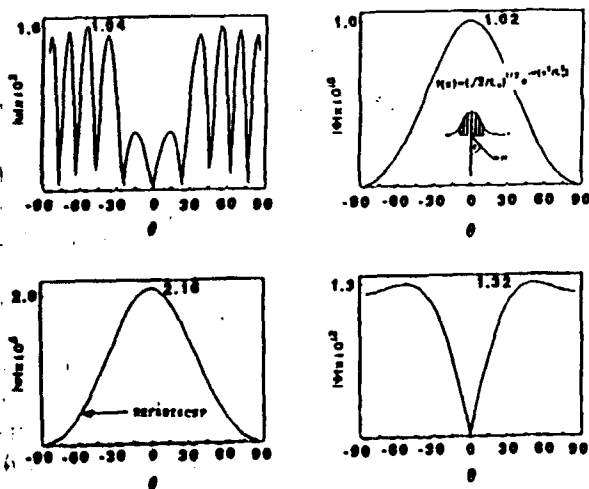


FIG. 5. Potential and displacement response in "near field" $R = 10\lambda_p$ to body force distribution defined by a single-basis function. Wide nontilted beam: $L_x = 10\lambda_p$, $n = 0$. Beam parameters (Fresnel lengths): $b_p = 100\lambda_p$, $b_s = 187\lambda_p$.

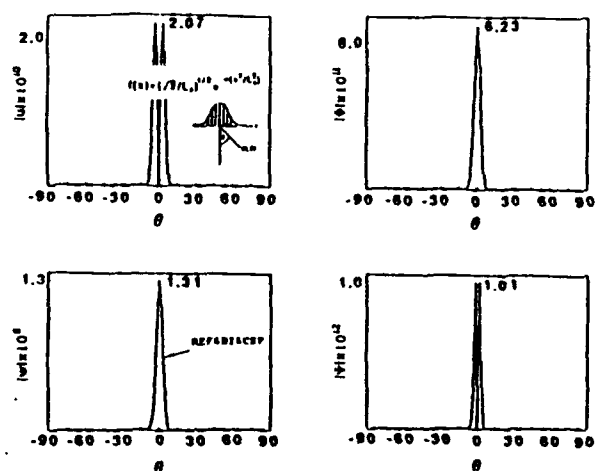


FIG. 6. Potential and displacement response in "far field" $R = 250\lambda_p$ to body force distribution defined by a single-basis function. Wide nontilted beam: $L_x = 10\lambda_p$, $n = 0$. Beam parameters (Fresnel lengths): $b_p = 100\lambda_p$, $b_s = 187\lambda_p$.

potentials but together in the displacements. In general, for a given index n , the Φ -beams are tilted more than the Ψ beams. With increasing tilt, the validity of the wide beam paraxial approximation becomes constrained to a smaller domain near the beam axis. Therefore, the CSP and BI results show more discrepancy for P than for SV . The calculations confirm that BI can be approximated by CSP in the $|\bar{\epsilon}| < 1$ regions of both wide and narrow beams. From these heuristic comparisons, it may be inferred that $|\bar{\epsilon}_{p,n}| < 1$, with $\bar{\epsilon}$ defined in (30), furnishes a good estimate for the range of validity of CSP asymptotics.

Because narrow-waisted beams have a broad angular spread, the $|\bar{\epsilon}| < 1$ domain does not cover the entire angular pattern. However, when such beam elements are employed

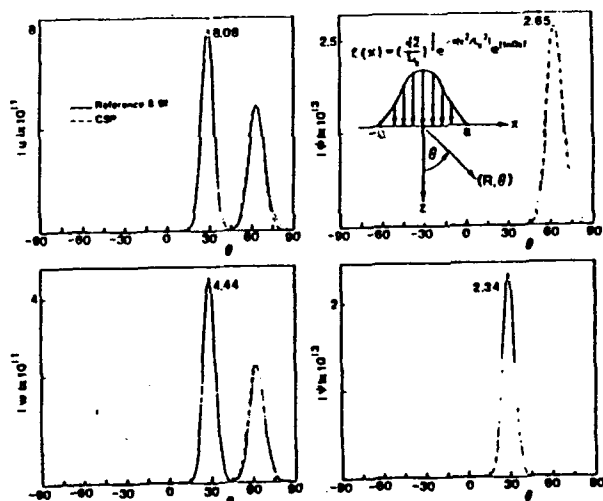


FIG. 7. Potential and displacement response at $R = 50\lambda_p$ to a body force distribution defined by a single-Gaussian basis function. Wide tilted beam: $L_x = 10\lambda_p$, $n = 9$. Beam parameters: $b_p = 19\lambda_p$, $b_s = 76\lambda_p$; $|\bar{\epsilon}_{p,n}| \leq 1$ corresponds to $|\theta - \theta_{p,n}| < 5^\circ$, $|\theta - \theta_{s,n}| < 20^\circ$.

in the lattice synthesis of an aperture field, their close spacing causes their far fields to overlap, thereby minimizing the damage from these inaccurate wide-angle contributions. Therefore CSP synthesis with nontilted narrow-waisted beams works well in the intermediate and far zones. The contrary is true when synthesizing with wide beams. Because of the asymmetry associated with tilted beams (see Fig. 3) and the narrowing of their $|\tilde{E}| < 1$ domains, CSP here is less satisfactory. This is demonstrated in the examples below.

B. Smoothly tapered aperture profile

1. Narrow beam synthesis

For narrow beams, with respect to aperture width, the A_{mn} expansion coefficients in (8) for a smoothly tapered aperture field profile are known to be concentrated around the $n = 0$ line in the phase space lattice of Fig. 2, and the A_{m0} coefficients can be determined directly by sampling the profile, thereby avoiding need for evaluating the integral in (11). (Ref. 10) This is confirmed in Fig. 8(a). For aperture plane synthesis, the individual $n = 0$ basis fields sample narrow regions, but the resulting spectral gaps [see oscillations in right-hand portion of Fig. 8(b)] can be filled by small but essential contributions from the $|n| > 0$ elements. Away from the aperture plane, the (tilted) beams corresponding to $|n| > 0$ are evanescent and therefore negligible except in the very near zone. For the parameters in Fig. 8, the $|n| > 0$ beams can already be omitted at $R = 5\lambda_p$, which is in the "far zone" of each element. CSP synthesis with nontilted beams is seen to be adequate and the number of beams required is relatively small (27 beams: $|m| < 13$, $|n| = 0$) (Fig. 9). Results obtained for linearly phased aperture distributions (Fig. 10) indicate that use of the same number of beams yields comparable accuracy in the far zone of each element.

2. Wide beam synthesis

For wide basis elements ($L_x = 10\lambda_p = 4a$ in the examples), phase shifts (beam tilts) $|n| > 0$ are important but

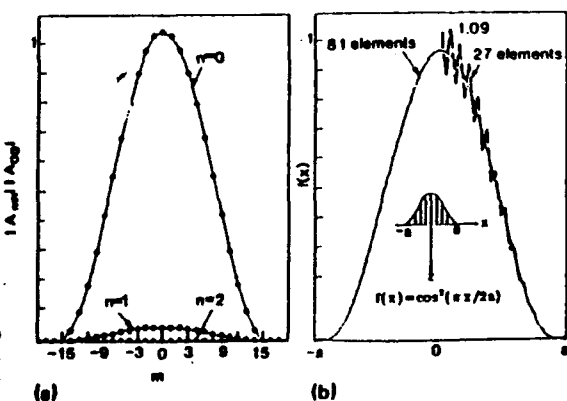


FIG. 8. Nonphased \cos^2 aperture field synthesis using narrow beams: $L_x = 0.2\lambda_p$, $2a = 5\lambda_p$. (a) Normalized expansion coefficients $|A_{mn}|/|A_{m0}|$ evaluated from (11). (b) Aperture synthesis using 27 ($|m| < 13$, $n = 0$) and 81 ($|m| < 13$, $|n| < 1$) elements.

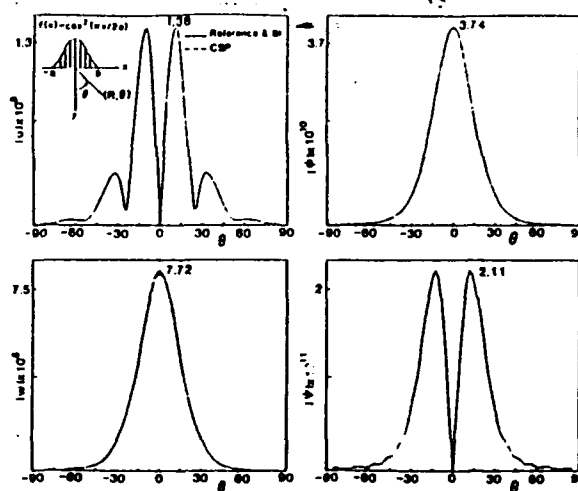


FIG. 9. Radiation patterns at $R = 5\lambda_p$ for nonphased \cos^2 aperture, using 27 ($|m| < 13$, $n = 0$) narrow-beam ($L_x = 0.2\lambda_p$) elements. Fresnel zone of aperture: $b_{ap} = (2a)^2/\lambda_p = 25\lambda_p$. Aperture field synthesis with same number of beams is shown in Fig. 8(b).

shifted locations $|m| > 0$ are much less important (Fig. 11). Although only the $|n| < 5$ ($m = 0$) beams were required to synthesize the Gaussian-like aperture field, many more are needed for field synthesis in the near and far zones because each of the tilted beams covers only a narrow angular interval. The expansion coefficients A_{0n} have amplitudes that match the far zone angular pattern (not shown) at the spectral sampling points;¹⁰ this allows the estimation of these coefficients without going through the numerical evaluation of (11). Discrepancies due to omission of spatially displaced beams can be remedied here by including all spectrally displaced (tilted) beams at the $m = \pm 1$ spatial locations as illustrated in Fig. 12 for near field ($R = 10\lambda_p$) observations. Comparison of extensive numerical data generated by BI and CSP in (22) and (37), respectively, has shown that CSP summation is adequate when $R > 10 - 15\lambda_p$, which represents $0.1b_p$ and $0.05b_s$; it may be recalled that the CSP com-

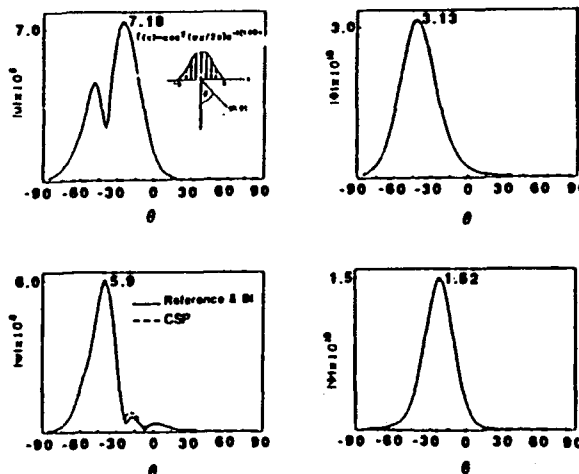


FIG. 10. Radiation patterns at $R = 5\lambda_p$ for phased \cos^2 aperture, using 27 ($|m| < 13$, $n = 0$) narrow-beam ($L_x = 0.2\lambda_p$) elements. Fresnel zone of aperture: $b_{ap} = 25\lambda_p$.

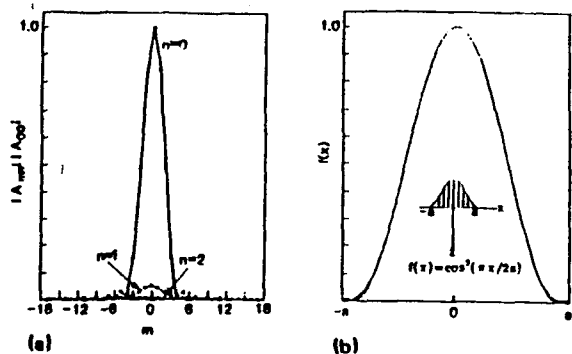


FIG. 11. Nonphased \cos^2 aperture field synthesis, using wide beams: $L_x = 10\lambda_p$, $2a = 5\lambda_p$. (a) Normalized expansion coefficients $|A_m|/|A_0|$ evaluated from (11). The dominant coefficients are localized around $m = 0$. (b) Aperture synthesis using 11 ($m = 0, |n| < 5$) elements.

plex displacement b_p , [see (24)] expresses the Fresnel length for each beam. CSP inaccuracies, which arise for strongly tilted beams, affect especially the Φ -beam contributions (the deterioration of the corresponding displacement fields is small when Ψ contributions predominate). These effects are illustrated in the far zone results for a highly phased smooth (\cos^2) aperture function (Fig. 13).

3. Matched beam synthesis

Basis elements matched to the aperture size ($L_x \approx 2a$) afford still another synthesis option. Now, the contributing elements (m, n), with approximately equal weighting, are localized around the central element $m = n = 0$, which gives the dominant contribution for a smooth nonphased aperture field profile. Considerably more beams would be required for accurate synthesis of radiated, and especially aperture, fields when the aperture profile deviates strongly from a Gaussian. For the smooth Gaussian-like profile chosen for illustration in Fig. 14, the number of beams required to synthesize the aperture fields (Fig. 14) and radiated fields (Fig. 15) is moderate. One feature of interest with matched

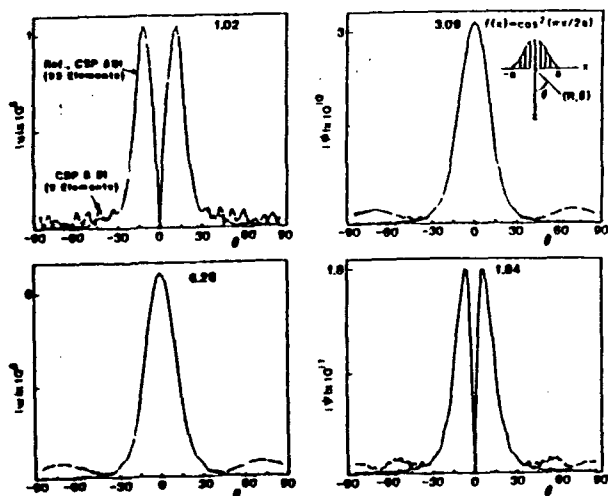


FIG. 12. Radiation patterns at $R = 10\lambda_p$ for nonphased \cos^2 aperture, using 5 ($m = 0, |n| < 2$) and 93 ($|m| < 1, |n| < 15$) wide-beam ($L_x = 10\lambda_p$) elements. Fresnel zone of aperture: $b_{ap} = 25\lambda_p$.

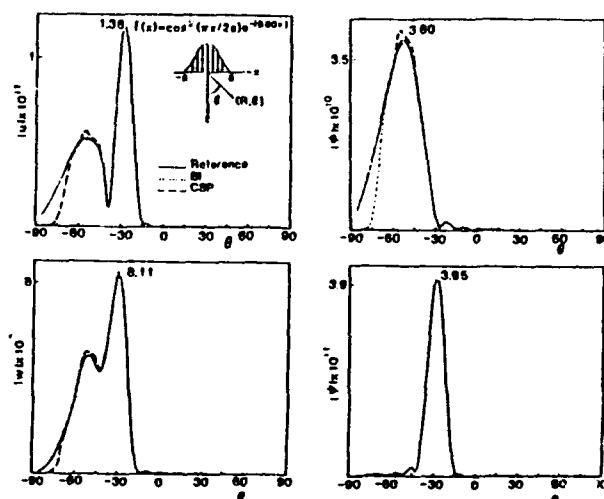


FIG. 13. Far-field radiation patterns at $R = 250\lambda_p$ for phased aperture, using 48 ($|m| < 1, -15 < n < 0$) wide-beam ($L_x = 10\lambda_p$) elements. Fresnel zone of aperture: $b_{ap} = 25\lambda_p$.

beams is the dominant contribution made by the $m = n = 0$ beam to the main lobe of Φ and w in the far field pattern. Because of the increased contribution of the tilted beams for the phased aperture profile, CSP inaccuracies occur in the radiated fields due to the inability of the CSP to reproduce the highly tilted, nonsymmetric Φ beams.

C. Abruptly truncated aperture profile

A much more severe test of the beam synthesis technique is posed by an abruptly truncated aperture profile as in case b of (42). Narrow basis elements, as in Fig. 8, now have amplitude coefficients that include more $|n| > 0$ contributions, and the exact A_{mn} coefficients reveal irregularities and spikes caused by the discontinuities at the profile edges [Fig. 16(a)]. Aperture synthesis with beams comparable to those in Fig. 8 does correspondingly more poorly [Fig. 16(b)]. The discrepancies can be reduced, but not removed entirely, by increasing the number of beams retained. Near and far zone synthesis, however, proceeds as before, and with comparable accuracy. Analogous conclusions pertain to the wide

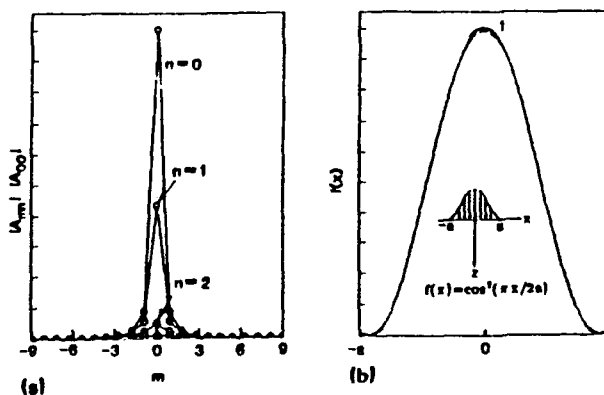


FIG. 14. Nonphased \cos^2 aperture field synthesis, using matched beams: $L_x = 5\lambda_p$, $2a = 5\lambda_p$. (a) Normalized expansion coefficients $|A_m|/|A_0|$. (b) Aperture synthesis using 25 ($|m| = |n| < 2$) elements.

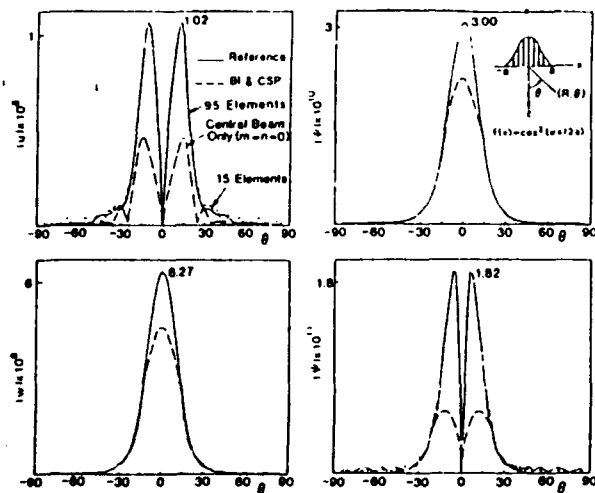


FIG. 15. Near-field radiation pattern at $R = 10\lambda_p$ for nonphased aperture, using 15 ($|m| < 1$, $|n| < 2$), and 95 ($|m| < 2$, $|n| < 9$) matched-beam ($L_s = 5\lambda_p$) elements. Fresnel zone of aperture: $b_{ap} = 25\lambda_p$. Aperture field synthesis for 25 elements is shown in Fig. 14.

beam synthesis, illustrated in Fig. 17 for the near field. A comparable number of matched beams fared much worse than either narrow or wide beams, and adding more beams produced no systematic improvements.

V. CONCLUSIONS

A self-consistent superposition of Gaussian basis elements on a configuration-wavenumber phase space lattice, and the corresponding Gaussian beam propagators, have been utilized here for the rigorous representation of finite planar source distributions and the resulting radiated fields in an unbounded homogeneous elastic solid. For two simple linearly phased aperture profiles with smoothly tapered and abruptly truncated amplitude behavior, it has been shown how the choice of nontilted and tilted narrow, wide or matched beams with respect to the aperture size affects the field synthesis, how well asymptotic approximations of the beam propagator integrals (BI) agree with a numerical reference solution, and how well the asymptotic BI can be ap-

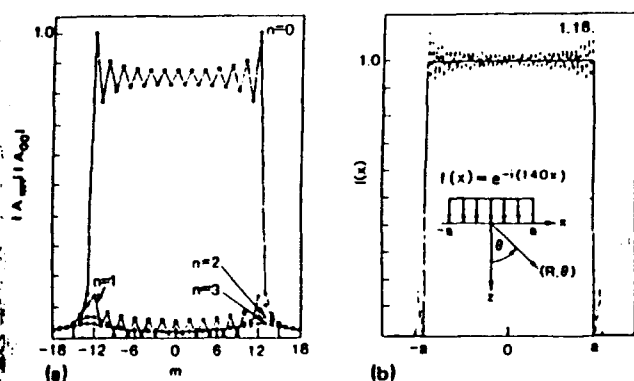


FIG. 16. Phased uniform aperture field synthesis, using narrow beams: $L_s = 0.2\lambda_p$, $2a = 5\lambda_p$. (a) Normalized expansion coefficients $|A_m|/|A_0|$; (b) Aperture synthesis using 93 ($|m| < 13$, $|n| < 1$) elements.

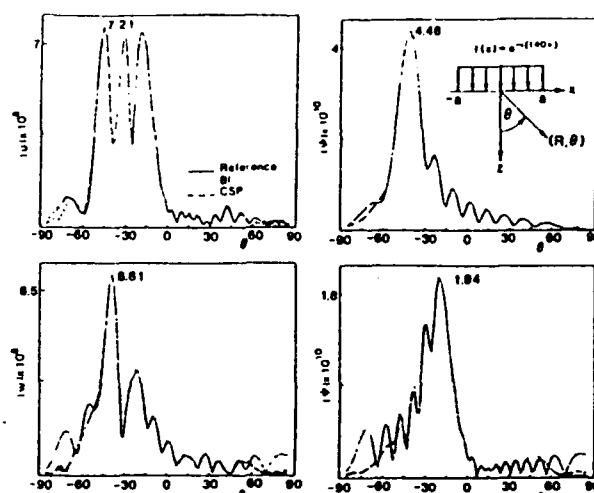


FIG. 17. Near-field radiation pattern at $R = 10\lambda_p$ for phased uniform aperture, using 93 ($|m| < 1$, $|n| < 15$) wide-beam ($L_s = 10\lambda_p$) elements. Fresnel zone of aperture: $b_{ap} = 25\lambda_p$.

proximated by more convenient complex source point (CSP) fields. Narrow beam synthesis away from the aperture plane involves nontilted ($n = 0$) beams only (the tilted $|n| > 0$ beams are evanescent), and these beams can be tracked along almost real trajectories because of the small complex displacement component of the narrow beam source location. This ray-like behavior makes narrow beams interesting candidates for negotiating complicated environments at high frequencies.^{11,12} However, many of them are required for accurate field synthesis.

The algorithm developed so far is for two-dimensional fields but extension to three dimensions has been initiated.¹³ It is intended to explore this technique for modeling of transducer outputs, and for coupling these outputs across interfaces and other structural inhomogeneities. Being rigorously based, the Gaussian beam algorithm presented here may provide a potentially more accurate (though probably more computation intensive) alternative to beam formulations employed elsewhere.^{2,3} The virtue of the algorithm is its rigorous foundation that makes possible the systematic assessment of approximations that *must* be incorporated into a working computer code. This can help toward establishing confidence. The algorithm may also furnish a potentially more accurate NDE option for the modeling of scattering due to induced source distributions in fault zones. These matters remain to be explored.

ACKNOWLEDGMENT

This work has been supported by the Air Force Office of Scientific Research under Grant No. AFOSR-86-0318.

APPENDIX: REFERENCE SOLUTION

To synthesize the distributed body force $f(x)$ in terms of a scalar line unit force excitation at $(x', z') = (x', 0)$ we proceed as follows.

Green's displacement tensor defined by⁸

$$G_{ij}(x,z;x',z') = \frac{1}{4\pi\rho\omega^2} \left(k^2 \delta_{ij} g_s - \frac{\partial}{\partial x_i} \frac{\partial}{\partial x_j} (g_p - g_s) \right),$$

$$ij = x \text{ or } z, \quad (\text{A1})$$

represents the displacement vector component in the i th direction at point (x,z) due to a unit concentrated body force in an unbounded medium applied in the j th direction at (x',z') . Here, $g_{p,s}$ is the scalar two-dimensional free-space Green's function

$$g_{p,s} = i\pi H_0^{(1)}(k_{p,s}r), \quad r = \sqrt{(x-x')^2 + (z-z')^2}, \quad (\text{A2})$$

which satisfies the two-dimensional wave equation

$$(\nabla^2 + k^2)g_{p,s}(x,z;x',z') = -4\pi\delta(x-x')\delta(z-z'). \quad (\text{A3})$$

Upon equating the displacements in the horizontal and vertical directions as given in (5a) and (A1), and appealing to (A2), we obtain

$$u = \frac{\partial\Phi}{\partial x} - \frac{\partial\Psi}{\partial z} = -\frac{1}{4\pi\rho\omega^2} \frac{\partial^2}{\partial x \partial z} (g_p - g_s),$$

$$w = \frac{\partial\Phi}{\partial z} + \frac{\partial\Psi}{\partial x} = -\frac{1}{4\pi\rho\omega^2} \left(\frac{\partial^2}{\partial x^2} g_s + \frac{\partial^2}{\partial z^2} g_p \right). \quad (\text{A4})$$

From the above, it is observed that the potentials for a unit concentrated z -directed body force are

$$\Phi = -\frac{1}{4\pi\rho\omega^2} \frac{\partial g_p}{\partial z}, \quad \Psi = -\frac{1}{4\pi\rho\omega^2} \frac{\partial g_s}{\partial x}. \quad (\text{A5})$$

Consequently, for the distributed source $f(x)$, the potentials and displacements are given by

$$\Phi(x,z) = \frac{-1}{4\pi\rho\omega^2} \int_{-\infty}^{\infty} f(x') \frac{\partial g_p}{\partial z} dx',$$

$$\Psi(x,z) = \frac{-1}{4\pi\rho\omega^2} \int_{-\infty}^{\infty} f(x') \frac{\partial g_s}{\partial x} dx', \quad (\text{A6})$$

and

$$u(x,z) = \int_{-\infty}^{\infty} f(x') G_{xz}(x,z;x',0) dx',$$

$$w(x,z) = \int_{-\infty}^{\infty} f(x') G_{zz}(x,z;x',0) dx'. \quad (\text{A7})$$

It can readily be shown that the plane-wave spectral representations of these functions are

$$\Phi(x,z) = \frac{1}{4\pi\rho\omega^2} \int_{-\infty}^{\infty} \hat{f}(k) e^{ikx + \kappa_p z} dk,$$

$$\Psi(x,z) = \frac{1}{4\pi\rho\omega^2} \int_{-\infty}^{\infty} \frac{k}{\kappa_s} \hat{f}(k) e^{ikx + \kappa_s z} dk, \quad (\text{A8})$$

and

$$u(x,z) = \frac{i}{4\pi\rho\omega^2} \int_{-\infty}^{\infty} k \hat{f}(k) e^{ikx} (e^{\kappa_p z} - e^{\kappa_s z}) dk,$$

$$w(x,z) = \frac{i}{4\pi\rho\omega^2} \int_{-\infty}^{\infty} \hat{f}(k) e^{ikx} \left(\kappa_p e^{\kappa_p z} + \frac{k^2}{\kappa_s} e^{\kappa_s z} \right) dk, \quad (\text{A9})$$

where $\kappa_{p,s} = \sqrt{k^2 - k_{p,s}^2}$, and $\hat{f}(k)$ is the spatial spectrum of $f(x)$.

¹V. Cervený, M. M. Popov, and I. Psencik, "Computation of Wave Fields in Inhomogeneous Media-Gaussian Beam Approach," *Geophys. J. R. Astron. Soc.* 70, 109 (1982).

²B. P. Newberry, T. A. Gray, E. F. Lopes, and R. B. Thompson, "Evaluation of Ultrasonic Beam Models for the Case of a Piston Transducer Radiating through a Liquid-Solid Interface," in *Review of Progress in Quantitative NDE*, edited by D. O. Thompson and D. E. Chimenti (Plenum, New York, 1986), Vol. 5A, pp. 127-138.

³J. J. Wen and M. A. Breazeale, "A Diffraction Beam Field Expressed as the Superposition of Gaussian Beams," *J. Acoust. Soc. Am.* 83, 1732 (1988).

⁴J. J. Maciel and L. B. Felsen, "Systematic Study of Fields Due to Extended Apertures by Gaussian Beam Discretization," *IEEE Trans. Antennas Propag.* AP-37, 884 (1989).

⁵J. D. Achenbach, *Wave Propagation in Elastic Solids* (North-Holland, Amsterdam, 1973).

⁶M. J. Bastiaans, "Gabor's Expansion of a Signal into Gaussian Elementary Signals," *Proc. IEEE* 68, 538 (1980).

⁷L. B. Felsen and N. Marcuvitz, *Radiation and Scattering of Waves* (Prentice-Hall, Englewood Cliffs, NJ, 1973), Chap. 4.

⁸L. B. Felsen, "Complex Rays," *Philips Res. Rep.* 30, 187 (1975).

⁹L. B. Felsen, "Complex-Source-Point Solutions of the Field Equations and their Relation to the Propagation and Scattering of Gaussian Beams," in *Symposia Matematica Istituto Nazionale di Alta Matematica* (Academic, New York, 1976), Vol. XVIII, pp. 40-56.

¹⁰P. D. Einziger, S. Raz, and M. Shapira, "The Gabor Representation and Aperture Theory," *J. Opt. Soc. Am.* A3, 508 (1986).

¹¹J. J. Maciel and L. B. Felsen, "Gaussian Beam Analysis of Propagation from an Extended Plane Aperture Distribution through Dielectric Layers: I—Plane Layer," *IEEE Trans. Antennas Propag.* AP-38, 1607 (1990).

¹²J. J. Maciel and L. B. Felsen, "II—Circular Cylindrical Layer," *IEEE Trans. Antennas Propag.* AP-38, 1618 (1990).

¹³J. M. Klosner, L. B. Felsen, I. T. Lu, and Z. Grossfeld, "Source Field Modeling by Self-Consistent Gaussian Beam Superposition (Three-Dimensional)," in preparation.

APPENDIX E

Three-dimensional source field modeling by self-consistent Gaussian beam superposition

J. M. Klosner

*Department of Mechanical and Industrial Engineering, Polytechnic University, Farmingdale,
New York 11735*

L. B. Felsen and I. T. Lu

*Department of Electrical Engineering, Weber Research Institute, Polytechnic University, Farmingdale, New
York 11735*

H. Grossfeld

*Department of Mechanical and Industrial Engineering, Polytechnic University, Farmingdale,
New York 11735*

(Received 12 April 1991; revised 13 September 1991; accepted 15 October 1991)

A self-consistent superposition of Gaussians on a discretized (configuration)-(wave number) phase space lattice has recently been applied to two-dimensional wave propagation into an elastic solid [Felsen *et al.*, *J. Acoust. Soc. Am.* **89**, 63 (1991)]. It is here generalized to three dimensions by modeling the radiation from planar finitely extended two-dimensional source distributions into an elastic solid. A distribution of forces over the source aperture is expanded self-consistently into Gaussian basis elements, which are then propagated into the unbounded medium. Numerical results are presented for simple smoothly tapered and abruptly truncated source profiles. As for the two-dimensional case, the validity of complex-source-point modeling of the Gaussians is explored by comparing the fields obtained from them with those generated by an independent numerical reference solution. Moreover, it is demonstrated how different self-consistent choices of beams affect the convergence of the Gaussian series expansion.

PACS numbers: 43.20.Bi, 43.20.Rz, 43.60.Cg

INTRODUCTION

Interpretation of ultrasonic NDE tests requires understanding of the propagation properties of source-excited high-frequency fields in an elastic environment. An effective approach in dealing with wave phenomena in the source-excited environment is to decompose the source distribution into basis elements, propagate each element from the source region to the receiver, and recombine to synthesize the total field. Because Gaussian beams have favorable propagation characteristics and represent physically observable entities, they have been used as elements in many modeling schemes.^{1,2} However, when excitation or scattering processes are not beam preserving, it may be necessary to account for marked deviations from a well-collimated Gaussian.

To cope with non-Gaussian effects without losing the attractiveness of the Gaussians, various efforts have been made to employ a superposition of Gaussian basis fields for modeling general source configurations.¹⁻³ A new procedure, which has recently been applied to electromagnetic and acoustic fields⁴ and more recently to two-dimensional elastic fields,⁵ is now extended to three-dimensional elastic fields. In this scheme, an arbitrary source distribution is decomposed rigorously into a discrete superposition of linearly phased and nonphased Gaussian elements distributed self-consistently over a lattice in a configurational-spectral wave-number phase space. Nonphased elements generate forward

propagating beams, whereas the phased elements generate tilted beams.

In what follows, the beam synthesis is illustrated for two axisymmetric simple models of time-harmonic finite aperture source distributions in an unbounded elastic solid: linearly phased smoothly tapered, and abruptly truncated, aperture profiles. These source distributions may be due to a transducer on an air-solid interface (although wave effects attributable to the interface are neglected here), or they may account for forces induced on cracklike imperfections inside the solid. The formulation and formal solution by Green's function and spectral techniques is presented in Sec. I. The beam lattice expansion is summarized in Sec. II, and various options for evaluating the propagation of individual beams are developed in Sec. III. Some representative numerical results for aperture and field synthesis are shown in and discussed in Sec. IV, with concluding remarks in Sec. V.

I. FORMULATION

The analysis for the three-dimensional case follows along the same lines as described in Ref. 5. The unbounded domain is assumed to be excited by a two-dimensional, z -directed time-harmonic pressure or body force distribution $f(x,y)e^{-i\omega t}$ acting on a constant $z=0$ surface as shown in Fig. 1. For the general case, the elastic fields can be derived from a scalar potential $\Phi(x,y,z)$ and a vector potential $\Psi(x,y,z)$ with components (Ψ_x, Ψ_y, Ψ_z) , which represent

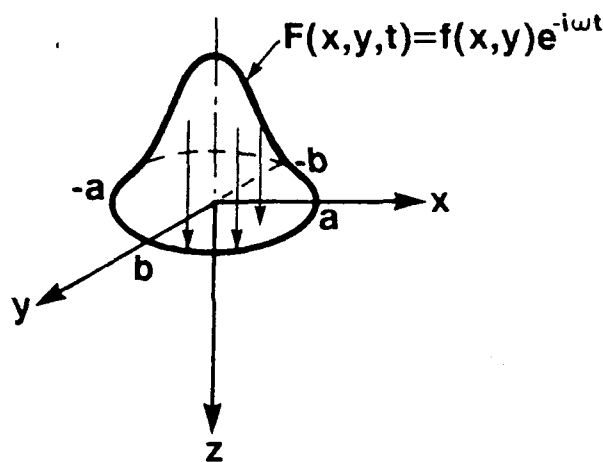


FIG. 1. Body force distribution in an infinite domain.

pressure (P) and shear (S) waves with wave propagation speeds $v_p = \sqrt{(\lambda + 2\mu)/\rho}$ and $v_s = \sqrt{\mu/\rho}$. The shear waves are equivoluminal; thus

$$\nabla \cdot \Psi = 0. \quad (1)$$

With u, v , and w denoting the displacements in the horizontal and vertical directions, respectively, the body force problem can be reformulated as⁶

$$\sigma_{xx}(x,y,0^+) = \begin{cases} -\frac{1}{2}f(x,y) & \text{for } -a < x < a, \quad -b < y < b \\ 0, & \text{for } |x| > a, \quad |y| > b \end{cases}$$

$$u(x,y,0) = 0, \quad v(x,y,0) = 0.$$

The relevant potentials satisfy the wave equations

$$(\nabla^2 + k_p^2)\Phi(\mathbf{x}, \mathbf{x}', \omega) = 0, \quad k_p = \omega/v_p, \quad (2)$$

$$(\nabla^2 + k_s^2)\Psi(\mathbf{x}, \mathbf{x}', \omega) = 0, \quad k_s = \omega/v_s, \quad (3)$$

where $\mathbf{x} \equiv \mathbf{x}(x,y,z)$ and $\mathbf{x}' \equiv \mathbf{x}'(x',y',z')$ locate the field and source points, respectively.

In terms of these potentials,

$$\begin{aligned} u(x,y,z) &= \frac{\partial \Phi(x,y,z)}{\partial x} + \frac{\partial \Psi_z(x,y,z)}{\partial y} - \frac{\partial \Psi_y(x,y,z)}{\partial z}, \\ v(x,y,z) &= \frac{\partial \Phi(x,y,z)}{\partial y} - \frac{\partial \Psi_z(x,y,z)}{\partial x} + \frac{\partial \Psi_x(x,y,z)}{\partial z}, \\ w(x,y,z) &= \frac{\partial \Phi(x,y,z)}{\partial z} + \frac{\partial \Psi_y(x,y,z)}{\partial x} - \frac{\partial \Psi_x(x,y,z)}{\partial y}, \end{aligned} \quad (4)$$

and

$$\begin{aligned} \sigma_{xx}(x,y,z) &= \lambda \nabla^2 \Phi(x,y,z) + 2\mu \left(\frac{\partial^2 \Phi(x,y,z)}{\partial z^2} \right. \\ &\quad \left. + \frac{\partial^2 \Psi_y(x,y,z)}{\partial x \partial z} - \frac{\partial^2 \Psi_x(x,y,z)}{\partial y \partial z} \right). \end{aligned} \quad (5)$$

It can readily be shown (Appendix A) that the potentials due to the force $f(x',y')$ distributed over the surface area S can be expressed as

$$\begin{aligned} \Phi(x,y,z) &= \frac{-1}{4\pi\rho\omega^2} \int_S f(x',y') \frac{\partial g_p}{\partial z} dx' dy', \\ \Psi_x(x,y,z) &= \frac{1}{4\pi\rho\omega^2} \int_S f(x',y') \frac{\partial g_s}{\partial y} dx' dy', \\ \Psi_y(x,y,z) &= \frac{-1}{4\pi\rho\omega^2} \int_S f(x',y') \frac{\partial g_s}{\partial x} dx' dy', \end{aligned} \quad (6)$$

where

$$g_{p,s} = \exp(ik_{p,s}r)/r, \quad (7)$$

$$r = \sqrt{(x-x')^2 + (y-y')^2 + (z-z')^2}$$

is the scalar Green's function for the compressional and shear waves. The displacement components in (4) can thus be expressed as

$$\begin{aligned} u(x,y,z) &= \int_S f(x',y') G_{xx}(x,z,x',z') dx' dy', \\ v(x,y,z) &= \int_S f(x',y') G_{yz}(x,z,x',z') dx' dy', \\ w(x,y,z) &= \int_S f(x',y') G_{zx}(x,z,x',z') dx' dy', \end{aligned} \quad (8)$$

where Green's displacement function is⁷

$$\begin{aligned} G_{ij}(x,y,z;x',y',z') &= \frac{1}{4\pi\rho\omega^2} \left(k_s^2 \delta_{ij} g_s - \frac{\partial}{\partial x_i} \frac{\partial}{\partial x_j} (g_p - g_s) \right), \\ i,j &= x,y,z, \end{aligned} \quad (9)$$

with $\delta_{ij} = 1$ or 0 for $i=j$ or $i \neq j$, respectively.

The potential formulation in the spectral wave-number domain, (k_x, k_y) corresponding to the spatial domain (x,y) is obtained by Fourier transformation along x and y coordinates

$$\begin{aligned} \hat{\Lambda}(k_x, k_y, z) &= \int_{-\infty}^{\infty} \int_{-\infty}^{\infty} \Lambda(x,y,z) e^{-i(k_x x + k_y y)} dx dy, \\ \Lambda &= \Phi \text{ or } \Psi, \end{aligned} \quad (10a)$$

with the inverse

$$\Lambda(x,y,z) = \frac{1}{4\pi^2} \int_{-\infty}^{\infty} \int_{-\infty}^{\infty} \hat{\Lambda}(k_x, k_y, z) e^{i(k_x x + k_y y)} dk_x dk_y. \quad (10b)$$

The spectral amplitudes are given in terms of the spectrum $\hat{f}(k_x, k_y)$ of the source distribution $f(x,y)$ as (Appendix B)

$$\begin{aligned} \hat{\Phi}(k_x, k_y, z) &= [\hat{f}(k_x, k_y)/2\rho\omega^2] e^{ik_p z}, \\ \hat{\Psi}_x(k_x, k_y, z) &= -[\hat{f}(k_x, k_y)k_y/2\rho\omega^2\kappa_s] e^{ik_s z}, \\ \hat{\Psi}_y(k_x, k_y, z) &= [\hat{f}(k_x, k_y)k_x/2\rho\omega^2\kappa_s] e^{ik_s z}, \\ \hat{\Psi}_z(k_x, k_y, z) &= 0, \end{aligned} \quad (11)$$

where $\kappa_{p,s} = \sqrt{k_{p,s}^2 - k_x^2 - k_y^2}$. The representation for Φ , Ψ_x , and Ψ_y in the space domain follows by inserting (11) into (10b), and the corresponding representation for the displacements and normal stress by the subsequent insertion into (4) and (5), with the partial differentiations performed on the integrand.

II. GAUSSIAN BEAM EXPANSION

By a straightforward generalization of the procedure in Ref. 5, the expansion of the aperture function $f(x,y)$ into a series of Gaussian basis functions distributed over an infinite Gabor lattice in a discretized four-dimensional (x_m, y_p, k_n, k_q) phase space takes the form

$$f(x,y) = \sum_m \sum_n \sum_p \sum_q A_{mnpq} w(x - mL_x, y - pL_y) \times \exp(i(n\Omega_x x + q\Omega_y y)), \quad (12)$$

where the spatial lattice separations L_x, L_y , and spectral separations Ω_x, Ω_y are constrained by the conditions

$$\Omega_x L_x = 2\pi, \quad \Omega_y L_y = 2\pi, \quad (13)$$

and $-\infty < (m,n,p,q) < \infty$. The two-dimensional normalized Gaussian basis function is defined by

$$w(x,y) = \left(\frac{\sqrt{2}}{L_x}\right)^{1/2} \left(\frac{\sqrt{2}}{L_y}\right)^{1/2} \exp\left[-\pi\left(\frac{x^2}{L_x^2} + \frac{y^2}{L_y^2}\right)\right],$$

$$\int |w(x,y)|^2 dx dy = 1. \quad (14)$$

The amplitude coefficients are

$$A_{mnpq} = \int_{-\infty}^{\infty} \int_{-\infty}^{\infty} f(x,y) \gamma(x - mL_x, y - pL_y) \times \exp(-i(n\Omega_x x + q\Omega_y y)) dx dy, \quad (15)$$

where $\gamma(x,y)$ is determined from the bi-orthogonality condition

$$\int_{-\infty}^{\infty} \int_{-\infty}^{\infty} w(x) \gamma^*(x - mL_x, y - pL_y) \times \exp(-i(n\Omega_x x + q\Omega_y y)) dx = \delta_m \delta_n \delta_p \delta_q, \quad (16)$$

$$\delta_j = \begin{cases} 1, & \text{for } j = 0, \\ 0, & \text{for } j \neq 0, \end{cases}$$

and the asterisk denotes the complex conjugate.

For the Gaussian window function in (14), the function $\gamma(x,y)$ is given by⁸

$$\gamma(x,y) = \left(\frac{1}{2L_x L_y}\right)^{1/2} \left(\frac{K_0}{\pi}\right)^{-3} \exp\left(\pi\left(\frac{x^2}{L_x^2} + \frac{y^2}{L_y^2}\right)\right) S_j S_i \quad (17a)$$

with

$$S_j S_i = \sum_{j > x/L_x - 1/2}^{\infty} (-1)^j \exp\left(-\pi\left(j + \frac{1}{2}\right)^2\right) \times \sum_{i > y/L_y - 1/2}^{\infty} (-1)^i \exp\left(-\pi\left(i + \frac{1}{2}\right)^2\right) \quad (17b)$$

and $K_0 = 1.854\,074\,68$ representing the complete elliptic integral of the first kind of argument $1/2$. A similar expansion exists in the spectral domain

$$\hat{f}(k_x, k_y) = \sum_m \sum_n \sum_p \sum_q A_{mnpq} \times \hat{w}(k_x - n\Omega_x, k_y - q\Omega_y) e^{(-i(mL_x k_x + pL_y k_y))}, \quad (18)$$

where

$$\hat{w}(k_x, k_y) = (2L_x L_y)^{1/2} \exp(-\pi(k_x^2/\Omega_x^2 + k_y^2/\Omega_y^2)) \quad (19)$$

is the Fourier spatial spectrum of $w(x,y)$.

Substituting the aperture function spectrum (18) into (11) and inverting the order of integration and summation yields the following Gabor series representation for the potentials and displacements

$$\{\Phi, \Psi_x, \Psi_y\}(x,y,z) = \frac{(2L_x L_y)^{1/2}}{2\rho\omega^2} \sum \sum \sum \sum A_{mnpq} \{B_1, B_2, B_3\}(x,y,z),$$

$$u(x,y,z) = \frac{(2L_x L_y)^{1/2}}{2\rho\omega^2} \sum \sum \sum \sum A_{mnpq} \left(\frac{\partial B_1}{\partial x} + \frac{\partial B_3}{\partial z}\right), \quad (20)$$

$$v(x,y,z) = \frac{(2L_x L_y)^{1/2}}{2\rho\omega^2} \sum \sum \sum \sum A_{mnpq} \left(\frac{\partial B_1}{\partial y} + \frac{\partial B_2}{\partial z}\right),$$

$$w(x,y,z) = \frac{(2L_x L_y)^{1/2}}{2\rho\omega^2} \sum \sum \sum \sum A_{mnpq} \times \left(\frac{\partial B_1}{\partial z} - \frac{\partial B_2}{\partial y} + \frac{\partial B_3}{\partial x}\right),$$

where the beam functions are defined as follows:

$$B_1(x,y,z) = \frac{1}{4\pi^2} \int_{-\infty}^{\infty} \int_{-\infty}^{\infty} \exp(i\hat{q}_p(k_x, k_y, z)) dk_x dk_y,$$

$$B_2(x,y,z) = \frac{1}{4\pi^2} \int_{-\infty}^{\infty} \int_{-\infty}^{\infty} \frac{-k_y}{\kappa_s} \exp(i\hat{q}_s(k_x, k_y, z)) dk_x dk_y, \quad (21)$$

$$B_3(x,y,z) = \frac{1}{4\pi^2} \int_{-\infty}^{\infty} \int_{-\infty}^{\infty} \frac{k_x}{\kappa_s} \exp(i\hat{q}_s(k_x, k_y, z)) dk_x dk_y,$$

with

$$\hat{q}_{p,s}(k_x, k_y, z) = k_x(x - mL_x) + k_y(y - pL_y) + \kappa_{p,s}z + (i/4\pi)[(k_x L_x - 2\pi n)^2 + (k_y L_y - 2\pi q)^2]. \quad (22)$$

The generally tilted beam fields corresponding to the beam functions are expressed more conveniently in angular spectrum form tied to the local rotated, beam-centered coordinates (η, ρ, θ) (see Fig. 2):

$$(x - mL_x) = (\eta \sin \gamma_{p,s}^{(n,q)} \cos \phi^{(n,q)} - \rho \sin \theta \sin \phi^{(n,q)}) + \rho \cos \theta \cos \gamma_{p,s}^{(n,q)} \cos \phi^{(n,q)},$$

$$(y - pL_y) = (\eta \sin \gamma_{p,s}^{(n,q)} \sin \phi^{(n,q)} + \rho \sin \theta \cos \phi^{(n,q)}) + \rho \cos \theta \cos \gamma_{p,s}^{(n,q)} \sin \phi^{(n,q)},$$

$$z = \eta \cos \gamma_{p,s}^{(n,q)} - \rho \cos \theta \sin \gamma_{p,s}^{(n,q)}, \quad (23)$$

where

$$\gamma_{p,s}^{(n,q)} = \sin^{-1} [(2\pi n/k_{p,s}L_x)^2 + (2\pi q/k_{p,s}L_y)^2]^{1/2} \quad (24)$$

is the angle of tilt of the P and S beam axes away from the normal to the aperture plane, and

$$\phi^{(n,q)} = \tan^{-1}(qL_x/nL_y) \quad (25)$$

is the circumferential angle in the plane of the aperture (Fig. 3). Introducing the angular spectrum variables,

$$\alpha_{p,s} = \sin^{-1}(\sqrt{k_x^2 + k_y^2}/k_{p,s}), \quad \beta = \tan^{-1}(k_y/k_x), \quad (26)$$

where the subscripts p,s distinguish the spectral domains for the compressional and shear waves, respectively, one finds for the transformation from the rectilinear to the angular domain,

$$\begin{aligned} k_x &= k_{p,s} \sin \alpha_{p,s} \cos \beta, & k_y &= k_{p,s} \sin \alpha_{p,s} \sin \beta, \\ \kappa_{p,s} &= k_{p,s} \cos \alpha_{p,s}. \end{aligned} \quad (27)$$

When $L_x = L_y$, the phase in (22) becomes, accordingly,

$$\begin{aligned} \hat{q}_{p,s}(\alpha_{p,s}, \beta) &= k_{p,s} [\eta (\sin \alpha_{p,s} \sin \gamma_{p,s}^{(n,q)} \cos(\beta - \phi^{(n,q)}) + \cos \alpha_{p,s} \cos \gamma_{p,s}^{(n,q)}) + \rho (\sin \alpha_{p,s} \cos \theta \cos \gamma_{p,s}^{(n,q)} \\ &\quad \times \cos(\beta - \phi^{(n,q)}) + \sin \alpha_{p,s} \sin \theta \sin(\beta - \phi^{(n,q)}) - \cos \alpha_{p,s} \cos \theta \sin \gamma_{p,s}^{(n,q)}) \\ &\quad + (ik_{p,s}L_x^2/4\pi) (\sin^2 \alpha_{p,s} + \sin^2 \gamma_{p,s}^{(n,q)} - 2 \sin \alpha_{p,s} \sin \gamma_{p,s}^{(n,q)} \cos(\beta - \phi^{(n,q)}))]. \end{aligned} \quad (28)$$

The beam integrals are

$$B_1(x, y, z) = \frac{1}{4\pi^2} \iint \exp(i\hat{q}_{p,s}(\alpha_{p,s}, \beta, z)) J_p d\alpha_p d\beta, \quad (29a)$$

$$\begin{aligned} B_2(x, y, z) &= -\frac{1}{4\pi^2} \iint \tan \alpha_s \sin \beta \\ &\quad \times \exp(i\hat{q}_s(\alpha_s, \beta, z)) J_s d\alpha_s d\beta, \end{aligned} \quad (29b)$$

$$B_3(x, y, z) = \frac{1}{4\pi^2} \iint \tan \alpha_s \cos \beta \exp(i\hat{q}_s(\alpha_s, \beta, z)) J_s d\alpha_s d\beta, \quad (29c)$$

where $J_{p,s}$ is the Jacobian transforming from (k_x, k_y) to $(\alpha_{p,s}, \beta)$,

$$J_{p,s} = \begin{vmatrix} \frac{\partial k_x}{\partial \alpha_{p,s}} & \frac{\partial k_x}{\partial \beta} \\ \frac{\partial k_y}{\partial \alpha_{p,s}} & \frac{\partial k_y}{\partial \beta} \end{vmatrix} = k_{p,s}^2 \sin \alpha_{p,s} \cos \alpha_{p,s}. \quad (30)$$

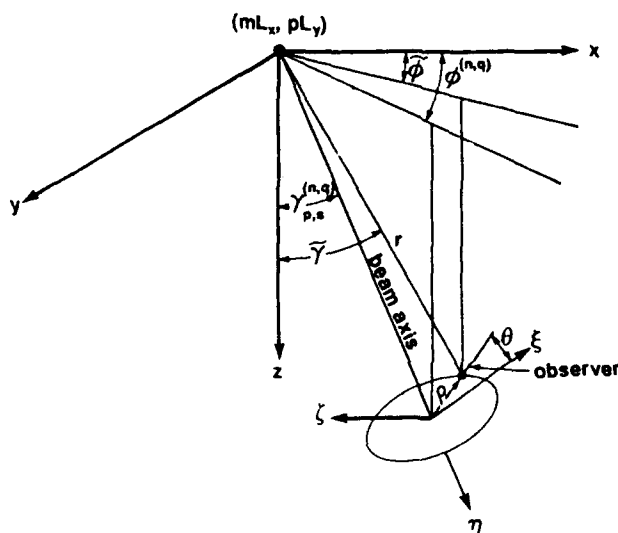


FIG. 2. Coordinate transformation for tilted beam.

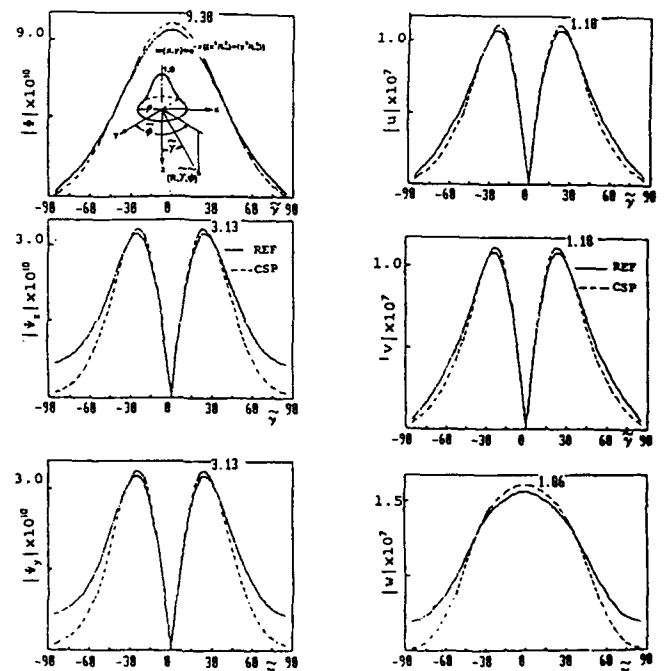


FIG. 3. Potential and displacement response in "far field" $R = 5\lambda_p$, to body beam force distribution defined by a single Gaussian basis function. Narrow nontilted: $L_x = L_y = 0.5\lambda_p$, $n = q = 0$. Beam parameters [Fresnel lengths: see (38)]: $b_p = 0.25\lambda_p$, $b_s = 0.47\lambda_p$. Solid curves: reference solution in (6), (8). Dashed curves: CSP in (60), (61).

III. APPROXIMATE EVALUATION OF THE BEAM INTEGRALS

A. Saddle point asymptotics

Following Ref. 1, the beam integrals in (29) are approximated asymptotically by the saddle point method, which may now be applied in the two-dimensional $(\alpha_{p,s}, \beta_{p,s})$ domain. The generic form for the lowest-order approximation for integrals having the form

$$I = \int_{-\infty}^{\infty} \int_{-\infty}^{\infty} f(\alpha_{p,s}, \beta_{p,s}) \exp(i\Omega \hat{q}_{p,s}(\alpha_{p,s}, \beta_{p,s}, z)) d\alpha_{p,s} d\beta_{p,s} \quad (31)$$

is given by⁹

$$I(\Omega) \sim f(\alpha_{p,s}^{(0)}, \beta_{p,s}^{(0)}) (2\pi/\Omega) [e^{i(\pi/4)\sigma} / |(\det)_{p,s}|^{1/2}], \quad (32)$$

where

$$(\det)_{p,s} = \left[\left(\frac{\partial^2 \hat{q}_{p,s}(\alpha_{p,s}^{(0)}, \beta_{p,s}^{(0)})}{\partial \alpha_{p,s}^{(0)2}} \right) \left(\frac{\partial^2 \hat{q}_{p,s}(\alpha_{p,s}^{(0)}, \beta_{p,s}^{(0)})}{\partial \beta_{p,s}^{(0)2}} \right) - \left(\frac{\partial^2 \hat{q}_{p,s}(\alpha_{p,s}^{(0)}, \beta_{p,s}^{(0)})}{\partial \alpha_{p,s}^{(0)} \partial \beta_{p,s}^{(0)}} \right)^2 \right], \quad (33)$$

$$\sigma = \sum_{i=1}^2 \text{sgn } d_i \quad (34)$$

and d_i are the eigenvalues of the matrix whose determinant is given in (33). Applied to (29), one finds

$$B_1 \sim (i/2\pi) k_p^2 \sin \alpha_p^0 \cos \alpha_p^0 |(\det)_p|^{-1/2} \times \exp(i\hat{q}_p(\alpha_p^0, \beta_p^0, z)), \quad (35a)$$

$$B_2 \sim -(i/2\pi) k_s^2 \sin^2 \alpha_s^0 \sin \beta_s^0 |(\det)_s|^{-1/2} \times \exp(i\hat{q}_s(\alpha_s^0, \beta_s^0, z)), \quad (35b)$$

$$B_3 \sim (i/2\pi) k_s^2 \sin^2 \alpha_s^0 \cos \beta_s^0 |(\det)_s|^{-1/2} \times \exp(i\hat{q}_s(\alpha_s^0, \beta_s^0, z)). \quad (35c)$$

The saddle point $(\alpha_{p,s}^{(0)}, \beta_{p,s}^{(0)})$ is defined by

$$\frac{\partial \hat{q}_{p,s}(\alpha_{p,s}^{(0)}, \beta_{p,s}^{(0)})}{\partial \alpha_{p,s}^{(0)}} = 0, \quad \frac{\partial \hat{q}_{p,s}(\alpha_{p,s}^{(0)}, \beta_{p,s}^{(0)})}{\partial \beta_{p,s}^{(0)}} = 0, \quad (36)$$

which relations imply, respectively,

$$\eta [\cos \alpha_{p,s}^{(0)} \sin \gamma_{p,s}^{(n,q)} \cos(\beta_{p,s}^{(0)} - \phi^{(n,q)}) - \sin \alpha_{p,s}^{(0)} \cos \gamma_{p,s}^{(n,q)}] + \rho [\cos \alpha_{p,s}^{(0)} \cos \theta \cos \gamma_{p,s}^{(n,q)} \cos(\beta_{p,s}^{(0)} - \phi^{(n,q)}) + \cos \alpha_{p,s}^{(0)} \sin \theta \sin(\beta_{p,s}^{(0)} - \phi^{(n,q)}) + \sin \alpha_{p,s}^{(0)} \cos \theta \sin \gamma_{p,s}^{(n,q)}] + (ik_{p,s} L_x^2 / 2\pi) [\sin \alpha_{p,s}^{(0)} \cos \alpha_{p,s}^{(0)} - \cos \alpha_{p,s}^{(0)} \sin \gamma_{p,s}^{(n,q)} \cos(\beta_{p,s}^{(0)} - \phi^{(n,q)})] = 0, \quad (37a)$$

$$\eta \sin \gamma_{p,s}^{(n,q)} \sin(\beta_{p,s}^{(0)} - \phi^{(n,q)}) + \rho [\sin \theta \cos(\beta_{p,s}^{(0)} - \phi^{(n,q)}) - \cos \theta \cos \gamma_{p,s}^{(n,q)} \sin(\beta_{p,s}^{(0)} - \phi^{(n,q)})] + (ik_{p,s} L_x^2 / 2\pi) [\sin \gamma_{p,s}^{(n,q)} \sin(\beta_{p,s}^{(0)} - \phi^{(n,q)})] = 0. \quad (37b)$$

B. Far-field approximation

As for the two-dimensional case in Ref. 5, we look for approximate alternatives to exact solution of the saddle point equations in (37). Assume that the distance r from the beam waist center at $(mL_x, pL_y, 0)$ is so large as to satisfy the inequality

$$\epsilon_{p,s} = b_{p,s}/r \ll 1, \quad b_{p,s} = k_{p,s} L_x^2 / 2\pi. \quad (38)$$

Here, $b_{p,s}$ are Fresnel lengths corresponding to the widths L_x of the Gaussian basis fields in the aperture. This suggests the expansions

$$\alpha_{p,s}^{(0)} = \alpha_0 + \epsilon_{p,s} \alpha_1 + \dots, \quad \beta_{p,s}^{(0)} = \beta_0 + \epsilon_{p,s} \beta_1 + \dots, \quad (39)$$

which will be substituted in (37). Before performing the substitution, the observer location is expressed in spherical coordinates as (see Fig. 2)

$$x - mL_x = r \sin \bar{\gamma} \cos \bar{\phi}, \quad y - pL_y = r \sin \bar{\gamma} \sin \bar{\phi}, \quad z = r \cos \bar{\gamma}. \quad (40)$$

Letting $L_x = L_y$, and inserting these and (27) into (22), we can write the phase of the integrands as

$$\hat{q}_{p,s} = k_{p,s} r [\sin \alpha_{p,s} \sin \bar{\gamma} \cos(\beta - \bar{\phi}) + \cos \alpha_{p,s} \cos \bar{\gamma}] + (ik_{p,s} L_x^2 / 4\pi) [\sin^2 \alpha_{p,s} + \sin^2 \gamma_{p,s}^{(n,q)} - 2 \sin \alpha_{p,s}^{(n,q)} \sin \gamma_{p,s}^{(n,q)} \cos(\beta - \phi^{(n,q)})] \quad (41)$$

and thereby the saddle point equations in (37) as

$$r (\cos \alpha_{p,s}^{(0)} \sin \bar{\gamma} \cos(\beta^{(0)} - \bar{\phi}) - \sin \alpha_{p,s}^{(0)} \sin \bar{\gamma}) + (ik_{p,s} L_x^2 / 4\pi) (2 \sin \alpha_{p,s}^{(0)} \cos \alpha_{p,s}^{(0)} - 2 \cos \alpha_{p,s}^{(0)} \sin \gamma_{p,s}^{(n,q)} \cos(\beta^{(0)} - \phi^{(n,q)})) = 0, \quad (42a)$$

$$- r \sin \bar{\gamma} \sin(\beta^{(0)} - \bar{\phi}) + (ik_{p,s} L_x^2 / 4\pi) \times (2 \sin \gamma_{p,s}^{(n,q)} \sin(\beta^{(0)} - \phi^{(n,q)})) = 0. \quad (42b)$$

Substituting (39) and equating the coefficients of powers $\epsilon_{p,s}$ to zero, one obtains the saddle point approximations

$$\beta_{p,s}^{(0)} = \bar{\phi} + i(b_{p,s}/r \cos^2 \gamma_{p,s}^{(n,q)}) \times (\sin \gamma_{p,s}^{(n,q)} / \sin \bar{\gamma}) \sin(\bar{\phi} - \phi^{(n,q)}) + \dots, \quad \alpha_{p,s}^{(0)} = \bar{\gamma} + i(b_{p,s}/r \cos^2 \gamma_{p,s}^{(n,q)}) \cos \bar{\gamma} \times (\sin \bar{\gamma} - \sin \gamma_{p,s}^{(n,q)} \cos(\bar{\phi} - \phi^{(n,q)})) + \dots \quad (43)$$

Inserting these into (35) yields the far-field approximation for the beam integrals

$$B_1 \sim (ik_p/2\pi r) \cos \bar{\gamma} \exp\{ik_p r \\ \times [1 + (ib_p/2r \cos^2 \gamma_p^{(n,q)}) (\sin^2 \bar{\gamma} + \sin^2 \gamma_p^{(n,q)}) \\ - 2 \sin \bar{\gamma} \sin \gamma_p^{(n,q)} \cos(\bar{\phi} - \phi^{(n,q)})]\}, \quad (44a)$$

$$B_2 \sim (-ik_s/2\pi r) \sin \bar{\gamma} \sin \bar{\phi} \exp\{ik_s r \\ \times [1 + (ib_s/2r \cos^2 \gamma_s^{(n,q)}) (\sin^2 \bar{\gamma} + \sin^2 \gamma_s^{(n,q)}) \\ - 2 \sin \bar{\gamma} \sin \gamma_s^{(n,q)} \cos(\bar{\phi} - \phi^{(n,q)})]\}, \quad (44b)$$

$$B_3 \sim (ik_s/2\pi r) \sin \bar{\gamma} \cos \bar{\phi} \exp\{ik_s r \\ \times [1 + (ib_s/2r \cos^2 \gamma_s^{(n,q)}) (\sin^2 \bar{\gamma} + \sin^2 \gamma_s^{(n,q)}) \\ - 2 \sin \bar{\gamma} \sin \gamma_s^{(n,q)} \cos(\bar{\phi} - \phi^{(n,q)})]\}. \quad (44c)$$

C. Paraxial approximation

In the paraxial region near the beam axis, the saddle point can be expanded in powers of alternative small dimensionless complex parameters $\bar{\epsilon}_{p,s}$ and $\bar{\epsilon}'_{p,s}$ so that

$$\beta_{p,s}^{(0)} = \beta_0 + \bar{\epsilon}_{p,s} \beta_1 + \dots, \quad \alpha_{p,s}^{(0)} = \alpha_0 + \bar{\epsilon}'_{p,s} \alpha_1 + \dots, \quad (45)$$

where

$$\epsilon'_{p,s} = \rho/(\eta - ib_{p,s}), \quad \bar{\epsilon}'_{p,s} = \rho/(\eta - ib'_{p,s}), \quad (46)$$

and

$$b'_{p,s} = k_{p,s} (L_x \cos \gamma_p^{(n,q)})^2 / 2\pi = b_{p,s} \cos^2 \gamma_p^{(n,q)}. \quad (47)$$

Introducing these into (37) and equating coefficients of the powers of $\bar{\epsilon}$, $\bar{\epsilon}'$ to zero, one obtains the following saddle point approximations

$$\alpha_{p,s}^{(0)} = \gamma_p^{(n,q)} + \cos \theta \bar{\epsilon}'_{p,s}, \\ \beta_{p,s}^{(0)} = \phi^{(n,q)} + (\sin \theta / \sin \gamma_p^{(n,q)}) \bar{\epsilon}_{p,s} + \dots \quad (48)$$

Retaining $\bar{\epsilon}$ terms of first order in the phase and zeroth-order terms in the amplitude, one may reduce the asymptotic expressions in (35) in the paraxial region defined by $|\bar{\epsilon}| \ll 1$ explicitly to

$$B_1 \sim \frac{ik_p \cos \gamma_p^{(n,q)}}{2\pi \sqrt{(\eta - ib_p)(\eta - ib'_p)}} \exp(ik_p Q_p), \quad (49a)$$

$$B_2 \sim \frac{-ik_s \sin \gamma_s^{(n,q)} \sin \phi^{(n,q)}}{2\pi \sqrt{(\eta - ib_s)(\eta - ib'_s)}} \exp(ik_s Q_s) \quad (49b)$$

$$B_3 \sim \frac{ik_s \sin \gamma_s^{(n,q)} \cos \phi^{(n,q)}}{2\pi \sqrt{(\eta - ib_s)(\eta - ib'_s)}} \exp(ik_s Q_s), \quad (49c)$$

where

$$Q_{p,s} = \eta \left[1 - \frac{1}{2} (\bar{\epsilon}_{p,s}^2 \sin^2 \theta + \bar{\epsilon}'_{p,s} \cos^2 \theta) \right] \\ + \rho^2 \left(\frac{\cos^2 \theta}{\eta - ib'_{p,s}} + \frac{\sin^2 \theta}{\eta - ib_{p,s}} \right) + \frac{ib_{p,s} \rho^2}{2} \\ \times \left(\frac{\cos^2 \theta \cos^2 \gamma_p^{(n,q)}}{(\eta - ib'_{p,s})^2} + \frac{\sin^2 \theta}{(\eta - ib_{p,s})^2} \right). \quad (50)$$

When $\gamma_p^{(n,q)}$ is small so that $\cos^2 \gamma_p^{(n,q)} \approx 1$ and $b'_{p,s} \approx b_{p,s}$, the approximate values of the beam integrals can be written as

$$B_1 \sim \frac{ik_p \cos \gamma_p^{(n,q)}}{2\pi(\eta - ib_p)} \exp \left[ik_p \left(\eta + \frac{(\eta + ib_p) \rho^2}{2(\eta^2 + b_p^2)} \right) \right], \quad (51a)$$

$$B_2 \sim \frac{-ik_s \sin \gamma_s^{(n,q)} \sin \phi^{(n,q)}}{2\pi(\eta - ib_s)} \\ \times \exp \left[ik_s \left(\eta + \frac{(\eta + ib_s) \rho^2}{2(\eta^2 + b_s^2)} \right) \right], \quad (51b)$$

$$B_3 \sim \frac{ik_s \sin \gamma_s^{(n,q)} \cos \phi^{(n,q)}}{2\pi(\eta - ib_s)} \exp \left[ik_s \left(\eta + \frac{(\eta + ib_s) \rho^2}{2(\eta^2 + b_s^2)} \right) \right]. \quad (51c)$$

D. Complex source representation

We now investigate whether the complex source point (CSP) method can here provide a useful alternative to approximating the beam integrals in the paraxial region. Assigning complex values $\bar{\xi}' = 0$, $\bar{\zeta}' = 0$, $\bar{\eta}' = ib_{p,s}$ to the source coordinates leads to the three-dimensional free-space Green's function

$$g_{p,s}(x, y, z) = \exp(ik_{p,s} \bar{r}) / \bar{r}, \quad (52)$$

where the complex distance \bar{r} to the observer is

$$\bar{r} = [\xi^2 + \zeta^2 + (\eta - ib_{p,s})^2]^{1/2} \\ = [\rho^2 + (\eta - ib_{p,s})^2]^{1/2}, \quad \text{Re}(\bar{r}) > 0. \quad (53)$$

The analytically continued function generates a beamlike field that is symmetric about, and propagates along, the η axis, satisfying the source free-wave equation with outgoing wave condition.¹⁰

1. Far zone approximation of complex source field

In the far zone, the complex distance can be expanded in terms of the small parameter $\epsilon_{p,s} = b_{p,s}/r$ in (38) as

$$\bar{r} = r(1 - i(b_{p,s}/r) \cos(\bar{\gamma} - \gamma_p^{(n,q)}) + \dots). \quad (54)$$

Consequently, the free-space complex Green's function field can be expressed as

$$g_{p,s} \sim (1/r) \exp(k_{p,s} b_{p,s}) \\ \times \exp[ik_{p,s} r [1 + i(b_{p,s}/r) \{1 - \cos(\bar{\gamma} - \gamma_p^{(n,q)})\}]] \quad (55)$$

and its derivatives as

$$\frac{\partial g_p}{\partial z} \sim \frac{ik_p}{r} \cos \bar{\gamma} \exp(k_p b_p) \\ \times \exp[ik_p r [1 + i(b_p/r) \{1 - \cos(\bar{\gamma} - \gamma_p^{(n,q)})\}]],$$

$$\frac{\partial g_s}{\partial y} \sim \frac{ik_s}{r} \sin \bar{\gamma} \sin \bar{\phi} \exp(k_s b_s) \quad (56)$$

$$\times \exp[ik_s r [1 + i(b_s/r)(1 - \cos(\bar{\gamma} - \gamma_s^{(n,q)}))]],$$

$$\frac{\partial g_s}{\partial x} \sim \frac{ik_s}{r} \sin \bar{\gamma} \cos \bar{\phi} \exp(k_s b_s)$$

$$\times \exp[ik_s r [1 + i(b_s/r)(1 - \cos(\bar{\gamma} - \gamma_s^{(n,q)}))]].$$

Comparing (56) with (44), we note that these far-field expressions are not equivalent. However, when the observer is in the paraxial zone of the beam axis such that $\bar{\phi} \approx \phi^{(n,q)}$ and $\bar{\gamma} \approx \gamma_s^{(n,q)}$, the amplitudes and phases of both expressions are equal. Thus, in the far paraxial zone, the beam integrals can be written in the terms of complex source field as

$$\{B_1, B_2, B_3\}$$

$$= \frac{1}{2\pi} \left\{ e^{-k_p b_p} \frac{\partial g_p}{\partial z}, -e^{-k_s b_s} \frac{\partial g_s}{\partial y}, e^{-k_s b_s} \frac{\partial g_s}{\partial z} \right\}, \quad (57)$$

where $b_{p,s}$ is defined in (46).

2. Paraxial approximation of complex source field

In the paraxial region ($|\bar{e}_{p,s}| = |\rho/(\eta - ib_{p,s})| \ll 1$), \bar{r} can be approximated by

$$\bar{r} \approx (\eta - ib_{p,s}) + \rho^2/2(\eta - ib_{p,s}). \quad (58)$$

Thus

$$g_{p,s} \sim \frac{\exp(k_{p,s} b_{p,s})}{(\eta - ib_{p,s})} \exp \left[ik_{p,s} \left(\eta + \frac{(\eta + ib_{p,s}) \rho^2}{2(\eta^2 + b_{p,s}^2)} \right) \right] \quad (59)$$

is of the form as given in (51). Substituting (59) into (57) and comparing with (51) confirms that both results agree for $\gamma_{p,s}^{(n,q)} \ll 1$.

In summary, the above formulations are valid under the following conditions: (a) $(\gamma_{p,s}^{(n,q)})^2 \ll 1$; (b) the observer is in the paraxial zone of the beam $\bar{\phi} \approx \phi^{(n,q)}$ and $\bar{\gamma} \approx \gamma_s^{(n,q)}$. Thus CSP field replacement of the three-dimensional beam integrals, which simplifies numerical computations substantially, is justified for narrow beams (where all tilted beams are evanescent in the far field) and for moderately tilted wide beams in the paraxial region. Subject to these restrictions, the potentials may be expressed as [see (20)]

$$\{\Phi, \Psi_x, \Psi_y\} = \frac{(2L_x L_y)^{1/2}}{4\pi\rho\omega^2} \sum \sum \sum \sum A_{mnpq}$$

$$\times \left\{ e^{-k_p b_p} \frac{\partial g_p}{\partial z}, e^{-k_s b_s} \frac{\partial g_s}{\partial y}, e^{-k_s b_s} \frac{\partial g_s}{\partial x} \right\} \quad (60)$$

and the displacements, via (20), as

$$u(x, y, z) = \frac{(2L_x L_y)^{1/2}}{4\pi\rho\omega^2} \sum A_{mnpq} \left(e^{-k_p b_p} \right)$$

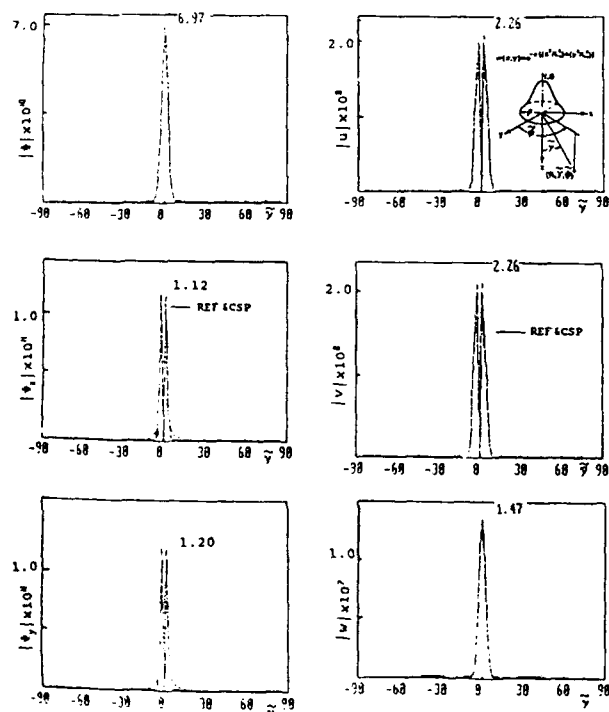


FIG. 4. Potential and displacement response in "far field" $R = 250\lambda_p$, to body force distribution defined by a single Gaussian basis function. Wide nontilted beam: $L_x = L_y = 10\lambda_p$, $n = q = 0$. Beam parameters (Fresnel lengths): $b_p = 100\lambda_p$, $b_s = 187\lambda_p$.

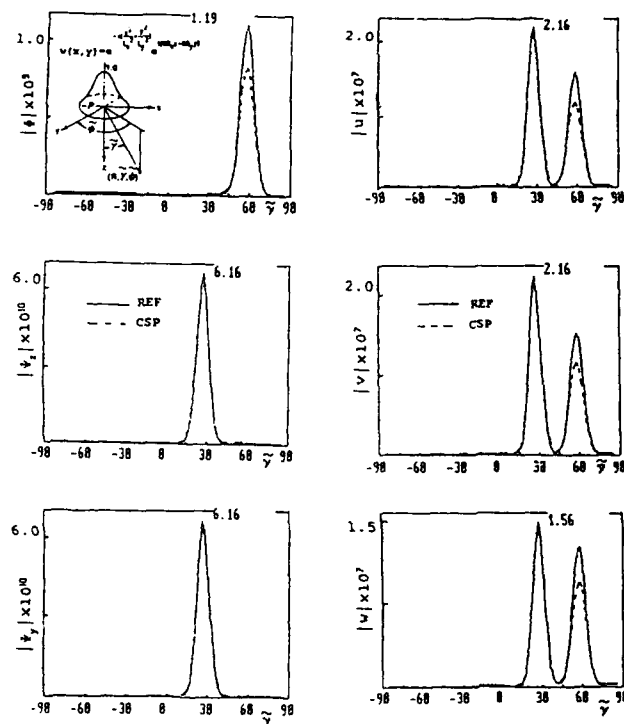


FIG. 5. Potential and displacement response in "far field" $R = 250\lambda_p$, along $\bar{\phi} = 45^\circ$, to body force distribution defined by a single Gaussian basis function. Wide tilted beam: $L_x = L_y = 10\lambda_p$, $n = q = 6$ (tilt angles: $\gamma_p^{(6,6)} = 59^\circ$, $\gamma_s^{(6,6)} = 28.8^\circ$, $\bar{\phi}^{(6,6)} = 45^\circ$). Beam parameters (Fresnel lengths): $b_p = 28\lambda_p$, $b_s = 79\lambda_p$.

$$\begin{aligned}
& \times \frac{\partial^2}{\partial z \partial x} (g_p) - e^{(-k_p b_p)} \frac{\partial^2}{\partial x \partial z} (g_s) \Big), \\
v(x,y,z) &= \frac{(2L_x L_y)^{1/2}}{4\pi\rho\omega^2} \sum A_{mnpq} \left(e^{(-k_p b_p)} \right. \\
& \times \frac{\partial^2}{\partial z \partial y} (g_p) - e^{(-k_p b_p)} \frac{\partial^2}{\partial y \partial z} (g_s) \Big), \quad (61) \\
w(x,y,z) &= \frac{(2L_x L_y)^{1/2}}{4\pi\rho\omega^2} \sum A_{mnpq} \left(e^{(-k_p b_p)} \right. \\
& \times \frac{\partial^2}{\partial z^2} (g_p) + e^{(-k_p b_p)} \frac{\partial^2}{\partial y^2} (g_s) \\
& \left. + e^{(-k_p b_p)} \frac{\partial^2}{\partial x^2} (g_s) \right).
\end{aligned}$$

The numerical calculations that follow are based on the expressions in (57), (60), and (61). Use of the CSP representation, when it applies, simplifies the numerically more cumbersome saddle point asymptotics. For the parameters selected in the computations, g_p , can be approximated by its far zone expression in (55). Although the validity of the CSP format in (60) and (61) has been established only for the paraxial region, it has been used for *all* observation angles away from each beam axis. A detailed discussion of the errors introduced by applying CSP outside the paraxial region follows.

IV. NUMERICAL RESULTS

Because of the numerical advantages associated with the CSP formulation discussed in Sec. III D, extensive nu-

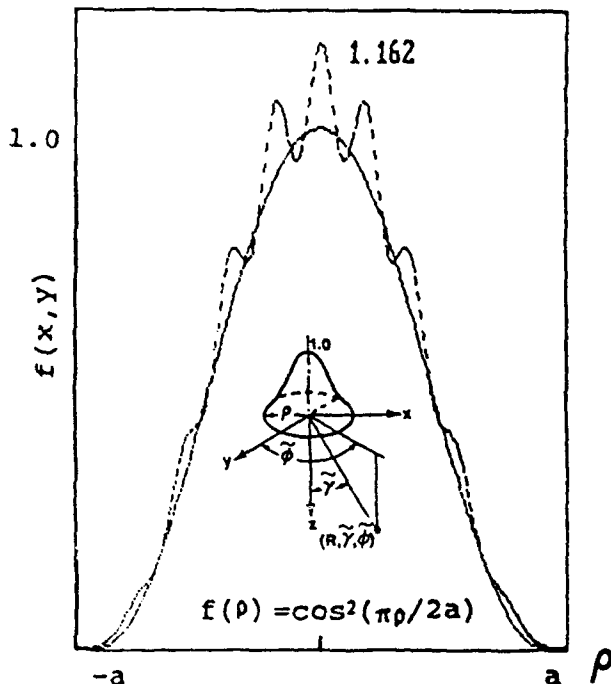


FIG. 6. Nonphased \cos^2 aperture field synthesis using 69 ($|m| = |p| < 5$, $n = q = 0$) narrow beams with $L_x = L_y = 0.5\lambda_p$, $2a = 5\lambda_p$.

merical tests have been conducted to assess the quality of this approximate treatment of the beam integrals in the Gabor lattice synthesis. In all cases, the reference data for comparison are established by direct numerical integration of the exact forms in (6) and (8).

A. Beam integral asymptotics versus CSP

Typical results of a study to determine the validity of the CSP representation are presented here for narrow and wide Gaussian beam aperture profiles. All results are plotted for observation points along a circular contour with radius R centered in the aperture. The radiation pattern obtained at $R = 5\lambda_p$ for a narrow nontilted Gaussian beam profile ($L_x = L_y = 0$) is shown in Fig. 3. CSP from (58) is seen to reproduce the reference solution (REF), obtained by direct numerical integration of (6) and (8), over the entire angular region for Φ , and within the narrow angular region $|\tilde{\gamma}_s| < 35^\circ$ for Ψ_x and Ψ_y ; agreement for the u and v displacement components is excellent over the entire angular region, while the w displacement is reproduced for $|\tilde{\gamma}_s| < 35^\circ$. The Fresnel length is of the order of a fraction of the wavelength, so that the far zone has already been reached at $R = 5\lambda_p$. Far-field ($R = 250\lambda_p$) results for wide nontilted and tilted beams ($L_x = L_y = 10\lambda_p$) are shown in Figs. 4 and 5. Note that for the nontilted beam, CSP reproduces the REF results over

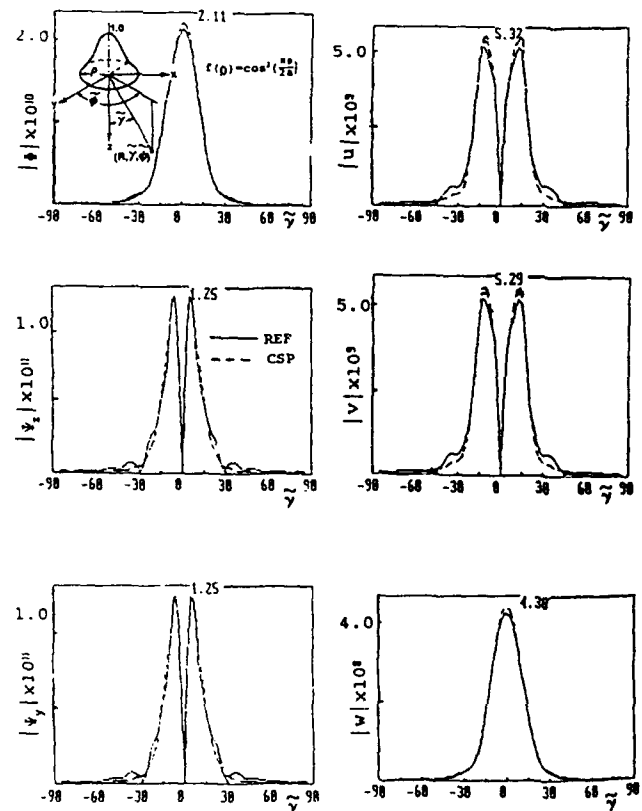


FIG. 7. Radiation patterns at $R = 10\lambda_p$ for nonphased \cos^2 aperture using 69 ($|m| = |p| < 5$, $n = q = 0$) narrow beam ($L_x = L_y = 0.5\lambda_p$) elements. Fresnel zone of aperture: $b_{ap} = 25\lambda_p$.

the narrow angular region within which the amplitudes are significant. For the tilted beam ($n = q = 6$), the angle of tilt of the P and S beams away from the normal to the aperture plane is $\gamma_p^{(6,6)} = 59^\circ$ and $\gamma_s^{(6,6)} = 28.8^\circ$, respectively, and the circumferential angle is $\phi^{(6,6)} = 45^\circ$. While CSP agreement is good for Ψ_x and Ψ_y , this is not the case for Φ , due to deviations in CSP for highly tilted beams.

B. Aperture and field synthesis

For illustration, the Gabor expansion is applied to two aperture profiles, which are analogs of those used for the two-dimensional problems discussed previously (Ref. 5). The aperture fields are axisymmetric and nonphased with (a) a smooth terminated profile, and (b) a uniform abruptly terminated profile:

$$f(\rho) = \begin{cases} \cos^2(\pi\rho/2a), & |\rho| < a, \text{ case (a),} \\ 1, & |\rho| < a, \text{ case (b),} \end{cases} \quad (62)$$

where $\rho = (x^2 + y^2)^{1/2}$, and $2a = 5\lambda_p$.

Narrow ($L_x = L_y = 0.2a$), wide ($L_x = L_y = 4a$), and matched ($L_x = L_y = 2a$) beams are used for aperture synthesis. For narrow beams, the Gabor coefficients are estimated from the aperture profile, while for the matched and wide beams they are calculated by numerical integration of (15). Results, which here are independent of the circumferential angle ϕ , are plotted for observation points along a circular contour of radius R centered in the aperture. The CSP paraxial representation [(59), (60), (61)] is compared with the reference solution obtained by direct numerical integration of (6) and (8). Due to the time-consuming evaluation of the exact Gabor coefficients on the PC, which was

used throughout, no numerical examples are presented here for phased aperture fields.

1. Smooth aperture profile

a. Narrow beam synthesis. For narrow beams ($L_x = L_y = 0.5\lambda_p = 0.2a$), the A_{m0p0} coefficients were determined by sampling the profile $[A_{m0p0} = (\sqrt{2}/L_x) \times f(mL_x, pL_y)]$, thereby avoiding the excessively time-consuming evaluation of the integral in (15). As was demonstrated in the two-dimensional problem, oscillations like those in Fig. 6 can be eliminated by including small but essential contributions from the tilted beams $|n|, |q| > 0$. The tilted beam fields are evanescent, however, and therefore negligible except in the very near zone. For the parameters used, the tilted beams can already be omitted at $R = 10\lambda_p$, which is in the "far zone" of each element. CSP synthesis with nontilted beams (Fig. 7) is seen to be adequate. Using all the beams contained within the aperture, good agreement with the reference solution is obtained for the main component of the displacement vector (w). The two other components, u and v , show discrepancies of about 4.5% in the mainlobe but these components are small compared to w .

b. Wide beam synthesis. For wide beam elements ($L_x = L_y = 10\lambda_p = 4a$), phase shifts with $|n|, |q| > 0$, are important but shifted locations with $|m|, |p| > 0$ are not (see Ref. 5). Both the aperture and near fields were synthesized using $|n| = |q| \leq 5$ beams (Figs. 8 and 9). Discrepancies in

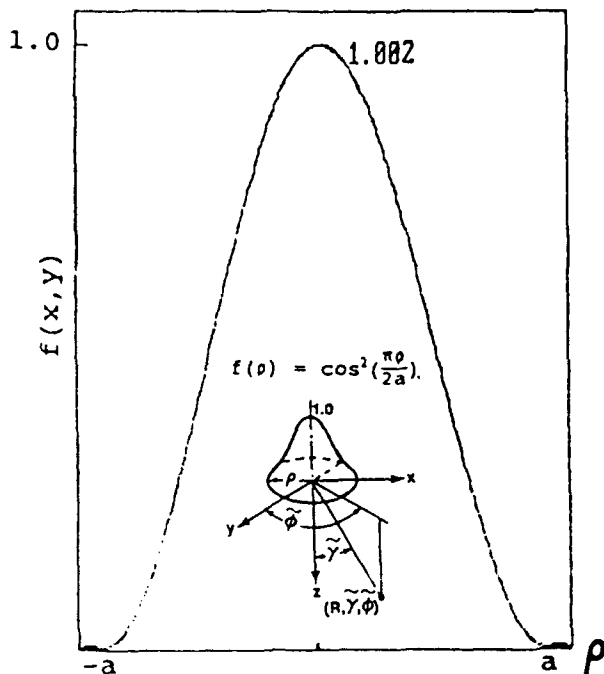


FIG. 8. Nonphased \cos^2 aperture field synthesis using 121 ($|m| = |p| = 0$, $|n| = |q| \leq 5$) wide beams with $L_x = L_y = 10\lambda_p$ elements. $2a = 5\lambda_p$.

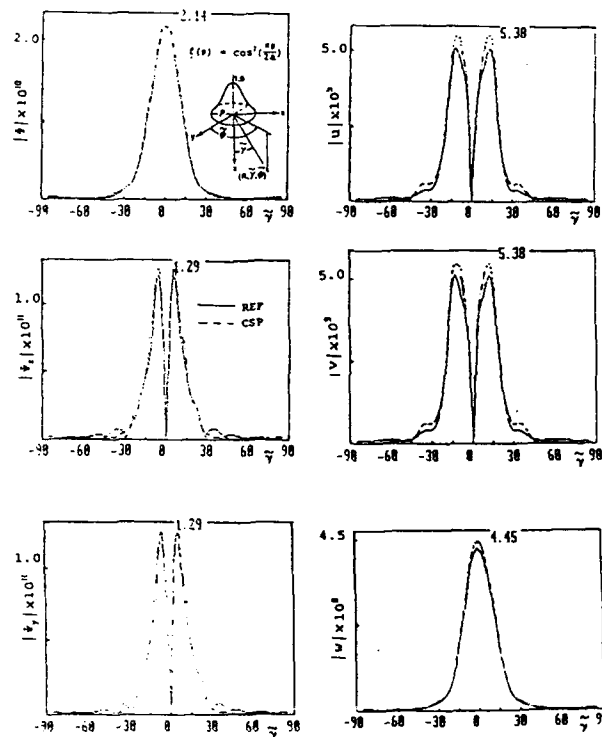


FIG. 9. Radiation patterns at $R = 10\lambda_p$ for nonphased \cos^2 aperture using 121 ($|m| = |p| = 0$, $|n| = |q| \leq 5$) wide beam ($L_x = L_y = 10\lambda_p$) elements. Fresnel zone of aperture: $b_{ap} = 25\lambda_p$.

the mainlobes are within 5% for the dominant w displacement and about 8% for the smaller u and v transverse displacements.

c. *Matched beam synthesis* ($L_x = L_y = 5\lambda_p = 2a$). For the smooth Gaussian-like profile chosen for illustration, only nine beams ($m = p = 0, |n| = |q| < 1$) were used to synthesize the aperture and radiated fields (Figs. 10 and 11). At $R = 10\lambda_p$, the observer is in the near field of each individual beam. Satisfactory (within 3%) synthesis of the mainlobes of the displacement fields is accomplished with only nine beams.

2. Abruptly terminated aperture profile

a. *Narrow beam synthesis*. As has been noted for the two-dimensional case, a much more severe test of the beam synthesis technique is posed by an abruptly truncated aperture profile as in case (b) of (62). The A_{m0p0} coefficients were estimated from the aperture profile. Convergence of the beam series to the aperture profile is slow, and many elements are needed to reduce the resulting oscillations (Fig. 12). Near zone synthesis using 49 beams (Fig. 13) is seen to be inadequate, and it is not until 81 beams are used (Fig. 14) that CSP synthesis is acceptable. Even for this case the smaller u and v displacements reveal significant errors.

b. *Wide beam synthesis*. Aperture synthesis (Fig. 15) using the same number of beams as for the smooth profile (Fig. 8) reveals that many more elements are required here. Comparison of the near-field results ($R = 10\lambda_p$) show (Fig. 16), however, that comparable accuracy is obtained by using

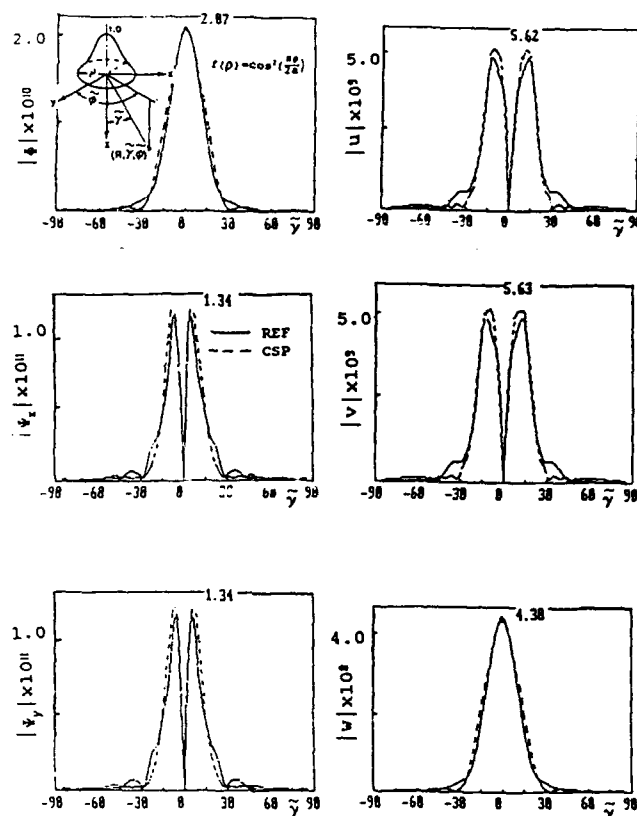


FIG. 11. Radiation patterns at $R = 10\lambda_p$ for nonphased \cos^2 aperture using 9 ($|m| = |p| = 0, |n| = |q| < 1$) matched beam ($L_x = L_y = 5\lambda_p$) elements. Fresnel zone of aperture: $b_{ap} = 25\lambda_p$.

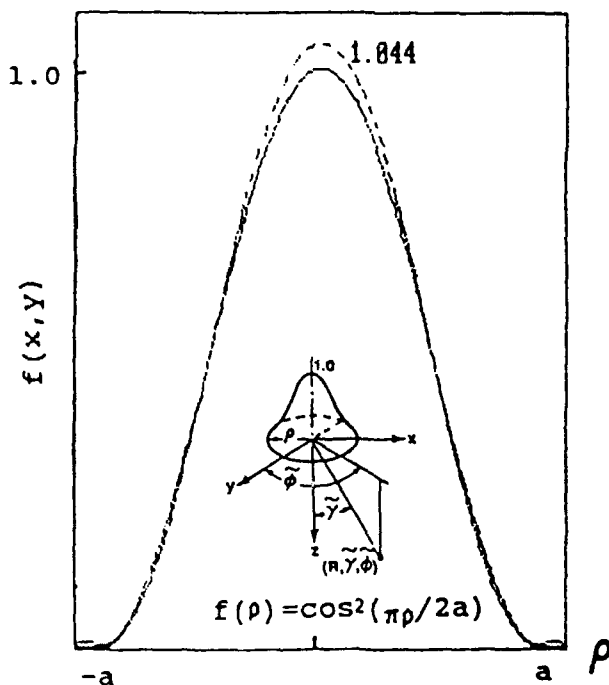


FIG. 10. Nonphased \cos^2 aperture field synthesis using 9 ($|m| = |p| = 0, |n| = |q| < 1$) matched beams with $L_x = L_y = 5\lambda_p, 2a = 5\lambda_p$.

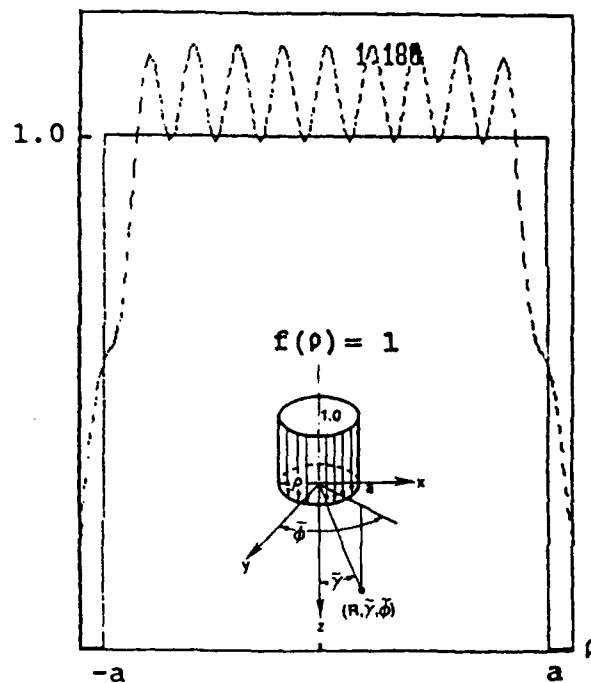


FIG. 12. Nonphased uniform aperture field synthesis using 81 ($|m| = |p| < 5, |n| = |q| = 0$) narrow beams with $L_x = L_y = 0.5\lambda_p, 2a = 5\lambda_p$.

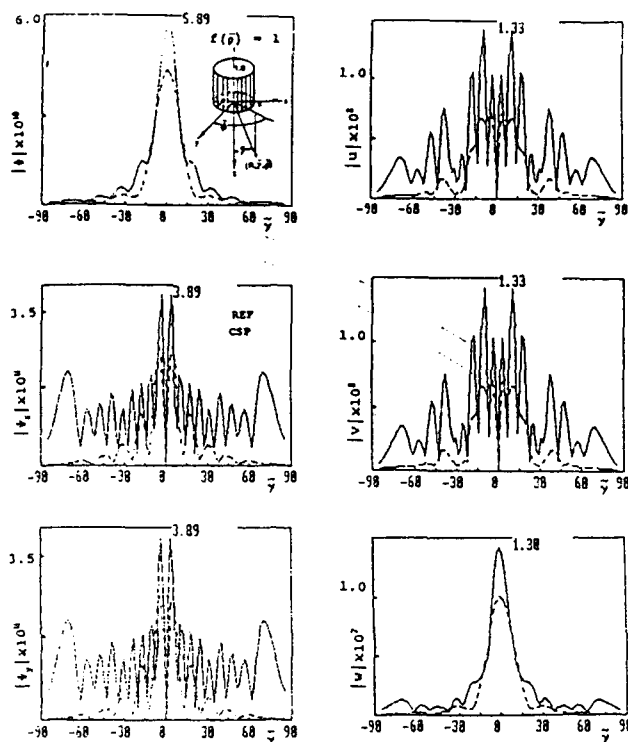


FIG. 13. Radiation patterns at $R = 10\lambda_p$ for nonphased uniform aperture using 49 ($|m| = |p| < 3$, $|n| = |q| = 0$) narrow beam ($L_x = L_y = 0.5\lambda_p$) elements. Fresnel zone of aperture: $b_{ap} = 25\lambda_p$.

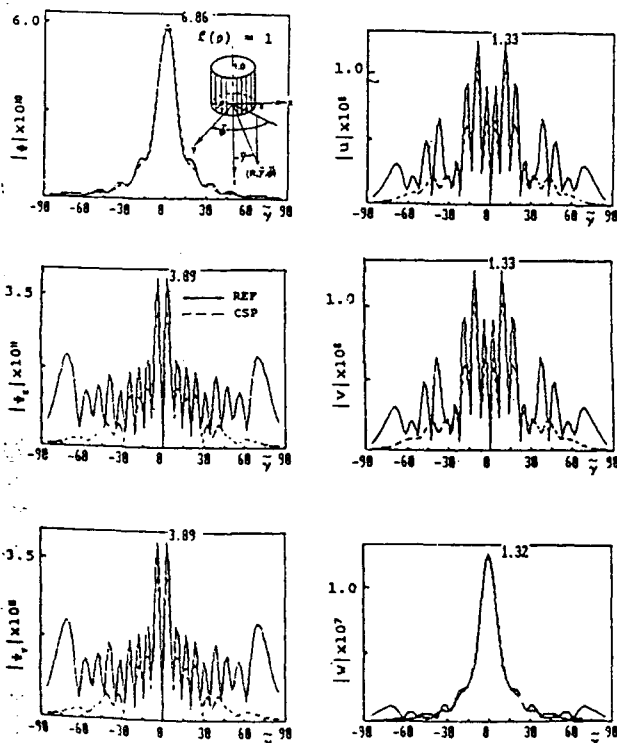


FIG. 14. Radiation patterns at $R = 10\lambda_p$ for nonphased uniform aperture using 81 ($|m| = |p| < 5$, $|n| = |q| = 0$) narrow beam ($L_x = L_y = 0.5\lambda_p$) elements. Fresnel zone of aperture: $b_{ap} = 25\lambda_p$.

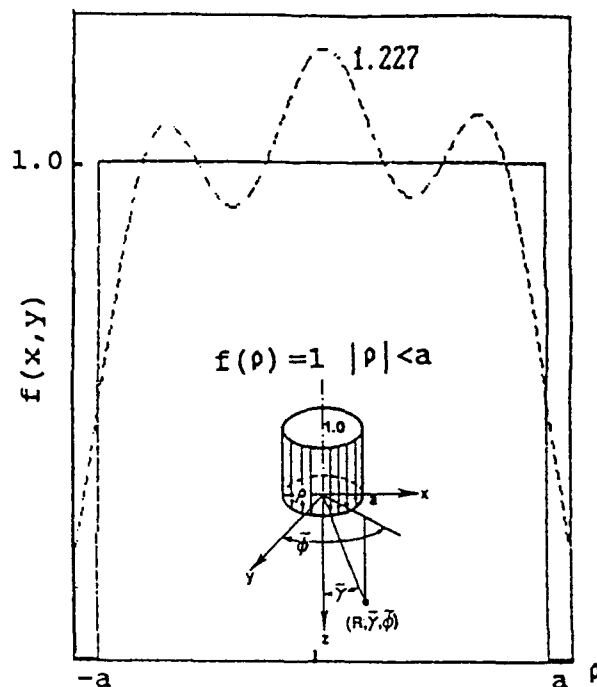


FIG. 15. Nonphased uniform aperture field synthesis using 121 ($|n| = |q| < 5$, $m = p = 0$) wide beams with $L_x = L_y = 10\lambda_p$, $2a = 5\lambda_p$.

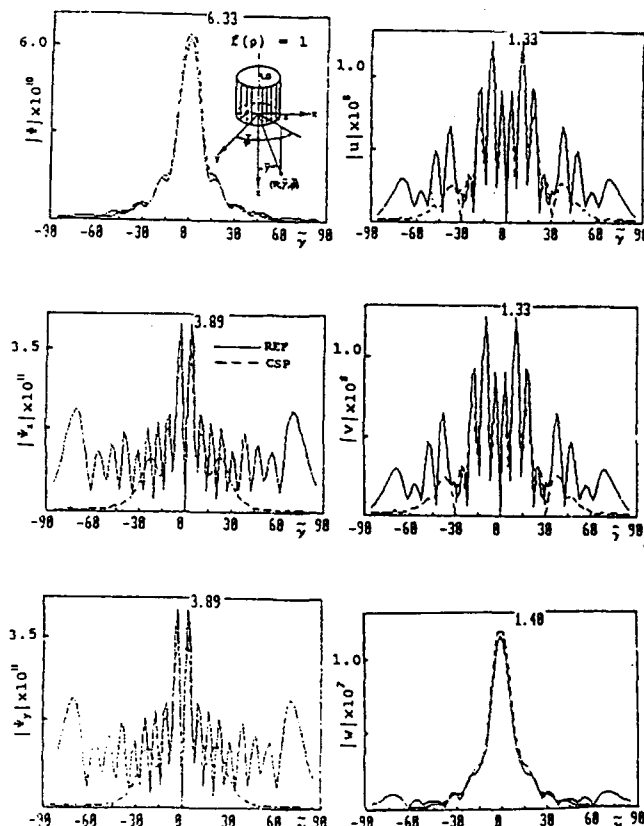


FIG. 16. Radiation patterns at $R = 10\lambda_p$ for nonphased uniform aperture using 121 ($|n| = |q| < 5$, $|m| = |p| = 0$) wide beam elements. Fresnel zone of aperture: $b_{ap} = 25\lambda_p$.

the same number of elements as for the smooth profile. Accurate synthesis of the rapid oscillations in the sidelobes, which are due to the abrupt termination of the aperture profile, would require the use of many tilted beams. However, as has been shown (Sec. III), the CSP tilted beams are not good approximations of the tilted beam integrals. Consequently, it is expected that the addition of the tilted beams will not repair the discrepancies.

V. CONCLUSIONS

A discrete superposition of linearly phased and non-phased Gaussian elements distributed self-consistently over a lattice in a configuration-spectral wave-number phase space, and the corresponding beam propagators, have been utilized for the representation of two-dimensional finite planar source distributions and the resulting three-dimensional radiated fields in an unbounded homogeneous elastic solid. Using two simple axisymmetric aperture profiles with smoothly tapered and abruptly truncated amplitudes, it has been shown how the choice of nontilted and tilted narrow, wide or matched beams with respect to the aperture size affects the field synthesis, and how well the asymptotic beam integrals can be approximated by the more convenient complex source point (CSP) fields. Due to the inaccuracies inherent in using CSP for highly tilted beams (such was not the case for the two-dimensional beams in Ref. 5), synthesis of the field away from the aperture might best be carried out with narrow beams since the tilted $|n| > 0$ beams are evanescent. These beams can be tracked along almost real trajectories because of the small complex displacement components of their source location, and this raylike behavior makes them interesting candidates for negotiating complicated environments at high frequencies.^{4,11} However, many beams are required for accurate field synthesis.

More numerical calculations need to be performed to assess the full potential of the beam summation method for prediction of three-dimensional fields radiated from more general source distributions; for example, those generated by practical transducers or induced on more realistic flaw profiles, and their subsequent interaction with elastic propagation environments. Broadly speaking, the present study has been comprehensive enough to provide guidelines for the potential use of the modeling schemes examined here. Concerning the *complex source point (CSP) method*, its advantages as a *rigorous* solution of the dynamical equations have been exploited systematically in a variety of applications for *single* Gaussian-beamlike inputs. These applications include beam-to-mode conversion in an elastic plate,¹² interaction with weak debonding in a layered plate,¹³ and nonspecular reflection of a beam incident from a fluid onto a plane or curved interface near the Rayleigh angle.¹⁴

For the decomposition of *arbitrary* source distributions into Gaussians, the most robust procedure, as noted above, involves narrow, but many beams. This decomposition is particularly effective when wide aperture inputs interact with relatively arbitrary interfaces, local inhomogeneities, etc. Here, the environmental variations may be appreciable over the Fresnel beamwidth, thereby invalidating direct

beam tracing, even in the paraxial approximation. By decomposing into narrow Gaussian basis beams, each of which has a very short Fresnel length and is already in its far zone when it encounters the environmental changes, *local* CSP ray tracing is validated and readily implemented for each basis beam. The *global* effect on the wide incident beam is established by recombining the individual basis beams. Because the Gabor decomposition is *rigorous*, the algorithm has the potential of producing *benchmarks* for wide-beam interaction with curved interfaces, irregularities, etc., which are "large" on the scale of the basis beams but have critical dimensions on the scale of the input beam. For plane aperture field transmission through curved fluid layers, this procedure has been implemented (within the context of electromagnetics) with remarkable success.¹⁰ Extension to fluid-solid interfaces and layers is presently being considered. Because many basis beams need to be considered, the algorithm is computation intensive but, we repeat, of potential accuracy not achievable with other methods employed at present. It may therefore serve to generate reference data for comparison with other, more efficient but approximate, techniques.

ACKNOWLEDGMENT

This work has been supported by the Air Force Office of Scientific Research under Grant No. AFOSR-86-0318.

APPENDIX A: REFERENCE SOLUTION

To synthesize the distributed body force $f(x, y)$ in terms of a scalar unit force excitation at $\mathbf{x}' = (x', y', z') = (x', y', 0)$, we proceed as follows. Green's displacement tensor defined by⁷

$$G_{ij}(x, \mathbf{x}') = \frac{1}{4\pi\rho\omega^2} \left(k_s^2 \delta_{ij} g_s - \frac{\partial}{\partial x_i} \frac{\partial}{\partial x_j} (g_p - g_s) \right), \quad i, j = x, y, \text{ or } z \quad (\text{A1})$$

represents the displacement vector component in the i th direction at point (x, y, z) due to a unit concentrated force in an unbounded medium applied in the j th direction at (x', y', z') . The scalar Green's function

$$g_{p,s} = \exp(ik_{p,s}r)/r, \quad r = \sqrt{(x - x')^2 + (y - y')^2 + (z - z')^2} \quad (\text{A2})$$

satisfies the wave equation

$$(\nabla^2 + k_{p,s}^2)g_{p,s}(x, \mathbf{x}') = -4\pi\delta(\mathbf{x} - \mathbf{x}'). \quad (\text{A3})$$

Upon equating the displacements in the horizontal and vertical directions as given in (4) and (A1), and appealing to (A2), we have

$$\begin{aligned} u &= \frac{\partial\Phi}{\partial x} + \frac{\partial\Psi_z}{\partial y} - \frac{\partial\Psi_y}{\partial z} = -\frac{1}{4\pi\rho\omega^2} \frac{\partial}{\partial x} \frac{\partial}{\partial z} (g_p - g_s), \\ v &= \frac{\partial\Phi}{\partial y} - \frac{\partial\Psi_z}{\partial x} + \frac{\partial\Psi_x}{\partial z} = -\frac{1}{4\pi\rho\omega^2} \frac{\partial}{\partial y} \frac{\partial}{\partial z} (g_p - g_s), \end{aligned} \quad (\text{A4})$$

$$w = \frac{\partial \Phi}{\partial z} + \frac{\partial \Psi_y}{\partial x} - \frac{\partial \Psi_x}{\partial y}$$

$$= -\frac{1}{4\pi\rho\omega^2} \left(\frac{\partial^2}{\partial x^2} g_s + \frac{\partial^2}{\partial y^2} g_s + \frac{\partial^2}{\partial z^2} g_p \right).$$

Thus the potentials for a unit concentrated z -directed body force are

$$\Phi = -\frac{1}{4\pi\rho\omega^2} \frac{\partial g_p}{\partial z}, \quad \Psi_x = \frac{1}{4\pi\rho\omega^2} \frac{\partial g_s}{\partial y},$$

$$\Psi_y = -\frac{1}{4\pi\rho\omega^2} \frac{\partial g_s}{\partial x}, \quad \Psi_z = 0, \quad (A5)$$

and the potentials for the distributed source $f(x,y)$ are given by

$$\Phi(x,y,z) = -\frac{1}{4\pi\rho\omega^2} \iint f(x',y') \frac{\partial g_p}{\partial z} dx' dy',$$

$$\Psi_x(x,y,z) = \frac{1}{4\pi\rho\omega^2} \iint f(x',y') \frac{\partial g_s}{\partial y} dx' dy', \quad (A6)$$

$$\Psi_y(x,y,z) = -\frac{1}{4\pi\rho\omega^2} \iint f(x',y') \frac{\partial g_s}{\partial x} dx' dy'.$$

APPENDIX B: BODY FORCE POTENTIALS

An infinite elastic isotropic medium characterized by Lamé constants λ and μ and by density ρ is assumed to be excited by a z -independent time harmonic pressure or body force distribution $\tilde{f}(x,y,z,t) = f(x,y)e^{-i\omega t}$ acting on a constant $z = 0$ surface as shown in Fig. 1. The body force problem can be reformulated as the following boundary-value problem⁶

$$\sigma_{zz}(x,y,0^+) = \begin{cases} -f(x,y) & \text{for } -a \leq x \leq a, \quad -b \leq y \leq b, \\ 0.0 & \text{for } |x| > a, \quad |y| > b, \end{cases}$$

$$u(x,y,0) = 0, \quad v(x,y,0) = 0, \quad (B1)$$

where σ_{zz} is the normal stress while u and v are horizontal displacements. Using the Helmholtz vector decomposition, the displacement vector is expressed as

$$\mathbf{u} = \nabla\Phi + \nabla \times \Psi, \quad \nabla \cdot \Psi = 0, \quad (B2)$$

where Φ and $\Psi = (\Psi_x, \Psi_y, \Psi_z)$ are scalar and vector elastic potentials, respectively. Upon introducing the above into the elastodynamic displacement equations, we obtain the wave equations, for the potentials

$$(\nabla^2 + k_p^2)\Phi(\mathbf{x}, \mathbf{x}', \omega) = 0, \quad (B3)$$

$$(\nabla^2 + k_s^2)\Psi_i(\mathbf{x}, \mathbf{x}', \omega) = 0, \quad i = x, y, z,$$

where $\mathbf{x} \equiv \mathbf{x}(x,y,z)$ and $\mathbf{x}' \equiv (x',y',z')$ denote the field and source points, respectively. In terms of these potentials, the displacements u, v in the horizontal direction and w in the vertical direction are

$$u = \frac{\partial \Phi}{\partial x} + \frac{\partial \Psi_z}{\partial y} - \frac{\partial \Psi_y}{\partial z},$$

$$v = \frac{\partial \Phi}{\partial y} - \frac{\partial \Psi_x}{\partial x} + \frac{\partial \Psi_x}{\partial z}, \quad (B4)$$

$$w = \frac{\partial \Phi}{\partial z} + \frac{\partial \Psi_y}{\partial x} - \frac{\partial \Psi_x}{\partial y},$$

whereas the normal stress is

$$\sigma_{zz}(x,y,z) = \lambda \nabla^2 \Phi + 2\mu \left(\frac{\partial^2 \Phi}{\partial z^2} + \frac{\partial^2 \Psi_y}{\partial x \partial z} - \frac{\partial^2 \Psi_x}{\partial y \partial z} \right). \quad (B5)$$

In the spectral domain, the reduced wave equations are given by

$$\left(\frac{\partial^2}{\partial z^2} + \kappa_p^2 \right) \hat{\Phi}(k_x, k_y, z, \omega) = 0,$$

$$\left(\frac{\partial^2}{\partial z^2} + \kappa_s^2 \right) \hat{\Psi}_i(k_x, k_y, z, \omega) = 0, \quad i = x, y, z, \quad (B6)$$

where

$$\kappa_{p,s} = \sqrt{k_{p,s}^2 - k_x^2 - k_y^2}, \quad \text{Im}(\kappa_{p,s}) \geq 0. \quad (B7)$$

The displacement spectra become

$$\hat{u}(k_x, k_y, z) = ik_x \hat{\Phi} + ik_y \hat{\Psi}_z - \frac{\partial \hat{\Psi}_y}{\partial z},$$

$$\hat{v}(k_x, k_y, z) = ik_y \hat{\Phi} - ik_x \hat{\Psi}_z + \frac{\partial \hat{\Psi}_x}{\partial z}, \quad (B8)$$

$$\hat{w}(k_x, k_y, z) = \frac{\partial \hat{\Phi}}{\partial z} + ik_x \hat{\Psi}_y - ik_y \hat{\Psi}_x,$$

and the normal stress spectrum,

$$\hat{\sigma}_{zz}(k_x, k_y, z) = \lambda \left[-k_x^2 - k_y^2 - \kappa_p^2 \right] \hat{\Phi}$$

$$+ 2\mu \left(-\kappa_p^2 \hat{\Phi} + ik_x \frac{\partial \hat{\Psi}_y}{\partial z} - ik_y \frac{\partial \hat{\Psi}_x}{\partial z} \right) \quad (B9a)$$

or

$$\hat{\sigma}_{zz}(k_x, k_y, z)/\rho = -v_p^2 k_p^2 \hat{\Phi} + 2v_s^2 [k_x^2 + k_y^2] \hat{\Phi}$$

$$+ 2v_s^2 \left(ik_x \frac{\partial \hat{\Psi}_y}{\partial z} - ik_y \frac{\partial \hat{\Psi}_x}{\partial z} \right). \quad (B9b)$$

For waves propagating in the positive z direction,

$$\hat{\Phi} = Ae^{i\kappa_p z}, \quad \hat{\Psi}_x = Be^{i\kappa_s z},$$

$$\hat{\Psi}_y = Ce^{i\kappa_s z}, \quad \hat{\Psi}_z = De^{i\kappa_s z}, \quad (B10)$$

which, when substituted into (B8) and (B9a) and evaluated at $z = 0$, results in

$$\hat{u}(k_x, k_y, 0) = (ik_x)A + (ik_y)D - (i\kappa_s)C,$$

$$\hat{v}(k_x, k_y, 0) = (ik_y)A - (ik_x)D + (i\kappa_s)B,$$

$$\hat{w}(k_x, k_y, 0) = (i\kappa_p)A + (ik_x)C - (ik_y)B, \quad (B11)$$

and

$$\hat{\sigma}_{zz}(k_x, k_y, 0)/\rho = -\omega^2 A + 2v_s^2 (k_x^2 + k_y^2) A$$

$$- 2v_s^2 (k_x \kappa_s C - k_y \kappa_s B). \quad (B12)$$

Matching the transformed boundary conditions

$$\hat{\sigma}_{zz}(k_x, k_y, 0) = -\hat{f}(k_x, k_y)/2,$$

(B13)

$$\hat{u}(k_x, k_y, 0) = 0, \quad \hat{v}(k_x, k_y, 0) = 0$$

to (B11) and (B12), results in the following

$$A = \frac{\hat{f}(k_x, k_y)}{2\rho\omega^2}, \quad B = -\frac{k_y\hat{f}(k_x, k_y)}{2\kappa_s\rho\omega^2},$$

$$C = \frac{k_x\hat{f}(k_x, k_y)}{2\kappa_s\rho\omega^2}, \quad (B14)$$

$$D = 0.$$

Thus, in the spectral domain,

$$\hat{\Phi}(k_x, k_y, z) = [\hat{f}(k_x, k_y)/2\rho\omega^2]e^{i\kappa_z z},$$

$$\hat{\Psi}_x(k_x, k_y, z) = -[\hat{f}(k_x, k_y)/2\rho\omega^2](k_y/\kappa_s)e^{i\kappa_z z},$$

$$\hat{\Psi}_y(k_x, k_y, z) = [\hat{f}(k_x, k_y)/2\rho\omega^2](k_x/\kappa_s)e^{i\kappa_z z},$$

$$\hat{\Psi}_z(k_x, k_y, z) = 0. \quad (B15)$$

¹ V. Cervený, M. M. Popov, and I. Psencik, "Computation of Wave Fields in Inhomogeneous Media-Gaussian Beam Approach," *Geophys. J. R. Astron. Soc.* 70, 109 (1982).

² B. P. Newberry, T. A. Gray, E. F. Lopes, and R. B. Thompson, "Evaluation of Ultrasonic Beam Models for the Case of a Piston Transducer Radiating through a Liquid-Solid Interface," in *Review of Progress in Quantitative NDE*, edited by D. O. Thompson and D. E. Chimenti (Plenum, New York), Vol. 11.

tative NDE, edited by D. O. Thompson and D. E. Chimenti (Plenum, New York, 1986), Vol. 5A, pp. 127-138.

³ J. J. Wen and M. A. Breazeale, "A Diffraction Beam Field Expressed as the Superposition of Gaussian Beams," *J. Acoust. Soc. Am.* 83, 1752 (1988).

⁴ J. J. Maciel and L. B. Felsen, "Systematic Study of Fields Due to Extended Apertures by Gaussian Beam Discretization," *IEEE Trans. Antennas Propag.* AP-37, 884 (1989).

⁵ L. B. Felsen, J. M. Klosner, I. T. Lu, and H. Grossfeld, "Source Field Modeling by Self-Consistent Gaussian Beam Superposition (Two-Dimensional)," *J. Acoust. Soc. Am.* 89, 63 (1991).

⁶ J. D. Achenbach, *Wave Propagation in Elastic Solids* (North-Holland, Amsterdam, 1973).

⁷ P. M. Morse and H. Feshbach, *Methods of Theoretical Physics* (McGraw-Hill, New York, 1953).

⁸ M. J. Bastiaans, "The Expansion of an Optical Signal into a Discrete Set of Gaussian Beams," *Optik* 57, 95 (1980).

⁹ L. B. Felsen and N. Marcuvitz, *Radiation and Scattering of Waves* (Prentice-Hall, Englewood Cliffs, NJ, 1973), Chap. 4.

¹⁰ L. B. Felsen, "Geometrical Theory of Diffraction, Evanescent Waves, Complex Rays and Gaussian Beams," *Geophys. J. R. Astron. Soc.* 79, 77 (1984).

¹¹ J. J. Maciel and L. B. Felsen, "Gaussian Beam Analysis of Propagation from an Extended Plane Aperture Distribution through Dielectric Layers. I—Plane Layer; II—Circular Cylindrical Layer," *IEEE Trans. Antennas Propag.* AP-38, 1607, 1618 (1990).

¹² I. T. Lu, L. B. Felsen, and J. M. Klosner, "Observables Due to Beam-to-Mode Conversion of High Frequency Gaussian P-wave Input in an Aluminum Plate in Vacuum," *J. Acoust. Soc. Am.* 87, 42 (1990).

¹³ I. T. Lu, L. B. Felsen, J. M. Klosner, and C. Gabay, "Beams and Modes for Scattering from Weak Bonding Flaws in a Layered Aluminum Plate," *J. Acoust. Soc. Am.* 88, 496 (1990).

¹⁴ S. Zeroug and L. B. Felsen "Non-Specular Reflection of Bounded Beams from Multilayer Fluid-Immersed Elastic Structures: Complex Ray Method Revisited," to be published in *Review of Progress in Quantitative NDE*, edited by D. O. Thompson and D. E. Chimenti (Plenum, New York), Vol. 11.

APPENDIX F

*Submitted to J. of Nondestructive Evaluation
March 1992*

NON-SPECULAR REFLECTION OF BEAMS FROM SUBMERGED ELASTIC STRUCTURES

Smaine Zeroug and Leopold B. Felsen
Department of Electrical Engineering / Weber Research Institute
Polytechnic University
Farmingdale, N.Y. 11735

ABSTRACT

Nonspecular reflection plays an important role in acoustic beam interaction with fluid-immersed elastic media. Such anomalous reflection is attributed to the strong interaction which occurs when the incident beam is phase-matched to one of the leaky waves supported by the structure. The properties of the incident beam as well as those of the interface geometry exert a marked influence on the observed nonspecular return. Previous investigations have been limited to rather special beam and interface conditions. The present study removes many of these limitations by allowing for arbitrarily collimated beams incident on plane and (cylindrically) curved layered geometries as well as simultaneous excitation of multiple leaky waves. By use of the complex source point (CSP) method for modeling quasi-Gaussian beams, the reflection problems are solved rigorously by wavenumber spectral decomposition. They are then reduced by asymptotic techniques to yield physically meaningful wavefield contributions, which explain the phenomenology and also allow efficient computation. The accuracy of the CSP asymptotic algorithms, and that of more restrictive conventional algorithms, is assessed by comparison with purely numerically generated reference data. The results establish the accuracy and versatility of the CSP strategy for a broad range of beam-interface conditions. While the present study is for two-dimensional problems, the method has also been extended to the three dimensional case.

I. INTRODUCTION AND SUMMARY

The excitation of various types of leaky waves in layered elastic media by beams incident from an exterior fluid at or near the leaky wave phase-matching angle is of interest for NDE applications. In particular, much attention has been given to the non-specular reflection of beams under such conditions of incidence. While various methods have been employed to study and clarify these phenomena for well collimated beams in plane layered environments [1-21], much less has been done on the corresponding effects when the incident beams are diverging and/or when the layers are curved. To extend the plane layer results to more general conditions, it is desirable to employ analytic modeling that adapts the wave phenomenology locally from planar to curved geometries. Because the phenomena occur in the range of high frequencies, ray field modeling affords an attractive option. By the complex-source-point (CSP) technique, which places a radiating source at a complex coordinate location, a conventional line or point source excited field can be converted into a two- or three-dimensional quasi-Gaussian beam field that is an exact solution of the dynamical equations [22-25]. When the CSP field interacts with a plane or cylindrically layered elastic medium, the resulting internal and external fields can be expressed rigorously in terms of wavenumber spectral integrals [26]. Asymptotic reduction of these integrals, achieved by the method of saddle points applied to deformed contours in the complex spectral wavenumber plane, accounts for all relevant wave phenomena. For the reflected field, this yields explicit waveforms which are synthesized by interacting specularly reflected beam, leaky wave, and possible lateral wave contributions.

The solution strategy outlined above offers a systematic approach to analyzing beam interaction with fluid-immersed layered elastic media, especially the anomalous nonspecular reflection that occurs when the incident beam couples strongly -- by phase matching -- to a leaky wave supported by the structure. Previous studies of this effect have been concerned primarily with well collimated Gaussian and plane layered configurations. Here, we broaden these studies to arbitrary incident beams, well or poorly collimated, and to curved layer geometries. In addition, simultaneous phase matching to multiple leaky waves is accounted for. This reveals a substantially enriched range of nonspecular phenomena which can be explained by the various (reflected-wave)-(leaky wave) interactions pertaining to the generalized conditions. Moreover, the CSP generated quasi-Gaussian beams remain valid for arbitrary incidence angles and degrees of collimation, whereas the customary spectral decomposition for oblique

incidence, based on projected linearly phased Gaussians, is valid only for moderate departures from normal incidence. These issues are critically explored here, both with respect to modeling of the incident beam field and to its interaction with plane or cylindrically layered elastic media. The various problems are formulated and solved rigorously, and thereafter evaluated asymptotically for extracting their physical content as well as simplifying the generation of numerical data. Selected numerical results, by comparison with numerically generated reference data, demonstrate the accuracy of the physically based asymptotic algorithms. It may be concluded from this study that the present application of the CSP technique offers a versatile tool for modeling Gaussian beam interaction with general layered elastic environments. While only two-dimensional problems are treated here, extension to three-dimensional beams has been carried out as well and will be reported in the future.

II. EXCITATION OF GAUSSIAN BEAMS (GB)

In this section, we discuss two methods for modeling excitation and propagation of a two-dimensional Gaussian beam (GB) inside an unbounded fluid medium. In the first method, excitation is from a line source at a complex coordinate location, which converts the cylindrical wave field due to a line source at a real coordinate location into a beam-type field. In the second method, excitation is from an aperture with a linearly phased Gaussian profile.

A. Complex-Source-Point (CSP) Beam

By this approach, one finds first the wave field radiated by a line source located at a real source point ($\underline{\rho}'$), and then analytically continues the solution by displacing the source point into the complex coordinate plane. Let $\Phi(\underline{\rho}; \underline{\rho}')$ be the potential in the fluid emanating from the "real" line source, satisfying the wave equation

$$(\nabla^2 + k_f^2)\Phi(\underline{\rho}; \underline{\rho}') = -\delta(\underline{\rho} - \underline{\rho}'), \quad k_f = \omega/v_f. \quad (1)$$

Here, ω is the angular frequency, and v_f is the sound speed in the fluid. A time dependence $\exp(-i\omega t)$ is suppressed. The pressure field \mathcal{P} in the fluid can be derived from the potential Φ by the relation

$$\mathcal{R}(\underline{\rho}; \underline{\rho}') = C_f \nabla^2 \Phi(\underline{\rho}; \underline{\rho}') = -\rho_f \omega^2 \Phi(\underline{\rho}; \underline{\rho}'), \quad \text{for } \underline{\rho} \neq \underline{\rho}' \quad (2)$$

The quantity C_f is the fluid compressibility, and ρ_f is the fluid density.

We seek spectral wavenumber decompositions of the line-source-generated field along a plane or cylindrical surface for subsequent application to interaction with plane or cylindrically layered geometries, respectively [26]. For the plane layered geometry, where $\underline{\rho} = (x, y)$ and layer interfaces lie on planes $y = \text{const.}$, the spectral decomposition is along x , and the spectral wavenumber is denoted by k ; for the cylindrically layered geometry, where $\underline{\rho} = (\rho, \phi)$ and the layer interfaces lie on surfaces $\rho = \text{const.}$, the spectral decomposition is along ϕ and the spectral wavenumber is v . Denoting spectral domain quantities with a caret, the spectral representations for the planar and cylindrical cases yield, respectively, [26]

$$\Phi_{\text{pl}}(x, y; x', y') = \frac{1}{2\pi} \int_{-\infty}^{+\infty} \hat{\Phi}_{\text{pl}}(k, y, y') \exp\{ik(x - x')\} dk \quad (3a)$$

$$\Phi_{\text{cyl}}(\rho, \rho'; \phi, \phi') = \frac{1}{2\pi} \int_{-\infty}^{+\infty} \hat{\Phi}_{\text{cyl}}(v, \rho, \rho') \exp\{iv(\phi - \phi')\} dv \quad (3b)$$

Note that k has the dimensions of length^{-1} while v is dimensionless. In (3b), the physical $-\pi \leq \phi \leq \pi$ azimuthal domain has been extended to a multisheeted infinite domain $-\infty < \phi < \infty$ in order to remove the 2π -periodicity constraint from the azimuthal wave spectra. This extension, with a radiation condition at $|\phi| \rightarrow \infty$, allows the inclusion of angularly traveling waves with arbitrary angular periodicity and makes the treatment in cylindrical coordinates analogous to that in rectangular coordinates [26-28]. The reduced wave equations for the planar and cylindrical spectra are solved to yield

$$\hat{\Phi}_{\text{pl}}(k, y, y') = \frac{i}{2\kappa_f} \exp\{i\kappa_f |y - y'|\} \quad (4a)$$

$$\hat{\Phi}_{\text{cyl}}(v; \rho, \rho') = \frac{i\pi}{4} H_v^{(2)}(k_f \rho_<) H_v^{(1)}(k_f \rho_>) \quad (4b)$$

with κ_f defined as

$$\kappa_f = \sqrt{k_f^2 - k^2}, \quad \text{Re}\{\kappa_f\} > 0 \text{ when } |k| < k_f, \quad \text{Im}\{\kappa_f\} > 0 \text{ when } |k| > k_f \quad (5)$$

In (4b), $\rho_<$ and $\rho_>$ denote the lesser and greater of ρ and ρ' , respectively.

Using (4a) in (3a) or (4b) in (3b), one obtains the spectral integral representing the incident cylindrical wave field corresponding to a line source at the real coordinates $\underline{\rho}'$. To convert this isotropic wave field into a directional or beam-type field, we perform the following substitution [22-25],

$$x' \rightarrow \tilde{x}' = x' + ib \sin \alpha_o, \quad y' \rightarrow \tilde{y}' = y' + ib \cos \alpha_o, \quad b \text{ real} > 0, \quad -\pi \leq \alpha_o \leq +\pi \quad (6a)$$

$$\rho' \rightarrow \tilde{\rho}' = \sqrt{\tilde{x}'^2 + \tilde{y}'^2}, \quad \text{Re}\{\tilde{\rho}'\} \geq 0; \quad \phi' \rightarrow \tilde{\phi}' = \tan^{-1} \left\{ \frac{\tilde{x}'}{\tilde{y}'} \right\} \text{ with } \tilde{\phi}' = \pi \text{ when } \tilde{x}' = 0 \quad (6b)$$

where the tilde \sim denotes complex quantities generated by the CSP substitutions in (6a) and (6b). The field radiated by this complex-coordinate source has a quasi-Gaussian profile which attains its maximum along the direction α_o (see Fig.1a). Its waist is centered at $\underline{\rho}'$, and its width w_o is specified by the real parameter b via $w_o = \sqrt{2b/k_f}$, which identifies b as the Fresnel length of the excited beam. The spectral integrals representing the incident beams now become

$$\bar{\Phi}_{\text{CSP}}|_{\text{pl}}(x, y) = \frac{i}{4\pi} \int_{-\infty}^{+\infty} [\kappa_f]^{-1} \exp[i\tilde{P}_{\text{pl}}(k)] dk, \quad \tilde{P}_{\text{pl}}(k) = k(x - \tilde{x}') + \kappa_f(y - \tilde{y}') \quad (7a)$$

$$\bar{\Phi}_{\text{CSP}}|_{\text{cyl}}(\rho, \phi) = \frac{i}{8} \int_{-\infty}^{+\infty} H_v^{(2)}(k_f \rho_<) H_v^{(1)}(k_f \rho_>) \exp[iv\{\phi - \tilde{\phi}'\}] dv \quad (7b)$$

Non-Specular Reflection of Beams

where $\rho_<$, $\rho_>$, and $[\phi - \bar{\phi}']$ are defined as follows

$$\begin{cases} \rho_> = \bar{\rho}' & \text{if } \text{Re}\{\bar{\rho}'\} > \rho \\ \rho_< = \bar{\rho}' & \text{if } \text{Re}\{\bar{\rho}'\} < \rho \end{cases}, \quad [\phi - \bar{\phi}'] = \begin{cases} \bar{\phi}' - \phi & \text{if } \text{Re}\{\bar{\phi}'\} \geq \phi \\ \phi - \bar{\phi}' & \text{if } \text{Re}\{\bar{\phi}'\} < \phi \end{cases} \quad (7c)$$

These integrals furnish the exact (reference) solution for the CSP beam. A radiation condition has been imposed in the beam integral in (7a) through the conditions on the propagation coefficient k_f in (5) that ensure bounded and outgoing fields away from the source plane. The integration path in (7a) and (7b) runs along the real axis with indentations around the branch point pair for the former integral, due to the square root in (5), specified as shown in Fig.2a. In observation domains located a few fluid wavelengths away from the source, the integrands in (7a) and (7b) vary rapidly along the real k and v axes, respectively. It is therefore appropriate to evaluate these integrals asymptotically by the saddle point method [26] applied in the complex k and v planes to the analytically continued integrands. To separate the highly oscillating phase from the quasi-constant amplitude in the integrand of (7b), the Hankel functions are approximated by their Debye asymptotic forms that are valid in the parametric regimes of interest here [26],

$$H_v^{(1,2)}(\tau) \sim \sqrt{2\pi\tau\sin\gamma} \exp\{\mp i\pi/4\} \exp\{\pm i\tau\sin\gamma \mp iv\gamma\} \quad (8)$$

where

$$\cos\gamma = v/\tau, \quad 0 < \text{Re}\gamma < \pi, \quad \arg\{\tau\} < \pi/2, \quad |v| < |\tau|, \quad |v - \tau| > O(|v|^{1/3}) \quad (8a)$$

Assuming

$$k_f \rho \gg 1, \quad k_f |\bar{\rho}'| \gg 1 \quad (9)$$

then

$$\bar{\Phi}_{\text{CSP}}|_{\text{Cyl}}(\rho, \phi) \approx \frac{i}{4\pi k_f \sqrt{\rho \bar{\rho}'}} \int_{-\infty}^{+\infty} \frac{\exp\{i\bar{P}_{\text{Cyl}}(v)\}}{\sqrt{\sin\gamma \sin\bar{\gamma}'}} dv \quad (10)$$

where

$$\tilde{P}_{\text{cyl}}(v) = k_f(\rho_> \sin \gamma_> - \rho_< \sin \gamma_<) - v(\gamma_> - \gamma_< - [\phi - \tilde{\phi}']) \quad (10a)$$

$$\gamma = \cos^{-1} v / k_f \rho, \quad \tilde{\gamma}' = \cos^{-1} v / k_f \tilde{\rho}' \quad (10b)$$

To apply the saddle point method, the original integration contour running along the real axis is deformed into the steepest descent path (SDP) (see Fig.2) that traverses the saddle point $\tilde{\zeta}_s$ of the phase $i\tilde{P}(\zeta)$. The first-order complex saddle point $\tilde{\zeta}_s = \tilde{k}_s$ or \tilde{v}_s is defined by

$$\left. \frac{d\tilde{P}(\zeta)}{d\zeta} \right|_{\tilde{\zeta}_s} = 0, \quad \text{with} \quad \left. \frac{d^2\tilde{P}(\zeta)}{d\zeta^2} \right|_{\tilde{\zeta}_s} \neq 0. \quad (11)$$

For the planar case, the saddle point condition can be solved explicitly to yield

$$\tilde{k}_s = k_f \sin(\tilde{\theta}_{\text{is}}), \quad \tilde{\theta}_{\text{is}} = \tan^{-1} \left\{ \frac{x - \tilde{x}'}{y - \tilde{y}'} \right\} \quad (12a)$$

whereas for the cylindrical case, the condition remains implicit,

$$\cos^{-1} \left(\tilde{v}_s / k_f \rho_> \right) - \cos^{-1} \left(\tilde{v}_s / k_f \rho_< \right) = [\tilde{\phi}' - \phi] \quad (12b)$$

The SDP, along which the phase is constant, satisfies the requirement $\text{Re}\{\tilde{P}(\zeta)\} = \text{const.}$, where $\tilde{P}(\zeta)$ denotes either $\tilde{P}_{\text{pl}}(k)$ or $\tilde{P}_{\text{cyl}}(v)$. Since no spectral singularities are intercepted during the deformation from the original contour into the SDP, the SDP integral is well approximated by its saddle point contribution [26]

$$\tilde{\Phi}_{\text{CSP}}|_{\text{pl}}(x,y) \sim \frac{i}{4\pi} \frac{1}{\sqrt{k_f^2 - \tilde{k}_s^2}} \sqrt{\frac{-2\pi}{i d^2 \tilde{P}(\tilde{k}_s) / d\tilde{k}_s^2}} \exp\{i \tilde{P}_{\text{pl}}(\tilde{k}_s)\} \quad (13a)$$

$$\tilde{\Phi}_{\text{CSP}}|_{\text{cyl}}(\rho, \phi) \sim \frac{i}{4\pi} \frac{1}{k_f \sqrt{\rho \tilde{\rho}' \sin \gamma \sin \tilde{\gamma}'}} \bigg|_{\tilde{v}_s} \sqrt{\frac{-2\pi}{i d^2 \tilde{P}_{\text{cyl}}(\tilde{v}_s)/d\tilde{v}^2}} \exp\{i \tilde{P}_{\text{cyl}}(\tilde{v}_s)\} \quad (13b)$$

In (13a) and (13b), the argument of the square roots preceding the exponential equals the argument of dk and dv on the SDP at \tilde{k}_s and \tilde{v}_s , respectively. The saddle point conditions (12a) and (12b) have the geometrical (ray) interpretations shown in Figs. 3a and 3b, which permits rewriting of the asymptotic expressions (13a) and (13b) in ray form. Accordingly, the CSP incident beam field, synthesized either via planar or cylindrical spectral decomposition, can be expressed as a complex ray field

$$\tilde{\Phi}_{\text{CSP}}(x, y) \sim \frac{\exp\{i\pi/4\} \exp\{ik_f \tilde{L}_t\}}{2\sqrt{2\pi}} \frac{1}{\sqrt{k_f \tilde{L}_t}}, \quad \tilde{L}_t = \sqrt{(x - \tilde{x}')^2 + (y - \tilde{y}')^2}, \quad \text{Re}\{\tilde{L}_t\} \geq 0 \quad (14)$$

It is to be noted that in the numerical implementation, (14) has to be normalized by multiplication by the constant term $\exp\{-k_f b\}$. Each complex ray, parametrized by the corresponding complex saddle point, originates at the CSP with a complex angle of departure that leads to the observation point after traversing the complex coordinate space. When the complex ray field interacts with boundaries, it does so with the complex extensions of these boundaries; reflection coefficients, for instance, are evaluated at complex angles or complex wavenumbers.

To show that (13a) or (14) defines a real-space Gaussian beam, we reduce these CSP expressions by approximations. First it is convenient to define beam-centered coordinates (ξ, η) , which are related to the global coordinates (x, y) through the rotation (see Fig. 1a)

$$\xi = (x - x') \sin \alpha_o + (y - y') \cos \alpha_o, \quad \eta = (x - x') \cos \alpha_o - (y - y') \sin \alpha_o. \quad (15)$$

The inclination angle α_o corresponds to the real saddle point value $\theta_{is} = \tan^{-1}[(x - x')/(y - y')]$ in (12a), which defines the real ray on which the complex phase in (13a) or (14) assumes its maximum magnitude. Transforming (7a) to the (ξ, η) coordinate frame, carrying out a

quadratic expansion of the resulting phase in both the k variable and the off-axis distance η about their real on-axis values $k_s^{(o)} = k_f \sin \alpha_o$, $\eta=0$, and solving (11) for the resulting approximate saddle point yields [29],

$$\bar{k}_s \approx k_f \sin \alpha_o + k_f \cos \alpha_o \frac{\eta}{(\xi - ib)}, \quad |\eta| \ll \sqrt{\xi^2 + b^2} \quad (16)$$

The restriction in (16) defines the paraxial regime wherein the approximations apply. Substituting (16) into (13a), one finds for the paraxial beam field (normalized by omitting the constant term $\exp\{k_f b\}$ in (13a))

$$\tilde{\Phi}_{\text{CSP}}(x, y) \sim \frac{\exp(i\pi/4)}{2\sqrt{2\pi}} \frac{\exp\{ik_f(\xi + \eta^2/2R_{\text{CSP}}(\xi)) - \eta^2/w_{\text{CSP}}^2(\xi)\}}{\sqrt{k_f(\xi - ib)}} \quad (17)$$

where $w_{\text{CSP}}(\xi)$ and $R_{\text{CSP}}(\xi)$ are the beam width and the on-axis radius of curvature of the beam wavefront at ξ ,

$$R_{\text{CSP}}(\xi) = [\xi + b^2/\xi], \quad w_{\text{CSP}}(\xi) = w_o(1 + \xi^2/b^2)^{1/2} \quad (18)$$

The beam Fresnel length b and its $1/e$ width w_o at the waist are defined in the paragraph following (6b). These expressions agree with the conventionally used formulas for paraxial Gaussian beams [30,31].

B. Linearly Phased Gaussian (LPG) Aperture

The conventional alternative to the CSP formulation for the excitation of Gaussian beams in Sec.IIA is a real spectral decomposition applied to an aperture with an assumed linearly phased illumination tapered by a Gaussian amplitude profile. As noted in connection with (3a) and (3b), the choice of the "aperture plane" is conditioned by subsequent interaction of the beam with a plane or cylindrically stratified medium. For the former, the aperture is confined to a $y=\text{const.}$ plane, whereas for the latter, the aperture conforms to a cylindrical $\rho=\text{const.}$ surface. The assumed linear phasing steers

the beam away from the directions normal to the aperture surfaces, but at the expense of asymmetries about strongly inclined beam axes.

The spectral formulations adhere to the formats for the real-coordinate line source excitation in (3a) and (3b), with the same propagators as in (4a) and (4b) but different spectral amplitudes. For aperture profiles specified by

$$A_{pl}(x, y = y') = \frac{\exp\{-(x - x')^2 / w_x^2\} \exp\{i k_f \sin \alpha_o (x - x')\}}{\sqrt{\pi} w_x}, \quad (19a)$$

$$A_{cy}(\phi, \rho = \rho') = \frac{\exp\{-(\phi - \phi')^2 / \Delta_o^2\} \exp\{i k_f \rho' \sin \beta_o (\phi - \phi')\}}{\sqrt{\pi} \Delta_o}, \quad (19b)$$

the respective spectral amplitudes are

$$\tilde{A}_{pl}(k, y, y') = i [2 \kappa_f]^{-1} \exp\{-w_x^2 (k - k_f \sin \alpha_o)^2 / 4\} \exp\{i \kappa_f (y - y')\}, \quad (20a)$$

$$\tilde{A}_{cy}(v; \rho, \rho') = \frac{i\pi}{4} \exp\{-(v - k_f \rho' \sin \beta_o)^2 \Delta_o^2 / 4\} H_v^{(2)}(k_f \rho_-) H_v^{(1)}(k_f \rho_+). \quad (20b)$$

For the planar geometry, k_f and κ_f are defined in (1) and (5), respectively, w_x is the 1/e width of the Gaussian amplitude profile at $y=y'$, with waist centered at $x=x'$, and α_o is the angle along which the beam is steered (see Fig. 1b); for the cylindrical geometry, the beam waist is located at (ρ', ϕ') , $\beta_o = \pi - \phi' + \alpha_o$ is the beam axis angle measured with respect to the source radius ρ' (see Fig. 1d), and Δ_o is the 1/e width of the Gaussian amplitude profile specified along an arc of radius ρ' . If the 1/e width of the (actual) Gaussian profile on the oblique η axis (see Fig. 1b) is given by w_o , then w_o and w_x are related by the first-order approximation

$$w_x = w_o / \cos \alpha_o, \quad w_o = \sqrt{2b/k_f} \quad (21)$$

The spectral integral in (3a), with (20a), can be expressed in closed form if the paraxial expression for κ_f is utilized [2]

$$\kappa_f = k_f \cos \alpha_o - \tan \alpha_o (k - k_f \sin \alpha_o) - [2k_f \cos^3 \alpha_o]^{-1} (k - k_f \sin \alpha_o)^2 \quad (22)$$

The resulting paraxial field can be put in the following form

$$\Phi_{\text{LPG}}(x, y) \approx \frac{i}{2\sqrt{\pi} k_f w_r(\xi)} \exp\{ik_f \xi - [\eta^2/w_r^2(\xi)]\}, \quad w_r(\xi) = w_o[1 + i(1 - \eta \tan \alpha_o/\xi)\xi/b]^{1/2} \quad (23)$$

where the beam-centered coordinates (ξ, η) are defined in (15).

The paraxial expression (23) has been widely used in the literature [2,3,8]. It is interesting to cast it in the following form that shall be useful for direct comparison with the CSP-generated paraxial beam,

$$\Phi_{\text{LPG}}(x, y) \approx \frac{\exp(i\pi/4)}{2\sqrt{2\pi}} \frac{\exp\{ik_f(\xi - \eta^2/2R_{\text{LPG}}(\xi)) - \eta^2/w_{\text{LPG}}^2(\xi)\}}{\sqrt{k_f(\xi - ib)}}. \quad (24)$$

The beam width $w_{\text{LPG}}(\xi)$ and the on-axis radius of curvature of the beam wavefront $R_{\text{LPG}}(\xi)$ at ξ are given by

$$R_{\text{LPG}}(\xi) = [\xi + \beta^2 b^2/\xi]/\beta, \quad w_{\text{LPG}}(\xi) = w_o(1 + \beta^2 \xi^2/b^2)^{1/2}; \quad \beta = (1 - \eta \tan \alpha_o/\xi) \quad (24a)$$

It should be noted that in going from (23) to (24), the factor $w_r(\xi)$ in the algebraic term before the exponential has been approximated by replacing the factor β defined in (24a) with unity. The direct numerical integration of the integral in (3a) with (20a) furnishes a reference solution against which the paraxial expression in (23) can be checked.

The corresponding expression for the cylindrical case can be derived from the asymptotically (via (8)) reduced spectral integrand in (3b) weighted by (20b). The result is not required later on and is therefore not included here.

C. Comparing CSP and LPG Beams

In the LPG procedure, wide beams ($w_x \gg \lambda_f$, $\lambda_f = 2\pi/k_f$) are essential to approximate a tilted GB by a projected linearly phased Gaussian. Narrow beams diffuse very quickly, and render the assumptions (for the oblique case) of plane-wave-like phase progression as well as symmetric amplitude profile in the projected aperture plane inadequate. Using the paraxial phase in (17), one can assess when plane-wave-like progression is adequate. The resulting condition

$$\frac{w_o}{\lambda_f \tan \alpha_o} \gg 1 \quad (25a)$$

depends on the tilt angle of the radiated beam. Furthermore, the conventional GB expressions in (17) and (18) agree with those in (24) and (24a) when the factor β defined in (24a) is close to unity. This occurs when

$$\eta \tan \alpha_o / \xi \ll 1 \quad (25a)$$

i.e. for weakly tilted beams, and in observation domains confined to the vicinity of the central axis. Thus, the closed form paraxial expressions in (23) or (24) are good approximations in the paraxial zone of a well collimated GB where the contour lines of constant magnitude (the phase paths associated with the beam field) are all essentially parallel to the beam axis. On the other hand, the asymptotic CSP beam in (14), without paraxial approximation, is capable of modeling a GB everywhere except in the near zone of the complex source where the asymptotics used in the derivation are invalid. The excluded region is confined to a few wavelengths away from the equivalent real-space source distribution in Fig.1a. The numerical results in Figs.4a and 4b serve to quantify various comparisons between wide-waisted and narrow-waisted LPG and CSP beams.

Anticipating the reflection problem in Sec.III, the (moderate) chosen incidence angle $\alpha_o = 30.593^\circ$ is phase matched to the leaky Rayleigh wave supported by an aluminum half space in water. The wide and narrow waisted beam parameters are $b=50$, $w_o=4.0$, and $b=5$, $w_o=1.26$, respectively, normalized with respect to the wavelength in the fluid. The profiles in Fig.4a show the magnitudes of the wide-waisted GB on the $y=0$ plane,

for beam waist locations offset to $(x',y')=(-19.56,-50)$ and $(-118.25,-200)$ which place the $y=0$ plane inside and outside the beam Fresnel zone b , respectively; both beam axes pass through the origin $x=y=0$. The curve with the largest magnitude in Fig.4a corresponds to the well collimated case inside the Fresnel zone. The LPG reference solution computed by numerical integration of (3a), with (20a), is shown as the solid curve, while its paraxial approximation, given by (23), yields the dashed curve. The dotted curve depicts both the reference and asymptotic CSP solutions computed from (7a), and (14), respectively; the results are essentially identical. Excellent agreement is noted between the reference and asymptotic solutions and also between the LPG and CSP solutions, although the profile outside the Fresnel zone is much broader than that inside the Fresnel zone. In the broader profile, there is a small discrepancy between the LPG reference solution and its paraxial approximation, which is magnified for the narrow-waisted strongly diverging beam in Fig.4b, also observed on the $y=0$ plane. The beam parameters here are $b=5$ ($w_0=1.26$), with $(x',y')=(-11.825,-20)$. Magnitude and phase for the LPG reference and paraxial solutions are shown by the solid and dashed curves, respectively; the reference and asymptotic CSP solutions, again being essentially identical, give rise to the dotted curve. There is now substantial disagreement between the LPG paraxial and reference solutions, thereby rendering the former inadequate.

III. REFLECTION OF GAUSSIAN BEAMS

A. CSP incident beams

The CSP spectral representations developed in Sec.II anticipate interaction of incident GB's with plane or cylindrically layered elastic structures. For evaluation of the field reflected from the outermost layer, the incident beam spectra in (4a) and (4b) must be augmented by reflected spectra whose amplitudes are given by spectral reflection coefficients $R_{pl}(k)$ and $R_{cyl}(v)$, respectively. These reflected spectra are propagated away from the interfaces into the fluid with "outgoing" propagators phase referenced to the outermost boundary in their respective coordinate systems. The resulting spectra are given by

$$\hat{\Phi}_{pl}(k, y, y') = \frac{i}{2\kappa_f} \left[\exp\{i\kappa_f(y - y')\} + R_{pl}(k) \exp\{-i\kappa_f(y + y')\} \right], \quad y \leq 0 \quad (26a)$$

$$\hat{\Phi}_{cyl}(v; \rho, \rho') = \frac{i\pi}{4} \left\{ H_v^{(2)}(k_f \rho_<) + R_{cyl}(v) \frac{H_v^{(2)}(k_f a)}{H_v^{(1)}(k_f a)} H_v^{(1)}(k_f \rho_<) \right\} H_v^{(1)}(k_f \rho_>), \quad \rho \geq a \quad (26b)$$

Insertion of (26a) and (26b) into (3a) and (3b), respectively, with subsequent extension into the complex domain via (6a) and (6b), synthesizes the total (incident plus reflected) CSP field in the presence of plane or cylindrical geometries. For the reflected CSP fields alone, one has (omitting the subscript CSP),

$$\tilde{\Phi}_{pl}^r(x, y) = \frac{i}{4\pi} \int_{-\infty}^{+\infty} R_{pl}(k) [\kappa_f]^{-1} \exp\{i\tilde{P}_{pl}(k)\} dk, \quad \tilde{P}_{pl}(k) = k(x - \tilde{x}') - \kappa_f(y + \tilde{y}') \quad (27a)$$

$$\tilde{\Phi}_{cyl}^r(\rho, \phi) = \frac{i}{8} \int_{-\infty}^{+\infty} R_{cyl}(v) \frac{H_v^{(2)}(k_f a)}{H_v^{(1)}(k_f a)} H_v^{(1)}(k_f \tilde{\rho}') H_v^{(1)}(k_f \rho) \exp\{iv[\phi - \tilde{\phi}']\} dv \quad (27b)$$

When evaluated numerically, the exact solutions in (27a) and (27b) furnish reference data for the reflected field in the fluid region. Asymptotic evaluation furnishes simpler explicit results with physical interpretation that highlights the relevant wave phenomena. Of special interest are GB's incident at the angle which phase matches to a leaky wave supported by the layer configuration. Leaky waves are manifested by poles k_p in the spectral reflection coefficients. In the phase matching regime, the pole lies near the saddle point of the k -integrand phase in (27a) or the phase of the asymptotically approximated v -integrand in (27b) (cf.(8)). The saddle point furnishes the reflected wave, and its proximity to a reflection coefficient pole implies strong (reflected wave)-(leaky wave) interaction. This requires uniform asymptotics as described, for example, in [26]. We first locate the saddle points $\tilde{\zeta}_s = \tilde{k}_s$ or \tilde{v}_s which are defined by (11) when applied to the phases

$$\tilde{P}_{pl}(k) = k(x - \tilde{x}') - \kappa_f(y + \tilde{y}') \quad (28a)$$

$$\tilde{P}_{\text{cyl}}(v) = k_f(\rho \sin \gamma + \tilde{\rho}' \sin \tilde{\gamma}' - 2a \sin \gamma_a) - v(\gamma + \tilde{\gamma}' - 2\gamma_a - [\phi - \tilde{\phi}']) \quad (28b)$$

in the reflected field integrals. The quantities γ and $\tilde{\gamma}'$ in (28b) are defined in (10b), whereas γ_a is given by

$$\gamma_a = \cos^{-1} v / k_f a \quad (28c)$$

As for the incident GB alone (cf. (12a) and (12c)), the reflected field saddle point is expressed explicitly for planar geometry but implicitly for cylindrical geometry,

$$\tilde{k}_s = k_f \sin(\tilde{\theta}_{rs}), \quad \tilde{\theta}_{rs} = \tan^{-1} \left\{ \frac{x - \tilde{x}'}{-(y + \tilde{y}')} \right\} \quad (29a)$$

$$\cos^{-1}(\tilde{v}_s / (k_f \rho)) + \cos^{-1}(\tilde{v}_s / (k_f \tilde{\rho}')) - 2\cos^{-1}(\tilde{v}_s / (k_f a)) = [\phi - \tilde{\phi}'] \quad (29b)$$

Deforming the original integration path into the SDP through the saddle point(s), due account being taken of intercepted spectral poles numbered $j=1$ to M , as well as poles near the saddle point(s), one obtains the following results

$$\begin{aligned} \tilde{\Phi}_{\text{pl}}^r(x, y) \sim & \frac{\exp(i\pi/4)}{2\sqrt{2\pi}} R_{\text{pl}}(\tilde{k}_s) \frac{\exp\{ik_f(\tilde{L}' + \tilde{L})\}}{\sqrt{k_f(\tilde{L}' + \tilde{L})}} \\ & - \frac{1}{2} \sum_{j=1}^M \frac{\text{Res}\{R_{\text{pl}}(k)\}_{k_{p_j}}}{k_f|_{k_{p_j}}} \exp\{i\tilde{P}_{\text{pl}}^r(k_{p_j})\} \left\{ -\frac{\exp\{-(-i\tilde{s}_{p_j})^2\}}{2\sqrt{\pi}(-i\tilde{s}_{p_j})} + \frac{1}{2} \text{erfc}(-i\tilde{s}_{p_j}) \right\} \end{aligned} \quad (30)$$

where (see Fig.3a)

$$\tilde{L}' = -\tilde{y}' / \cos \tilde{\theta}_{rs}, \quad \tilde{L} = -y / \cos \tilde{\theta}_{rs} \quad (30a)$$

and

$$\begin{aligned} \tilde{\Phi}_{\text{cyl}}^r(\rho, \phi) \sim R_{\text{cyl}}(\tilde{v}_s) \frac{\exp\{i\pi/4\} \exp\{ik_f(\tilde{L}' + \tilde{L})\}}{2\sqrt{2\pi}} \frac{1}{\sqrt{k_f(\tilde{L}' + \tilde{L})}} \sqrt{\frac{a(\tilde{L}' + \tilde{L})\sin\gamma_a}{2\tilde{L}'\tilde{L} + a(\tilde{L}' + \tilde{L})\sin\gamma_a}} \Big|_{\tilde{v}_s} \\ - \frac{1}{2} \sum_{j=1}^M \frac{\text{Res}\{R_{\text{cyl}}(v)\}_{v_{p_j}}}{k_f(\rho \tilde{\rho}' \sin\gamma \sin\tilde{\gamma})_{v_{p_j}}^{1/2}} \exp\{i\tilde{P}_{\text{cyl}}(v_{p_j})\} \left\{ -\frac{\exp\{-(-i\tilde{s}_{p_j})^2\}}{2\sqrt{\pi}(-i\tilde{s}_{p_j})} + \frac{1}{2} \text{erfc}(-i\tilde{s}_{p_j}) \right\} \end{aligned} \quad (31)$$

where (see Fig.3b)

$$\tilde{L}' = \tilde{\rho}' \sin\tilde{\gamma}' - a \sin\gamma_a \Big|_{\tilde{v}_s}, \quad \tilde{L} = \rho \sin\gamma - a \sin\gamma_a \Big|_{\tilde{v}_s}, \quad (31a)$$

In the above,

$$\tilde{s}_{p_j} = \sqrt{i \left[\tilde{P}_{\text{pl,cyl}}(\tilde{\zeta}_s) - \tilde{P}_{\text{pl,cyl}}(\zeta_{p_j}) \right]}, \quad \arg\{\tilde{s}_{p_j}\} = \arg\{(\zeta_{p_j} - \tilde{\zeta}_s)\} - \arg\{\text{SDP}_{\tilde{\zeta}_s}\} \quad (32a)$$

The quantity $\text{erfc}()$ is the error function complement of complex argument defined by,

$$\text{erfc}(z) = \frac{2}{\sqrt{\pi}} \int_z^\infty \exp\{-t^2\} dt \quad (32b)$$

and $\text{Res}\{R(\zeta)\}_{\zeta_{p_j}}$ is the residue of $R(\zeta)$ at ζ_{p_j} given by,

$$R(\zeta) = N(\zeta) [D(\zeta)]^{-1} \quad \text{and} \quad \text{Res}\{R(\zeta)\}_{\zeta_{p_j}} = N(\zeta_{p_j}) \left[dD(\zeta_{p_j})/d\zeta \right]^{-1} \quad (32c,d)$$

B. LPG incident beams: liquid-solid plane interface

The LPG incident beams in Sec.IIB give rise to reflected fields as in the spectral integrals in (27a) and (27b), without extension to CSP but with spectral amplitudes modified by the profile functions $\tilde{A}_{\text{pl}}(k, v, v')$ and $\tilde{A}_{\text{sl}}(v; \rho, \rho')$ in (20a) and (20b), respectively, and by the spectral reflection coefficients. The evaluation of these spectral

integrals can be effected by asymptotics as in Sec.II.A, with resulting expressions as in (30)-(32), but with different phase functions and corresponding saddle points. The results are not included here. Instead, for the special case of a plane liquid-solid interface, we follow the procedure first employed by Bertoni and Tamir (BT) [2] and used subsequently by them and other investigators. BT applied the paraxial approximation (see (22), etc.) to the phase and also used an approximate expression for the interface reflection coefficient $R_{pl}(k)$ when the incident beam impinges near or at the leaky Rayleigh angle,

$$R(k) = \frac{k - k_o}{k - k_p} = R_o + R_l(k), \quad k_{p,o} = k_p^r \pm ik_p^i, \quad k_p^i, k_p^r > 0, \quad k_p^i \ll k_p^r, \quad k_o = k_p^* \quad (33)$$

where

$$R_o = \frac{k_f \sin \alpha_o - k_o}{k_f \sin \alpha_o - k_p}, \quad R_l(k) = \frac{k_p - k_o}{k_p - k_f \sin \alpha_o} \frac{k - k_f \sin \alpha_o}{k - k_p} \quad (34)$$

The decomposition (34) into a geometrically reflected part R_o and a leaky wave part $R_l(k)$ highlights the strong interaction of these wave phenomena, and the resulting nonspecular effects, near the Rayleigh angle.

Assuming that the incident beam profile establishes on the interface plane $y=0$ a field profile as in (19a), then the total field on the interface expressed by the paraxially approximated spectral integral that includes the reflected wave spectra can be evaluated in closed form [3]

$$V_{\text{ref}}(x,0) = V_o(x,0) + V_l(x,0) \quad (35)$$

where

$$V_o(x,0) = \frac{R_o}{\sqrt{\pi} w_r} \exp\left\{-\left[(x-x')/w_r\right]^2 + ik_f \sin \alpha_o (x-x')\right\} = R_o V_{\text{inc}}(x,0) \quad (35a)$$

$$V_1(x,0) = v_{inc}(x,0) \frac{k_p - k_o}{k_p - k_f \sin \alpha_o} \left[1 + \frac{i\sqrt{\pi} w_x}{2} [k_p - k_f \sin(\alpha_o)] \exp\{\gamma_{BT}^2\} \operatorname{erfc}\{\gamma_{BT}\} \right] \quad (35b)$$

and

$$\gamma_{BT} = \gamma_{BT}' + i\gamma_{BT}'' = \frac{k_p^j w_x}{2} - \frac{(x-x')}{w_x} + i \frac{k_f \sin \alpha_o - k_p^f}{2} w_x \quad (35c)$$

Since the interface lies well within the Fresnel zone of the incident beam, BT approximated the $1/e$ width $w_r(\xi)$, given in (23), by w_o which is related to w_x through (21a).

In order to compare the expression for the nonspecular reflected CSP field obtained in (30) with the BT solution (35), the expression for $R(k)$ in (33) is used in (30). In addition only one pole, denoted by k_p , needs to be accounted for in (30). It can be shown that subject to the approximations already stated in the paragraph preceding (33), and for observers well within the Fresnel zone $(\xi/b) \ll 1$, the CSP solution reduces to (35). In particular, the argument $(-i\tilde{s}_p)$ of the complementary error function in (30) reduces to γ_{BT} defined above. This demonstrates the tremendous advantage gained by the much greater versatility of (30).

C. Behavior of the Leaky Wave Field

The 'uniform' field associated with a leaky wave excited by a GB on a planar or cylindrical interface is given by one of the terms in the sum in (30) or (31), respectively. When the corresponding pole is not near the saddle point, the term within the braces reduces either to unity, when the pole is intercepted by the SDP, or to zero, when it is not. In the former instance, the leaky wave field reduces to the isolated (nonuniform) value obtained from the residue of the intercepted pole. For small leakage, the phase accumulation of an isolated leaky wave field in the planar or cylindrical case can be interpreted to occur along the geometrical ray paths in Fig.5 which shows that the exponential amplitude of the leaky wave, for observations at $y = \text{const.}$ in plane geometry or $\rho = \text{const.}$ in cylindrical geometry, depends on the real lateral lengths

$$\exp\{i\tilde{P}_{\text{pl}}(k_p)\} \propto \exp\{i\text{Re}\{k_p\}L_2 - \text{Im}\{k_p\}L_2\}, |\text{Re}\{k_p\}/\text{Im}\{k_p\}| \ll 1 \quad (36)$$

$$\exp\{i\tilde{P}_{\text{cy}}(v_p)\} \propto \exp\{i\text{Re}\{v_p/a\}L_2 - \text{Im}\{v_p/a\}L_2\}, |\text{Re}\{v_p\}/\text{Im}\{v_p\}| \ll 1 \quad (37)$$

The exponential decay along the real lateral path lengths between the CSP and the observer as given in (36) and (37) correctly describes the isolated leaky wave field under the small leakage assumption. However, it also describes to a good approximation the behavior of the complex phase of the 'uniform' leaky wave field given by the full terms in (30) and (31) outside the transition region where the strong interaction between the specularly reflected field and the leaky wave field, quantified by the term within the braces in (30) and (31), diminishes. Thus, on the observation surfaces in Fig.5, the phase and magnitude of the leaky wave fields excited by a CSP Gaussian beam are given qualitatively by (36) and (37), which implies: 1) the lateral phase propagation coefficient of the leaky wave field is constant and given approximately by the real part of the spectral pole; 2) the leaky wave magnitude decays exponentially with lateral distance. As an observer on the interface moves from the region of weak excitation by the incident beam, which corresponds to isolated poles and saddle points, toward the beam axis, thereby decreasing the distance L_2 , the exponential profile does not increase indefinitely. Instead, it changes smoothly to the behavior shown in Figs.5 due to the now effective terms in the braces in (30) and (31). The profiles shown in Figs.5, which hold for beam incidence at or near the leaky wave angle, indicate that the leaky wave field is excited mostly by a narrow bundle of rays about the incident beam axis. One can therefore describe the extent of the leaky wave field by effective linear 1/e widths $[\text{Im}\{k_p\}]^{-1}$ and $[\text{Im}\{v_p/a\}]^{-1}$, respectively, for the planar and cylindrical cases.

The effective widths of the magnitude profiles of the leaky wave fields established above are to be compared with the widths of the magnitude profiles of the specularly reflected beams which, for observations at or near the interface, are given by the width of the incident beam profiles projected onto the interface. The 1/e width $w_x(\xi)$ can be approximated by

$$w_x(\xi) = w(\xi)/\cos\theta_0, \quad w(\xi) = w_0(1 + \xi^2/b^2)^{1/2} \quad (38)$$

where θ_0 is the incidence angle of the beam axis on the interface and ξ denotes the distance, along the beam axis, from the beam waist to the interface. For the plane case, $\theta_0 = \alpha_0$, and for the cylindrical case, $\theta_0 = \sin^{-1}\{(\rho'/a)\sin[\alpha_0 + \tan^{-1}(x'/|y'|)]\}$.

The ratio σ of the specularly reflected field 'width' and the leaky wave field width, given by $\sigma = \text{Im}\{k_p\} w_x(\xi)$ (planar) and $\sigma = \text{Im}\{v_p/a\} w_x(\xi)$ (cylindrical) can be used as a measure of the relative domains of influence of these field constituents. When $\sigma \approx 1$, the leaky wave field and the specularly reflected field have approximately the same extent whereas when $\sigma < 1$, the leaky wave field extends beyond the region of the specularly reflected field because $[\text{Im}\{k_p\}]^{-1}$ (or $[\text{Im}\{v_p/a\}]^{-1}$) $> w_x(\xi)$. When $\sigma > 1$, the leaky wave field decays to small values over the extent of the specularly reflected field. These considerations, depicted in Fig.6, are useful in explaining qualitatively the interaction of the leaky wave and specularly reflected fields and in predicting the pattern of the nonspecularly reflected field, as revealed by the numerical results in Sec.IV. It should be noted that σ is directly related to the relative spectral locations of the leaky wave pole and the reflected beam saddle point.

IV. NUMERICAL RESULTS

A comprehensive data base has been established by numerical calculations of nonspecular (NS) reflection for various plane and cylindrical configurations, various types of incident beams, and various observation domains. Because of space limitations, only a few examples will be cited, with compact discussion and interpretation. Detailed treatments are reserved for separate publication. For each case, the data includes a reference solution computed by direct numerical integration of initial spectral integrals, and the asymptotic approximations for these integrals. The comparisons establish the quality of the asymptotic results.

The first set of data, in Fig.7, shows a comparison between the CSP and BT results presented in (30) (with $M=1$) and (35), respectively. The parameters are for a typical curve in the original BT paper [3] and are listed in the figure caption. The plots show the magnitude and real part of the NS reflected field on the interface plane. For the listed parameters, with $\xi/b = 1/10$ (see paragraph following (35c)), the BT restriction

to observations well within the Fresnel zone is satisfied. The agreement between the two solutions is excellent. Discrepancies have been shown to arise when the observation plane is moved away from the CSP source such that the impinging beam on the interface is less well collimated. Such beam spreading, which is readily modeled by the CSP GB, cannot be accommodated by the BT solution. It may be noted that the BT parameter $2w_0/\Delta_s$, where Δ_s is the Schoch displacement, is equivalent to our $\text{Im}\{k_p\}w_x$, which is more universally applicable.

The schematization of interaction regions for various incident beams and interface configurations in Fig.8, with the incident wavenumber periodicities as shown, is helpful to explain the combined (leaky wave)-(reflected beam) effects. Referring to Sec.IIIC, assuming that $\sigma \approx 1$ or $\sigma < 1$, then when the various induced periodicities, which generate the geometrically reflected beam, interact with the constant periodicity of the leaky wave, the outcomes are different interference phenomena, that lead to splitting of the composite reflected field. For case (a), interference nulls are far apart, whereas for cases (b) and (c), the reflected beam and leaky wave constituents are in and out of phase repeatedly over their common interaction region, thereby producing patterns with multiple minima and maxima (multiple splitting) in addition to the conventionally observed splitting due to the reflection coefficient zero in (33). These qualitative predictions are confirmed in Fig.9 which shows generic NS reflection patterns from planar geometries for various values of the parameter σ and degrees of collimation of the incident beam. Two types of leaky wave poles are treated: the Rayleigh-type in Fig.9a and the Lamb-type in Fig.9b. In the first, the zero of $R(k)$ in (33) is the complex conjugate of the pole. In the second, the zero is real, with a value equal to the real part of the pole. Lamb-type leaky waves arise in multilayered structures, whereas Rayleigh-type leaky waves occur on interfaces between elastic and fluid half-spaces.

The versatility of the CSP algorithm is further demonstrated by application to beam reflection from an aluminum plate and solid cylinder immersed in water. Exact expressions for the reflection coefficients and their residues at the leaky wave poles are necessary to generate the data. Due to lack of space, these lengthy expressions are not included. The reader is referred to Ref.5 for $R(k)$ pertaining to the plate, and to Ref.32 for $R(v)$ pertaining to the solid cylinder. In the planar case, the symmetric and antisymmetric leaky Lamb modes yield separate residues. For the cylinder, Debye approximations are employed to derive a high-frequency $R(v)$ for use in the reference solution (27b), whereas a BT-like approximation as in (33) has been employed to

generate the asymptotic solution (31). These considerations will be reported in detail in a separate paper.

In Figs.10(a) and 10(b), the aluminum plate is insonified with a diverging GB at $f-d=6$ MHz-mm, where f is the signal frequency and d is the plate thickness; the plate and beam parameters are listed in the captions. The various leaky Lamb waves excited at this $f-d$ value give rise to the dips in the magnitude profile of $R(k)$ shown in Fig.10(a); the complex poles and corresponding zeros are listed in Table 1. In Fig.10(b), selecting the incident beam angle α_0 so as to establish strong phase matching to the A_1 mode, one obtains for the incident beam profile shown dashed the NS reflected field solid-curve reference solution generated from (27a), and the dotted uniform asymptotic solution generated from (30), with $M=4$ accounting for the S_1 , A_1 , S_0 , and A_0 mode contributions which are anticipated to be the dominant contributors. Their separate contributions are shown by the solid curves in Fig.10(c); the specular reflected field profile, shown by the dashed curve, is strongly dependent on the location of the saddle point relative to the poles and zeros of $R(k)$ in the complex spectral plane. It can be observed that the A_1 mode is strongly excited, but that the neighboring modes cannot be ignored. The A_1 mode has a broader extent along the interface due to its smaller leakage factor, as seen from Table 1. The large spikes in the magnitude profiles of the specular reflected field and the A_0 mode near $x=27$ are due to the proximity of the reflected field saddle point near the A_0 pole. However, the sum of these two terms behaves smoothly, as can be seen from the total field plot in Fig.10(b) which has been validated by comparison with purely numerically generated reference data.

Figure 11 contains results for the aluminum cylinder in water insonified by a well collimated GB that is phase matched to the leaky Rayleigh wave. The material properties of the cylinder are the same as in the caption of Fig.10(a); the incident beam parameters are listed in Fig.11. The magnitude of the NS reflected field shown in Fig.11 by the solid curve is generated from the asymptotic solution (31), with $M=1$, and $R(v)$ approximated similarly to (33). The spectral pole location given in the figure caption is based on assumption of locally planar conditions, i.e., $v_p=k_p a$ where k_p is given in the caption of Fig.7 and a is the cylinder radius. The reference solution shown in dots is obtained from (27b) with use of the Debye-approximated $R(v)$. The separate contributions of the leaky Rayleigh wave and the specularly reflected fields are shown by the short-dashed and long-dashed curves, respectively. The multiple splitting of the NS reflected field has been anticipated in the explanation of Fig.8. One notes that the

profiles of the strongly excited leaky wave in Fig.11 and in Fig.10(c) (A_1 mode) match closely the profiles sketched in Figs.6 and 5.

ACKNOWLEDGEMENT

This work has been supported by the U.S. Air Force Office of Scientific Research under Grant No. AFOSR-90-0088 and also, during its last phase, by the David Taylor Research Center under subcontract from Johns Hopkins University.

REFERENCES

- [1] F. Goos and H. Hanchen, "A New and Fundamental Experiment on Total Reflection," (in German), *Ann. Phys. (Leipzig)* 1, 333-346 (1947)
- [2] T. Tamir and H. L. Bertoni, "Lateral displacement of optical beams at multilayered and periodic structures," *J. Opt. Soc. Am.*, **61**, 1397-1415 (1971)
- [3] H. L. Bertoni and T. Tamir, "Unified theory of Rayleigh-angle phenomena for acoustic beams at liquid-solid interfaces", *Appl. Phys.*, **2**, 157-172 (1973)
- [4] W. G. Neubauer, "Observation of acoustic radiation fromn plane and curved surfaces," in *Physical Acoustics*, edited by W. P. Mason and R. N. Thurson (Academic, New York, 1973), Vol.60, 61-126
- [5] T. J. Plona, L. E. Pitts, and W. G. Mayer, "Ultrasonic bounded beam reflection and transmission effects at a liquid/solid-plate/liquid interface", *J. Acoust. Soc. Am.*, **59**, 1324-1328 (1976)
- [6] L. E. Pitts, T. J. Plona, and W. G. Mayer, "Theoretical similarities of Rayleigh and Lamb modes of vibration", *J. Acoust. Soc. Am.*, **60**, 374-377 (1976)
- [7] L. E. Pitts, T. J. Plona, and W. G. Mayer, "Theory of nonspecular reflection effects for an ultrasonic beam incident on a solid plate in a liquid", *IEEE Trans. Sonics Ultrason.*, **SU-24**, 101-109 (1977)
- [8] M. A. Breazeale, L. Adler, and G. W. Scott, "Interaction of ultrasonic waves incident at the Rayleigh angle onto a liquid-solid interface," *J. Appl. Phys.* **48**, 530-537 (1977)
- [9] T. D. K. Ngoc and W. G. Mayer, "Numerical integration method for reflected beam profiles near Rayleigh angle," *J. Acoust. Soc. Am.*, **67**, 1149-1152 (1980)
- [10] T. D. K. Ngoc and W. G. Mayer, "A general description of ultrasonic nonspecular reflection and transmission effects for layered media", *IEEE Trans. Sonics Ultrason.*, **SU-27**, 229-236 (1980)
- [11] T. D. K. Ngoc and W. G. Mayer, "Influence of a plate mode structure and Gaussian beam profile characteristics on ultrasonic reflection and transmission," *IEEE Trans. Sonics Ultrason.*, **SU-29**, 112-114 (1982).
- [12] J. M. Claeys and O. Leroy, "Reflection and transmission of bounded beams on half-spaces and through plates," *J. Acoust. Soc. Am.*, **72**, 585-590 (1982)
- [13] A. N. Norris, "Back reflection of ultrasonic waves from a liquid-solid interface," *J. Acoust. Soc. Am.*, **73**, 427-434 (1983)

- [14] J. Pott and J. G. Harris, "Scattering of an acoustic Gaussian beam from a fluid-solid interface," J. Acoust. Soc. Am., **76**, 1829-1838 (1984)
- [15] H. Schmidt and F. B. Jensen, "A full wave solution for propagation in multilayered viscoelastic media with application to Gaussian beam reflection at fluid-solid interfaces," J. Acoust. Soc. Am., Vol.77, 813-825 (1985)
- [16] J. G. Harris and J. Pott, "Further studies of the scattering of an acoustic Gaussian beam from a fluid-solid interface," J. Acoust. Soc. Am., **78**, 1072-1080 (1985)
- [17] M. Rousseau and Ph. Gatignol, "Short wave analysis for the reflection of bounded acoustic beams onto liquid-solid interfaces at the Rayleigh incidence", J. Acoust. Soc. Am., **78**, 1859-1867 (1985)
- [18] M. Rousseau and Ph. Gatignol, "Asymptotic analysis of nonspecular effects for the reflection and transmission of a Gaussian acoustic beam incident on a solid plate", J. Acoust. Soc. Am., **80**, 325-332 (1986)
- [19] D. E. Chimenti and A. H. Nayfeh "Ultrasonic leaky waves in a solid plate separating a fluid and vacuum," J. Acoust. Soc. Am., **85**, 555-560 (1989)
- [20] T. Kundu, "On the nonspecular reflection of bounded beams," J. Acoust. Soc. Am., **83**, 19-24 (1988)
- [21] H. C. Choi and J. G. Harris, "Scattering of an ultrasonic beam from a curved interface," Wave motion, **11**, 383-406, 1989
- [22] J. W. Ra, H. L. Bertoni, and L. B. Felsen, "Reflection and transmission of beams at a dielectric interface," SIAM J. Appl. Math. **24**, 396-413 (1973).
- [23] L. B. Felsen, "Complex rays," Phillips Res. Reps., Special Issue in honor of C. J. Bouwkamp, **30**, 187-195, 1975.
- [24] M. Couture and P. A. Belanger, "From Gaussian beam to complex-source-point spherical wave," Phys. Rev. A **24**, 355-359 (1981).
- [25] L. B. Felsen, "Geometrical theory of diffraction, evanescent waves and complex rays," Geophys. J. Roy. Astron. Soc., **79**, 77-88, July 1982.
- [26] L. B. Felsen and N. Marcuvitz, *Radiation and Scattering of Waves* (Prentice Hall, Englewood Cliffs, N.J., 1973).
- [27] L. B. Felsen, J. M. Ho, and I. T. Lu, "Three-dimensional Green's functions for fluid-loaded thin elastic cylindrical shell: Formulation and solution," J. Acoust. Soc. Am., **87**, 546-553 (1990)
- [28] L. B. Felsen, J. M. Ho, and I. T. Lu, "Three-dimensional Green's functions for fluid-loaded thin elastic cylindrical shell: Alternative representations and ray acoustic forms," J. Acoust. Soc. Am., **87**, 554-569 (1990).

- [29] L. B. Felsen and S. Zeroug, "Ultrasonic beam method for localized weak debonding in a layered aluminum plate," *J. Acoust. Soc. Am.*, **90**, 1527-1538 (1991).
- [30] A. E. Siegman, *Lasers*, (University Science Books, Mill Valley, CA, 1984), Chap. 16.
- [31] H. A. Haus, *Waves and Fields in Optoelectronics* (Prentice-Hall, Englewood Cliffs, NJ, 1984), Chap. 5.1.
- [32] G. V. Frisk, J. W. Dickey, and H. Uberall, "Surface wave modes on elastic cylinders," *J. Acoust. Soc. Am.*, **58**, 996-1008 (1975)

FIGURE CAPTIONS

FIG.1 Planar and cylindrical configurations excited by CSP and LPG beams, with relevant parameters and coordinates.

FIG.2 Integration paths, branch points, branch cuts, and poles in complex- k plane for two fluid-solid half spaces. The sketch depicts a single (Rayleigh) pole which is intercepted during the deformation from the original contour into the SDP. For layered media, there are additional poles but branch points only at $\pm k_f$. The integration paths in the complex v -plane are similar but there are no branch points.

FIG.3 Complex ray interpretation of CSP saddle point conditions for incident and reflected fields. Planar: see (12a) and (29a); cylindrical: see (12b) and (29b).

FIG.4

(a) Magnitudes of incident well-collimated GB along interface plane ($y=0$), for waist locations that place $y=0$ inside and outside the Fresnel zone b , respectively. LPG GBs: reference solution from (3a) with (20a), solid curve; paraxial from (23), dashed. CSP GBs: dots; both the reference solution (7a) and the asymptotic solution (14) yield the same curve. Parameters: $b=50$, $\alpha_0=30.593^\circ$. Waist at $(x',y')=(-19.56,-50)$ yields the larger and narrower profiles within the Fresnel zone. The LPG solution has been divided by 1.162 to match its maximum amplitude to CSP. All distances are normalized to fluid wavelength $\lambda_f=2\pi k_f$.

(b) Magnitude and phase of narrow-waisted diverging GB along interface. Comparison between LPG GB and CSP GB. Parameters: $b=5$, $\alpha_0=30.593^\circ$. $(x',y')=(-11.825,-20)$. All distances are normalized to fluid wavelength $\lambda_f=2\pi k_f$.

FIG.5 Ray trajectories for weakly damped leaky waves. The amplitude profiles sketched for the leaky wave fields are explained in the text.

FIG.6 Domains of influence of leaky wave and specularly reflected fields.

FIG.7 Magnitude and real part of NS reflected field along water-Al interface (not including the incident field), for incidence at the leaky Rayleigh wave angle. Comparison between Bertoni and Tamir (BT) solution (35) (solid) and CSP solution (30) with $M=1$ (dots). $R(k)$ is approximated as in (33). Parameters: BT: $w_x=4.264$, CSP: $b=42.33$, $(x',y')=(-2.152,-3.64)$. $\alpha_0=30.593^\circ$. $k_p=(\sin 30.593^\circ + i0.014944)$, $k_o=k_p^*$. All distances are normalized to the wavelength $\lambda_f=2\pi k_f$, and all wavenumbers (poles and

zeros) to the wavenumber k_p in the fluid. In the plots, both solutions are normalized to unit maximum amplitude for direct comparison.

FIG.8 Schematization of interaction regions created on plane and cylindrical interfaces by various incident GBs. The equiamplitude contours (phase paths) of the beams are shown up to the $(1/e)$ contours that define the effective beam widths. Wavenumber periodicities induced by wavevector projection along the interface are shown below the interface. θ_0 =beam axis incidence angle. a) Well-collimated wide-waisted beam; plane interface. Periodicity along interface is nearly constant (parallel phase paths, uniform projections). b) Diverging narrow-waisted beam; planar interface. Periodicities along interface vary from rapid to slow (diverging phase paths, nonuniform projections). c) Well-collimated beam as in a); cylindrical interface. Curvature induces periodicities along interface analogous to those in (b) (parallel phase paths, nonuniform projections). All distances are normalized to the fluid wavelength $\lambda_f=2\pi/k_f$.

FIG.9a NS reflected field magnitudes, on the interface, due to well collimated (left column) and diverging (right column) GBs phase matched to a Rayleigh-type leaky wave, as a function of $\sigma=w_x(\xi)\text{Im}\{k_p\}$. The NS reflected field (which excludes the incident field) shown by the solid curve is compared with the magnitude of the incident beam shown dashed. The horizontal coordinate x is normalized to the projected $1/e$ width $w_x(\xi)$ of the incident beam. The parameters of the incident beams, schematized in Figs. 8(a) and 8(b), are $\alpha_0=30.593^\circ$, $b=200$ ($w_0=8$, $w_x(\xi)=10.75$) and $b=20$ ($w_0=2.5$, $w_x(\xi)=17.25$) for the well-collimated and diverging beams, respectively. The plots have been generated by specifying σ , and determining therefrom $\text{Im}\{k_p\}$. These values are needed in (30) to generate the NS reflected field with $R(k)$ approximated by (33).

FIG.9b Same as Fig.9a, but phase matched to a single Lamb-type leaky wave with corresponding $R(k)$ approximated as in (33), but with a real zero equal to $\text{Re}\{k_p\}$. Large differences between incident beam and the NS reflected field magnitudes may be attributed to fields transmitted through the plate.

FIG.10

(a) Spectral magnitude of plane-wave reflection coefficient $R(k)$ for an aluminum plate immersed in water, at $f-d=6$ MHz-mm; several leaky Lamb waves are excited. Spectrum of the diverging beam incident at $\alpha_0=24.776^\circ$, phase matched to $\text{Re}\{k_p\}$ for leaky wave A_1 (see Table 1), is also shown. For beam parameters, see Fig.10(b). Plate parameters: $v_p/v_f=0.23548$, $v_p/v_f=0.4771$, and $\rho_p/\rho_f=0.37037$, where v_p , v_f , ρ_p are, respectively, the sound

speed in water and the longitudinal and transverse wave speeds in the plate; ρ_f/ρ_s is the density ratio of fluid to solid. The dips locations correspond to the $\text{Re}\{k_p\}$ values for the indicated leaky Lamb modes.

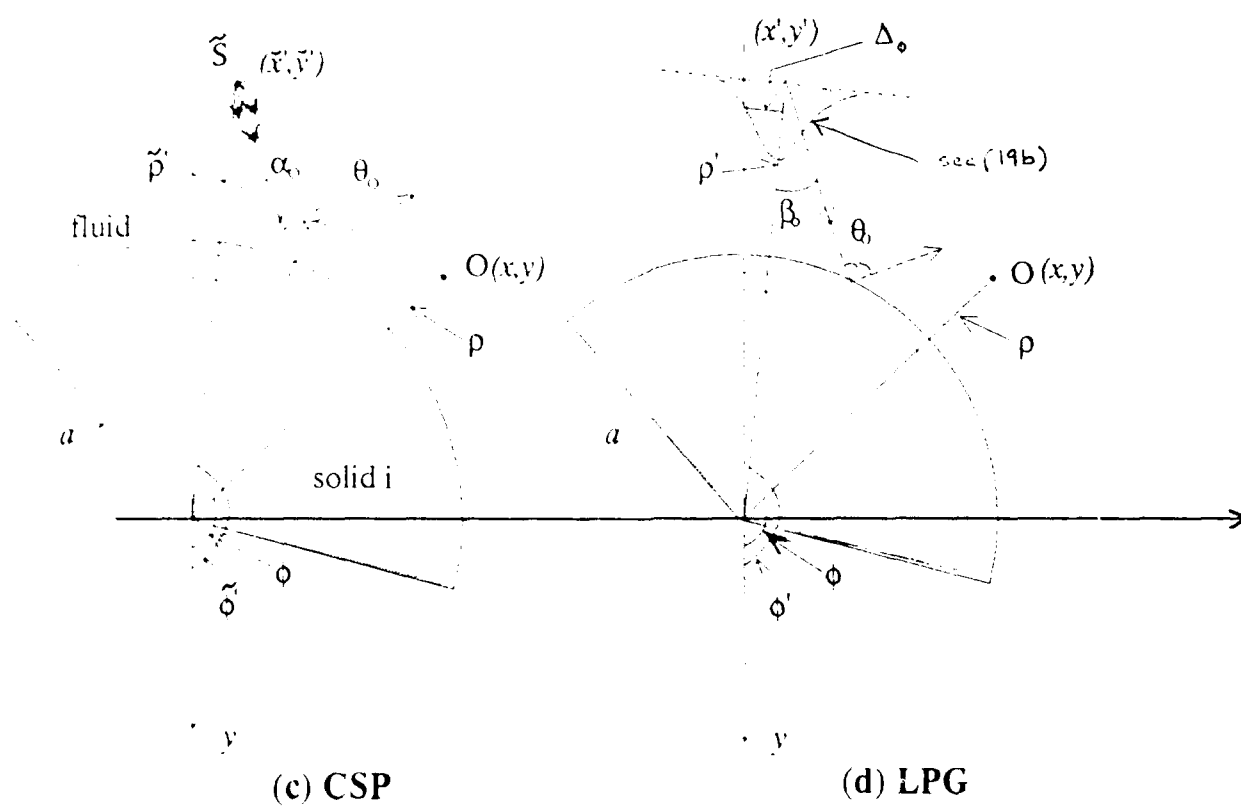
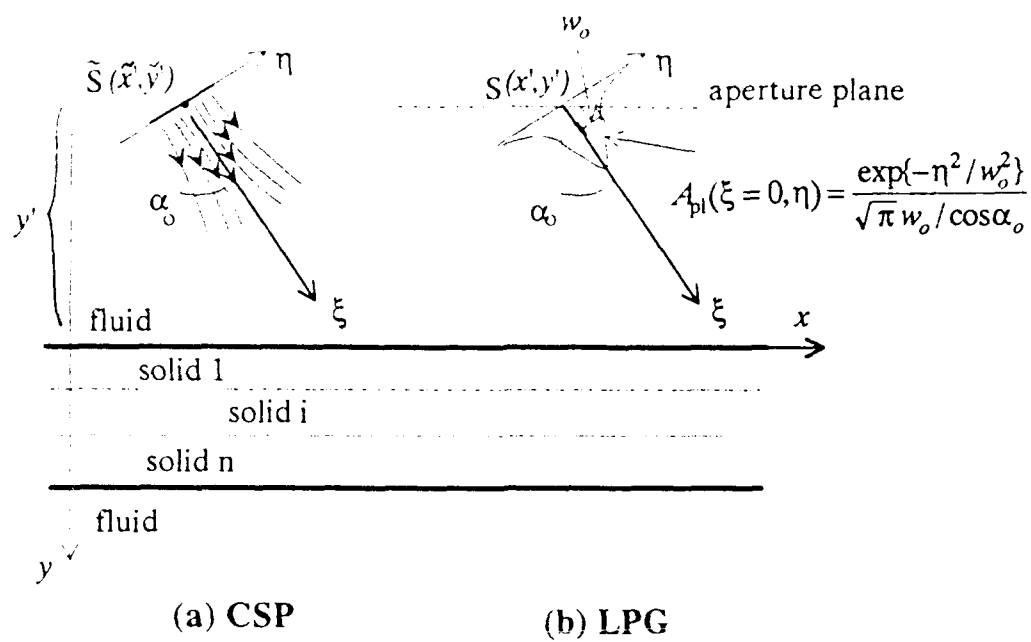
(b) Magnitude of NS reflected field for Al plate in water observed on $y=0$ plane. Solid: reference solution (27a); dots: asymptotic solution (30) with $M=4$ corresponding to S_1 , A_1 , S_0 , and A_0 (see Table 1). Diverging incident beam profile is shown dashed (see also Fig.10(a)). Parameters: $b=50$, $(x',y')=(-92.31,-200)$, $f \cdot d=6$ MHz-mm, $\alpha_0=24.776^\circ$ (strong phase matching to A_1 leaky Lamb wave)

(c) Magnitudes of separate contributions from specularly reflected field (dashed) and leaky wave fields S_1 , A_1 , S_0 , and A_0 (solid).

FIG.11 Magnitude of NS reflected field on surface of Al cylinder immersed in water, for well collimated incident beam (see Fig.8(c)). Dots: reference solution (27b). Solid curve: asymptotic solution (31) with $M=1$. Short-dashed: contribution of leaky wave field. Long-dashed: contribution of specularly reflected field. Beam axis intersects cylinder surface at $\varphi=18.37^\circ$. Parameters: $(x',y')=(10,-50)$, $\alpha_0=12.22^\circ$, $\theta_0=30.593^\circ$, $b=200$, $a=40$. Pole values $v_F=v_p^r+i v_p^i$; $v_p^r=127.9$, $v_p^i=3.75$.

Mode type	pole: k_p/k_f	zero: k_o/k_f
S_2	$(12.31295) + i 0.0031218$	$(12.3025) + i 0$
A_2	$(13.63707) + i 0.0018042$	$(13.6395) + i 0$
S_1	$(17.61137) + i 0.0095777$	$(17.6256) + i 0$
A_1	$(24.77660) + i 0.0076641$	$(24.7637) + i 0$
S_0	$(30.77763) + i 0.0166403$	$(30.5743) - i 0.014906$
A_0	$(30.74412) + i 0.0139146$	$(30.5743) + i 0.014906$

TABLE 1 Locations of poles and zeros of $R(k)$ for aluminum plate immersed in water at $f-d=6$ MHz-mm, with material parameters listed in caption of Fig. 10. The real parts of the poles and zeros are expressed in terms of the angular spectrum θ (degrees), i.e. $\text{Re}\{k_p/k_f\} = \sin^{-1}(\theta)$. Note that the S_0 mode approaches the leaky Rayleigh wave pole as $f-d$ becomes large [5].



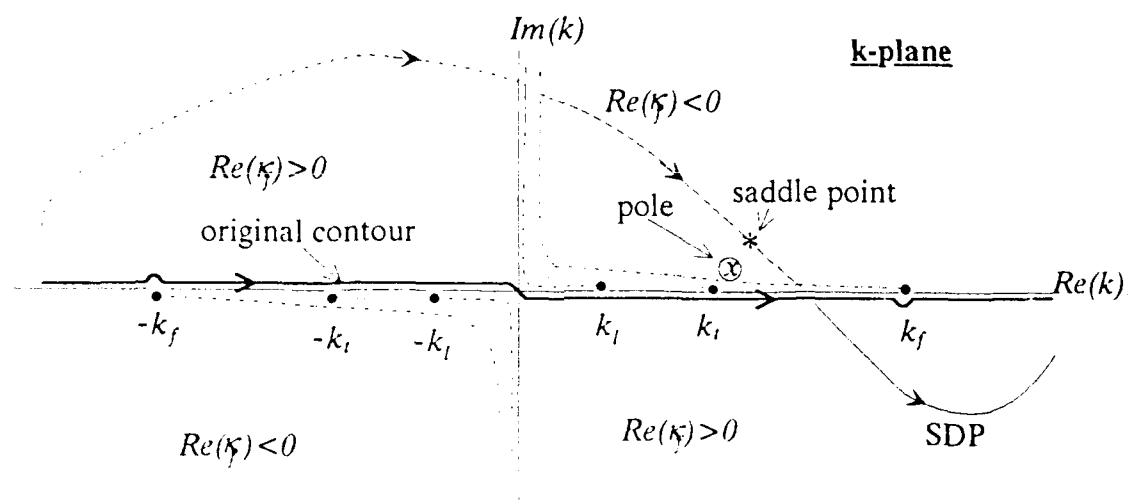
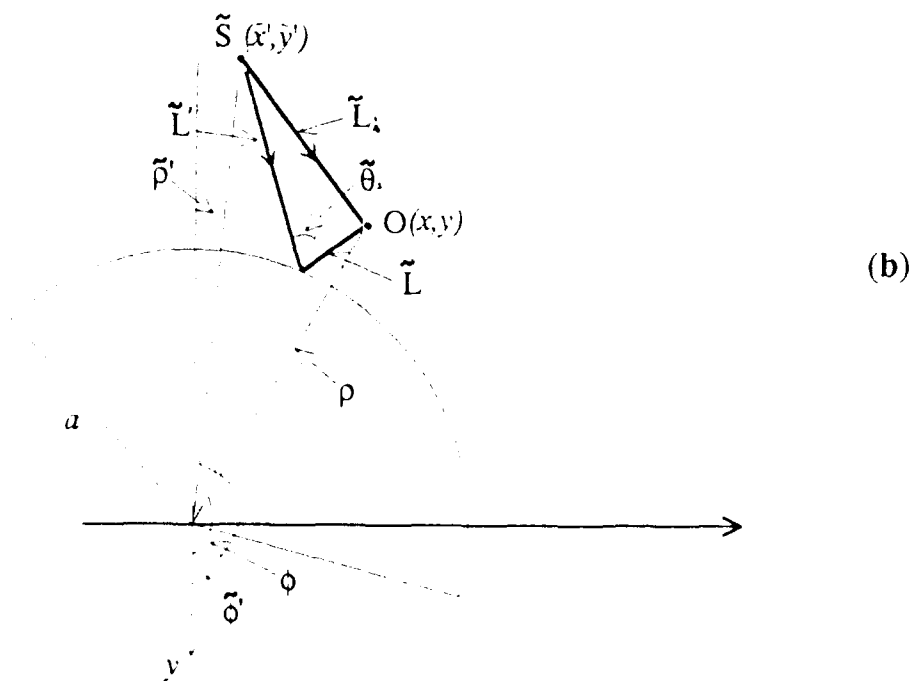
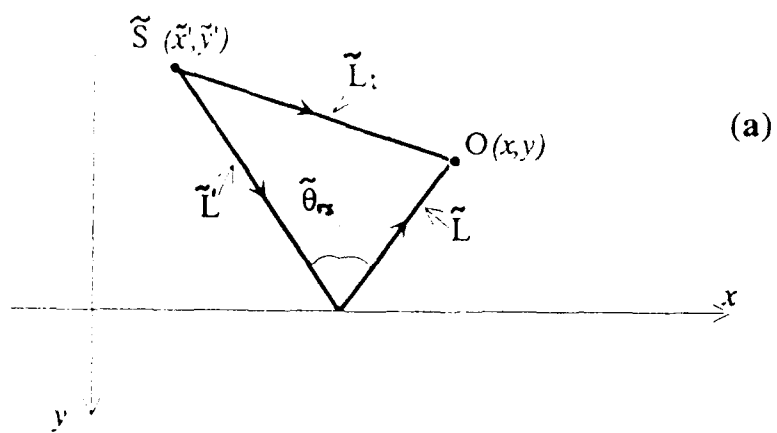
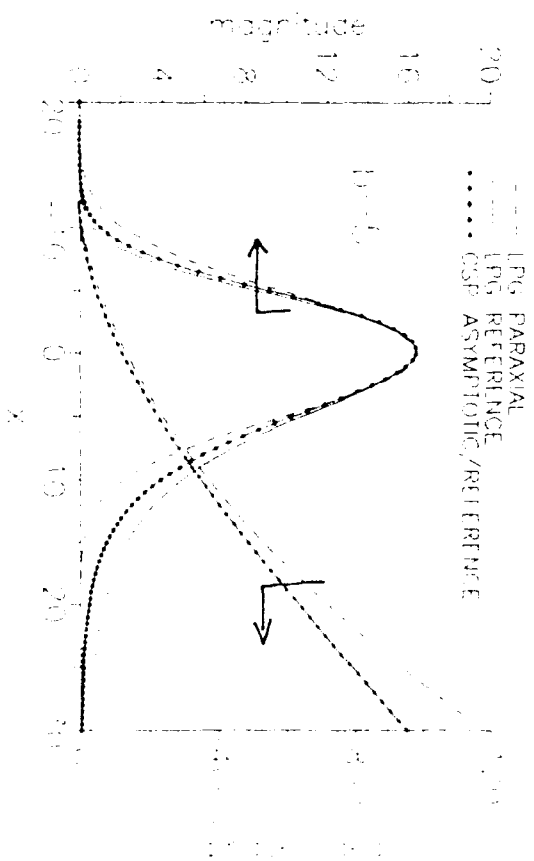
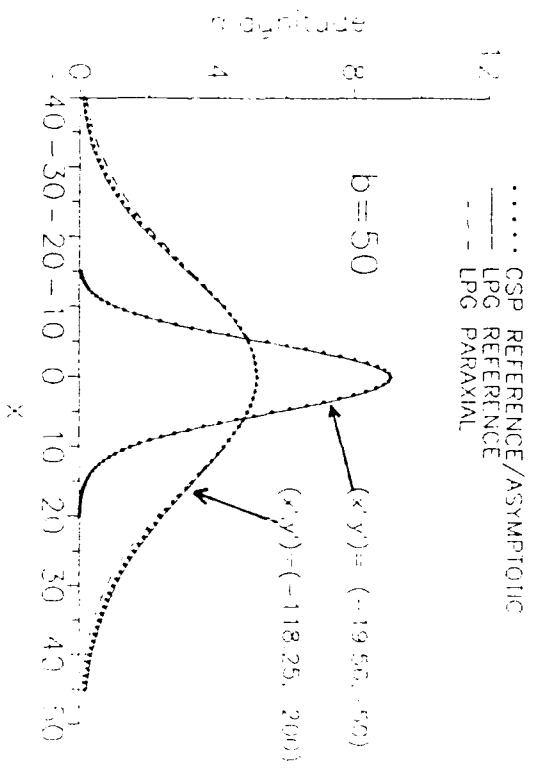
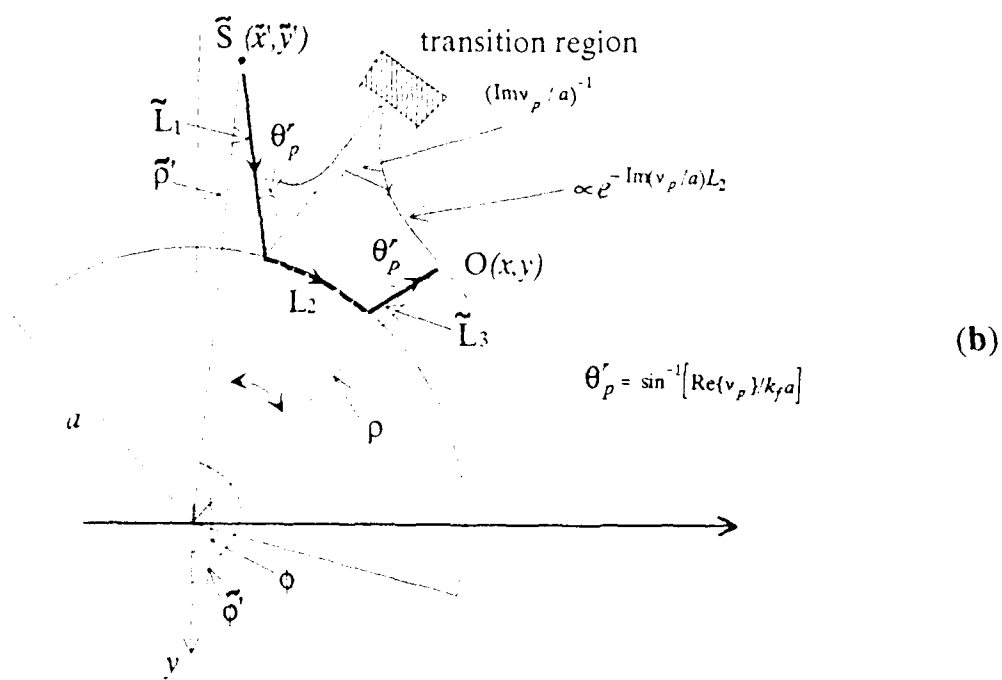
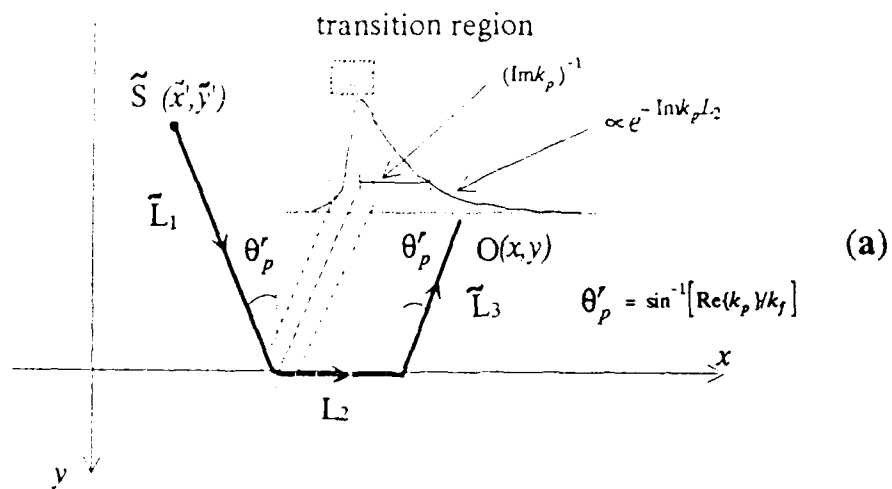
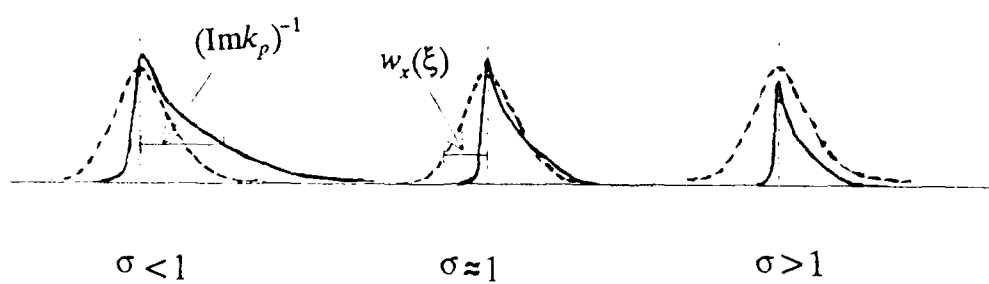


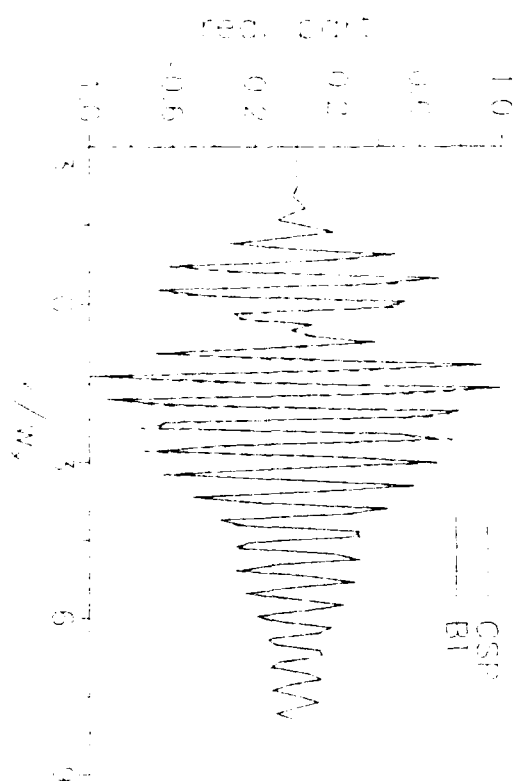
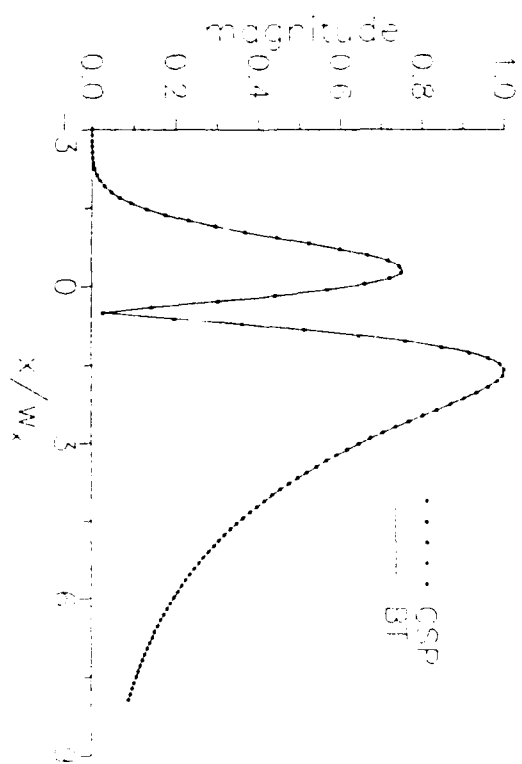
FIG. 2

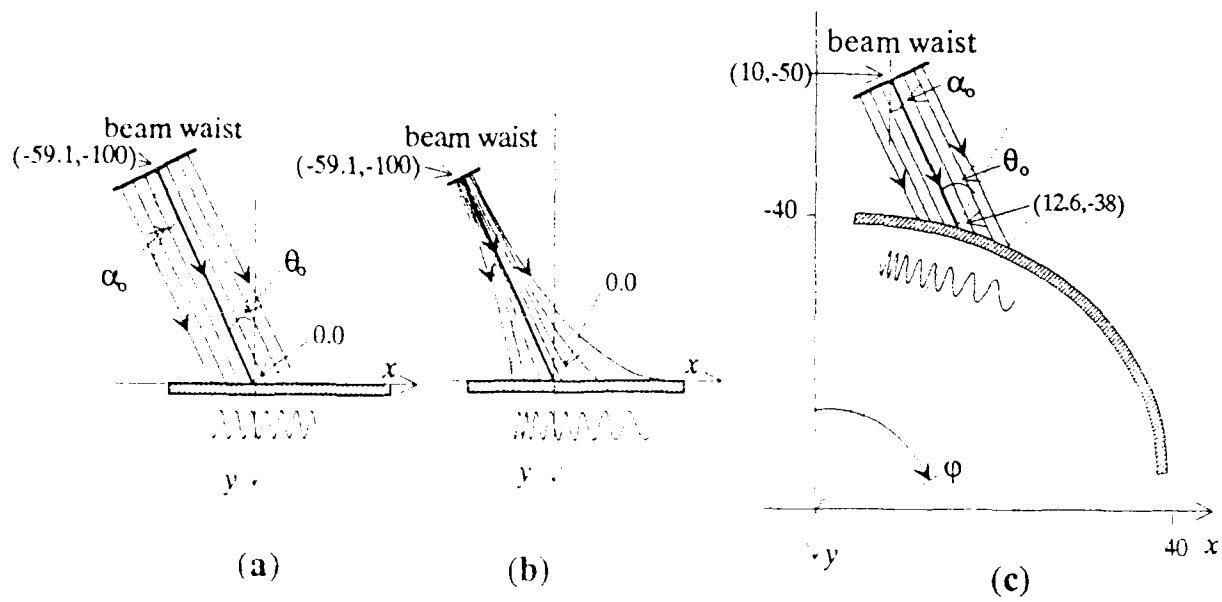


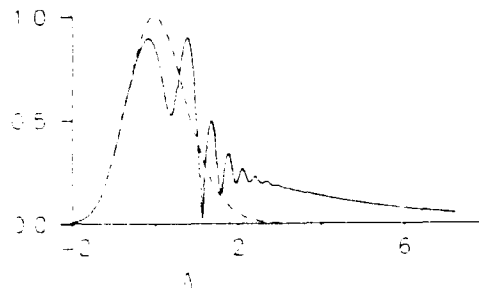
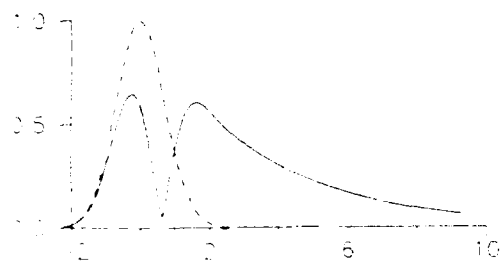




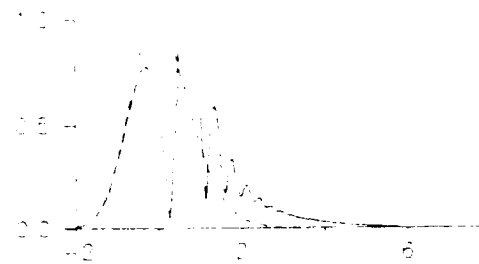
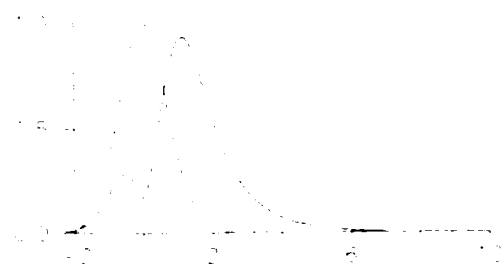




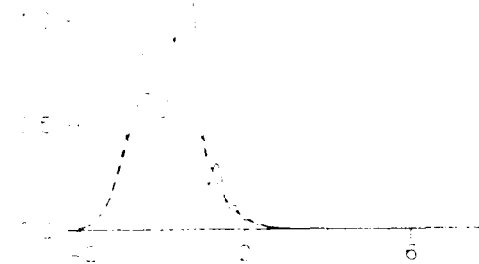
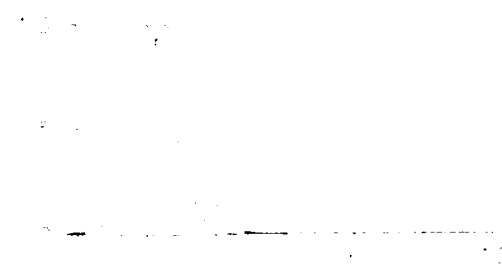




$\sigma=0.3$



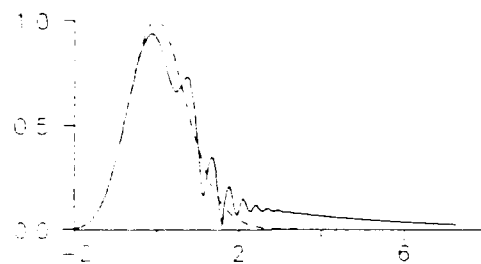
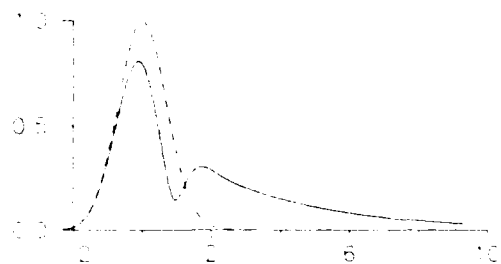
$\sigma=1.0$



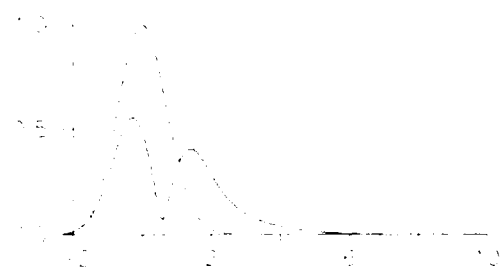
$\sigma=3.0$

WELL COLLIMATED

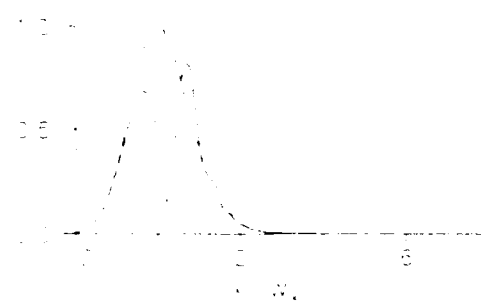
DIVERGING



$\sigma=0.3$



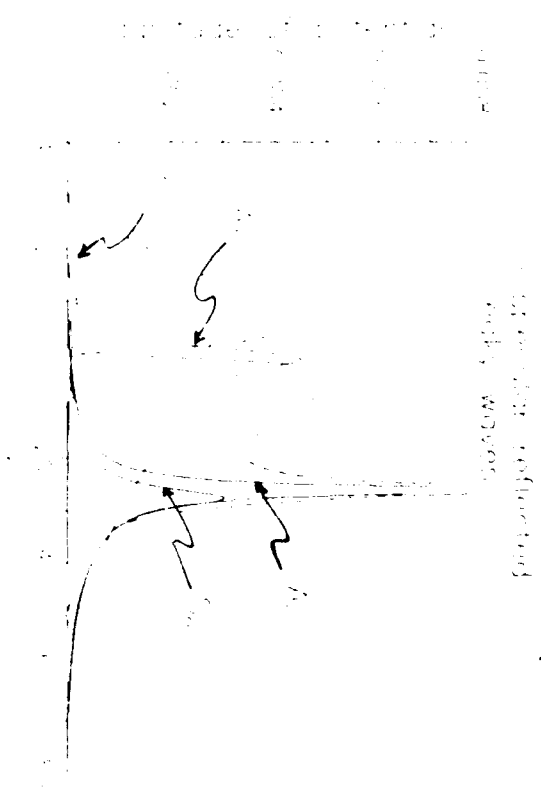
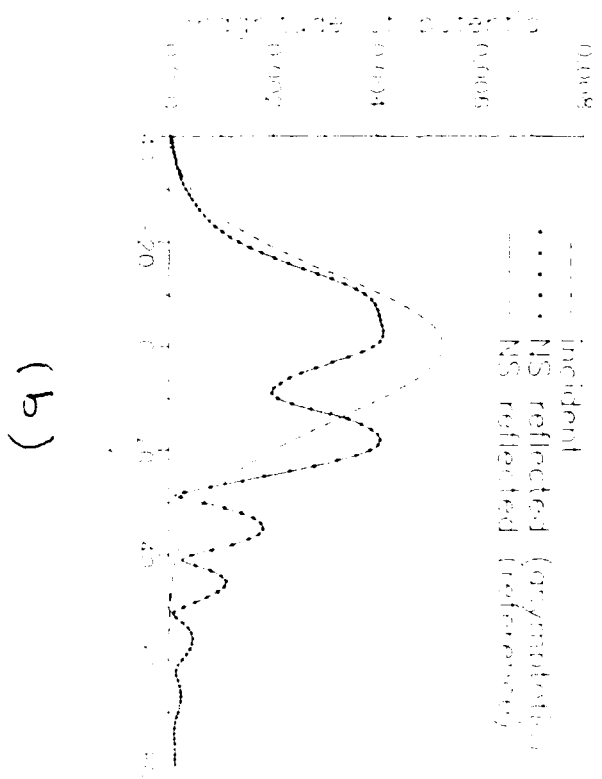
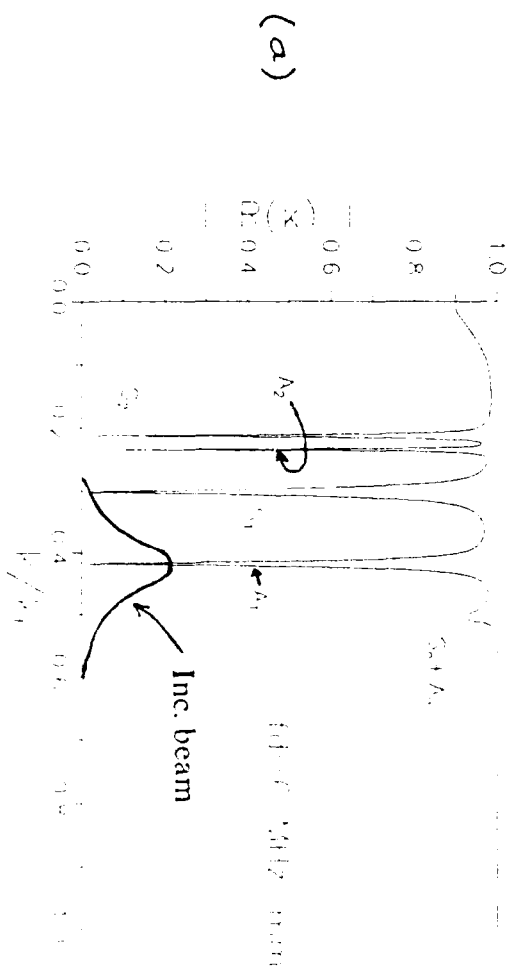
$\sigma=1.0$

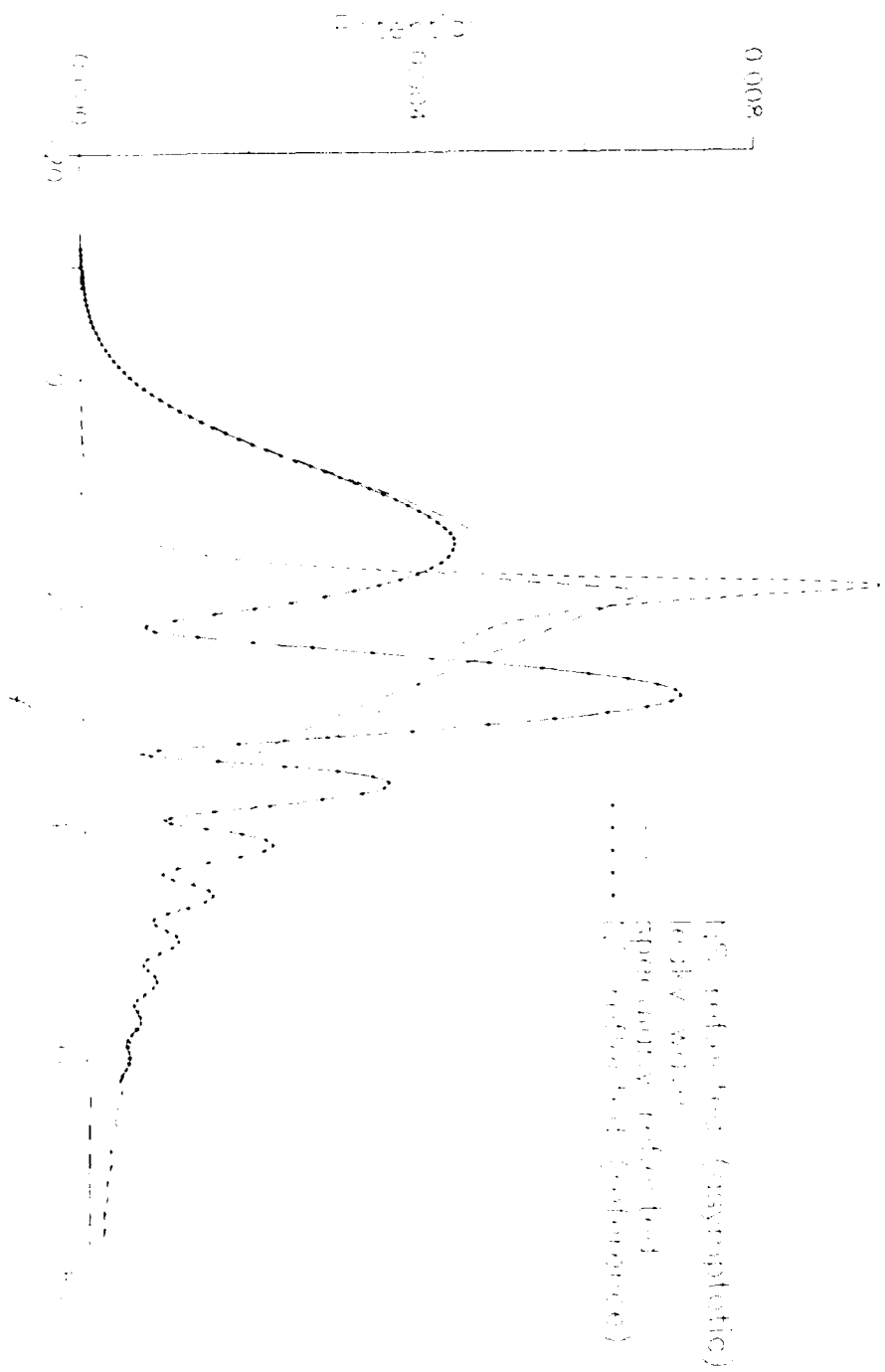


$\sigma=3.0$

WELL COLLIMATED

DIVERGING





NON-SPECULAR REFLECTION OF BOUNDED BEAMS FROM MULTILAYER FLUID-IMMERSED ELASTIC STRUCTURES: COMPLEX RAY METHOD REVISITED

Smaine Zeroug and Leopold B. Felsen
Department of Electrical Engineering / Weber Research Institute
Polytechnic University
Farmingdale, N.Y. 11735

INTRODUCTION

The excitation of various types of leaky waves in layered elastic media by beams incident from an exterior fluid at or near the leaky wave phase-matching angle is of interest for NDE applications. In particular, much attention has been given to the non-specular reflection of beams under such conditions of incidence. While various methods have been employed to study and clarify these phenomena for well collimated beams in plane layered environments [1-11], much less has been done on the corresponding effects when the incident beams are diverging and/or when the layers are curved. To extend the plane layer results to more general conditions, it is desirable to employ analytic modeling that adapts the wave phenomenology locally from planar to curved geometries. Because the phenomena occur in the range of high frequencies, ray field modeling affords an attractive option. By the complex-source-point (CSP) technique, which places a radiating source at a complex coordinate location, a conventional line or point source excited field can be converted into a two- or three-dimensional quasi-Gaussian beam field that is an exact solution of the dynamical equations [12,13]. When the CSP field interacts with a plane or cylindrically layered elastic medium, the resulting internal and external fields can be expressed rigorously in terms of wavenumber spectral integrals [14]. Asymptotic reduction of these integrals, achieved by the method of saddle points applied to deformed contours in the complex spectral wavenumber plane, accounts for all relevant wave phenomena. For the reflected field, this yields explicit waveforms which are synthesized by interacting specularly reflected beam, leaky wave, and possible lateral wave contributions.

The solution strategy outlined above has been applied here to arbitrarily collimated beams that impinge on plane and cylindrically layered geometries at or near the phase matching condition for a leaky wave. For the plane layered environment, the arbitrarily collimated beam formulas developed in this paper for the reflected field at all observation angles and distances reduce near phase matched incidence, and for the well-collimated and paraxial regime, to the non-specular results in the literature [1]. It is also shown that diverging beams incident at the phase-

matching angle give rise to a more complex reflected pattern than do well-collimated beams, owing to the more extended and nonuniform interaction region between the specularly reflected and the leaky wave field, which is established by the diverging beam. For the same reason (extended nonuniform interaction region) this behavior is obtained as well for the case of well-collimated beams incident upon a cylindrical interface. The entire formulation is two-dimensional. The three-dimensional case is in preparation.

The paper is organized as follows. The analytical foundation for plane and cylindrically layered elastic structures is presented in Sec.I, with incorporation of the CSP method and the asymptotic reductions. The asymptotic constituents include incident, specularly reflected, and leaky wave fields that are generated by a CSP-extended line source. The specular and leaky wave parts are treated by uniform asymptotics to account for their strong interaction near the phase-matching condition. Numerical results for beams with various collimations impinging on planar and cylindrical water-aluminum interfaces are shown and interpreted in Sec.II. Final remarks about the advantages of the complex ray method conclude the presentation.

I. FORMULATION

We consider two-dimensional scattering of the pressure field \mathcal{P} excited by a line source in a fluid in the presence of a submerged plane or cylindrically layered elastic structure. With the source located at $\underline{\rho}'$, the time-harmonic pressure field \mathcal{P} at an observation point $\underline{\rho}$ in the fluid can be derived from a displacement potential field Φ ,

$$\mathcal{P}(\underline{\rho}, \underline{\rho}') = -\rho_f \omega^2 \Phi(\underline{\rho}, \underline{\rho}') \quad (1)$$

where ρ_f is the fluid density, ω is the source frequency and a time dependence $\exp\{-i\omega t\}$ is suppressed. The potential field in the fluid satisfies the source-excited Helmholtz equation with boundary conditions that account for the layered elastic structure, in addition to a radiation condition at infinity. Solution of these boundary value problems is effected in the spectral wavenumber domain corresponding to the space coordinate tangential to the layer boundaries [14]. For the plane layered $\underline{\rho}=(x,y)$ geometry, with the layer interfaces along x , the spectral wavenumber is denoted by k , whereas for the cylindrically layered $\underline{\rho}=(\rho,\phi)$ geometry, with the layer interfaces along ϕ , the spectral wavenumber is v . With a caret denoting spectral domain quantities, the spectral decomposition yields for the planar and cylindrical cases, respectively,

$$\Phi_{pl}(x,y;x',y') = \frac{1}{2\pi} \int_{-\infty}^{+\infty} \hat{\Phi}_{pl}(k;y,y') \exp\{ik(x-x')\} dk \quad (2a)$$

$$\Phi_{cy}(\rho,\rho';\phi,\phi') = \frac{1}{2\pi} \int_{-\infty}^{+\infty} \hat{\Phi}_{cy}(v;\rho,\rho') \exp\{iv(\phi-\phi')\} dv \quad (2b)$$

Note that k has the dimensions of length^{-1} while v is dimensionless. In (2b), the physical $-\pi \leq \phi \leq \pi$ azimuthal domain has been extended to $-\infty < \phi < \infty$ in order to remove the 2π -periodicity constraint from the azimuthal wave spectra. This extension, which allows the inclusion of angularly traveling waves with arbitrary angular periodicity, properly describes high frequency phenomena arising from localized

interactions as in the present study [15]. The reduced forms of the wave equations for the planar and cylindrical cases are solved to yield [16]

$$\hat{\Phi}_{pl}(k, y, y') = \frac{i}{2\kappa_f} \left[\exp(i\kappa_f |y - y'|) + R(k) \exp(i\kappa_f |y + y'|) \right], \quad (3)$$

$$\kappa_f = \sqrt{k_f^2 - k^2}, \quad \begin{cases} \text{Re}\{\kappa_f\} > 0 & \text{if } |k| < k_f \\ \text{Im}\{\kappa_f\} > 0 & \text{if } |k| > k_f \end{cases} \quad (3a)$$

$$\hat{\Phi}_{cy}(v, \rho, \rho') = \frac{i\pi}{4} \left\{ H_v^{(2)}(k_f \rho_<) + R(v) \frac{H_v^{(2)}(k_f a)}{H_v^{(1)}(k_f a)} H_v^{(1)}(k_f \rho_<) \right\} H_v^{(1)}(k_f \rho_>); \rho, \rho' > a \quad (4)$$

where $k_f = \omega/v_f$ and v_f is the sound speed in the fluid, while $R(k)$ and $R(v)$ are, respectively, the spectral domain reflection coefficients accounting for the scattering environment [16].

Equations (2), (3), and (4) represent the formal solutions for line-source-excited inputs. The total field excited by a beam input can be constructed via the complex-source-point (CSP) technique [12]. With a tilde denoting a complex coordinate as well as functions of a complex coordinate, the line source is displaced into the complex coordinate plane via

$$x' \rightarrow \tilde{x}' = x' + ibs \sin \alpha_o, \quad y' \rightarrow \tilde{y}' = y' + ibc \cos \alpha_o, \quad b \text{ real} > 0, \quad -\pi \leq \alpha_o \leq +\pi \quad (5a)$$

$$\rho' \rightarrow \tilde{\rho}' = \sqrt{\tilde{x}'^2 + \tilde{y}'^2}, \quad \text{Re}\{\tilde{\rho}'\} \geq 0; \quad \phi' \rightarrow \tilde{\phi}' = \tan^{-1} \left\{ \frac{\tilde{x}'}{\tilde{y}'} \right\} \quad \text{with } \tilde{\phi}' = \pi \text{ when } \tilde{x}' = 0 \quad (5b)$$

The real-space field radiated by this complex source is a beam with quasi-Gaussian amplitude profile whose maximum lies along the angular direction α_o . The $1/e$ beam width w_o at the waist (x', y') is given by $w_o = (2b/k_f)^{1/2}$, which establishes b as the Fresnel length of the beam. Note that substitution of the complex extensions (5) into (2), (3) and (4) yields exact formal solutions for the beam input.

The exact spectral integrals representing Φ in the fluid can be evaluated asymptotically by the saddle point method applied in the complex wavenumber plane. Typically, one deforms the integration contour from the real axis in the complex k or v plane, along which the integrand is highly oscillatory, into the steepest descent path (SDP) passing through the stationary (saddle) point of the phase of the integrand. The dominant contribution to the high frequency field then arises from the saddle point and from the singularities (poles and branch points) intercepted during the SDP deformation. Non-specular reflection of bounded beams, which is the concern of this study, is characterized by the strong interaction of the reflected beam field contributed by the saddle point and a leaky wave pole singularity of the spectral reflection coefficient. This strong interaction, generated by phase matching between the incident beam and the leaky wave, manifests itself by the close proximity of the leaky wave pole and the saddle point, thereby requiring uniform asymptotics in the

reduction of the spectral integrals [14]. For the planar case, the final expression for the total potential field in the fluid is found to be given by

$$\begin{aligned} \bar{\Phi}_{pl}(\rho, \rho') \sim & \frac{\exp(i\pi/4)}{2\sqrt{2\pi}} \frac{\exp(ik_f \bar{l})}{\sqrt{k_f \bar{l}}} + \bar{R}(\bar{k}_s) \frac{\exp(i\pi/4)}{2\sqrt{2\pi}} \frac{\exp(ik_f (\bar{l}' + \bar{l}))}{\sqrt{k_f (\bar{l}' + \bar{l})}} \\ & - \frac{1}{4} \frac{\text{Res}\{R(\bar{k})\}_k}{(k_f^2 - k_p^2)^{1/2}} \text{erfc}(-i\bar{s}_b) \exp(i\bar{P}_{pl}^*(k_p)) + \frac{i}{4\pi} \frac{\text{Res}\{R(\bar{k})\}_k}{(k_f^2 - k_p^2)^{1/2}} \frac{\sqrt{\pi}}{\bar{s}_b} \exp(i\bar{P}_{pl}^*(\bar{k}_s)) \quad (6) \end{aligned}$$

where

$$\bar{P}_{pl}^*(\bar{k}) = [\bar{k}(x - \bar{x}') - \sqrt{k_f^2 - \bar{k}^2} (\bar{z} + \bar{z}')] \quad (6a)$$

$$\bar{l}' = -\bar{y}' / \cos \bar{\theta}_s, \quad \bar{l} = -y / \cos \bar{\theta}_s, \quad \bar{\theta}_s = \tan^{-1} \left[-\frac{x - \bar{x}'}{y + \bar{y}'} \right] \quad (6b)$$

For the cylindrical case,

$$\begin{aligned} \bar{\Phi}_{cy}(\rho, \rho') \sim & \frac{\exp(ik_f \bar{l}_i + i\pi/4)}{2\sqrt{2\pi k_f \bar{l}_i}} + \bar{R}(\bar{v}_s) \frac{\exp(ik_f (\bar{l}' + \bar{l}) + i\pi/4)}{2\sqrt{2\pi k_f (\bar{l}' + \bar{l})}} \sqrt{\frac{a(\bar{l}' + \bar{l}) \sin \bar{\gamma}_a}{2\bar{l}' \bar{l} + a(\bar{l}' + \bar{l}) \sin \bar{\gamma}_a}} \Big|_{\bar{v}_s} \\ & - \frac{1}{4} \frac{\text{Res}\{R(\bar{v})\}_v}{k_f (\rho \bar{\rho}' \sin \bar{\gamma} \sin \bar{\gamma}' \Big|_{\bar{v}_s})^{1/2}} \text{erfc}(-i\bar{s}_b) \exp(i\bar{P}_{cy}^*(v_p)) \\ & + \frac{i}{4\pi} \frac{\text{Res}\{R(\bar{v})\}_v}{k_f (\rho \bar{\rho}' \sin \bar{\gamma} \sin \bar{\gamma}' \Big|_{\bar{v}_s})^{1/2}} \frac{\sqrt{\pi}}{\bar{s}_b} \exp(i\bar{P}_{cy}^*(\bar{v}_s)) \quad (7) \end{aligned}$$

where

$$\bar{P}_{cy}^*(\bar{v}) = k_f (\rho \sin \bar{\gamma} + \bar{\rho}' \sin \bar{\gamma}' - 2a \sin \bar{\gamma}_a) - \bar{v}(\bar{\gamma} + \bar{\gamma}' - 2\bar{\gamma}_a - [\phi - \bar{\phi}']) \quad (7a)$$

$$\bar{l}' = \bar{\rho}' \sin \bar{\gamma}' - a \sin \bar{\gamma}_a \Big|_{\bar{v}_s}, \quad \bar{l} = \rho \sin \bar{\gamma} - a \sin \bar{\gamma}_a \Big|_{\bar{v}_s} \quad (7b)$$

$$\bar{\gamma} = \cos^{-1} \left(\frac{\bar{v}}{k_f \rho} \right), \quad \bar{\gamma}' = \cos^{-1} \left(\frac{\bar{v}}{k_f \bar{\rho}'} \right), \quad \bar{\gamma}_a = \cos^{-1} \left(\frac{\bar{v}}{k_f a} \right) \quad (7c)$$

In the above,

$$\bar{s}_b = \sqrt{i \left[\bar{P}_{pl,cy}^*(\bar{\zeta}_s) - \bar{P}_{pl,cy}^*(\bar{\zeta}_p) \right]}, \quad \bar{\zeta} \equiv k \text{ (planar) or } v \text{ (cylindrical)} \quad (8a)$$

$$\text{erfc}(z) = \frac{2}{\sqrt{\pi}} \int_z^\infty \exp\{-q^2\} dq \quad (8b)$$

$$\tilde{l} = \sqrt{(x - \tilde{x}')^2 + (y - \tilde{y}')^2}, \quad \text{Re}\{\tilde{l}\} \geq 0 \quad (8c)$$

The spectral variables \tilde{k}_s and \tilde{v}_s denote the complex saddle point value, while k_p and v_p denote the pole singularity of the reflection coefficient R which is approximated by

$$\tilde{R}(\zeta) = \frac{\zeta - \zeta_o}{\zeta - \zeta_p}, \quad \zeta_o = \zeta_p^* \quad (9)$$

with the asterisk expressing the complex conjugate. The commonly used simple form of (9) (see [1]) accounts for the relevant spectral phenomena associated with nonspecular reflection, in particular, the main splitting due to the close proximity of a pole and a zero in (9). The first two terms in (6) or (7) represent, respectively, the incident or direct beam field and the specularly reflected beam field. The third term accounts primarily for the leaky wave field in isolation and partly (via the complementary error function $\text{erfc}(z)$) for the strong (leaky wave)-(reflected beam) interaction, while the fourth term accounts for the strong interaction effects not included in the third term. When the observer moves outside the strongly interacting nonspecular reflection region, the third term reduces to the isolated leaky wave field plus a remainder, which is now canceled by the fourth term. The breakup into the third and fourth terms as shown is convenient for numerical computation over the entire regime near, or far from, the nonspecular region.

II. NUMERICAL RESULTS

The numerical results presented below implement (6) and (7) for a water-aluminum interface under conditions where the incident Gaussian beam is nearly or exactly phase matched to the leaky Rayleigh wave. Accordingly, for the planar case, the leaky wave spectral pole is located at [1],

$$k_p = k_p^r + i k_p^i; \quad k_p^r = k_f \sin(30.593^\circ), \quad k_p^i = 0.01494 k_f \quad (10)$$

For the cylindrical case, assuming locally planar conditions, the corresponding spectral pole is obtained via the relation [16]

$$k = v/a \quad (11)$$

which for a cylindrical interface of radius $a = 40$ yields

$$v_p = v_p^r + i v_p^i; \quad v_p^r = 127.9, \quad v_p^i = 3.75 \quad (11b)$$

The CSP-source is located at

$$(x', y') = (0, -20) \text{--planar geometry; } (x', y') = (10, -50) \text{--cylindrical geometry} \quad (12)$$

In the above, and henceforth, all distances are normalized to the fluid wavelength. Figures 1 to 3 contain typical samples of results extracted from a comprehensive data set that will be presented in greater detail elsewhere [16]. Figure 1 depicts schematically three beam-interface combinations, together with the wave periodicities induced along the interface over the extent of the incident beam. The

mechanism that establishes these periodicities is discussed in the caption of Fig.1. For the well collimated beams in Figs.1(a) and 1(c), the interfaces are well inside the Fresnel region, whereas for the strongly diverging beam in Fig.1(b), the interface is well outside the Fresnel region. When the various induced periodicities, which generate the geometrically reflected beam, interact with the constant periodicity of the leaky wave, the outcome are different interference effects, which lead to splitting of the composite reflected field. For case (a), interference nulls are far apart, whereas for cases (b) and (c), the reflected beam and leaky wave constituents are in and out of phase repeatedly over the interaction region, thereby producing patterns with multiple minima and maxima (multiple splitting). These qualitative predictions are confirmed in Figs.2 and 3. The conventionally observed splitting due to the reflection coefficient zero in (9) occurs in addition.

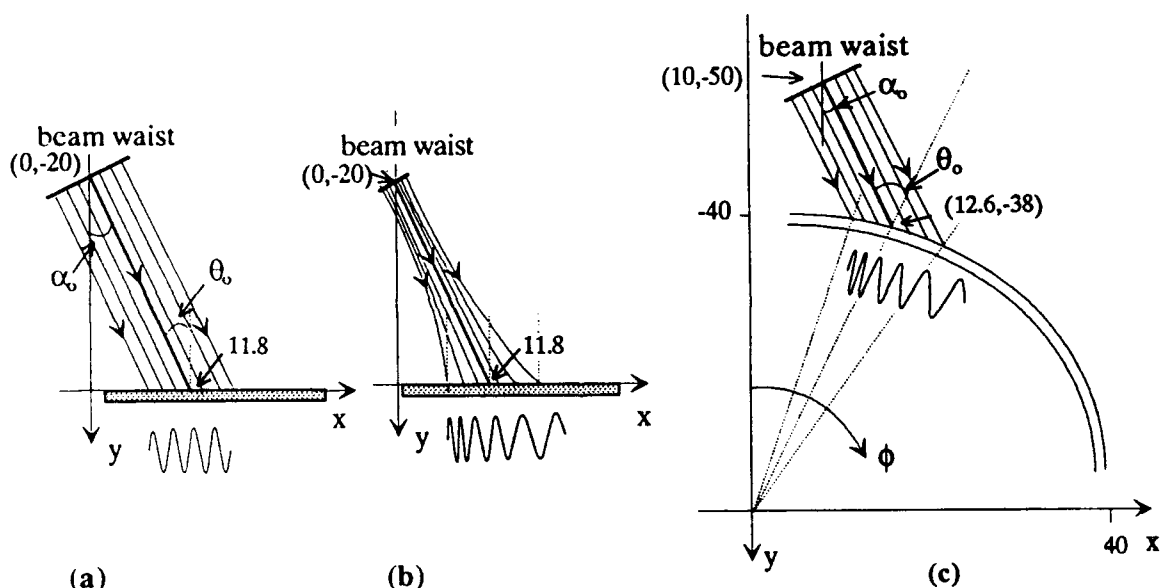


Fig.1 Schematization of interaction regions created on plane and cylindrical interfaces by various incident beams. The equiamplitude contours (phase paths) of the beams are shown up to the $(1/e)$ contours that define the effective beam widths. Wavenumber periodicities induced by phase matching (wavevector projection onto the interface) are shown below the interface. θ_0 = beam axis incidence angle. a) Well-collimated wide-waisted beam; plane interface. Periodicity along interface nearly constant (parallel phase paths, uniform projections). b) Diverging narrow-waisted beam; planar interface. Periodicities along interface vary from rapid to slow (diverging phase paths, nonuniform projections). c) Well-collimated beam as in a); cylindrical interface. Curvature induces periodicities along interface analogous to those in (b) (parallel phase paths, nonuniform projections). All distances are normalized to wavelength in fluid $\lambda_f = 2\pi/k_f$.

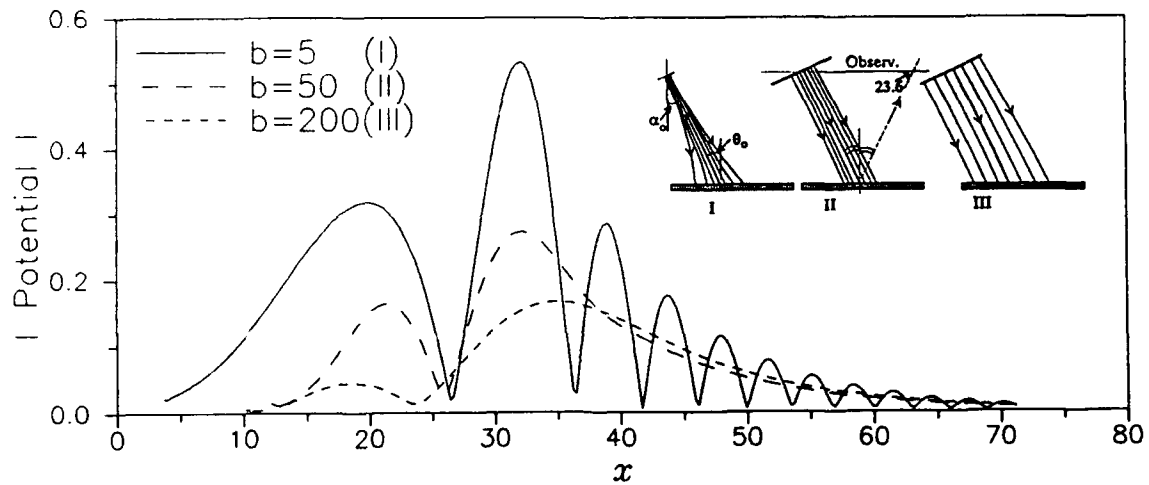


Fig.2 Detailed comparisons of total potential field magnitudes away from a plane water-aluminum interface, generated by various beams incident at the leaky Rayleigh wave angle $\theta_p = 30.593^\circ$. Beam waists located at $(x', y') = (0, -20)$ (coordinate designations as in Fig.1). Beam Fresnel lengths: $b = 5, 50$, and 200 . Corresponding $1/e$ widths at the waists: $w_0 = 1.3, 4$, and 8 . Beam launching angle with respect to y axis: $\alpha_0 = 30.593^\circ$. Observer at $y = -20$, in the plane passing through the incident beam waist. Schematics in insets show incident beam parameters, $(1/e)$ beam contours and phase paths: strongly divergent, "narrow" well collimated, wide well collimated. The geometrically reflected beam axis is drawn dashed. Plots show total potential magnitudes computed from (6), established by interference between reflected and leaky wave fields (incident field does not reach region of observation). For interpretation, see Figs.1(a) and 1(b), and discussion in the text.

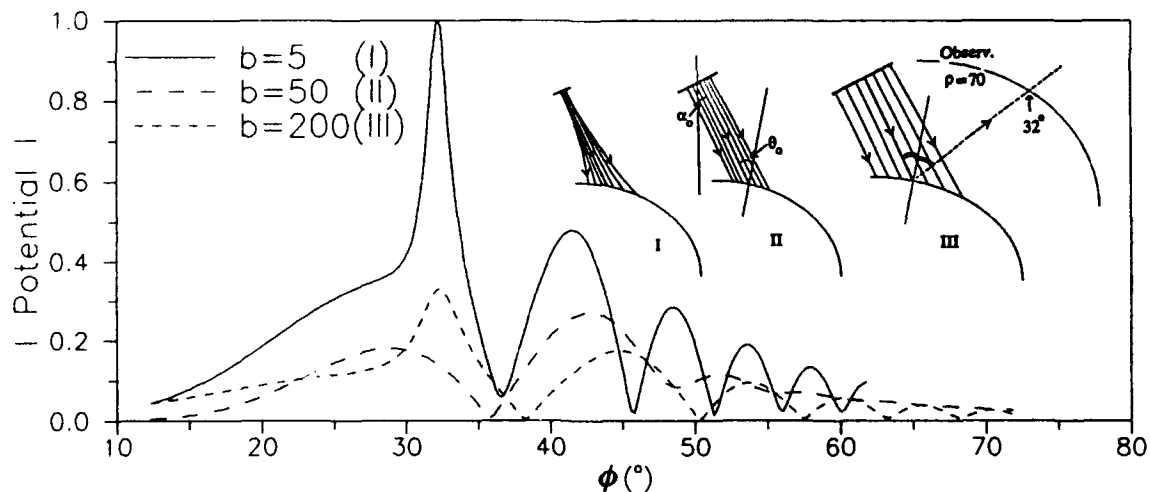


Fig.3 As in Fig.2, but for cylindrical interface, with radius $a = 40$. Beam waists located at $(x', y') = (10, -50)$. Beam launching angle with respect to y axis: $\alpha_0 = 12.22^\circ$, corresponding to incidence angle $\theta_0 = 30.593^\circ$ on cylindrical interface. Observer located on circle $\rho = 70$. Plots show total potential magnitudes computed from (7). For interpretation, see Figs.1(b) and 1(c), and discussion in the text.

CONCLUSIONS

The CSP method has been shown to furnish a versatile algorithm for predicting interaction of arbitrarily collimated quasi-Gaussian beams with plane and cylindrical fluid-solid interfaces, at arbitrary incidence angles that include phase matching to leaky waves. The algorithm can be implemented numerically without difficulty, can be generalized to arbitrarily curved and layered configurations, and can be extended to three dimensions. Details pertaining to the present applications and extensions will be submitted elsewhere for publication.

ACKNOWLEDGEMENT

This work has been supported by the U.S. Air Force Office of Scientific Research under Grant No. AFOSR-90-0088 and also, during its last phase, by the David Taylor Research Center under subcontract from Johns Hopkins University.

REFERENCES

- [1] H. L. Bertoni and T. Tamir, Appl. Phys. Vol.2, 157-172 (1973).
- [2] T. J. Plona, L. E. Pitts, and W. G. Mayer, J. Acoust. Soc. Am., Vol.59, 1324-1328 (1976).
- [3] L. E. Pitts, T. J. Plona, and W. G. Mayer, J. Acoust. Soc. Am., Vol.60, 374-377 (1976).
- [4] L. E. Pitts, T. J. Plona, and W. G. Mayer, IEEE Trans. Sonics Ultrason Vol.24, 101-109 (1977).
- [5] T. D. K. Ngoc and W. G. Mayer, J. Acoust. Soc. Am., Vol.67, 1149-1152 (1980).
- [6] J. M. Claeys and O. Leroy, J. Acoust. Soc. Am., Vol.72, 585-590 (1982).
- [7] J. Pott and J. G. Harris, J. Acoust. Soc. Am., Vol.76, 1829-1838 (1984).
- [8] H. Schmidt and F. B. Jensen, J. Acoust. Soc. Am., Vol.77, 813-825 (1985).
- [9] M. Rousseau and Ph. Gatignol, J. Acoust. Soc. Am., Vol.78, 1859-1867 (1985).
- [10] M. Rousseau and Ph. Gatignol, J. Acoust. Soc. Am., Vol.80, 325-332 (1986).
- [11] H-C. Choi and J. G. Harris, Wave Motion, Vol.11, 383-406 (1989).
- [12] L. B. Felsen, Geophy. J. R. Astron. Soc. Vol.79, 77-88 (1984)
- [13] M. Couture and P. A. Belanger, Phys. Rev. A Vol.24, 355-359 (1981).
- [14] L. B. Felsen and N. Marcuvitz, *Radiation and Scattering of Waves* (Prentice Hall, Englewood Cliffs, N.J., 1973).
- [15] L. B. Felsen, J. M. Ho, and I. T. Lu, J. Acoust. Soc. Am., Vol.87, 543-569 (1990).
- [16] Detailed manuscript to be submitted to J. Acoust. Soc. Am.